Mobile Magnetic Microrobots Control and Study in Microfluidic Environment : New Tools for Biomedical Applications

Hugo Salmon

THESIS

ÉCOLE DOCTORALE 422 :
SCIENCES ET TECHNOLOGIES DE L'INFORMATION
DES TÉLÉCOMMUNICATIONS ET DES SYSTÈMES
Laboratoire de photonique et de Nanostructures

A dissertation presented for the

DEGREE OF DOCTOR IN SCIENCES OF
L'UNIVERSITÉ PARIS-SUD

Specialty: Physics

Presented by

Hugo SALMON

Mobile Magnetic Microrobots Control and Study in Microfluidic Environment: New Tools for Biomedical Applications

Defended on the October 7^{th} 2014 on the recommandation of :

Pr.	Guang-Zhong YANG	(Rapporteur)
Pr.	Fumihito ARAI	(Rapporteur)
Dr.	Gilgueng HWANG	(Directeur de thèse)
Dr.	Anne-Marie HAGHIRI-GOSNET	(Directeur de thèse)
Pr.	Stéphane RÉGNIER	(Examinateur)
Pr.	Philippe LECŒUR	(Examinateur)
Dr.	Yong CHEN	(Examinateur)

Thèse préparée au
Laboratoire de Photonique et de Nanostructures (UPR 20), Bat. D1
CNRS
91 460 Marcoussis CEDEX

CONTRÔLE ET ÉTUDE DE MICROROBOTS MAGNÉTIQUES MOBILES EN MILIEU MICROFLUIDIQUE : NOUVEAUX OUTILS POUR LE BIOMÉDICALE

Résumé

Dans le domaine du développement d'outils de micromanipulation de haute précision pour le biomédical, les microrobots mobiles immergés font figures de technologie émergente prometteuse pour des applications in-vitro, puis à plus long terme pour l'in-vivo. Mes travaux portent sur l'étude de la propulsion de microrobots par voie magnétique dans des fluides circulant dans des microcanaux, à une échelle où les phénomènes d'adhérence et d'amortissement prévalent. Leur application pour des opérations de transduction est développée dans un deuxième volet. Un dispositif d'asservissement par vision à haute fréquence d'échantillonnage (5kHz) a été développé rendant possible le contrôle sous champ magnétique uniforme ou gradient. Les performances du système ont notamment demandé l'implémentation d'une interface multi-tâches afin de pouvoir acquérir et traiter les images en parallèle de l'actuation du robot. L'analyse de la dynamique permet de mieux appréhender les phénomènes parfois imprévisibles liés au déplacement du robot, MagPol, intégré dans une puce microfluidique. Il peut réciproquement servir de capteur dans son environnement fluidique. Ce design original de robot a été conçu pour la micromanipulation et permet également d'explorer des nouvelles stratégies de déplacement. Ces capacités ont été éprouvées sur des objets de même taille qu'en biologie cellulaire (billes, bulles). Enfin, une démonstration de l'asservissement visuel en planification de tâche a été effectuée. Sous réserve de posséder un algorithme suffisamment performant, l'échantillonnage haute fréquence en temps réel devient possible et l'observation de performances sur des trajectoires complexes est démontrée. Les performances, la portabilité et la reproductibilité du système démontrent des capacités de transduction à haut débit qui sont très prometteuses pour l'aspect applicatif.

Keywords : Microphysique, Microrobotique, Microrobot magnétique mobile, Micromanipulation, Microfluidique, Asservissement visuel, Vision.

Summary

In the research for new high performances tool for micrometric scale manipulation, mobile microrobots immersed are considered as a promising technology for in-vitro applications, and with a long term view in-vivo. My work focuses on the propulsion study of mobile microrobots immersed in microfluidic channels controlled through electromagnets. At this scale, surface and damping phenomena predominates. Application for transduction operation is developed in a second part. A high sampling rate ($\approx$ 5kHz) visual servoing setup have been developed making a control possible through uniform and gradient magnetic field. Performances of the system have notably required a multi-thread programmed user interface to acquire and analyze the frame in parallel of the robot actuation. Dynamic analysis allow to better apprehend the perturbation dynamics of the robot MagPol, integrated in a microfluidic chip. It can reciprocally serve as a sensor for in fluidic environment. MagPol design has been originally conceived for micromanipulation, and also allows to explore new displacement strategies. Its capacities have been tested on beads and bubbles equivalent to cell biology characteristic size ($10\mu m$–$100\mu m$). Finally, a demonstration of planned trajectory using visual servoing was accomplished. Though it has required an algorithm sufficiently efficient, high frequency real-time sampling is possible and lead to control and post observation on complex trajectory. Global performances, repeatability and portability of our system has demonstrated its capacities as a high-throughput transducer, promising for single microagent applications.

Mots-clefs : Microphysics, Microrobotics, Mobile Magnetic Microrobots, Micromanipulation, Microfluidics, Visual servoing, Vision.

Aux miens,

Remerciements

May the reader rest assured the content of this manuscript is in english, I simply allow myself a french parenthesis to thank all the people related to this project in one way or another.

Je ne peux commencer ces remerciements sans rendre hommage à l'**Etat français** et à son système éducatif qui a financé mes études de 4 à 28 ans et m'a permis d'effectuer un doctorat dans d'aussi bonnes conditions. J'ai conscience de la chance que j'ai d'être né en France et d'avoir obtenu la meilleure éducation possible dans des établissements publiques.

J'ai pu compter pendant ces 3 années sur les financements délivrés par l'**Agence Nationale de la Recherche** (ANR) et sur l'accueil du **Centre National de la Recherche Scientifique** (CNRS). Ce dernier, en plus d'avoir mis à disposition la plupart des consommables et matériels que j'ai employé pendant ma thèse, m'a donné accès à une centrale technologique de grande qualité et qui fut un atout incontournable dans la réalisation matérielle de mes recherches. Je remercie aussi l'Université Paris XI pour m'avoir donné l'opportunité, au travers de son école doctorale EOBS (anciennement STITS), de postuler au grade de docteur en physique et pour m'avoir accompagné, notamment administrativement, au cours de ces trois années de thèse.

Tout au long de mon doctorat, je me suis appuyé sur un ensemble de personne extraordinaire auxquelles je souhaiterais maintenant rendre hommage.

Je souhaite d'abord remercier **Gilgueng Hwang** qui a été derrière ce projet de recherche avant même que j'en prenne les commandes, m'a fait une confiance totale et a su prendre le temps nécessaire pour l'encadrement de cette thèse. Tu m'as appris plus que sur un simple plan scientifique et j'espère conserver cette grande humanité et cette passion qui anime ta démarche. Je remercie également sa famille, au sens large puisque nous avons eu le bonheur de découvrir le japon grâce à **Makiko et sa famille**. Evidemment, bienvenue parmi nous à la petite **Manon** qui j'espère s'épanouira dans cette belle vallée de Chevreuse ou ailleurs.

Merci à **Anne-Marie Haghiri-Gosnet**, pour l'encadrement bienveillant de cette thèse, tes conseils et pour m'avoir soutenu sur les différentes directions que nous avons décidé d'emprunter pour le projet.

Cette thèse n'aurait sans doute pas été la même sans mon ca¬marade de terrain **Laurent Couraud**. Sans peur, sans reproche et surtout sans tabac (je tire mon chapeau), Laurent a abattu à mes cotés un travail remarquable, non seulement sur tous les dépots métalliques que nos microrobots ont nécessité (paix au Plassys 550) mais surtout sur le travail d'architecte informatique, le tout en arrêtant de fumer. Nous avons ensemble eu le privilège de représenter et faire gagner les couleurs tricolores pour les compétitions de microrobotiques, ce qui s'est surtout solder à faire des bonds de géant aussi bien sur le plan technique, géographique et humain. Puisse cette richesse péricliter après mon départ et puisse Laurent continuer à garder ce language fleuri, en Anglais comme en Français, qui ne suffirait bien entendu pas à le caractériser. Ce qui m'amène naturellement à citer mon successeur, **Antoine Barbot**, avec qui j'ai pris plaisir à connaître durant cette année commune, à partager la petite escapade Vaudoise, et à qui je souhaite belle réussite pour sa thèse et surtout la suite.

Il n'est pas dit que je finirai le listing de mes mousquetaires sans mentionner Sébastien Alvo, dit **Sconly** dans certains milieux. Ne me demandez pas pourquoi, j'oublie à chaque fois. Sans lui, qui sait si j'aurais eu l'idée de postuler à l'ISIR pour mon stage de master, et

plus tard oser cette belle aventure. C'est grâce à toi si je suis docteur, aussi un grand merci.

Je remercie d'ailleurs **les équipes de l'ISIR** - **Bruno**, **Puco**, **Aude** - pour m'avoir donner le goût de la recherche durant mon stage de fin d'étude. Tout particulièrement je remercie **Sinan Haliyo** pour le coaching geek nécessaire au trop jeune programmeur que j'étais durant mon stage, **Cécile Pacoret** pour son aide sur mon banc d'optique, et le professeur **Stéphane Régnier** pour m'avoir suivi avec bienveillance et avec qui j'ai pu échanger du début à la fin de cette thèse, en prenant part à mon jury.

Cette thèse s'est faite au sein du groupe **Nanoflu**, un groupe indéniablement humain dans lequel j'ai pris plaisir à grandir et auquel je veux rendre hommage. Bien entendu merci à **Dominique** « **Cash** » **Decanini** pour ses échantillons et sa verve ma foi assez direct. **Jean-Christophe Galas**, qu'on pourrait à juste titre qualifier de MacGyver, l'accent du Vaucluse en plus, m'a transmis son goût pour la belle manip, la débrouille et je te remercie pour tous tes précieux conseils, ta patience et ta disponibilité. Merci aussi **André Estevez-Torres** pour ton soutien inestimable, sur le plan scientifique mais aussi dans mon rôle de représentant des thésards. Une « spéciale » à votre dream-team: **Jonathan-san**, **Anton** dit-le challenger et **Adrian** le latin lover. Merci également à **Antoine Pallandre** et **Charlie Gosse** avec qui les échanges scientifiques ont toujours été féconds. Bienvenue à l'ostie dchris'd'Montréalais que j'ai eu le plaisir de croiser quelques semaines avant mon départ, **Emmanuel Roy**. Enfin, **Xuan Zhao**, merci pour tes enseignements en salle blanche, mais aussi en Mandarin et en pantomime. Puisses-tu continuer à entretenir cette joyeuse folie qui fait si peur aux gens de la Sodexo, aux cygnes du parc, mais nous ravit quotidiennement.

Mon accueil au LPN s'est fait dans d'excellentes conditions aussi grâce à **Isabelle Sagnes** que je remercie et à qui je souhaite courage pour voir le bout du futur institut qui réunira IEF et LPN. Appelons le C2N, Inch'allah. Merci de m'avoir présenter **Rémy Braive**, qui a été d'une aide précieuse pour les questions d'optique, aussi rudimentaires étaient-elles, et le matériel prêté. Merci aussi **Sylvain Barbay**, **Andrea Cattoni** avec qui les échanges m'ont fait progressé sur des questions importantes de ma thèse.

Grand et sincère merci aux dames qui gèrent l'administration d'une main de maitre et sont d'une aide si précieuse : **Agnes Roux**, **Joelle Guitton**, **Marina Ferreira**, **Melissa Mauchien** et **Sandrine Bouvy**. Je vous rassure, je soigne cette vilaine phobie administrative aiguë et je suis sur la bonne pente. Un grand merci également à **Patrick Hisope**, gardien du temple et des clés de la salle Planel qui sont tout simplement caché sur ... on me fait signe qu'il faut que j'accélère. Merci d'ailleurs à Richard Planel pour sa salle polyvalente: pouvoir soutenir une thèse et faire du ju-jitsu, de la corde à sauter ou un pot de thèse le tout dans la même salle le même jour relève de la performance.

Merci aux dieux du petit écran LCD, # leserviceSI pour parler dans l'ère du temps: **Lorenzo Bernardi**, **Medhi Idouhamd**, **Olivier Orias** et **Alain Péan**.

Grand respect à mes co-thésards, je cite: **Inès** « **choupinette** » **Massiot**, **Nick Vandamme**, **Clément Collin**, **Benyamin Portier**, **Christelle Tuambilangana**, **Benoit BB Behagel**, **Juan** « **le dauphin** » **Castro**, **Emilie Steveler / Michael Verdun** « les apprentis lémuriens », **Valerian Giesz**, et j'en passe...

Un grand merci aux chicanos **Sébastien Le Baut** et Olivier Benaud (vous arborez des chapeaux mexicains dans l'atelier, assumez) pour avoir aidé aux développements de mes différents setup et pour mes plus folles demandes.

Des ingénieurs et techniciens m'ont également été d'une aide précieuse dans cette thèse aussi je leur rend hommage pour leur effort quotidien qui contribue à faire du LPN une belle exception : **David** « **Ballon d'or** » **Chouteau** et **Christophe Roblin** pour sa patience envers mes talents de lithographe, **Ali Madouri** pour les gravures TMAH, **Laëtitia Leroy** pour avoir porter le fardeau des dépots métalliques avec le sieur Couraud, toujours dans la meilleure humeur, **Christian Ulysse**, **Nathalie Bardou**, **John-Claude Esnault** et sa fidèle sonde d'humidité, **Xavier** « **les bons tuyaux** » **Lafosse** (je suis sur le coup pour Fight Club 2, même si les 2èmes opus égalent rarement le 1er), **Luc Le Gratiet** et **Edmond Cambril** pour m'avoir parfaitement accueilli en salle blanche, **Olivia Mauguin** que j'ai beaucoup fait scié avec la scie ESEC - paix à son âme, **MNM** pour les repas de noël et ses mails qui m'ont fait perdre deux dioptries à chaque oeil. Je conclue mes remerciements « technologiques » par Monseigneur **Christophe Dupuis** pour son amour du beau verbe, de la belle pensée et pour son mollet galbé, **Stéphane Guilet** sensei pour ses enseignements et ses mawashi geri et enfin **Laurence Ferlazzo** qui a su me laisser une grande autonomie pour les dépôts électrolytiques, pour sa pédagogie et son enthousiasme.

Il est logique de continuer avec mes camarades de **Klearia inc.**, tant j'ai bénéficié de leur savoir-faire en salle et je ne parle pas de salle de marché. Mais c'est surtout par nos multiples escapades, que ce soit sur un tatami, dans un bois ou autour d'une table ou d'une machine à café que j'ai pris plaisir à connaître **Clément** « **PDG**» **Nanteuil**, **Guillaume** « **kool shen** » **Da-Rold**, **Gregory** « **sponso the Kooples** » **March** et leur égérie **Anne-Claire Louer**. Longue vie à la boite, bonheur dans vos familles respectives, vous êtes des belles personnes, pas de doutes.

Anne-Claire Louer, vous m'avez avec **Elsa Mazari** pris sous votre aile quasiment dès mon arrivée au labo, alors que vous étiez toutes les deux vétérans chez Nanoflu. Certes, c'était au départ pour me protéger de Charlie qui essayait de me faire rentrer dans le crane le bon trajet de bus. Vous étiez bien plus qu'une Kate et qu'une Moss pour moi, et je crois pouvoir affirmer avec le recul qu'on a formé un sacré threesome, si vous me passez l'expression. Vous avez été mes petites bulles d'air pendant mes premières années (des petites bulles pleines de nicotines pour Elsa certes) et m'avez permis de croître sans douleur. Je vous en remercie beaucoup. Longtemps les murs du laboratoire raisonneront de nos fou-rires, de nos accents wallons. Puisse des statues de nous labélisés « client de l'année » être érigés à Cora au rayon apéritif et traiteur.

Merci à ceux qui ont fait de moi ce que je suis aujourd'hui et à qui je transmets mon amour sincère : mes doux **Parents Pascale** et **Danny**, mon frère **Lucas**, ma famille **Salmon** comme **Memery**, ma petite tante **Yolande**, mes frères de la **Street**, **Samuel Gonnet** que je n'oublie pas, mes **Centraliens**, mes **Ludiens**. Merci également aux **Torres** et aux **Bourgades**, qui m'ont accueilli à bras ouvert, m'ont sontenu et deviennent de jour en jour une belle seconde famille. Finalement, merci à celle qui m'a soutenu pendant toutes ces phases de rushs où je suivais l'évolution inverse de Darwin, celle qui a la faculté de m'émouvoir autant que me faire rire et avec qui je vis aujourd'hui. Merci à toi, **Margot**.

List of abbreviations

Table 1: Body mass and viscosity comparison between air and water in standard conditions.

BME	Biomedical Engineerings
MEMS	Micro ElectroMechanical systems
POC	Point of Care Diagnosis
OECD	Organisation for Economic Co-operation and Development
RFID	RadioFrequency IDentification
FIGS	Fluorescent Image Surgery
MIS	Minimal Invasive Surgery
PDMS	Poly-DiMethyl Siloxane
LOC	Laboratory On Chip
KLT	Kanade-Lucas-Tomasi algorithm
ViSP	VIsual Servoing Platform
CNRS	Centre National de la Recherche Scientifique (French National Centre for Scientific Research)
INRIA	Institut national de recherche en informatique et en automatique (French Institute for Research in Computer Science and Automation)
GMG	Glass-Metal-Glass chips
(G)UI	(Graphical) User Interface
SEM	Scanning Electron Microscope
MMM	Mobile Magnetic Microrobot

Contents

List of Figures

List of Tables

Introduction

This thesis work has been achieved in Laboratory of Photonics and Nanostructures (LPN), proper unit of research (UPR 20) of Centre National de Recherche Scientifique (CNRS). This laboratory is one of the five national technological centers. I have been part of Nanoflu team for my researcher formation and was financed by the Agence Nationale de Recherche (ANR) in order to become an expert in micro-nanorobotics for medical application. The ANR name was NOMAD coordinated by Dr. Gilgueng Hwang.

This PhD project has been proposed one year following my former master internship project in Institut des Systèmes Intelligents et de Robotique (ISIR, Universitée Pierre et Marie Curie - Paris), 2011. The preliminary studies of helical nanobelts by developing a helmholtz magnetic setup has brought me to consider better temporal resolution control and understanding of magnetic phenomenon. Following bibliographical research and discussions with different community, I figured out how crucial it would be to control microrobot dynamics before starting applying this technology as a transducer.

The non-linear phenomena involved with surface effects require better control and understanding. The importance of the environment we developped our system was as much a key point as controlling the propulsion magnetic forces. Micro & nanofabrication as well as computer science are now sufficiently mature to explore both of these points. Microrobotics experiences are considerably challenging in terms of instrumentation, particularly in liquids where interfaces effects become predominant. Microfluidic chips offer the most adapted experimental platforms and we relied on LPN know-how to adapt it for microrobotic usage. It has allowed us to conduct our research in a virtuous circle of development, where the chip constitutes a perfect environment for exploring robot's hydrodynamics on one side and a tool for in-vitro manipulation on the other-side.

— Chapter I introduces technical and application background of microrobotic, with different axes of development and different approaches. It will help the reader to apprehend my PhD work and the direction we will explore for biomedical applications.
— Chapter II details the technological development achieved at LPN to provide a unique microfabrication process of integrated microrobots in microfluidics, controlled through magnetic waves. We underline the design challenges to combine an external magnetic circuit to a microrobotic visual control loop. Relying on a transparent PDMS-Glass chip technology, we can control border conditions (surfaces) and their impact on the microrobot, named MagPol (for Magnetic Polarizable microrobot). This technique also allows to work with an optical feedback in transmission for high sampling rate imaging.
— Chapter III deals with the real-time open-loop control of microrobot with a human-computer interface. Motion capacities are explored using alternatively uniform field or gradients. Some original motions and new manipulation strategy are proposed and demonstrated on micro scale objects.
— Chapter IV is dedicated to the post-treatment analysis of acquired fast performances in fundamental mode of motions (planar translation and rotation). We build a model based on literature of the robot environment forces and deduce a direct relation between physical parameters and the robot time-response. Using the adapted tracking algorithm, we can better understand the robot motion in microfluidics and extract sensing capacities from it.

— Chapter V focuses on the high sampling rate visual servoing. Using a sufficiently fast shape detection algorithm for tracking position, we can develop a path planning command for complex trajectory. The importance of certain physical parameters as well as control corrections are studied experimentally.

Part I

Mobile Microrobots for transducing application in medecine

Summary

This introductory chapter offers a general context on the study of mobile microrobots applications in microfluidics. The socio-economical context is a real driving force for the development of new solutions in biomedical applications. Combined with the current available technology, it justifies this work purpose. Above all, this chapter attempts to describe why I have specifically worked in microfluidic environment as an original angle of mobile microrobots. Some of the current challenges in biological sciences and medicine can be overcome thanks to the fast-growing microrobotics sciences - a combination of recent advances in robotics and microsystems. We will then focus on a still emerging technology where untethered dynamic microrobots (mobile microrobotics) are studied and controlled in a challenging physical environment: fluids at microscale. For comparative purpose, we will define their capacities of swimmers compared to biological organisms. Finally, we introduce a particular environment of development for them with microfluidics, in which we can develop their capacities as a useful and functional transducing tool at microscale inside the confined liquid environment.

1 Microrobotic applications for biomedical sciences

Microrobotics [27] is a relatively young research field which might generate a revolution in our exploration of microworld, particularly for biomedical engineering, for therapeutical purpose as well as biological manipualtion and analysis. What justifies this revolution? What are the current requirements for microrobotics development? This bibliographical section is dedicated to provide answers to these questions through a synthesis, going sometimes beyond the pure scientific purpose.

1.1 Economical and societal context

We define biomedical sciences as a set of applied sciences extended from biological sciences with direct medical applications. It aims to develop knowledge, techniques, or technologies of use in healthcare or public health [28].

This field is also quite young and benefits of a growing interest in modern societies where healthcare expenses represent a non-neglectable part of their gross product. Statistics from the Organisation for Economic Co-operation and Development (OECD) reports [29] displays the important volume of market that healthcare constitutes(Fig.1). The more specific example of the budget of France [30] displayed 9.04% of its gross domestic product for health expenses in 2012. Though recent economical crisis has positively increased this ratio, it confirms the importance of this budget at our scale.

The continuous creations of global scale groups of research, start-ups and specialized formation in Biomedical Engineering (BME) are important signal to show how attractive this domain is [31, 32]. Medical devices constitute one of the 34 targeted markets by French governement in 2014. This strategy aligns to Europe's Horizon 2020 program on Health and well-being. The important framework that EU has recently develop for research and innovation [33] contains 4 general axes summarized as:

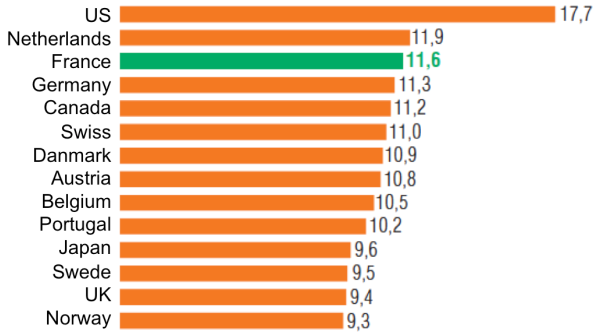

Figure 1: Overall gross domestic product percentage healthcare expenses in OECD countries in 2011, France's ranking 3^{rd}; Source:OCDE *from Insee TEF 2014*.

— improve our understanding of the causes and mechanisms underlying health, healthy ageing and disease
— improve our ability to monitor health and to prevent, detect, treat and manage disease
— support older persons to remain active and healthy
— test and demonstrate new models and tools for health and care delivery

and 1.2 billions *e* are being invested in these challenges just for 2014/15.

All these axes will require a deeper exploration of cellular scale and beyond - i.e. scaling down to μm scale and below, developing new microtools. One key step is the automation of these tools to improve healthcare quantitatively (speed, range of action) as well as qualitatively (precision, resolution of control). Automation has been an important step in our industrial development in the 20^{th} century and has contributed to the accessibility and fast improvement of many manufactured products. Robots have boosted the productivity to an impossible level for human, has made interventions possible in the environment with extreme physical conditions and is continuously overcoming user skill dependency [34].

Because of the population growth and ageing society, western societies have an urgent and growing need in healthcare, to assist medical doctors (MDs) and other health practitioners as well as improving life quality of patients. Whether it is for medical diagnoses and measurements, targeted therapy, or intelligent structures, the needs in automations applied to microsystems will continue to increase in future.

1.2 Medical diagnosis challenges

One of the key issue in hospital and patient life lies in early medical diagnosis. With increasing overpopulation, every part of the patients flow chain must be compressed and considered, minimizing their time in-situ. We do not study here the challenges in IT (information technology) - though I had the opportunity during a short training in a medical staff to notice it remains a important tool for diagnosis. This logistic issue is then a BME challenge in medical diagnosis, see Fig. 2. Every link of the chain takes time to the patient and the hospital, particularly diagnosis. It is a necessary preliminary to any treatment, and more importantly a repeated control to screen early apparition of disease as well as progression of treatments. In France, in-vitro diagnosis (IVDs) represented 1.77 billions *e* in 2010 - $< 3\%$ global market if we refer to a recent study from Les Echos [35].

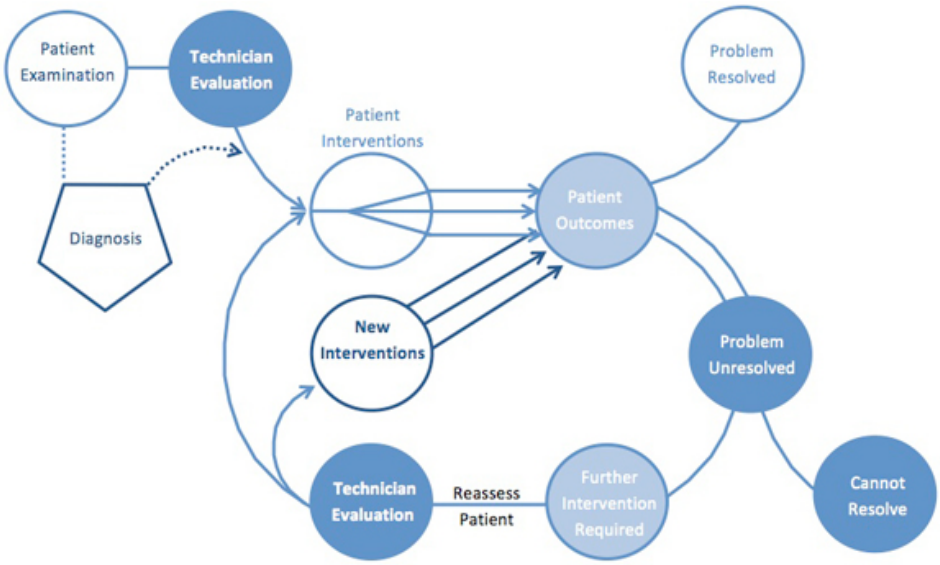

Figure 2: Simplified flow chart displaying general patients chain of treatment.

Point-of-Care diagnosis (POC) The diagnosis that brings tests closer to the site of patient care, flexibility requires low consumption of reagents and sample, miniaturize devices, and accelerate turn-around time for analysis. The short turnaround time and minimal manual interference enable quick clinical decisions. Growth in the POC diagnostics is being continuously fueled by the global burden of cardiovascular and infectious diseases. Early diagnosis and rapid initiation of medical treatment are crucial to the successful care for such patients [36, 37].

This technology contains 3 axes of development which are
— sample collection, concentration, and preparation [38]
— readout and signal transduction
— amplification and detection technologies

Many efforts are achieved in these directions, in microfluidic chip as well - see this further in next subsection. Most of the time, POC are a simple test like on Fig. 3 measuring a quantity or detecting a concentration. Some solutions can even be embarked, implanted subcutaneously (below patient's skin) for continuous monitoring.

Figure 3: Example of a quantitative POC giving glucose concentration from a blood drop via a amperometric sensor [1].

Screening strategies Diagnosis and detection allow to anticipate at sufficiently early stage diseases such as cancer or acquired immunodeficiency syndrome (AIDS) as well as Alzheimer based on their factors [39]. This has a critical importance because survival rate is better at early stages diagnosis. As it deals with healthy patients, false positive or negative tests must be minimized to have more efficient test. Automated tests allow to reach higher throughput and increase their efficiency in a massive screening context as well as a high risk selective screening, making them cheaper and more reliable [40].

Implantable devices An alternative evolutionary line of medical diagnosis technology is implantable devices. This was considered by Leyland C. Clark in his original paper in 1962 [41] and realized in a practical form, as a needle-type subcutaneous electrode by Shichiri et al as early as 1982 [42]. The first application of these devices are used for treatment purpose but it can be applied for monitoring as well [43]. MEMS technologies have led to next generation devices that are now industrialized and tested on patients [2] - Fig.4.

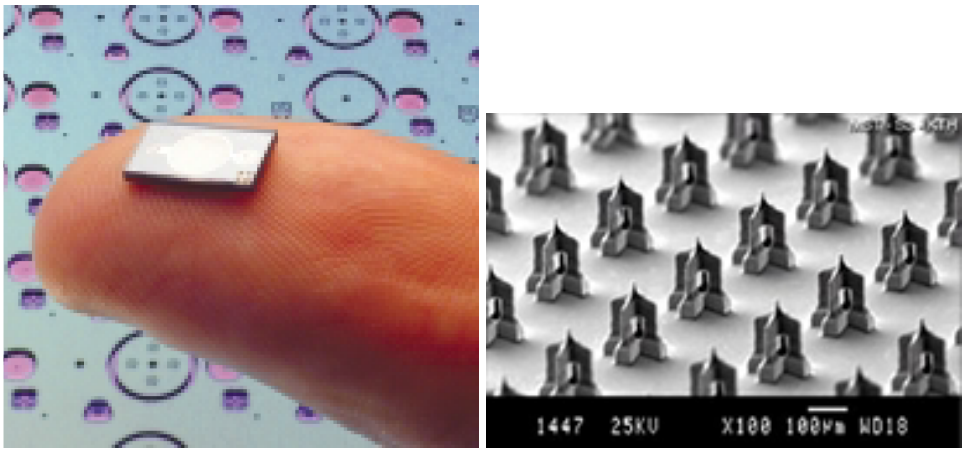

Figure 4: Implantable device based on MEMS (left) Micropump developped by Debiotech SA for insuline, injecting 150nL per cycle; The system is patched over the skin of the insulin dependent patient (right) SEM picture of integrated MEMS needles for injection [2].

It also consists of in-vivo remote monitoring of various vital signs using MEMS technology and physicochemical property [44] (chemical concentrations, pressure, temperature, pH) to transmit a measurable signal. Efforts are invested on wireless transmission, particularly using

— radiofrequency (RF) waves: covering radio frequency transmission, it is already used to tag patients with RFID technology [45].
— photonic: using photons covering the whole spectrum from ultraviolet to infrared. Many interesting properties are exploited with fluorescent particles, though signals can only be transmitted through thin tissue. Fluorescence image-guided surgery (FIGS) is already used by practicioners [46] and new fluorophore are being invested such as quantum dots (QDots) [47] or tagged proteins and Deoxyribonucleic acid (DNA) [48].
— acoustic: ultrasound-based (for its better propagation in tissues) diagnostic imaging technique used for visualizing internal body structures including tendons, muscles, joints, vessels and internal organs for possible pathology or lesions. Current efforts are done for enhancing contrast, using microbubbles [49].

Medical implants in the future will likely combine both monitoring and therapy such that both modalities work together to achieve optimized and personalized closed-loop therapy that

is informed by the patient's need [50], announcing a need in robotic technology.

1.3 Localized therapy with minimal impact

Most of the time, a positive diagnosis leads to a therapy. We can classify three mode of interventions: medical, surgical or medico-technical. Each of their adverse effects in certain case should be minimized either by acting exclusively with the pathogen (specificity) or by being active in the limited area of the disease.

Targeted therapy Targeted therapy or molecularly targeted therapy is one of the major modalities of medical treatment (pharmacotherapeutics) for cancer, others being hormonal therapy and cytotoxic chemotherapy. It consists in destroying or inhibiting a specific cell associated with carcinogenesis, usually using monoclonal antibodies or drugs. It requires strong identification of the cancer nature and does not have a 100% success rate.

The case of particularly aggressive pharmaceutical treatment such as for cancer, hormonal therapy of cytotoxic chemotherapy, pops the first in mind. But it is also the case of minimally invasive surgery (MIS) operation which presents a number of significant challenges due to the limited manoeuvrable workspace and the presence of many delicate structures that must be avoided, including sensitive cartilage surfaces, soft tissue structures, nerves, blood vessels and tendons. A famous example is appendectomy now achieved by laparoscopy [51] and only requires three small $0.5 - 1cm$ of incisions whereas laparotomy used to require longer recovering time. Thanks to these techniques, it now only takes a day for the patient to leave the hospital and recovery is much faster.

To optimize its effect, it is interesting to localize the treatment -Fig.5- in the predefined regions of interest using cargo transport on nanoparticles swarm [52] coated with biocompatible materials and functionalized with drugs, proteins or plasmids. Another possibility is to generate hyperthermia with a resonating swarm of ferromagnetic particles, raising temperatures up to to 45°C). Research has shown that high temperatures can damage and kill cancer cells, usually with minimal injury to normal tissues [53]. By killing cancer cells and damaging proteins and structures within cells [54], hyperthermia may shrink tumours [55].

Minimally invasive surgery (MIS) Minimally invasive surgery revolutionized conventional surging by drastically reducing patient recovery times by allowing surgeons to perform procedures through a series of small incisions [56]. However, MIS has also increased the complexity of the tasks as tools did not have the same degrees of freedom and dexterity compared to conventional surgery. Microsurgical procedures, such as nerve or blood vessel anastomosis, are further limited by the challenges of manipulating millimeter-scale and submillimeter-scale tissue structures that are exceedingly fragile and thin. Current commercial MIS instruments are morphologically simple and lack distal articulation or sensing. Additional degrees of freedom and sensing would enable greater access and dexterity and the ability to record and control force applied to the tissue. The surgeon require a simulated learning environment facilitated by intensive cadaveric training. Most of the time operation involves remote-control manipulation of instruments with indirect observation of the surgical field through an endoscope [57].

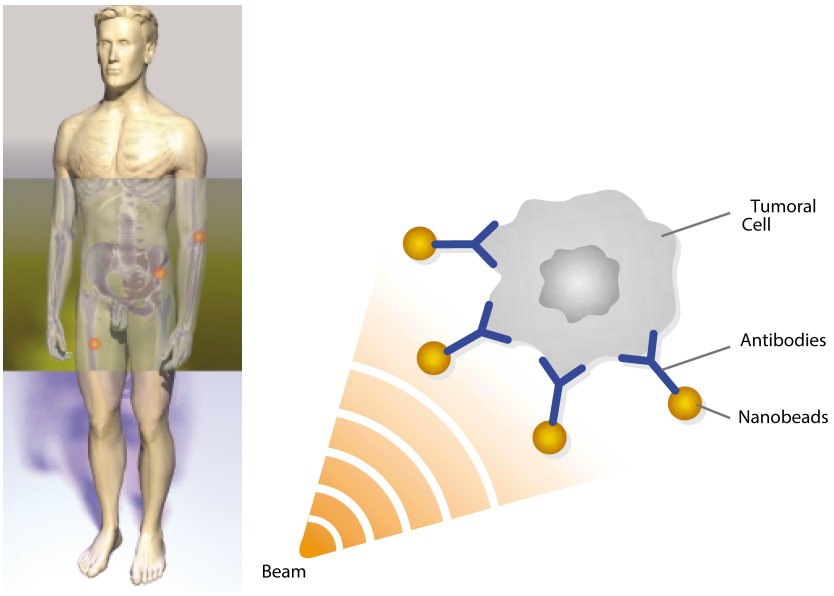

Figure 5: In-vivo drug targeting (left) The drug are cargo transported /active in the region of interest of the body (right) Here the nanobeads are coated with antibodies corresponding to the tumorous cells.

1.4 Biology and Medicine challenges requiring high performances tools: Microrobotics Contribution

Microrobotics [27] is the field of miniaturized robotics, more specifically robots with characteristic dimension $< 1mm$. Most of the time this dimension designates the end-effector, mostly transmitting a mechanical effort for contact interaction, and has usually been tethered to a bigger actuator [58] -Fig.6. As it covers the scale of cellular biology and can

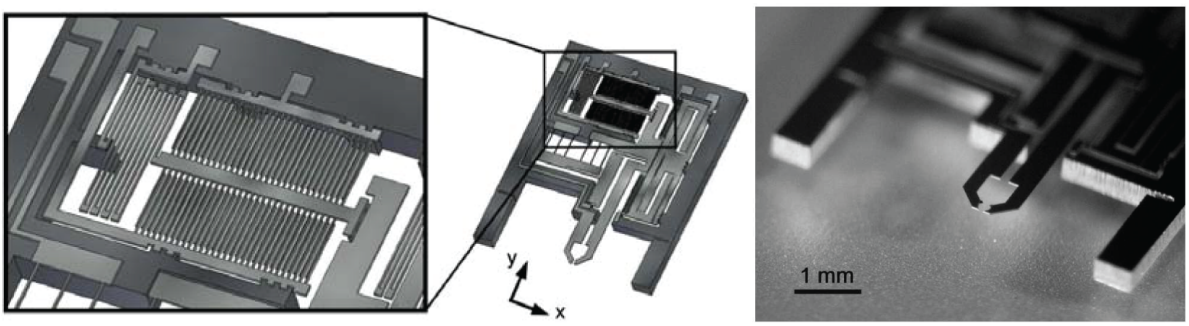

Figure 6: Microfabricated mechanical tweezer actuated by electrostatic forces, from Yamahata et al. [3] in LIMMS.

cargo transport molecules, it is a promising discipline [59] for BME next generation precision tools. Automated device already exists at macroscale and are revolutionizing medical therapies and diagnosis. Though miniaturization technologies and microworld physics have much progressed thanks to microelectronic process, microrobotics has needed more than 20 years to see emerging solutions assisting physicians. For visual servoing, diagnosis and teleoperated surgery, knowledge in process and physics are now mature enough to develop and explore mobile microrobotic solutions.

Automated medical device at macroscale Before going any further in the case of mobile microrobot, it is interesting to notice how robotic technology is already contributing today to understand what might be future challenges at lower scale. On an industrial level, automating the fabrication of tissue/organ engineering which requires a high throughput allows for example to assemble enough cell sheets to fabricate tissue/organs [60] for transplants. More generally, every redundant and/or complex task achieved in laboratory can now be achieved with automated actuator at higher throughput and precision on biological sample . It is particularly useful for massive task strategy such as screening [59]. Analysis algorithm in vision now contributes drastically to computer aided detection. It assists [61] or replace physicians for routine diagnosis to focus on the most challenging cases. Another type of biomedical that increases the quality of life of the patients are intelligent prosthesis [62] that can emulate the full biomechanical functionality of the healthy limb. Finally, human-machine interfacing is a key point for remote or assisted surgery [63].

Laboratory microscale task For ten years, miniaturization has tackled with medical laboraty process, trying to make it hold on a microchip [64], successfully [65]. We will detail in next subsection the principle of lab-on-chip. They have important applications for the operation such as manipulation from oocyte [66] to cells [67], intracellular delivery of nanoparticles [68], genetic analysis [69].

Pushing visual servoing limit Vision in medecine is used for diagnosis as well as necessary feedback during surgery [70]. It enables for example to guide a needle in real time using magnetic resonant imaging (MRI) [71]. It can also be used for micromanipulation tasks [72, 73]. It is now possible to access new spatiotemporal resolution of imaging in surgery videos. As the microcontrollers are increasingly precise and reliable, we can achieve visual tracking at high speed or high precision [74] for the most complex scenes [75].

Teleoperation for surgery: human-microtool interfacing Telesurgery has been more and more popular in robot-assisted medical intervention. Increasing practitioner comfort, robotic surgery enables difficult technical manoeuvres to be performed that facilitate the success of minimally invasive surgery. It can adapt with a homothetic transformation the action of the user to the targeted scale of interest,increasing precision and stability. Teleoperated robots are controlled by human operators and allow us to act in environments that are inaccessible for reasons of safety, scale, or remoteness.

Unfortunately, due to lack of tactile sense and dexterity and proprioception, task performance can suffer compared to direct object manipulation with the hands. Still, the use of human controlled robots is the only viable option for these dangerous or hard-to-reach applications, since autonomous robots do not yet have the capability to autonomously perform most unstructured tasks [76].

Current visible progress are then ergonomy and lead to the important development of haptic interfaces which produces a force feedback for the user control [77] but a considerable progress could be made on the miniaturization and mode of control of the end-effector [49].

1.5 Conclusion

We introduced BME development in diagnosis and localized therapy and identified what will be major scientific and technological incoming challenges. We have seen that robotic already provides at macroscale powerful solutions in terms of precision, force range, robustness, minimizes requirement of a user skill. It can help the surgeon as an interface between him and his tool, enhancing his capacities. After 30 years of development, robotics is now proposing solutions for medicine and biology at macroscale and is slowly scaling down to increase the range of potentialities. Next step is now scaling down robotic agents with embedded functions. Using advances in microtechnologies, we could expand their capacities in confined environment and complex situations - see Fig. 7. Providing remote information by telemeasurement

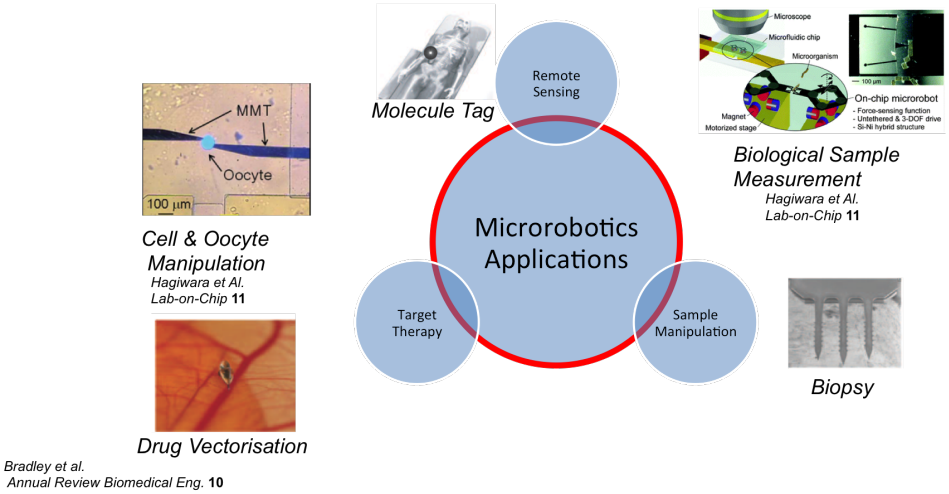

Figure 7: Medical major tasks for microrobots, including targeted therapy, material removal and telemetry.

2 Microrobots integrated in microfluidics

In this section, we decide to answer first the ”where?” question and keeps the ”what?” question for next section. In other words, where can we study mobile microrobots in liquids at microscale?

We describe the major issues of scaling down biomedical devices and the solution provided by microfluidics chip. The microfabrication process developed for microelectronics and MEMS [78] revealed themselves to be compatible with a wide range of existing technologies and in particular the design of microfluidic cavities on chip. The coupling of microfluidics with micrrobotics provide more and more powerful tool for research as well as industry or medicine. We will introduce first the few notions necessary to apprehend the challenges of this domain.

2.1 Microfluidics and Lab-on-Chip: Presentation and challenges

Microfluidics, definition Microfluidics is the science that deals with the liquid flow inside channels of micrometer scale. At least one dimension of the channel is of the order of a micrometer or tens of micrometers in order to consider it as microfluidics (see difference between nanofluidics, microfluidics, millifluidics and the behaviour of fluids at these scales) [79]. Microfluidics can be considered both as a science (study of the physical behaviour of fluids in micro-channels) and a technology (manufacturing of microfluidics devices for applications such as lab-on-a-chip). Generally, when researchers mention microfluidics, they refer to man-made channels. Fluid flow in natural microchannels as blood vessels or plants capillaries are mostly excluded from microfluidics, though they deal with the similar physical phenomena.

Microfluidic chip, lab-on-chip, definitions A microfluidic chip is a set of micro-channels etched or molded into the materials (glass, silicon, polymer PDMS). The micro-channels forming the microfluidics chip are connected together in order to achieve a desired function (such as mix, pump, redirect and/or allow chemical reactions in a cell).

This micro-channel network embedded in the microfluidic chip is connected to the outside by inputs and outputs holes, as an interface between the macro- and micro-environments - see Fig.8. It is through these holes that the liquids (or gas) are injected and removed from the microfluidic chip (through tubing, syringe adapters or even free holes in the chip).

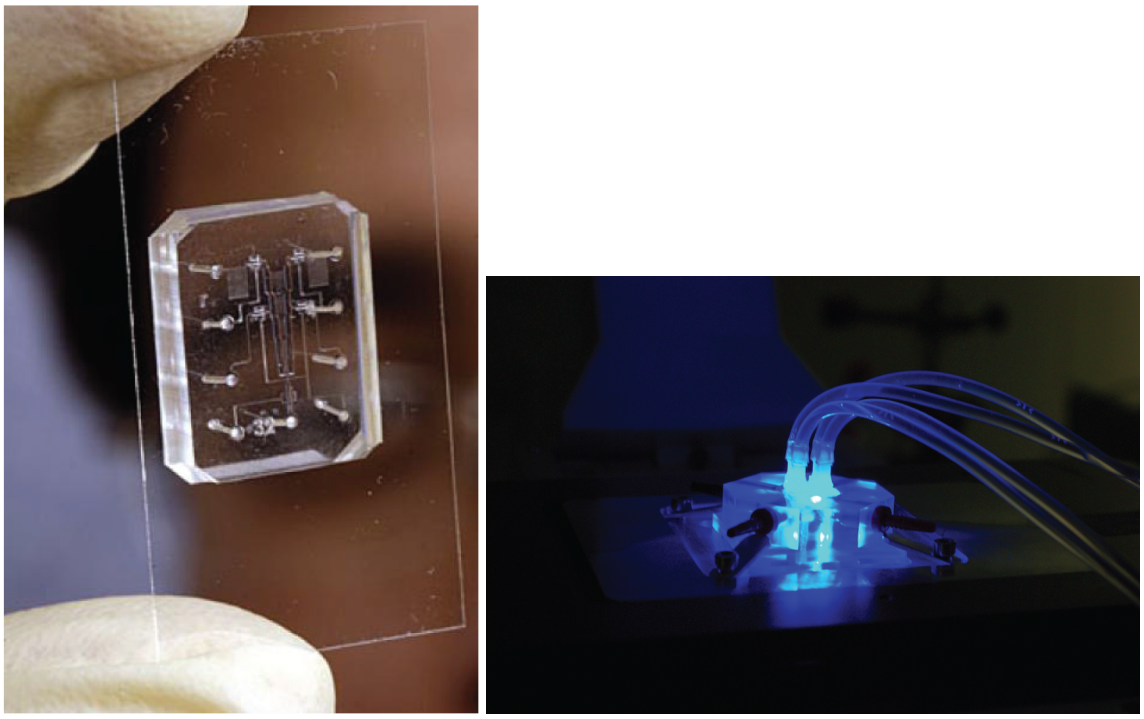

Figure 8: Microfluidic devices (left)Microfluidic chip made of PDMS from Plecis thesis for study of [4] (right)Connected microfluidic chip for fluorescence study by Louer [5].

By extension, a lab-on-chip (LOC) integrates **analysis**, **synthesis** and **separation** in a microfluidic chip to create a new class of laboratory. The virtues of low volume requirements for samples and reagents, rapid operation, high convenience and low cost has made it a promising

area of development for biomedical devices - see Fig.9.

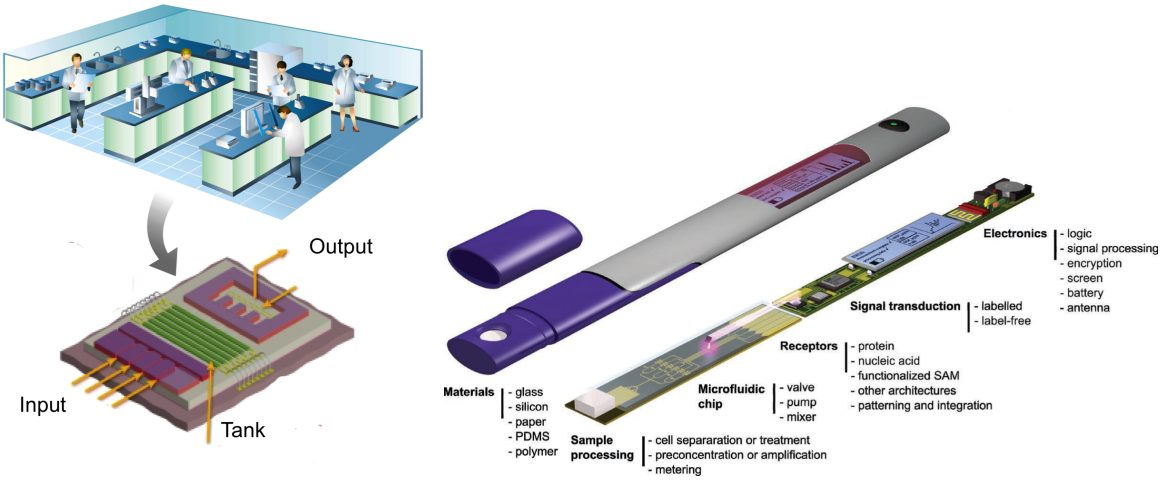

Figure 9: Lab-on-a-chip device (left) Principle of integration of laboratory process on a chip (right) Example of a Lab on Chip [6].

Lab-on chip devices are getting mature enough [65] to generate industrial activites and provide equal or extended function to standard laboratory functions.

A brief history of microfluidics The technologies developed to miniaturize transistors and manufacture microprocessors have enabled to produce microscopic channels and integrate them on chips. Thus, the history of microfluidics will take us to the first lunar expedition, from our printer heads to our hospitals.

The 1950s saw the invention and development of the first transistors, replicated on Fig. 10. Made in blocks of semiconductors, they have gradually replaced the lamps previously used in the manufacture of electronic devices (radio, computer ...)

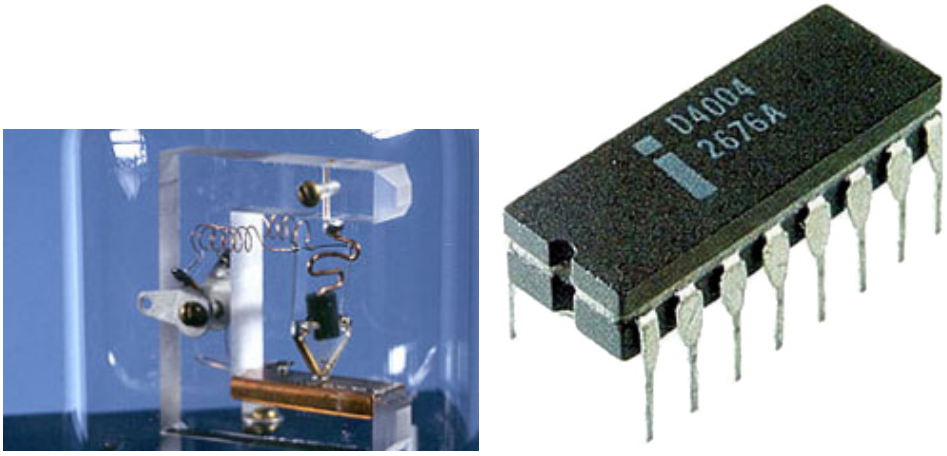

Figure 10: Miniaturization of technology (left) The first transistor (replica);(right) the first microprocessor(replica).

In the 1960s, space research, via the Apollo program with a budget of 25 G$, gave an opportunity to fund research programs on the miniaturization of computers to allow taking

them to space and particularly to the moon. The development of technologies such as photolithography have enabled the miniaturization and integration of thousands of transistors on semiconductor wafers, mainly of silicon. This research led to the production of the first integrated circuit and with them the first microprocessors, Fig. 13 (right).

Over the 1980s, the use of silicon etching procedures, developed for microelectronics industry, allowed the manufacture of the first device containing movable micro-elements integrated on a silicon wafer. These new types of devices called MEMS (Micro Electro Mechanical Systems) gave rise to industrial applications, particularly in the field of pressure sensors and printer heads.

In the 1990s, many researchers investigated the applications of MEMS in biology, chemistry and biomedical fields. These applications needed to control the movement of liquids in micro-channels and have significantly contributed to the development of microfluidics. A major research effort was made to develop laboratories on a chip to enable the integration of almost all diagnostic operations performed in a hospital on a single microfluidic chip.

At that time the majority of microfluidic devices were still made of silicon or glass, and thus, required the heavy infrastructure of the microelectronics industry.

Starting 2000, technologies based on molding micro-channels in polymers such as PDMS (PolyDiMethylSiloxane) experienced strong growth. Reducing the cost and production time of these devices enabled a large number of laboratories to conduct researches in microfluidics.

Potentiality of microfluidics and challenges Today, thousands of researchers are working in microfluidics to extend its application fields especially via on-chip laboratories for hospitals.

The Microfluidic technology has found many applications for therapy as well as diagnosis, mainly:

— in medicine with the laboratories on a chip because they allow the integration of several medical tests on a single chip, being biocompatible [43]
— in cell biology researches because the micro-channels have the same characteristic size as the cells and allow such manipulation of single cells and rapid change of drugs. [80] [81]
— In protein crystallization because microfluidic devices allow the generation on a single chip of a large number of crystallization conditions (temperature, pH, humidity...) [82]

It remains a stimulating research field, for BME especially [83] [84].

2.2 Microfluidics motivation: an in-vitro platform for immersed microrobotics

Microrobotics dealing with biological environment is mostly immersed and always dealing with high humidity levels. This leads to drastic consequences on the robot physics, in particular its dynamics which need to be precised. We will see then that microfluidics provide a simpler and controlled fluidic regime and has other experimental advantages.

Microphysics in dry environment Before dipping our first toe in water, we insist on microscale general specificity. This scale effect is the key to understand our decision of integrating microrobot in microfluidic chip. On the one hand, physical effects such as surface tension, electrostatic forces and interaction [85] get predominants over usual body forces (gravity) as is quantitatively described in Fig .11. On the other hand, the mass term is much smaller and

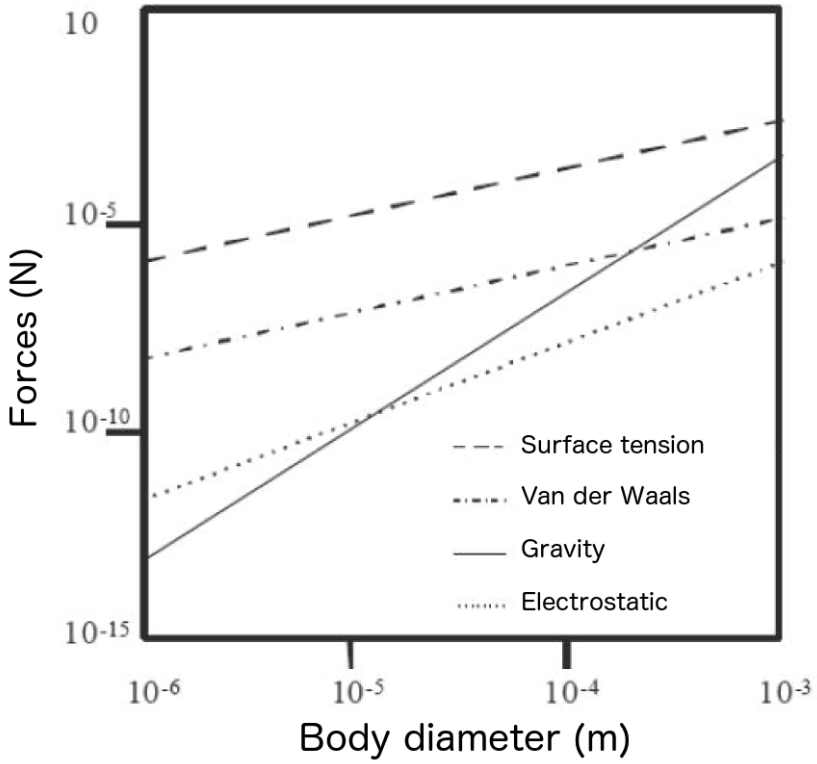

Figure 11: Asymptotic behaviour of forces at microscale and inversion of importance [7].

volume $\propto r^3$ decreases faster than surfaces $\propto r^2$, particularly for our high aspect ratio robot. The consequence on a simple Newton's second law is

$$\frac{\mathbf{F}}{m} = \mathbf{a} \tag{1}$$

is the divergence when $m \to 0$ [86] and very fast speed transition, leading to challenging control.

Physics of an immersed microrobot Now in immersed confined microvolumes (though air liquid interfaces could be considered),

$$Re = \frac{\rho u L}{\eta} < 1 \tag{2}$$

where ρ the density, η the viscosity and u and L characteristic speed and dimension of the considered flow. It has the advantage to simplify Navier Stokes equation to Stokes equation [79]

$$\nabla p - \rho \mathbf{f} = \nabla (p - p_0) = \nabla p' = \eta \Delta \mathbf{u} \tag{3}$$

Table 2: Body mass and viscosity comparison between air and water in standard conditions.

Property	water	air
Body mass	$1000kg.m^{-3}$	$1.2kg.m^{-3}$
Dynamic viscosity	$1 \times 10^{-3}Pa.s$	$18.5 \times 10^{-6}Pa.s$

where p is the pressure. As the system is heavily damped, non linear terms can be neglected. Speed is not limited by inertial effects but by liquid viscosity -see table 2, leading to more controllable objects.

This is already a sufficient argument to work in liquids, but we could also mention the importance of humidity creating local distribution of liquid drops. Working in an immersed environment avoid resulting surface effects from two-phase interface, a strong perturbation difficult to apprehend [87].

Another important effect of water on the dynamics is the reduction of electrostatic forces. Two phenomena [86] can explain this, the first being higher conductivity due to ion presents in liquids, the second being forces inverse dependency with dielectric constant. We compare it in table 3.

Table 3: Body mass and viscosity comparison between air and water in standard conditions.

Property	water	air
Dielectric constant ε	≈ 1	80.4
Conductivity	$10^{-7}S/\mathrm{m}$	$> 10^{-}4S/\mathrm{m}$

Experimental advantages of micromanipulation in liquid Micromanipulation in liquid, particularly when a part of the actuator is bigger than microscale, is challenging for several reasons:

— avoid contamination and allow good repeatability [88]
— easy instrumentation [19]
— simplify vision feedback (the robot remain located in the main chamber, no meniscus lens effect) [73]
— precisely control flow and pressure for dynamics study
— controllability of border effects: surface treatment, channel section control [87]

The following table sums up advantages of a microfluidic system for developing tests on immersed microrobotic tool.

Table 4: Advantages of using microfluidic as a test bench for immersed microrobots.

+	-
Cheap Process	Interface
Fast Process	Robot Integratio.
Reproducibility	Dynamics
Time-response	
Sample Comsuption	
High Sensing resolution	

Microfluidics displays enough advantages to be considered as a proper test bench. Integration issues are only minor technological issues and interface and dynamics are less important

than in dry environments. Made with biocompatible materials and adding cell cultures on their surfaces, chips could also evaluate toxicity and test in-vivo behaviour of the robot.

2.3 Microrobots as a tool for lab-on-chip

Microrobot can be used as a mobile tool for direct interaction with cellular sample for example, target size varying from $100\mu m$ for oocytes to few microns for dye. Many applications come out of single-cell manipulation and can be automated for isolated analysis or transformation (genetic alteration of a cell from the direct uptake and incorporation of exogenous genetic material).

As we are aiming for a simple robot control, even though it can perform fast operation in a short amount of time, it constitutes a single cell micromanipulator. It can assemble precisely several [60] for artificial tissue growing. The low contamination capability, repeatability, and high throughput ability are also interesting for mechanical sensing [66] [67]. Another possibility is cargo transport of molecule and delivery in a precise location.

2.4 Conclusion: microfluidics as a suitable environment for microrobotics

After detailing the available technology and science that offers microfluidics, we have quickly explained why working in liquids constitute both a proper environment oriented toward applications as well as a simpler framework in terms of physics.

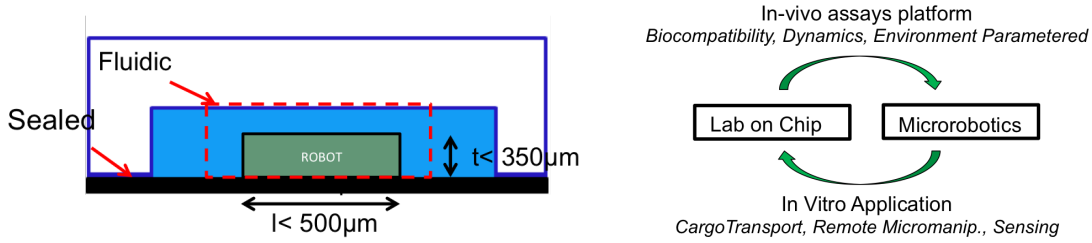

Figure 12: (left) Mobile microrobots in microfluidics (right) Virtuous circle of development between Microfluidics and Microrobotics in liquid.

The logic consequence becomes to integrate microrobot in these microfluidic chip, as described in left Fig. 24. The question of how we proceed will be detailed in next chapter. In this way, microrobots can provide new capacities of transduction for lab-on-chip different steps and microfluidic chips become an appropriate test-bench. We can describe as a virtuous circle the interaction between the robot and its environment, see right Fig. 24.

3 Development of mobile microrobots in microfluidics

A completely untethered mobile agents would push the current limits of precision tools in BME, their range of action as well as their dynamic performances. In this section, we explain what choices of actuation and control can be made to develop a mobile microrobot

depending on its targeted environment and applications. We will discuss first on the physical rules allowing these choices. How microrobots can be actuated remotely defines the limitation in power of the system. The question of feedback control defines the control of the system and how we can automate it. Finally, we synthesize the current solutions developed for mobile microrobotics and compare it to standard biological organisms.

3.1 Untethered microrobots: mobility complications

As a starting point to define the challenges related to mobile microrobots, it is necessary to provide a precise definition with examples from litterature and what changes it brings compared to standard microrobotic.

Definition We call in this thesis mobile microrobots untethered microsystems that aims to achieve automated or assisted tasks wirelessly, being sufficiently small to reach confined and critical areas. Behind this definition and particularly the micrometric notion, several generations of robot have emerged in the past 10 years. Scale effects variations make them completely different depending on their chosen scale [87]. We can mention millimetric robots with interaction at microscale [89] [90] as well as smaller micrometric bodies with submicron dimensions [91]. If one of the dimension is sub-micrometric, they are generally called nanoswimmers. The Fig. 13 is an illustration of how going below millimeter changes the fabrication method. We will in next chapter detail further how it impacts our way to design and fabricate our robots.

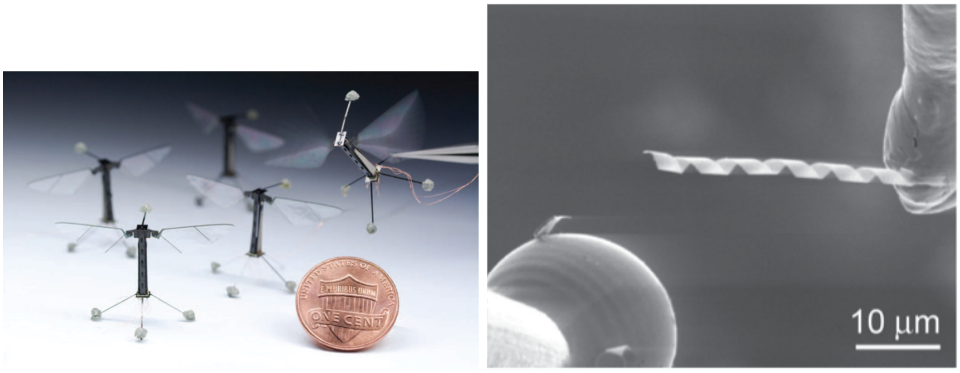

Figure 13: Extreme differences of dimension for two (mobile) microrobots. As we can observe, standard mechatronic fabrication process are only possible beyond millimeter (left) Harvard Microrobotics Laboratory recent mechatronic design of a microprehensor [8] (right)Hwang et al. Helical nanobelt (thickness being nano) for sensing applications [9].

As a corollary of this definition, the simplest loop of control we can describe contains an actuator, an untethered end-effector with biggest dimension below millimeter (let's say containable in a 1mm diameter sphere) and a feedback control. In the following part of the text, we will name by abuse of terminology microrobot the end-effector of the system. If actuator can be embedded and some research groups are exploring this way [92], we will see it remains mostly external to the robot body.

Axes of development After having discussed in previous sections the motivations of developing a microrobot mobility and its environment of study, we can describe design issues in 4 axes of development: actuation, control, environment and targeted applications. **Actuation** and **control** of the system will define the capacities of the robot to evolve in a specific **environment** and achieve transducing **applications**. The specific approaches of this thesis, for each axes, appear on Fig. 14. The choice of magnetic field **actuation** is mostly based

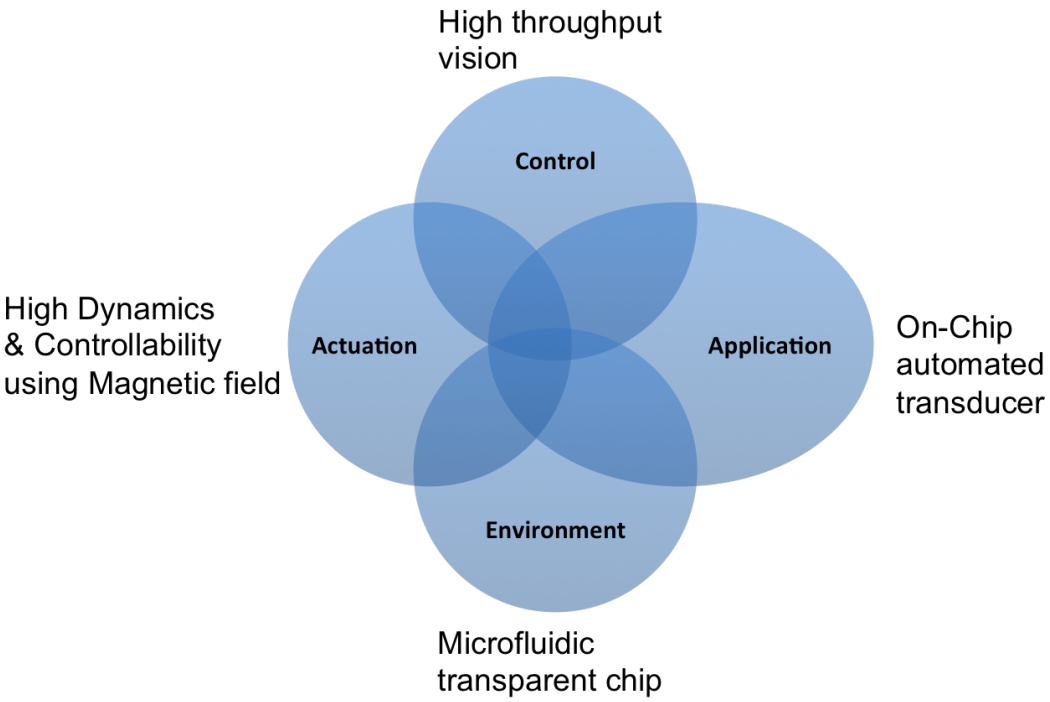

Figure 14: Designing a mobile microrobot can be summed up in 4 parts.

on its non-destructive remote influence and a slightly higher degree of control. We aim to work in relatively low amplitude field. Aiming for higher dynamics and controllability would allow to increase the rate of action of our system, and require sufficient magnetic power (in our case 1mT-100mT) and sampling rate (5kHz). **Controlling** these dynamics require consequently a higher rate of images ($> 5kframe/s$) in real-time, possible through vision devices. Choosing a transparent **environment** in the visible spectrum allow reflexion and transmission imaging with standard high speed camera. We have previously detailed our interest to work in microfluidic chip and we naturally aim for on-chip automated transduction **applications**.

This anticipated description of our design is further justified and detailed, based on the state of the art, in the next sections.

3.2 Environment: Scale effect drawbacks

If macroscale robots have demonstrated their capacities as autonomous mobile agents, it is far from simple to reproduce these capacities at smaller scale. As seen in the previous section miniaturization induces a scale effects. To deal with mobile microrobots, particularly in the case where they are mobile in wet environment, we need to estimate the impact on the technology, process and physics. We need to understand what is happening with the dynamics and what is at stake at interfaces.

Scaling down and physical effects The mobility and autonomy of robots have been constantly explored at macroscale but they are still one of the most important challenges [93] [94]. As microelectronics progresses have pushed the limits of clean room fabrication for increasing the transistor density on microcontrollers, a great range of new techniques has emerged and allow to consider automated artificial structures such as robots with embedded functions. This is impossible though to think our design the same way as for macrorobot.

Miniaturization of an object or process can prove complex, because the involved range of physical phenomena may not all change in the same manner as the scale is reduced, generating not one but several scale effects [86]. Fig. 15 sums up in 3 axes the impact of scale effect and the approximative threshold.

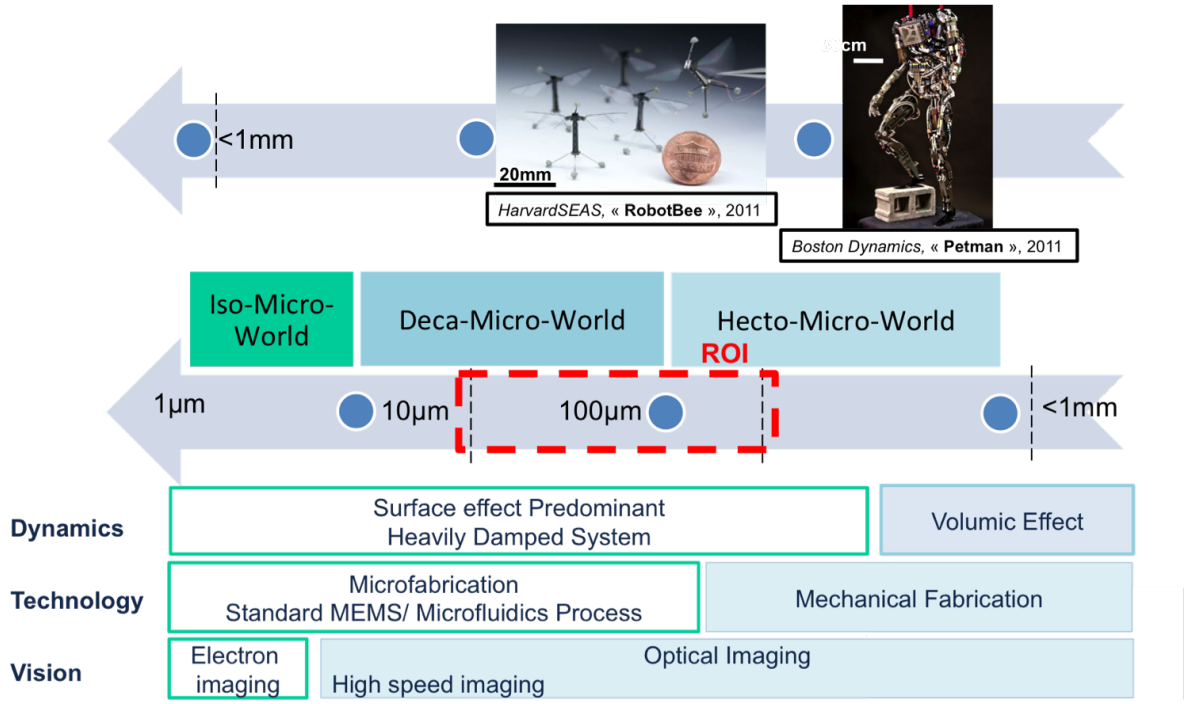

Figure 15: Scale effects appear below millimetric scale and several mesoscopic threshold are encountered while scaling down; working at microscale completely revise the physics thus the method of fabrication, experimentation and manipulation.

The dynamics, as seen in Fig.11, changes drastically. The transition from mechanical fabrication techniques to clean room process for microsystems also changes drastically engineering issues [78]. As adhesion forces and friction are increasingly important, it makes it preferable to use monolithic or compliant structures rather than articulated mechanisms, at least close to end-effectors [58], though self-assembly on bottom-up approach exists. Finally it also becomes challenging to obtain visual feedback as objects speed varies strongly and depth of focus gets smaller [73]. The optical limits due to diffraction is getting closer and electron imaging or alternative might be required, with less good performances.

Breaking some preconceived ideas on microrobots We target a high resolution robotic systems in order to achieve repeatable and precise operation compatible with the dimensions of the objects being manipulated. Because of dry friction, we will prefer compliant structures to articulated mechanisms which resolution would decline with use. In addition, the actuators

used to motorize microrobots must respect these constraints. This is why an embedded motor is a difficult actuation mean. [58].

3.3 Actuation: energy transmission and movement

Actuation consists in non-contact energy transfer, remotely or not, to overcome surface effects of our end-effector and reach high dynamics for high throughput applications. It also requires a fast time-response -i.e. sampling rate- to be controlled sufficiently quick. If power transmission is the key factor, we must not forget the impact on the environment.

The first and intuitive idea of converting power source encounters several issues. Though new methods of energy storage are being studied for MEMS batteries [95], the stored energy is proportional to volume then decreases very quickly and cannot be sufficient for the microrobot autonomy. The only possibility then becomes taxes, inspired from biology, which basically consists in collecting a physical signal gradient and converting it in movement, and direct power transmission using physical effects from robots materials.

Collecting power: taxes inspired from biology A taxes is the movement of an organism in response to a stimulus such as light or the presence of food. By imitating biology [96] or controlling it [97], we can control microagent as remote actuator using a stimulus gradient. Several external stimulus and their resulting converted movements have been studied, from chemotaxes [98] to magnetotaxes [99], and it can be described [10] as a self-regulated closed loop system, see in Fig. 16.

The overall number of publications since 1975, in right Fig. 16, confirms chemotaxis has been widely studied. The principle has indeed been much explored by biophysicist and still constitute a stimulating area of research for applications [100]. *Escherichia Coli* (E.Coli), one the most common bacteria, is still captivating [10] and is often used as a comparative reference for its flagellar motor with mobile microrobot.

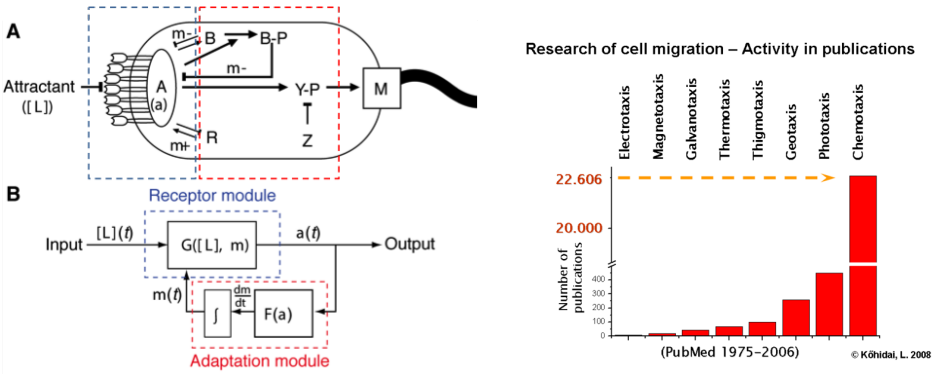

Figure 16: (left) Bacterial chemotaxes of *E. Coli* can be described as a [L] kinase concentration gradient-sensing network [10]. It is assimilated to a closed loop linear system where input is received by receptor-kinase complex A, regulated by inner enzymatic chain (m,B,Y-P,B-P,R,Z) and converted as motion by flagellar motor M (right) Publications in taxes research in 2008, chemotaxis being predominant, from Köhidai.

Some robotic team are also considering a hybrid method between microfabrication and biology, coating their structures with functional bacteria *E. Coli* [98] or modifying the bacteria

itself to be sensitive to electromagnetic control [99]. Last emerging approach has been using vascular plants coated with magnetic material [101].

Controlling chemical gradient implies being able to define concentration patterns, which limits a lot real time control. Even with a good spatial resolution, diffusive phenomenon are rather slow (particularly compared to electromagnetic waves). The movement power (speed and force generated) are also strongly limitated.

Transmitted power To propagate and transmit power to a remote body, physics provides several solutions offering quite complementary media, mostly using electromagnetic beams (magnetic or electric field, photonics) but also heat waves. These phenomena are directly depending on microrobot design and materials used. The choice of the force involved is important as it defines the degree of freedom, range of power and resolution of control of our microrobot.

Optical Tweezers Optical trap have been developed with laser technology [102]. Using a highly focused laser beam, it provides an attractive or repulsive force (typically on the order of piconewtons), depending on the refractive index mismatch to physically hold and move microscopic dielectric objects- Fig.17.

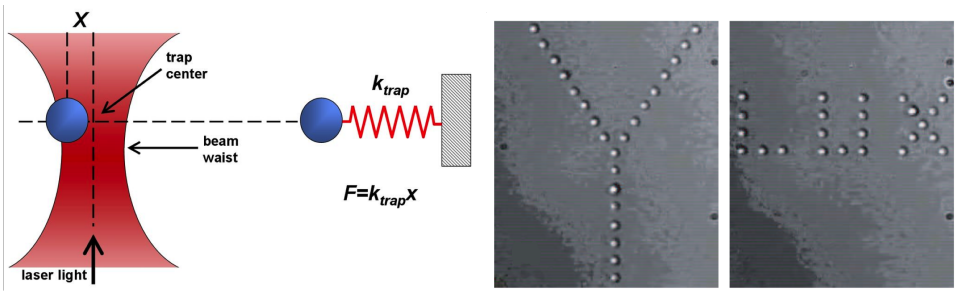

Figure 17: (left)A strongly focused beam of light creates an optical tweezer. Intensity gradients in the converging beam draw small objects, such as a colloidal particle toward the focus, while the beam's radiation pressure tends to blow them down the optical axes. Under conditions where the gradient force dominates, a particle can be trapped in three dimensions near the focal point (right)Twenty-five silica $1\mu m$ beads are transformed from Y to LUX using optical tweezers [11].

It is based on the radiation pressure of the emitted photons then is a surfacic force with pN range of force,

$$\mathbf{F} \propto \nabla E^2 \tau \propto \mathbf{P} \times \mathbf{E} \tag{4}$$

with $\mathbf{P}$ the electric polarization, $\mathbf{E}$ the electric field,τ and F the resulting torque and force. The degree of freedom and precision of this system make it a relevant media to manipulate electrically polarizable material (typically dielectric material). This force is more adapted though for trapping light object such as $< 1\mu m$ beads [11] and nanorobots [103]. The radiation of laser is dangerous for user then requires proper safety precautions and can be destructive by local heating. Its speed limitation comes from the optical material response.

Electrophoresis Electrical fields require electrodes and involve Lorentz forces on electric charges at a local level. From the simple rule $\mathbf{F} = q\mathbf{E}$, with $\mathbf{F}$ the induced force by $\mathbf{E}$ the

electrif field and q the charge, two different effects can be exploited for motion generation.

The first effect is electrophoresis and was discovered in the early 19^{th} century on clay particles and has been exploited for years for separation purpose in biological sample analysis [38]. On any material, a certain layer of charges remains on its surface and an electrical field will generate a force as described by Schmulowski.

$$F_{EP} = \mu_{EP}\mathbf{E} \tag{5}$$

with F_{EP} the resulting force, $\mathbf{E}$ the electric field, μ_{EP} the electrophoretic mobility (depending on geometry and surface charges σ). It includes dielectric and metallic material.

The second one is electroosmosis and involves the ionic layer (Debye layer) at the interface of any immersed object.When an electric field is applied, the ions in the Debye layer move (the flow is the EOF), equivalent to a moving walkway generating a force

$$\mathbf{F}_{EOF} = \mu_{EOF}\mathbf{E} = \varepsilon\zeta\mathbf{E} \tag{6}$$

with $\mathbf{F}_{EOF}$ the resulting force, $\mathbf{E}$ the electric field, μ_{EOF} the electroosmotic mobility, ε the permittivity and ζ the electrostatic potential. The combination of both can reach very high speed [12] and steering can be achieved by positioning the two electrodes. Parameters of the robot that influences the electrical power are related to the ζ potential and its surface charges σ.

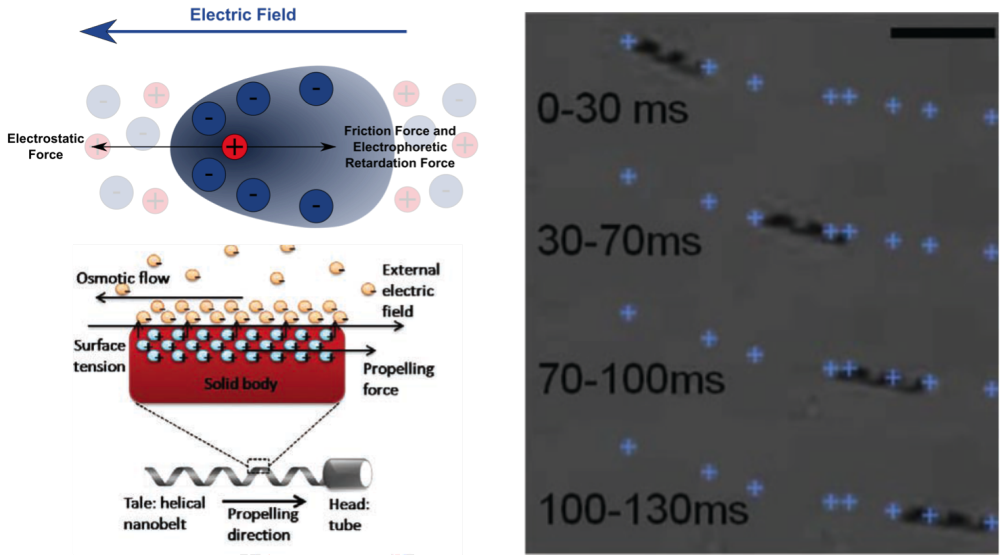

Figure 18: (left-top) Schematic of the competition between electrostatic force (electrophoresis) under the influence of an external electric field and viscous drag (left-bottom) Schematic diagrams of the experiments for helical nanobelt (HNB) swimming using electro-osmosis force [12]. (right) Swimming propulsion of the helical nanobelt (HNB) from high-speed camera analyses (342 fps): captured images of the HNB at each discontinuous motion [9].

Electrical fields have several drawbacks. The electrodes need to be in contact with the liquid medium that is a constraint in confined biological system. Electrical current generates gas at the electrode in case of non perfect electrodes and can release ionic metal. Finally and most of all, the generation of electrical current in biological medium can destroy cellular organism or elelectroporate them (inducing a permeability on the membrane) [48].

Magnetophoresis Magnetic fields are produced by moving electrical charges and the intrinsic magnetic moments of elementary particles associated with a fundamental quantum property, their spin. As a consequence two kinds of sources can generate magnetic field: permanent magnet and electromagnets (electrical circuits). Some particles being sensitive to magnetic field (ferromagnetic or paramagnetic), it will induce a local magnetic moment at atomic level and an integral over the whole volume gives us the global magnetization M. We can describe the actuation as follow

$$\begin{cases} \mathbf{F} = (\mathbf{M}.\nabla\mathbf{B}) \\ \tau = \mathbf{M} \times \mathbf{B} \end{cases} \tag{7}$$

If both magnetic sources behave as a magnetic dipole with the same apparent distribution of magnetic flux, their control are complementary. Magnetization of permanent magnets cannot be varied as it is the remanent magnetization of a (generally) hard ferromagnet. We have to control their position with motors to vary their amplitude and direction [104]. Magnetization of hard ferromagnets can reach high magnetization $> 1T$. Electromagnets are electrically controllable, see Fig. 19 left, but require more design efforts [105] as we will see in section 2. The field of magnetically actuated microrobot is under intense investigation and offers a wide range of motion capacities. Fig. 19 right shows the examples of mobile magnetic microrobots.

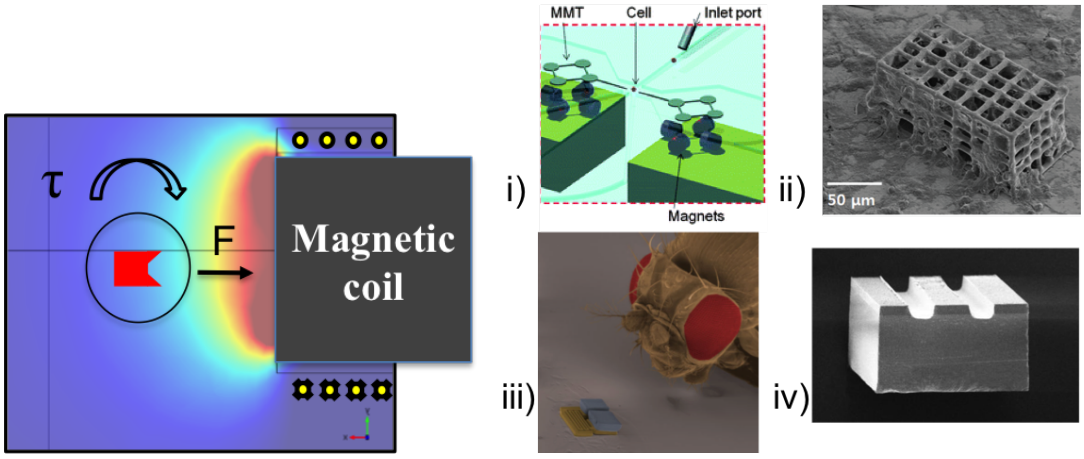

Figure 19: Magnetic propulsion:(left) Schematic of magnetic actuation principle, robot being superposed with magnetic field amplitude distribution for an electromagnetic coil (right) Several recent examples of mobile magnetic microrobots with different scale and propulsion method, illustrating the wide range of possible approach i) Three-Dimensional design for for cell culture from Kim et al. [13] ii) Robot with ultrasonic vibration for single cell manipulations, actuated by permament magnet driven by motor from Hagiwara et al. [14] iii) MagMite resonant magnetic micro-agents from Frutiger et al. [15] iv) Combining magnetic and piezoelectric vibration microrobot from Ivan et al. [16].

Thermal actuators Thermal actuation consists in enhanced thermal deflexion due to material properties, such as multi-layer structures exploiting the difference of coefficient of thermal expansion or shape memory alloy (SMA) [106]. The bilayer bending has been simply described with Timoshenko law

$$1/R = K(\alpha_1 - \alpha_2)\Delta T \tag{8}$$

with R the radius of curvature of a bilayer beam, K being a coefficient (depending on thicknesses and Young's moduli of the layers),$\alpha 1$ and $\alpha 2$ the thermal expansion coefficient and T the local temperature. The principle is summed up on the Fig.20 and further detail can be found in Smela litterature and website [107]. The interesting exploitation of robots compliance has the advantage of changing the global shape and proposing eventual motion. It has been explored prehensing solutions [108]. To our knowledge, even though solution of

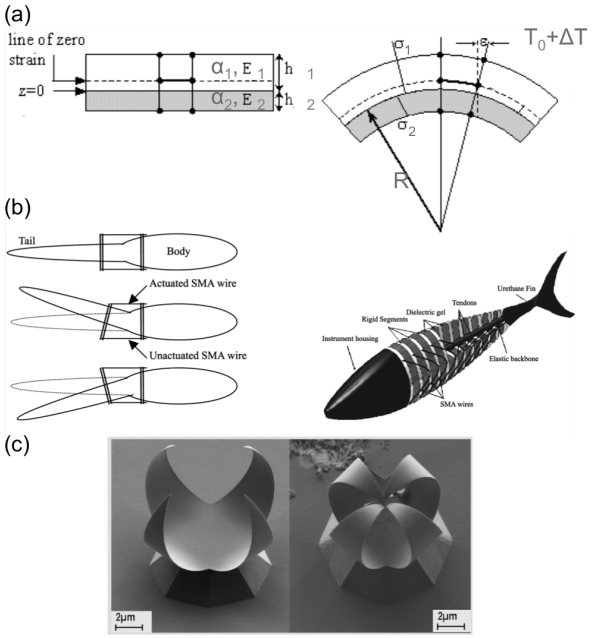

Figure 20: (top) Illustration of a bilayer bending principle, with resulting stree and strain due to temperature variation(middle) Example of macrorobot design actuated by Ti-Ni SMA from Shinjo [17] (bottom) Integrated microrobotic platform using hydrogel bilayer structure [18].

thermaly actuated swimmer exists at macroscale [17], no mobile microrobot design involves thermal actuator for motility purpose. One of the main reason remain the slow transition time of thermal mechanism.

Even with an adapted experimental setup, thermal diffusion is a relatively slow process due to inherent thermal inertia. Resulting from Fourier's law, the heat equation

$$\partial_t T = \kappa \partial^2_{x^2} T \tag{9}$$

with T the temperature, the thermal diffusivity $\kappa = \frac{k}{c_p \rho}$, k the thermal conductivity, c_p the specific heat capacity and ρ is the mass density of the material. κ, in gives an approximation of performances of diffusion depending on geometry. Even with an integrated on-robot thermal source, performances are already limited to ms inside the metallic material of the robot. For a $100\mu m\, Ni$ square section, characteristic time is around 1 ms. It is more interesting to consider thermal actuator as prehensive tool which can be done in slower time and still be quite useful for mechanically trappin object, as it has been recently demonstrated with hydrogel structure by Fusco et al. [18] with approximately 10s time to release an object and 60s to grasp it.

Add-on physical effects If existing actuation solutions known from us have all been mentioned previously, techniques exists controlling other physical phenomenon combined with

aforementioned. They would not be sufficient to actuate the robot alone. We have not include combination of electro-osmosis with electrophoresis in this category because the user only control one physical parameter, the difference of potential. These solutions target mostly two issues: selectivity of control and improving dynamics. They are of course equivalent if we consider that selectivity of control promotes the mobility of one single robot over several of them.

Improving dynamics by induced vibration is an effective known technique and can be achived by magnetic [109], acoustic [14] or piezoelectric [16] effect.

Some solutions like the one from Frutiger et al. [109] can actually lead to a selective control if each robot of a group has a different resonance frequency. Selectivity of control is often realized by switching on or off the mobility of the microrobot, vibration acting as a motion enhancer. It has been also demonstrated by demagnetizing a hard ferromagnetic robotic body [110]. or changing the surface contact of the robot using thermal effects and a polymer coat [110].

These ideas gravitate around the same concepts of modifying and controlling the surface adhesion, which again is the critical factor, between robots and the solids edges of its external environment.

Synthesis and motivation for magnetic field All the actuation methods we have mentioned have complementary qualities, summarized in table 5, in terms of:

— force generated over the microrobot body, often depending on the body geometry and materials themselve
— energy source device
— performances in time: how fast can we correct the signal over the robot
— controllability, i.e. degree of freedom $\times$ resolution of control of each degree

We also try to briefly sums up in one main advantage / disadvatange, what makes the actuation method different. A reference is added for the reader so he can refer to more details in bibliography. Some propulsion methods needs to be enhanced using mechanical vibration resulting from a defined phenomena (acoustic, piezoelectric or magnetic). As we are aiming to develop the control of a single robot, we aim for the optimal precision of control and speed. This thesis will thus shed the light on magnetic solutions, more specifically controlled with electromagnetic coils, having a better control over the magnetic field distribution than with permanent magnets driven on electric motors. It also has the advantage of being non-destructive (necessary for applications toward biology). Further optimization of our system and details will be introduced in next chapter to justify the technological choices we have taken.

3.4 Dynamic control at microscale

We have detailed in section 3.1 and 3.2, the two first blocks of our chain of command. The robot and its actuation device are now under the control of an intelligent system, driven by a microcontroller (for user interfacing as well as automation). How can microrobot move in liquids? Which are the technologies available to detect a single microrobot which one would be the most adapted? Localizing the robot and using algorithm to track its position have had several proposition in literature, spatiotemporal resolution being one of the most important factor. Another more practical aspect is the size and perturbation emission and sensitivity of

Table 5: Comparison of different actuation methods.

Category	Electro-phoresis	Electro-magnets	Permanent magnet	Heat	Optical	Taxies
Force	$10\mu N$	$0.1\mu N$	$10\mu N$	nN	pN	pN
Source	Electrodes	Coils	Permanent magnet	Thermoelastic effect	Laser	Stimulus
Time-response	$< 1s$	$\approx 1\mu s$	$> 1ms$	$0.1s$	$1ms$	$10ms$
Controlla-bility	-	++	+	-	++	–
Advantage	High Power	$\frac{Power}{Controlability}$	High Power	Flexible	Controlla-bility	Efficient transfer
Disadv-antage	Destructive	Power decreases fast	Constant power	Perturbative	Low Power	Gradient control
Reference	Hwang [12]	Salmon [111]	Arai [14]	Wang [112]	Maruyama [104]	Martel [113]

our actuating system.

For the closed-loop motion control of helical microswimmers, the main challenge is tolocalize and track the helical swimmers position. Various methods have been proposedto localize and track a microrobot. Spatial resolution is an important factor in thedetermination of microrobots positions. The maximum rate at which the positionestimation can be updated is also an important factor for real-time control. Energy effectiveness should be as well considered.

Swimming method Swimming has been described as more adapted to microworld by Purcerll [96] in 1973, and has actually shown an interesting path for mobile microrobotics, as many solutions provide helical design (adapted for swimming by screw motion) [89]. But several other ways exists in nature. We can lean on the description made by Berg group over *E. Coli*, see Fig. 21 left, to enumerate the different immersed movements possible for microbodies [10], more specifically with bacteria *E. Coli*. Displacement of other motile cell such as spermazoon, see Fig. 21 of different species are also studied [114] as the average motility of a group of them is a critical parameter for reproduction mechanisms. Bibliographical work on E. Coli provide more quantitative details about single cell motion. Though their main interest is free-swimming cells, they also study cells that swarm (swim in a coordinated manner over moist surfaces, $2-10\mu m/s$), twitch (Pseudomonas) or glide (Cytophaga, Mycoplasma). In some species, swarming motility requires the self-production of biosurfactant to occur.

By extension, we will call swimming any method of displacement of mobile micrometric body in microfluid. Swimming microrobot, or artificial microswimmer, will be artificially made controllable bodies in microliquids.

Localization for feedback control Robotics describe two main categories of control. **Open-loop control** does not provide regulation on the system which means it must be under the direct control of a user who uses sensorial signals. **Closed-loop control** integrates the

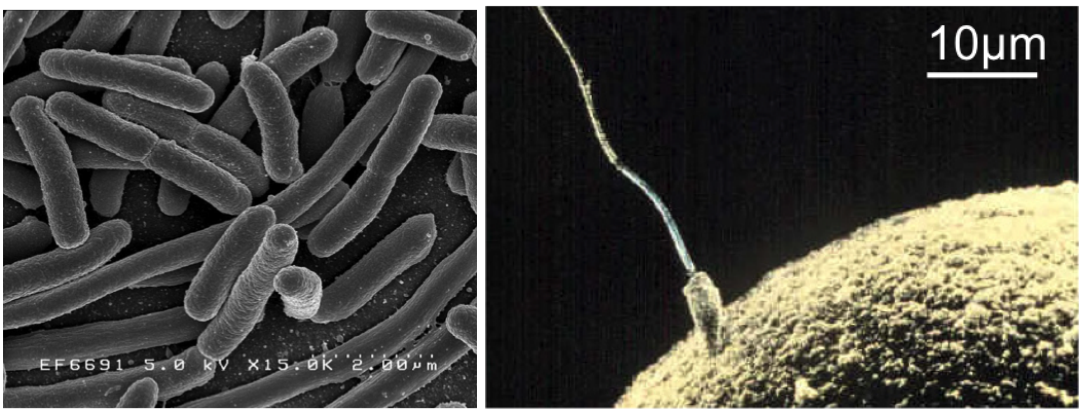

Figure 21: Biological swimmers: (left) SEM view of a Escherichia Coli (right) SEM view of a human sperm cell fertilizing an egg cell.

feedback using a sensor and, most-of the time, generates a counter reaction (correction). In any case, they require a measurement extracting the position. Localization of the microrobot can be achieved with different signal emitted by the microrobot: sound or electromagnetic emission. Medicine exploits both and offers a wide range of technological solution in terms of resolution, control and cost.

Computed Tomography: Xrays and Magnetic Resonance Imaging (MRI) Computed tomography is a medical imaging procedure that uses computer-processed imaging to assemble tomographic images or 'slices' of specific areas of the body and obtain a 3D-image. The patient is placed between a source and a detector array. It is possible to obtain imaging from various signals (photonic by fluorescence, xray and magnetic resonance)

A set of projected X-ray images gathered from various view points is used to reconstruct the interior of the final image in 3D. Pixel resolution can reach 0.8mm for a 512x512 pixel matric image in 3D. [115], and an isotropic pixel size of 0.195 mm is achieved recently [116]. CT scans are not well suited for imaging regions of soft tissue surrounded by large volumes of high-density material such as bone, because of the underlying process of image reconstruction based on radiation attenuation.

A clinical Magnetic Resonance Imaging (MRI) system is a powerful non invasive imaging technique that has played and will keep an important role in the medical community. A clinical MRI has the ability to generate large magnetic fields. Ferromagnetic objects, or magnetotactic bacteria are tracked and navigated under real-time MRI [113]. The typical field strength is 1.5 T or stronger. The MRI systems can also be used to provide microrobots locomotion capabilities.Kalambur presents in his paper the localization of groups of nanoparticules in an MRI system [117]. Martel et al. magnetotactic bacteria are localizedas single objects [99]. The spatial resolution of the MRI system is similar to that of the early multislice x-ray system [118], reaching 0.25 mm 0.25 mm 1.5 mm in a 3.0 T MRI machine [77]. In the same work, an isotropic resolution of 0.57 mm is achieved, but the scan time is 25 s, which is too long for microrobotic applications. The mean error of a 3.0 T MRI machine is less than 1.0 mm [119]. Besides the limitation of the resolution of MRI machine, another drawback of MRI localization is the limited choice of material for fabrication of microrobots [120]. Ferromagnetic objects cause image artefacts that are sometimes larger than the object to be localized [121]. The main issue with tomography is the cost in time for acquiring and

processing slices, the spatial resolution making it increasingly important.

Scanning Electron Microscope A scanning electron microscope (SEM) is a type of electron microscope that produces images of a sample by scanning it with a focused beam of electrons. It is and will remain one of the best tool to obtain a 2D picture at a 30 frame/s rate below micrometric scale [122]. The first drawback is that it requires high vacuum for electron diffusion. The optoelectronic parts, containing an electron canon and its magnetic lenses, is quite important in terms of volume. It is possible to observe biological bodies under certain conditions that destroys the sample by coating it with a metallic layer.

Acoustic imaging For localization in soft tissue, only ultrasound combines good resolution, minimal adverse health effects, high speed, safety, adequate frame rates (up to 100 frames per second) [49], and low cost. The major drawbacks of ultrasound are related to low signal-to-noise ratio and the presence of strong wave reflectors such as bones and air pockets. These may produce artifacts in ultrasound images or shield an ultrasound signal. The disadvantage of ultrasound imaging may be partially overcome through passive localization techniques, based on ultrasound transmission. In applications of the localization, frequencies up to 3 MHz are reasonable, resulting in a resolution of about $500\mu m$ and a penetration depth of 15-20cm. The localization of a wireless medical microrobot can be accomplished with a microrobot. that acts as an emitter by carrying an ultrasound transducer on-board. A cantilever or any other mechanical structure can act as such, vibrating at its resonant frequency. The emitted signal is measured by a set of receivers placed on the surface of the patient's body. Through the use of MRI data gathered off-line, localization accuracy can be greatly improved.

Vision: optical miscroscopy Much explored in robotics with servovision control in particular for micromanipulation [73], vision is a useful robotic sensor since it mimics the human sense of vision and allows for non-contact measurement of the environment. The images are transmitted optically by cameras in combination with optical lenses. Obviously, vision can not be used for tracking microrobots in patient's body because of line-of-sight problems. The illuminating conditions have to be considered as well. However, vision has several advantages compared to other imaging methods. First, high spatial resolution can be achieved by microscopic lenses. The spatial resolution is limited by the light diffraction. A resolution of 200 nm can be reached with visible spectrum light. The limitation can be overcome by using a camera in combination with a SEM, as shown by Sievers et al. [123]. Another advantage of vision is to avoid the conflict between the imaging and the actuating magnetic field (particularly important when manipulating mobile microrobot sensitive to magnetic field). Third, great energies are required to generate a magnetic field or to emit radiation for MRI, CT and ultrasound. It is not the case for vision, which is a energy-saving method.

Synthesis and motivation for vision based control We synthetize these different imaging methods in table 6.This table gives an idea about the performances of each imaging system. Parameters can of course be adapted, values being only indicative of the range and we will see further that high speed camera for vision system provides a wide variety of solutions.

Different technical features - such as contrast enhancement project or different mode of

Table 6: Different feedback method for position detection and control of microrobot.

Method	advantage	disadvantage	temporal res.	spatial res.	cost	ref.
Photonic	high resolution and control	visible light	$> 50\mu s$	$> 1\mu m$	very low	[73]
MRI	non invasive, limited toxicity	expensive, perturbative, resolution	$> 3s$	$0.1mm$	low	[124]
CT	non invasive	carcinogen X-rays, resolution	$> 3s$	$0.1mm$	very high	[115]
Sonography	subcutaneous localization	low signal-to-noise ratio	$> 10ms$	$300\mu/s$	low	[49]
SEM	highest spatial resolution, vacuum	incompatible with biology	$> 10ms$	$> 10nm$	high	[9]

analysis- exists to push the limits of non invasive device (MRI, CT or even echography. Vision remains the best choice of biologically compatible imaging, in terms of spatiotemporal resolution as well as experimental ergonomics (smaller and non-perturbative). It can reach region of interest from $1mm \rightarrow 1\mu m$ but cannot anything opaque to the visible light such as tissue. Consequently, it will provide us the adapted tool for the high performances control and proof of automation of our microrobot but will limit the applications area, as we see in next section.

3.5 Emerging applications: toward in-vivo

Mobile microrobots are being studied mostly in-vitro, and as we have mentioned in section 2, microfluidics is a fertile ground for this development. But some results are encouraging enough to let imagine that collaboration between physicist and biologist will lead one day to in-vivo operations using teleoperated microrobots [125, 126]. There is a sense that surgical microrobots "are just around the corner" [127]. cite There are first technological limitations due to injection of the robot and vision. What could be the different area for teleoperated mobile microrobotic operations? What are the challenges in terms of cytotoxicity?

Applications areas Nelson et al. review [128] proposes different scenario for in-vivo mobile microrobots intervention, based on existing development. It is important to identify from that the future challenges. Considering a vision based microrobotic system, the accessible zones are **peripheral**:

— eardrum [129]

— retina: retinal microsurgery requires sensitive manipulations that are constrained by the limits of human performance [130] and that require forces below the threshold of

human perception [131]
— skin

It could also be possible to use it for foetal open surgery [132] [133], which can prevent death or life-long impairments and malformations. It would offer non-neglectable alternatives to abortion, intra-uterine death, or a life with disability.

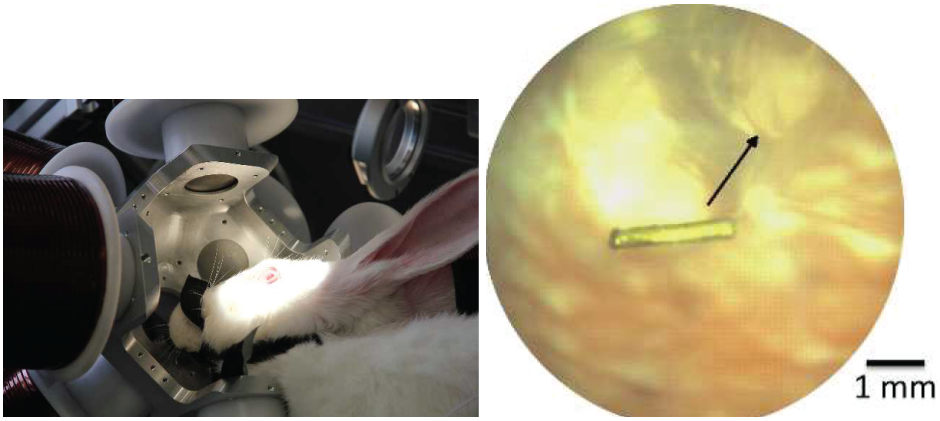

Figure 22: In-vivo applications of microrobots: (left) Intravitreal surgery on anesthetized rabbit placed with the studied eye centrally in the OctoMag workspace (right) Microrobot in rabbit vitreous [19].

More hypothetically, mostly because CT and echography technologies offer less spatiotemporal resolution, robots could be one day driven through

— cardiovascular system: heart and vessel constitutes the circulatory system and nearly every site of the body can be accessed by blood. It is arguably the most important application area for wireless microrobots though it is extremely challenging to perform control with blood flow perturbations [99]
— central nervous system consisting of the brain, the spinalcord, and the cerebrospinal fluid in which both the brain and spine [134]
— urinary system and prostate: the urinary tract includes two kidneys, the urinary bladder; two ureters, which are lumens leading from the kidneys to the bladder, and the urethra which leads from the bladder to the exterior of the body. [135]

ETHZ microrobotic team, see Fig.22, is leading intravitreal surgery using injected microrobots [19] and next step will probably be intense investigations on corpses surgery before starting demonstration with physicians.

Cytotoxicity Cytotoxicity of microrobotic injected in body are challenging to prevent; even with surface treatment and adapted method of extraction after operations, cytotoxicity still need to be quantified. It is a particularly long statistical analysis with sometimes insufficient precision.

Current cytotoxicity studies have been attempted on gold nanoparticles for hyperthermia and drug delivery, particularly for assisting cancer treatment (cf subsection 1.3) [136]. Knowledge about their potential toxicity and health impact is essential before these nanomaterials can be used in real clinical settings. Furthermore, the underlying interactions of these nanomaterials with physiological fluids is a key feature of understanding their biological impact, and these interactions can be exploited to mitigate unwanted toxic effects [137]. Again, microfluidics constitute a high-throughput analysis tool to achieve sufficient statistical analysis.

Protective coating exists [138] but medical regulation requires toxicity assays, which is particularly difficult to quantify for nano/microsystems. Limitations of in vivo (cytotoxicity, perturbation from biological activity and difficult remote control).

3.6 Magnetic Mobile Microrobots zoo

With the four main axes of development (actuation, control, environment, and application) mentioned in Fig. 14, mobile microrobots have constituted for less than 10 years a stimulating field. Their sizes, fabrication method and actuation method have displayed great diversity so much that we can divide them in taxonomy as seen in Fig. 23.

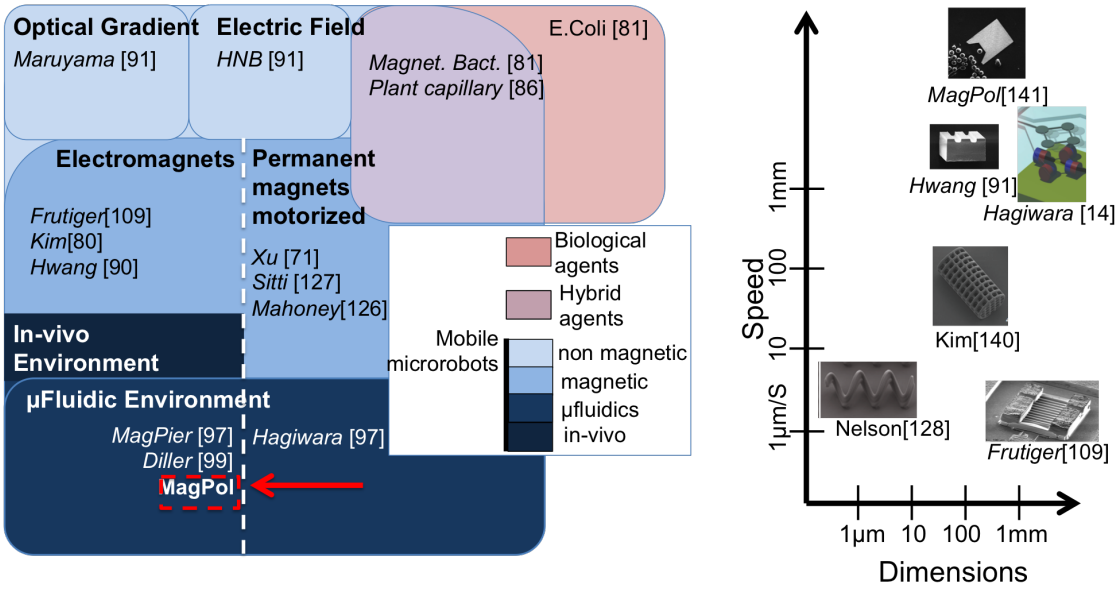

Figure 23: (left) Subjective map of mobile microagents development in liquids; this map is on purpose centered on mobile magnetic microrobots which is this thesis framework (right) Synthesis of magnetic mobile microrobot by plotting their speed and dimension.

We achieve several dichotomy to generate the Figure 23 map with a code of colour as described in the legend. We divide them by nature (artificial or biological), energy transmission, type of magnetic actuator and environment, in this order and zooming every time on our framework, which is magnetic mobile microrobots.

Though it could deserve an exhaustive enumeration, the diversity has become increasingly important and exceed this thesis work. We plot the different performances of speed and dimension of the magnetic mobile, proposing a classification which does not include all the emerging features for microrobot such as selective multi-control, prehensive capacities or sensing. We propose to sum up in table 3.6 the particular parameters of taxon of mobile magnetic microrobots. We provide as a point of comparison two well known biological swimmer: human male gamete (spermatozoon) and *E. Coli*.

Table 7: Summary of magnetic mobile microrobot and comparison with biology; dimension gives the characteristic sizes of the robot (sometimes they can have a high aspect ratio due to thin thickness)

Propulsion mode	Dimension	Speed	Environment	Applications	Reference
multiple	$1-10\mu m$	$10\mu m/s$	intestine	x	E Coli [139]
corkscrew motion	$10\mu m$	$10\mu m/s$	seminal	x	Spermato-zoon [114]
rolling	$10\mu m$	$10\mu m/s$	in-vitro	drug delivery	Nelson [128]
tumbling	$100\mu m$	$50\mu m/s$	in-vitro	transducing	Zhang [140]
vibrating	$300\mu m$	$1.8\mu m/s$	in-vitro	bio manipulation	Frutiger [109]
vibrating	$400\mu m$	$71m/s$	dry	bubble manipulation	Regnier [91]
tumbling, aqua-planing levitation	$100-400\mu m$	$560mm/s$	immersed	lab-on-Chip transducing	Salmon [141]
aquaplaning levitation	$5mm$	$5mm/s$	liquid surface	lab-on-Chip transducing	Hagiwara [14]

4 Overview of thesis work

Biomedical engineering is rapidly innovating its tools through micro and nanotechnology. Mobile microrobotics is progressing almost at the same speed as the one of fabrication and characterization process. There exist different ways to consider and it is tempting to accelerate its contact with biological matter.

Magnetic mobile microrobots are particularly promising transducer in wet environment because of their non destructive remote control. Several branches have emerged in the state of the art and we believe there is a strong interest in developing mobility and automation inside microfluidic chip for lab-on-chip application and experimental development. The three major challenges of this thesis are:

— developping a high speed (below millisecond sampling rate) control microrobotic station for high throughput transduction (high number of actions within a second)
— improve the robot motility, method of motions, for automation as well as interfaced control
— extend the microrobot transducing capacities (physical manipulation such as cargo transport & environmental sensing)

To do so, we develop a control chain that can be described as a loop, as in Fig. 24, in which our microrobot effector is integrated in a microfluidic chip. The scale effect make surface effect predominent, in particular drag force and adhesion forces, and it requires a high range of force to actuate it as well as a high sampling rate sensor to detect its position and control it. We develop an electromagnet based setup actuating a microrobot integrated in lab on chip, which has the advantage of being non-destructive. We use a high-speed (5kHz) vision-based control to analyse motion and develop automation of action.

Virtuous circle of development between microfluidics and microrobotics in liquid generates better understanding of motion as well as new transducing applications. We justify in next chapter the technological effort developped around the microrobot to obtain high dynamics performances. The quantitive analysis of the dynamics result in a capacity to diagnose the robot's motility as well as sensing its local environment, detailed in chapter III. Then we analyze these dynamics and the potential motion and manipulation strategies resulting from it in chapter IV. We will finally "close the loop" in chapter V, working on plannified trajectories to reach the dynamics limits.

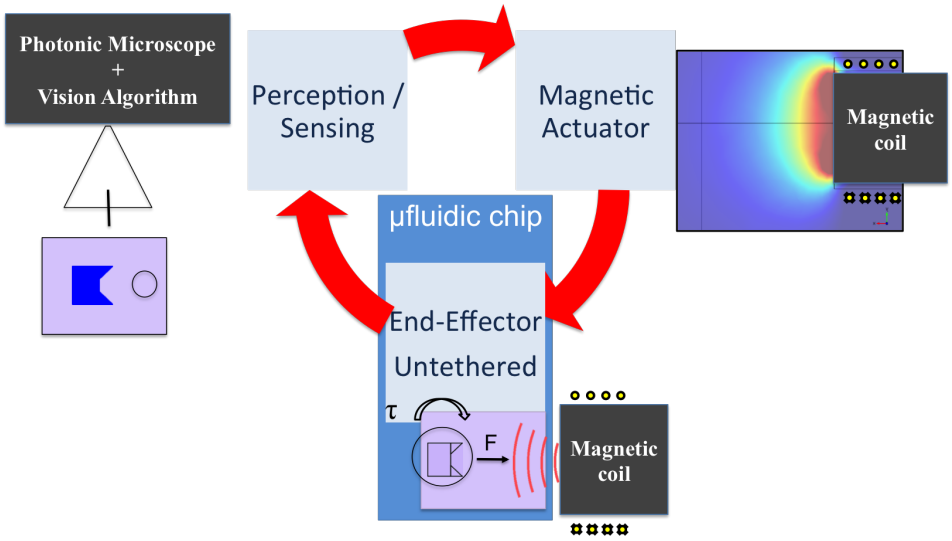

Figure 24: Schematic of system development of MagPol.

Part II

Mobile Magnetic Microrobots integrated in microfluidics for high dynamics performances

Summary

The order in which we design our microrobotic system matters. The complete description of its command chain is necessary to understand how the robot works and how we design it. In this chapter we introduce the fundamental device we propose for achieving movement, manipulation and sensing in the next parts. The successful integration to its expected environment - here in the μfluidic system - has an impact on how we conceive it and requires to be detailed as well. We then observe the first movements speed using a high throughput imaging.

1 Mobile Magnetic Microrobot: ferromagnetic end-effector

We decide to tackle the design question by starting from the microrobot designs. This arbitrary choice gives us the highest freedom to then adapt our instrumentation (fluidic, eletromagnetic and optics).

1.1 MagPole: Mobile Magnetic MicroRobot design

What we call a Mobile Magnetic Microrobot requires a definition. It does not necessarily fit our first expectations (cf. Part1) as below millimetric scale, we prefer monolithic compliants bodies with an external power source than articulated self propelled systems.

As a consequence, an operable robotic system requires a looped interaction between a sensor, an external magnetic actuator and a mobile untethered ferromagnetic effector. Though we cannot exclude its remote control part to define it, we further call microrobot the mobile ferromagnetic body. We start the system description from there.

We introduce here our design as MagPol, standing for Magnetically Polarized μ robot.

Hydrodynamicity We suppose our microrobot in a low Reynolds number fluid.

$$Re = \frac{\rho u L}{\eta} << 1 \tag{10}$$

Stokes flow physics [79] lead to neglect inertia, leading to a simple relation from Navier-Stokes equation

$$\nabla p - \rho \mathbf{f} = \nabla (p - p_0) = \nabla p' = \eta \Delta \mathbf{u} \tag{11}$$

$\mathbf{f}$ being an external conservative force so that $\rho \mathbf{f} = \nabla p_0$. One of the consequences is a linear dependency between the fluidic friction over microrobot's edges and the speed of the robot. With two perpendicular symmetry axis (horizontal and vertical), we obtain simplification.

$$F_i = -\eta (A_{ij} U_j + B_{ij} \Omega_j) = -\eta \lambda_i U_i \tag{12}$$

$$\Gamma_i = -\eta (C_{ij} U_j + D_{ij} \Omega_j = -\eta \beta_i \Omega_i \tag{13}$$

λ_i and β_i depending on the robot's geometry. To simplify dynamics control and interpretations, we will conserve two symmetry axis to minimize to zero cross effect of force induced by rotations or torque generated by translation.

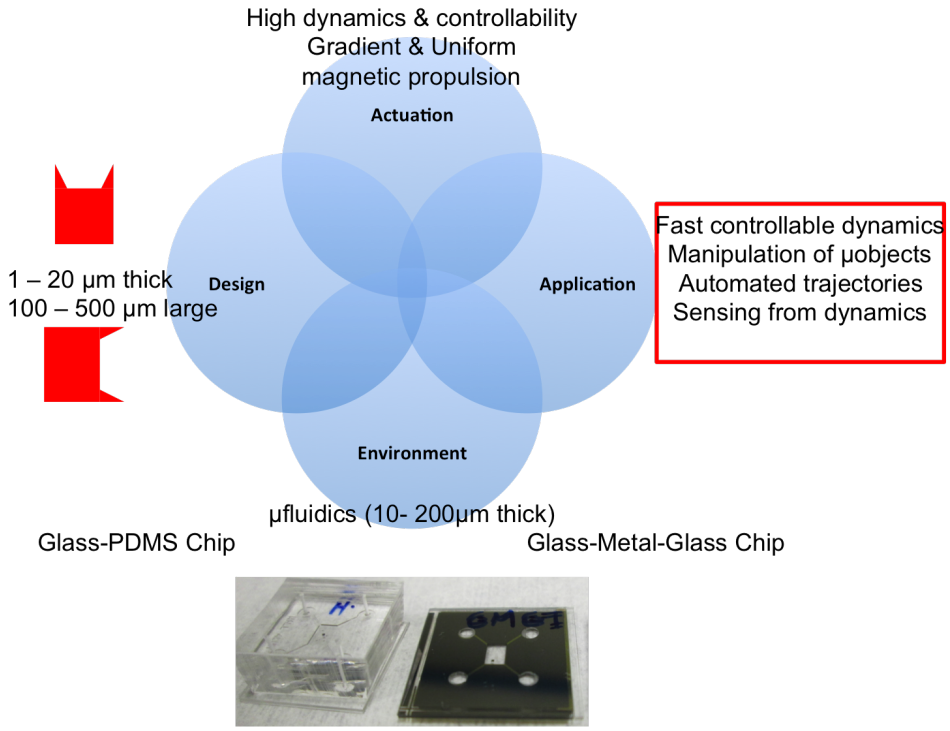

Figure 25: Mobile μrobot controlled trough magnetic waves using vision: each part of the cycle constitutes a part of the robot design.

Bulk Ferromagnetic Material Choice [24] [142]

To obtain a control using magnetic field, we first need material sensitive to magnetic field, paramagnetic or ferromagnetic material - i.e. with a magnetic susceptibility $\chi > 0$

$$\mathbf{M} = \chi \mathbf{H} \tag{14}$$

$$\mathbf{B} = \mu_0(1+\chi)\mathbf{H} \tag{15}$$

$$\mathbf{B} = \mu_0\mu_r\mathbf{H} = \mathbf{B} = \mu\mathbf{H} \tag{16}$$

It is then possible to write

$$\begin{cases} \mathbf{F} = (\mathbf{M}.\nabla\mathbf{B}) \\ \tau = \mathbf{M} \times \mathbf{B} \end{cases} \tag{17}$$

The decision whether it is ferromagnetic or paramagnetic lies first in the remanent magnetization. Paramagnetic is a simpler phenomenon that does not maintain the magnetization after the external field is removed. For polarization purpose as well as high magnetization value, we choose a ferromagnetic one. The table provide a comparison between both choices.

Table 8: Comparative table of magnetizable material

Criteria	Hard Ferromagnets	Soft Ferromagnets	Paramagnets
Examples	Sm-Co, Ferro-platinum	Fe, Co, Ni, Permalloy	Al, Pt, Mn
χ	$\approx 50-10000$	$\approx 10^-3-10^-5$	$\approx -10^{-5}$
H_c(kA/m)	> 10	< 1	0
$(BH)_max$kJ/m^3	170-255	¡10	0

We can notice that hard ferromagnets constitute excellent candidate for permanent magnets as they have a wide range of power before saturating but the necessary field H_c to reverse the magnetization is too important and generates a non desired heath (which power equals the area of a hysteresis loop, i.e. $\approx (BH)_{max}$).

As we choose soft ferromagnet, Ni becomes the best candidate for fabrication purpose (easy to sputter and electroplate, cheap) as well as its bulk properties:

Table 9: Fe, Co, Ni magnetic specifications

Bulk Properties	H_c(A/m)	M_s(10^6A/m)	Curie temperature (°C)	density (kg/m^3)
Ni	$0.05-23$	0.48	358	8.90
Co	$0.80-71.62$	1.42	1130	8.908
Fe	0.16	1.71	770	7.874

Micromanipulation We aim to develop tools for biological objects manipulation from single cells ($1-10\mu m$) to young oocytes ($< 100\mu m$), see Fig.26. A characteristic size between $50-500\mu$m is aimed, we also add two static arms to the original shape to stabilize the grip, being careful to not break the robot symmetry.

Elasticity of biological object vary with growth phase, temperature and environmental conditions [143]. As we are taking Saccharomyces cerevisiae yeast a reference and a final target for this project, at standard conditions ($T = 25$°C), we know young modulus is $112\pm$ 6MPa and 107 ± 6MPa [144] in exponential and stationary growth phases, respectively. As a comparison, for a healthy red blood cell, Young modulus is much smaller with 26 ± 7kPa [145]. Yeast is then a simpler candidate to start manipulating biological bodies, but some can be much more diluted.

Diverse scale and shape for wide range of use At this scale, though shape factor changes necessarily the hydrodynamics performances, the dependency is almost linear and with a small coefficient [79] because of thin thickness. With a high aspect ratio, functionality is then preponderant on hydrodynamics considerations.

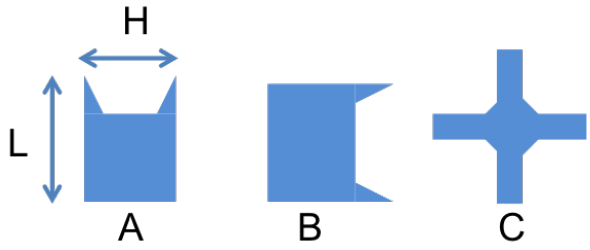

Figure 26: We focus our study on three different shapes oriented toward manipulation, both with complementaru functions: (A) MagPole forward arms (B) Magpole side arms (C) 4 arms.

The important aspect ratio should not be an issue for manipulating object thanks to surface attractive forces. We design arms though to maintain the contact on sides. The demonstration of manipulation will be done on equivalent size object to biological targets, mostly cellular. Manipulating biological requires more restrictive experimental conditions (in particular

chemicals concentration and temperature) and objects are more challenging to handle, as they are soft with complex surfaces.

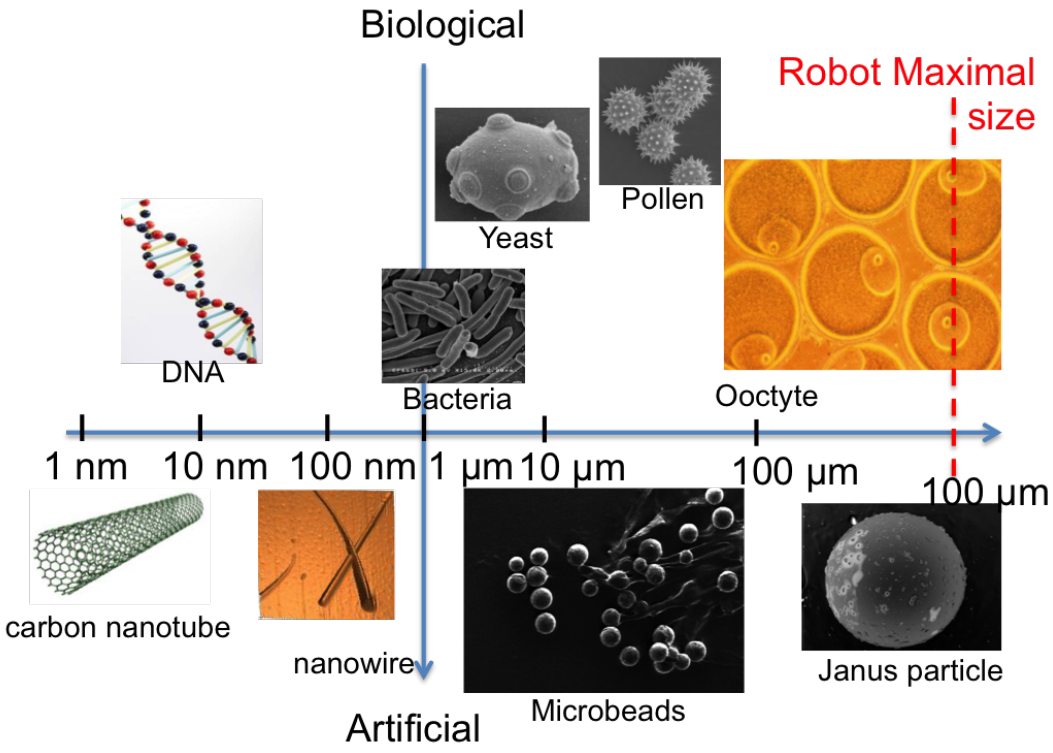

Figure 27: Scale graph summarizing the object size in biology and equivalent artificial object created in clean room.

We will describe later that it is difficult to precisely anticipate the thickness during metallic growth. We have tried two range of thickness. One is ultra-thin with a $2-6\mu m$ thickness, the other has a bigger range with $25-30\mu m$.

1.2 Miniaturisation challenges: microtechnologies

Fabricating tools below millimetric scale involves - as we have mentioned in Part 1 - completely different physics, i.e. requires new process methods and working conditions as well as new design approach. We present the different method used in clean room to achieve standard MEMS design. μfluidics specific techniques such as PDMS Molding and bonding will be discussed further.

Clean Room Facilities The fabrication steps require a controlled environment where humidity, particle concentration, pressure and temperature are maintained at a precise level (ISO 14644-1). Most of the environment we work in LPN are class 100 or 10 implying a condition on C concentration

$$C < 10^N * (\frac{10^{-7}}{D})^{2.08} \tag{18}$$

MEMS Technology A silicon wafer is the most commonly used platform for microfabrication, but there is a trend toward different substrate materials, especially in the field of BioMEMS Standard techniques can be categorized in three main categories, the patterning technologies, which define a shape generally on a polymer mask, negative and positive transfer which respectively remove or add material on a subtrate.

Patterning Technology: lithography Lithography, see Fig. 28 is the main patterning technology and can be achieved using photons or electrons. The resolution is dependent of the insulated resin and more importantly of the insulation source, due to diffraction. We use a UV lamp for pattern bigger than $\approx 5\mu m$ and e-beam lithography for smaller patterns. Typically, smaller robots ($< 100\mu m$) with arms are difficult patterns.

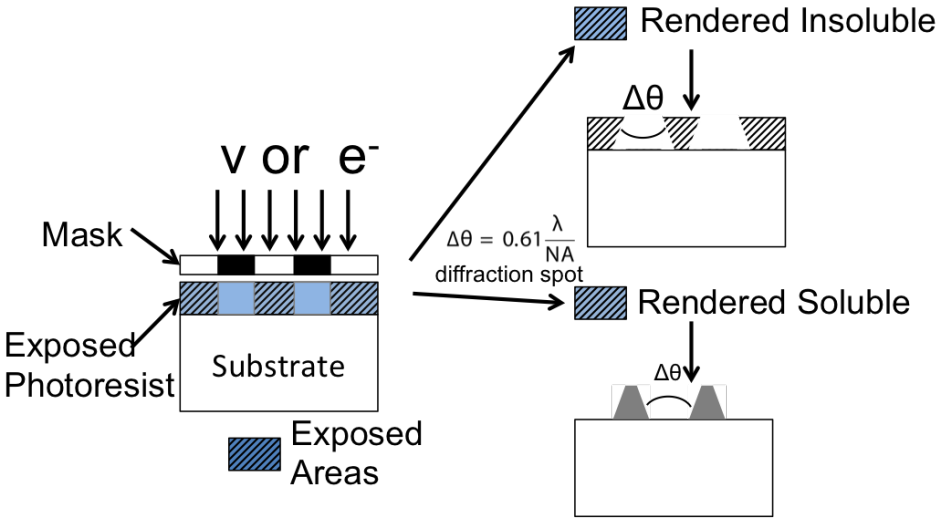

Figure 28: Using Photons or electrons, we insulate patterns on polymers to then transfer using Negative or Positive Techniques.

As seen on the schematic, the insulation generates a natural default due to light or electron diffraction and influence the vertical profile. This has an incidence on the vertical pattern and we usually reduce it by optimizing the contact between the lithography mask and the sample. In cases in which the photoresist is a permanent part of the final device (e.g., microfluidics, carbon MEMS [C-MEMS]), further processing may not be necessary.In most other cases, the sacrificial photoresist pattern is used as a mask for etching (subtractive) or deposition (additive) on the underlying substrate (a subtractive process).

Pattern Transfer: Negative (or subtractive) techniques In a subtractive process, the mask acts as a protective barrier to the etching agent, which can be a liquid solution, a gas, or plasma. After pattern transfer, the resist can be removed for further process steps -see Fig. 10.

Pattern Transfer: Positive Techniques (or additive) Similarly, pattern transfer can involve a deposition technique, as Fig. 30 describe it. With or without a mask for transferring pattern, positive techniques are bottom-up strategies. In our case we use: sputtering, e-beam evaporation or electrochemical deposition for metallic and plasma-enhanced chemical vapor deposition for dielectric deposition.

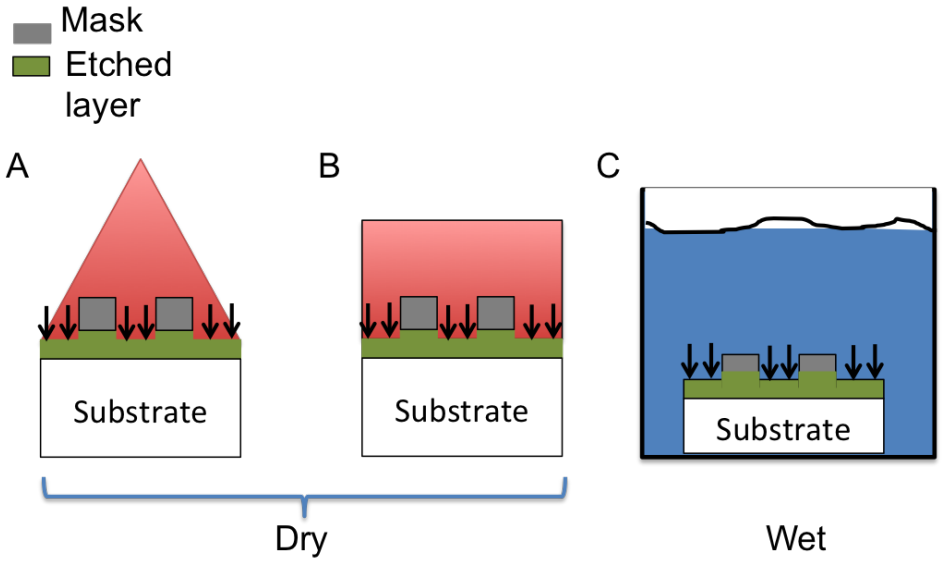

Figure 29: With or without a mask for transferring pattern, negative techniques constitutes rather top-down approaches; (A) Glow discharge (RIE: CCP, ICP) (B) Ion beam (IBE) (C) Wet-etching(acid, base,solvant).

Table 10: Negative technique to transfer a pattern on a layer; speed defines etch rate in the principal direction

Etching Technique	Type	Isotropy	Speed	Material
Reactive-ion etching	Yes	No	Yes	Resin or Dielectric
Ion-beam etching	Yes	No	No	Resin, Metal or Dielectric

We need metal layer masking, electrolytic growth seed layer and grown metal. Sputtering being the most precise metal deposition technique, it is often use at the an intermediary process, while electroplating or evaporation are used to conclude with a thicker growth, as the grain is to big for good adhesion

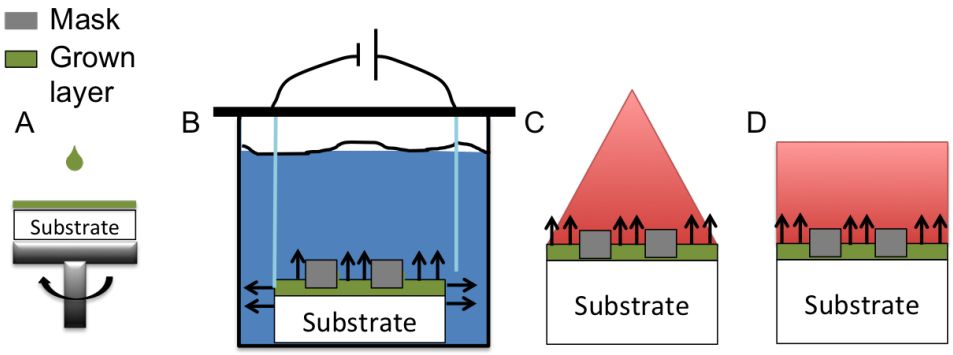

Figure 30: Listing of different positive techniques used for our process.

Table 11: Deposition techniques

Deposition Technique	Uniformity	Material	Thickness	Thickness Precision	Adhesion	Grain
Metal evaporation	difficult	Ni	$< 2\mu m$	bad	poor	bad control
Metal sputtering	good	Au, Ni, Cr	$< 300nm$	excellent	excellent	good
Plasma-enhanced chemical vapor deposition	fair	Si_xN_y, αSi	$< 1\mu m$	weak	good	-
Electro-plating	difficult	Au, Ni	almost unlimited	bad	fair	increase w/ thickness

1.3 Fabrication of ferromagnetic microrobot

We have seen previously how important the shape and its symmetry were for dynamics, control and fabrication. To achieve quantitative measurement with repeatability in time and obtain comparable results, we need a robust technology allowing to control geometries and material properties as well as we need to know what are the precision limitations of our process.

MagPol Technology: Flat Monolithic Nickel Body with symmetries MagPol was microfabricated (Fig. 31) in our facilities, designed with sketches from L-Edit (CAD software dedicated to microfabrication) for the optical lithography masks (a,b). We conceived 3 different shapes including a range of various dimensions and ratios. We focused on one kind and made it our standard for our experiments, the dimensions giving fine and repeatable motions, and the shape more adapted to the interaction with several 50μm beads.

Lithography masks The mask having close to microns details, we rather use a LEICA EBPG 5000+ electron lithography to write on a PMMA layer over a Pyrex thick substrate (2mm). The pattern is written on a file exported from L-Edit for the LEICA. We then develop the PMMA resin and sputter a thin Cr layer on it. A lift-off process allows us to develop in Aceton the structure and obtain the pattern on a Cr mask.

Substrate preparation We prepare a standard cleaned 4" Si wafer (525μm thick) with a sacrificial layer of PMMA - for releasing the robots at the end of the process. We then sputter,using e-beam metal evaporation, a first thin 10 nm Cr layer for guaranteeing adhesion and a sufficiently conductive (i.e. sufficiently thick) 70nm Ni layer on top. The conductivity will reduce heating generation during the electrolithic growth and guarantee a smoother grown surface.

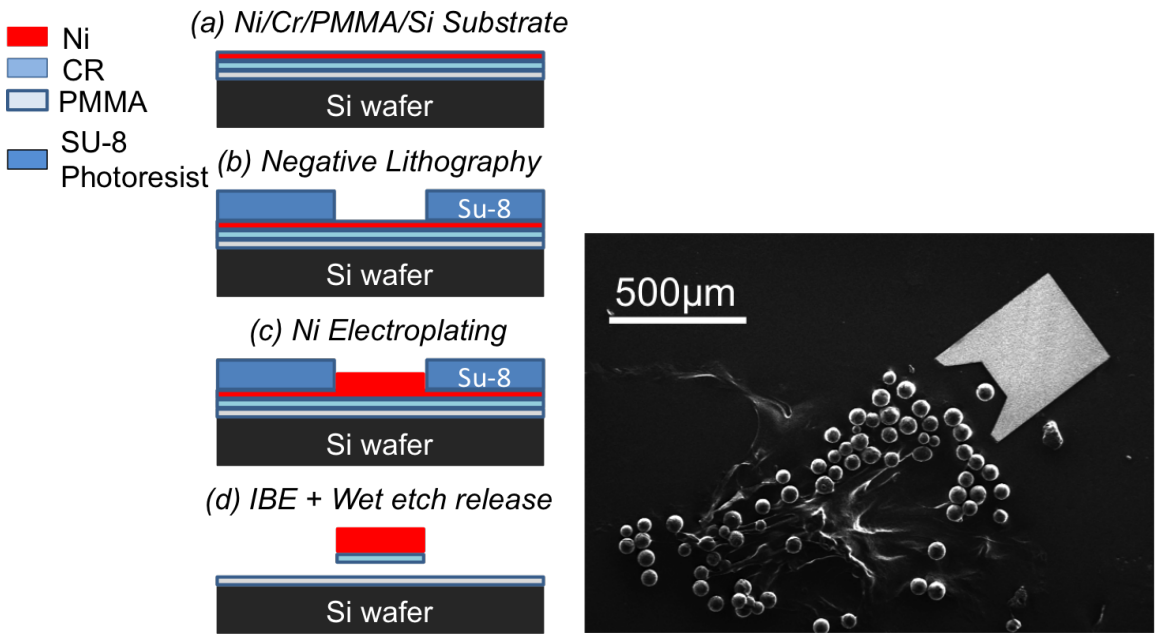

Figure 31: (left)Fabrication process to obtain ultra-thin magnetically polarized MagPol microrobot (right) SEM View of MagPol in with 50μm microbeads.

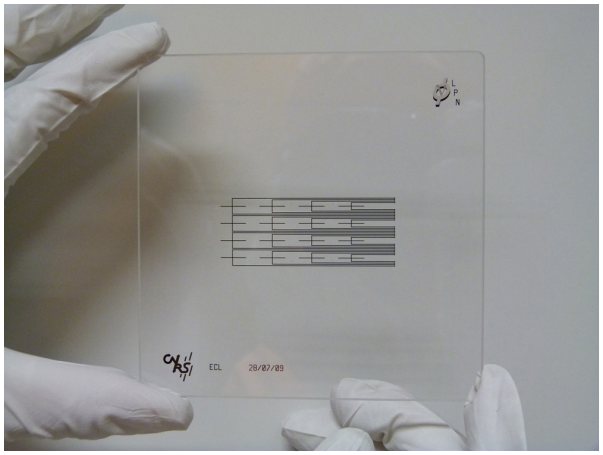

Figure 32: Schematic of principle of development of a Cr mask using electron lithography technique; Picture of a 4" Cr mask dedicated for optical lithography.

Patterning using optical Lithography We write the microrobot pattern on a thick photoresist using a SUSS Microtec Model MJB4 UV lithography (310-320nm standard bandwith). Depending on the vertical profile we want the type of thick resist can be either AZ9260, either epoxy based SU-8 (2XXX series; where XXX can be 005, 050 or 100 μm). They have quite complementary properties summed up on table 12.

AZ resins are faster to use and simpler to remove but we have to then grow metal quickly enough ($< 45'$) because of their short resisting time in bath chemical activity. It also has a lower maximum thickness around 10μ m.

SU-8 resists require a lift-off resin (LOR 50A) and still remain more complicated to remove, but they have an incomparable high aspect ratio, as seen on Fig. 36, due to their mechanical properties

Table 12: Different "thick" lithography resin comparison

Bulk Properties	AZ9260	SU-8 2050	SU-8 2005
Type	+	-	-
Thickness	$5-20\mu$ m	20 - 100 μ m	3 - 10 μ m
Post-bake wet-etch	++	-	-
Developer	AZ 400K	SU-8 Dev	SU-8 Dev
Process Time	20'	2h	1h
Resisting Time in bath	$< 45'$	-	-

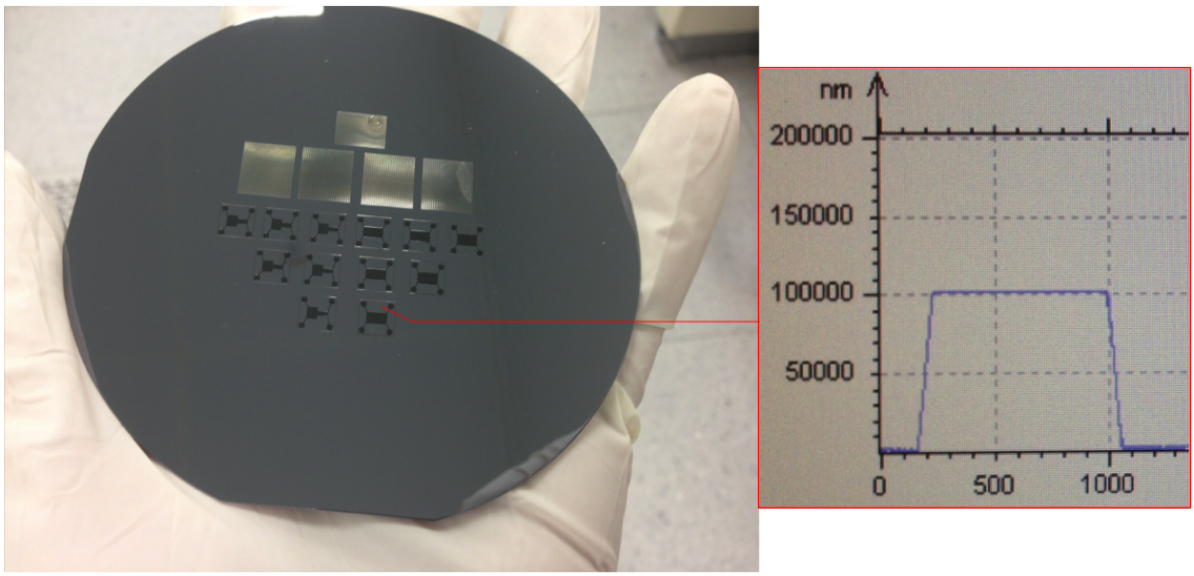

Figure 33: (left) SU-8 mold used for microchannels molding of PDMS chips, with very high aspect ratio (right) associated profile measured using profilometer.

Transferring pattern in Ni The simplest method to transfer pattern is to sputter a metallic layer over the patterned photoresist and achieve a lift-off. The problem of this technique (which would also imply to change the polarity of the pattern) is that e-beam deposition cannot deposit thick metallic layer and costs much more in terms of material. This is why MEMS standard processes use a lot more electroplating - though we will see it generates other issues. The growth increases the grain size of the metallic polycrystalline structure [146].

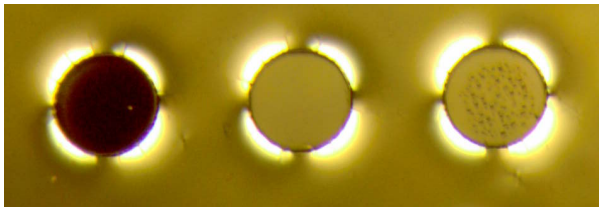

Figure 34: Post growth surface comparison; only left circle had a completely clean surface, appearance is less bright.

1.4 Nickel Monolithic Body: Soft Ferromagnetic materials Magnetization

As Nickel growth breaks the horizontal symmetry, we need to detail a little more what influences this phenomenon and how can we minimize it.

Electrodeposition setup Electrodeposition has been carried out in an home made reactor designed in order to increase reproducibility and uniformity on small samples. The anode is constituted by a spiral of platinum. Several materials and shapes have been investigated for the anode. Using platinum instead of nickel, avoids the anode material oxidation that reduce the efficiency of the bath. The cathode is constituted by the sample. The growth of Ni over the conductive layer is achieved in a Ni $0.1M$ electrolithic bath (composed of a $NiSO_4 26.2g/L, NiCl_2 3.5g/L$ and $H_3BO_3 3.1g/L$). The sample constitutes the anode and a second electrode is placed at a$\approx 1cm$ distance with a spiral shaped Pt electrode. They are both connected to a generator which induces a current in the direction of the platinum electrode. The current sign defines the direction of the redox equation.

$$Ni^{2+} + 2e^{-} = Ni \tag{19}$$

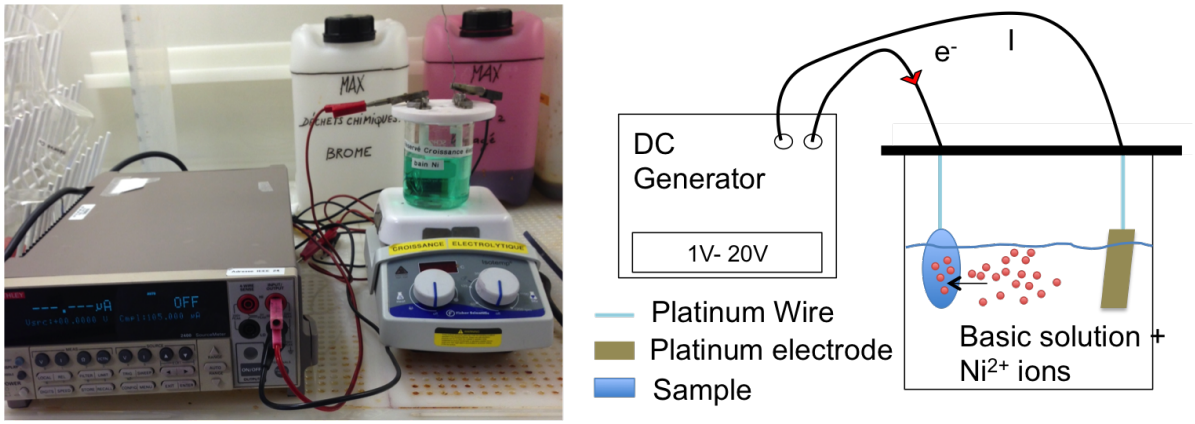

Figure 35: Electroplating device (left) and schematic of reaction (right).

Nickel Deposition We use a sputtered metallic layer with a metallic seed layer In our configuration, it is difficult to control the average precision of the thickness of the growth as the deposition is function of the distance with the Pt electrode, the immersed surface of the sample, the concentration of the bath and of course the electrical power.

We obtain a thick metal layer with a bright surface. The deposition rate is around $100nm/min$ for a $1mm^2$ surface.

Conclusion on Nickel electrodeposition Though electrodeposition is relatively simple to initiate, it becomes more expensive when trying to obtain some reproducible.

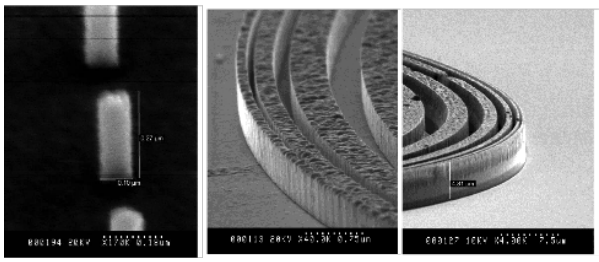

Figure 36: Ni structures grown for masking purpose, made in LPN [20], on Ti(10nm)/Au(100nm) (left) a 100nm diameter dot before etching (middle) nickel rings, 500nm thick, smaller width (right) 4.8μm thick.

2 Microrobot integration in fluidic chamber

The fluidic chip works here as an experimental platform for microrobotic as well as a support for in-vitro application. The technology developed from LPN allows us to control precisely the geometries (dimensions and shape) of the channels as well as the hydrodynamics (pressure and velocity). The microrobot need to be easily integrated and contained in a microchamber.

In this section we describe how the PDMS-Glass technology allows us to produce lab-on-chip including untethered microrobots.

2.1 Design of Fluidic Chamber

Our microfluidic chip aiming to study hydrodynamics of the robot, three parts need to be considered for design, the chamber, the channels and the inlets.

The chamber The chamber is the place where the microrobot is located and can move. The area need to be vast enough to observe movement and interaction with µobjects. Our robots are $< 500\mu m$ and we aim for at least 5 times their maximal bodylength - i.e. $2.5mm$.

As current advances in microrobotic have led to a microrobotic competition [16] where two arena design are proposed as a template - see Fig. 37, we adapt these to a microfluidic circuit in order to make it our experimental chamber, for dynamics characterization as well as manipulation and automated trajectory.

For two reasons, we take that value as the maximum size of the chamber. The first one is to have a sufficiently high magnetic power anywhere in the chamber - i.e. to be close enough from the magnetic sources). The second reason is that optical feedback remains immobile to simplify the system control and as we always want the chamber in the frame of the camera, we then have to do a trade between the size of a frame size and the spatial resolution (choosing the focal).

Finally, to limit the influence of the top part of the chamber, we aim for a thickness $t > 5t_{robot,max} > 100\mu m$. The section shape is function of the fabrication method.

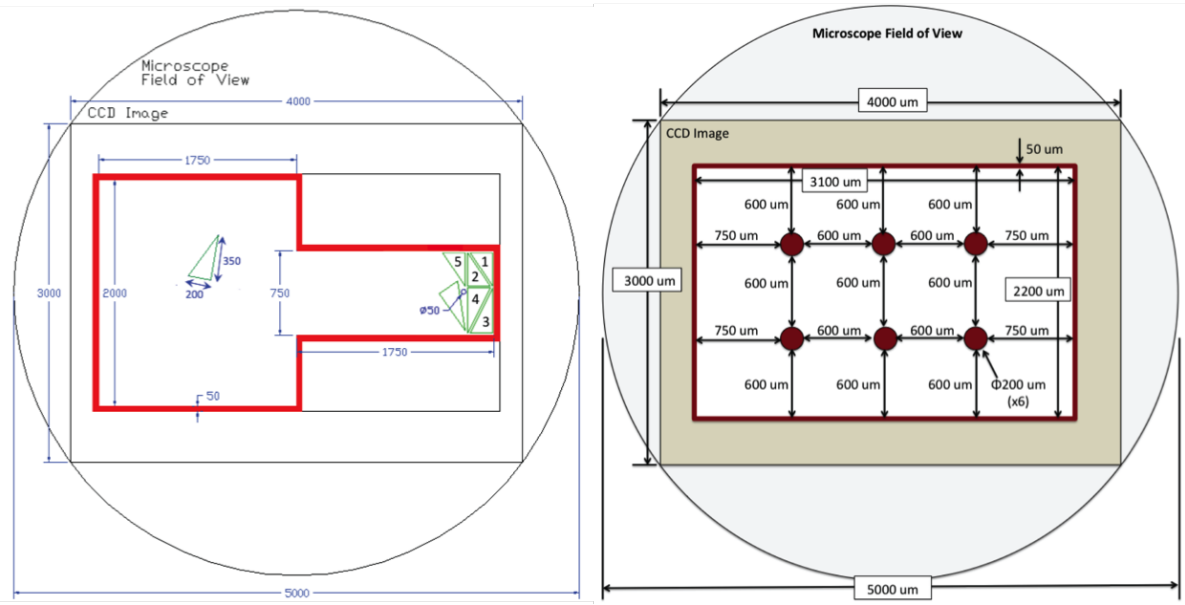

Figure 37: Arena dimensions and design for: (left) Microassembly Challenge where green rectangle are expected to be assembled inside a channel (right) Autonomous Mobility where automated trajectory are defined avoiding obstacles.

World-to-chip interface: inlets and outlets Conducting the flow inside and outside the chamber is an important design issued called world-to-chip problem. We need to evacuate bubbles, minimizing pressure drops due to sealing defect. Using a sufficiently large circular shape is a good solution to avoid the bubbles getting stuck in angles. The interfacing of the chip can then be achieved using an intermediary layer with connectors screwd, glued or plasma bonded depending mostly on the pressure in the circuit and the chemicals in the flow. In our case, we use metallic pin tightened in a PDMS bonded interface

The channels Our objective is to always keep inside of the chamber the robots - requiring smaller channels than the robot size - while being able at the same time to drive objects in and out. In particular, some objects can get stuck in position where creating a flow is a faster way to move them than using the robot. Bubbles can also appears, PDMS being porous, and must be evacuated.

2.2 Fabrication of Fluidic Chamber

We achieve our microfluidic device in a soft technology using PDMS over a Pyrex glass substrate. We can describe the fabrication as followed:

Fabrication Principles The manufacture of a microfluidic device starts with the design of the channels on a dedicated software (LEDIT, Illustrator ...).Once this design is made, it is sent to a manufacturer of photomask to be transferred on a glass medium or a plastic film. The micro-channels are printed with UV opaque ink (if the medium is a plastic film) or thin layer (70 nm) of chromium (if the medium is a glass plate), with very different capacities of resolution.

One of the wide spread technology to produce it consist in micro-channels molded in PDMS. The PDMS is a transparent, biocompatible (very similar to silicone gel used in breast implants), deformable, inexpensive elastomer, easy to mold and bond with glass. For these reasons it has been acclaimed by researchers.

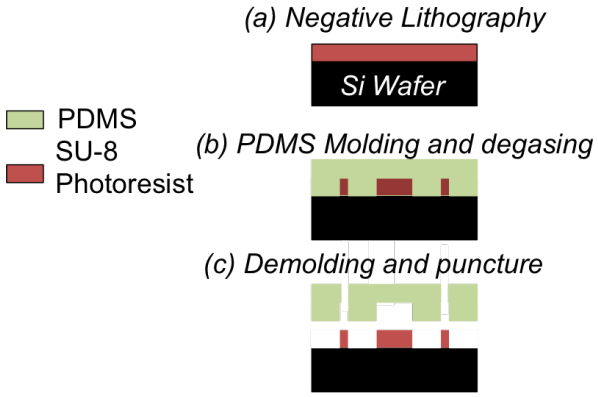

Figure 38: Fabrication of a PDMS microfluidic using SU-8 molding.

We call molding the phase when sketches of the microchannels on the photomask are transformed into tangible micro-channels. Negative micro-channels are ”sculpted” on the mold; resulting in replicas that will enable the carving of the channels into the future material of the microfluidic chip. (1) Resin is spread on a flat surface (often a silicon wafer) with the desired thickness (which determines the height of the channel) (2) The resin, protected by the mask on which channels are drawn, is partially exposed to UV light. Thus (in the case of a negative resin, SU8 type) only the parts representing the channels are exposed to UV light and cured, the other parts of the mold being protected by the opaque areas of the mask. (3) The mold is developed in a solvent that etches areas of resin that were not exposed to UV light.(4) We obtain a microfluidic mold with a resin replica of the patterns that were present on the photomask (future micro-channels make ”walls” on the mold). The height of the channels is determined by the thickness of the original resin. Most of the time the mold is then treated with a stick (Silane) to facilitate the release of microfluidic devices during steps of molding.

Other technics such as hard microfludics using glass structures [147] or paper microfluidics [148] exist, based on the same principle but using different process and or material.

Structuration of microchannels using a SU8 mold Obtaining the pattern is usually achieved with standard photolithography technique using more viscous SU8 than previously (usually 2100). The high aspect ratio structures, sharp edges and good resistance to most of solvent make it a perfect candidate for molding a high number of square section channels in PDMS.

This resin is negative and as we will see, it compensates the molding negative replication. We then need to design our lithography mask positive, i.e. directly how we wants the channels (transparent where are the channels and opaque where are the PDMS walls). This technique has been widely explored by Yang et al. - high aspect ratio is illustrated on Fig. 39 and exploited by Whitesides or Quake research groups, the last one having extended it to multilayer soft technology.

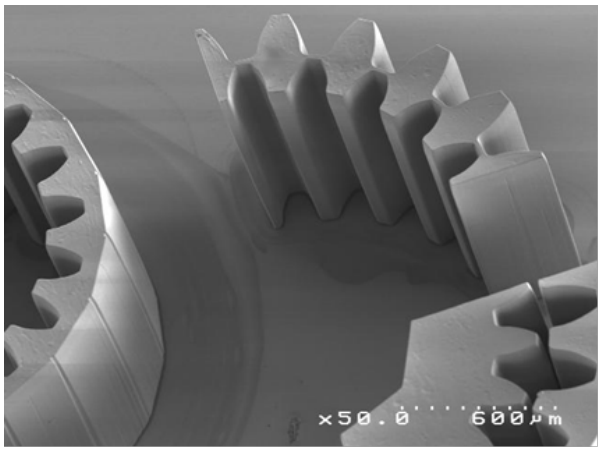

Figure 39: This photoresist can be as thick as 2 mm and aspect ratio > 20 and higher have been demonstrated with a standard contact lithography equipment (picture courtesy of R. Yang) [21].

Realization of microchannels in polymer The most common technology to achieve microchannels is using a liquid silicon oil called PDMS -for Polydimethylsiloxane- on top of a glass substrate. Because of PDMS flexibility after baking (cross-linkage), it is named soft technology. One of the most remarkable physical properties of this polymer is its Young modulus (10 to 100 times lower than elastomer).

The molding transfer the SU8 pattern to the PDMS. After evacuating the bubbles inside the PDMS volume, we reticulate it inside an oven for a minimum 2 h. cycle and then can manipulate it.

Chip bonding This flexibility allows in particular to adapt to most topology, guaranteeing an optimal bonding. It is naturally hydrophobic, contributing to watertightness (robust to $> 1 bar$pressure) of the device. Using a Harrick plasma cleaner, see fig.40, we expose inside the plasma generator chamber the PDMS block and its pyrex substrate. The plasma generated using HF electric field and $\approx 500 mTorr$ pressure ambient air changes the surface. 45" is enough to create very reactive O-H bonds on top of both surfaces. They recombine quickly in covalent bonds when in contact and a 2 h. at 78°C post-baking to finalize the process and guarantee. The bonding is reversible, which means it can be reopened - generating for example a sufficiently pressure, for cleaning purpose or to change the robot inside. The same process need then to be done.

Fluidic access to the chip Junctions in fluidic are an important challenge, particularly with the microfluidic chip, especially for watertightness and pressure drop minimization. The accesses must be thought well before fabrication and drilled before bonding. A 0.5 mm hole puncher guarantees a sufficiently tight hole for Glass PDMS technology range of pressure.

To minimize the chip size, cutting glass substrate - isotropic fragile material is challenging. We prefer using a dicing saw machine to precisely control the sample fitting inside the electromagnetic setup.

We use 1 mm metallic pin to interface the pin holes with the small fluidic tubes.

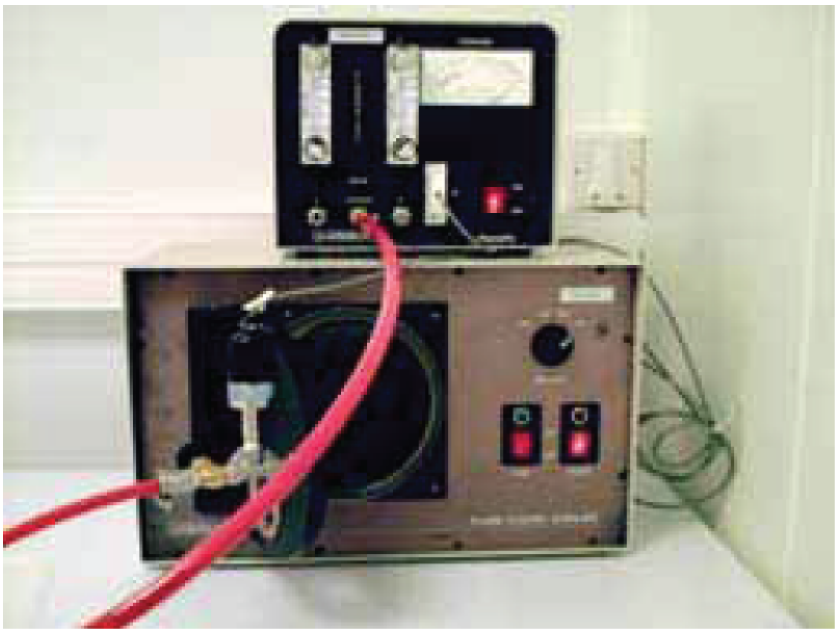

Figure 40: Plasma Generator

2.3 Integration and fluidic circuit

Integration of the robot: Pick & drop or injection? On the one hand, injection can be achieved using standard polymer tubes and a flow generator, which remain quite elegant and oriented toward biological applications. Supposing we can generate a flow to move the robot in the circuit, there are risks it requires a long time and/or the robot gets sticked on a polymer surface, due to adhesion force and liquid pressure. Moreover, at least one channel section must be large enough so robot can go through, risking the robot to go out in case of brutal motion.

On the other hand pick-and-drop can be destructive with the robot and in any case it remains challenging to evaluate the material stress induced once the transfer is achieved. Difficulties and fragility increases as the objects get smaller, particularly in environment where humidity is not controlled enough. To minimize this there exists tools depending on the scale, from the simple macro tweezers with an adapted surface adhesion to nanoprobes. The main criterium is a compromise between low pull-off (to release) and high adhesion (to capture). This question has already been studied in Alvo thesis [87].

Table 13: Integration comparison

Criteria	Pick-and-drop	Injection	Magnetic force
Skill Dependency	Yes	No	Yes
Destructive / Modify Material	Yes	No	No
Scale dependent	$> 100\mu m$	$< 50\mu m$	No
Success rate	High	Low	Depend of transfer
Selectivity	High	Low	Low

We here mostly work on relatively high dimensions which allows us to use Pick-and-drop without critically modifying the robot. We use nitrile material from gloves to achieve our transfer, which happens to be soft ($\approx 10MPa$) and having an important adhesion / pull-off

force ratio.

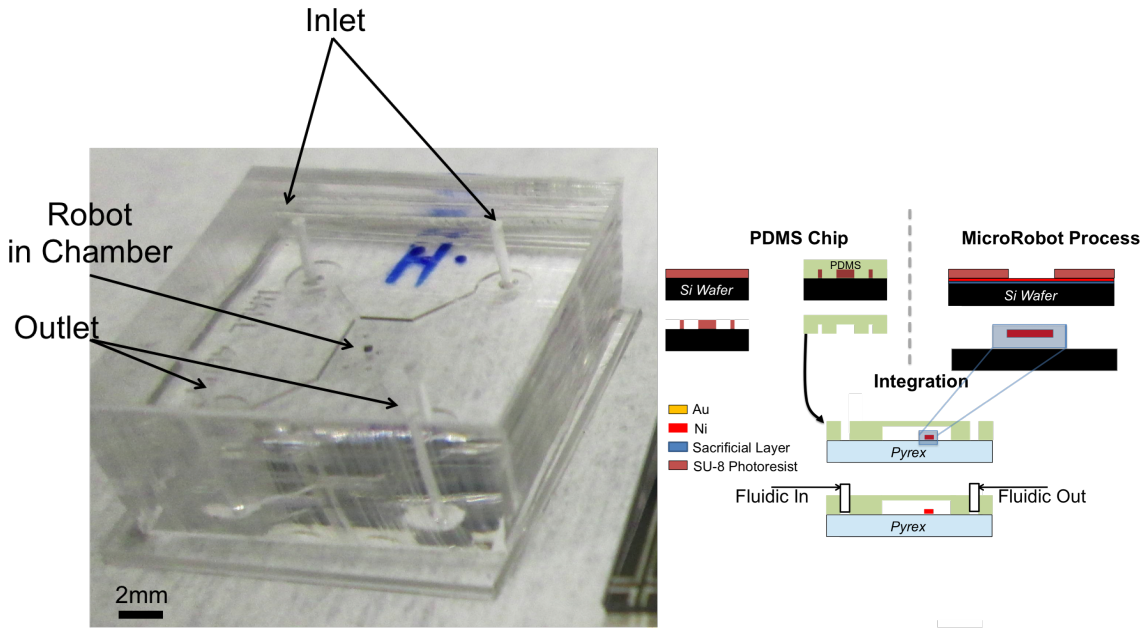

Figure 41: (left) Picture of a completed chip with 500 μm robot integrated, ready to be plugged to the fluidic circuit and placed inside a magnetic device (right) Global Process of Magpol from fabrication to integration in a μfluidic chip.

To avoid pressure drop coming from tubes (linear) and junctions (singular), we reduce the size of the circuit to a minimum. The junctions have an important impact on the differential of pressure between the two input channels, but reducing it requires a more controlled geometry, and hermetic material.

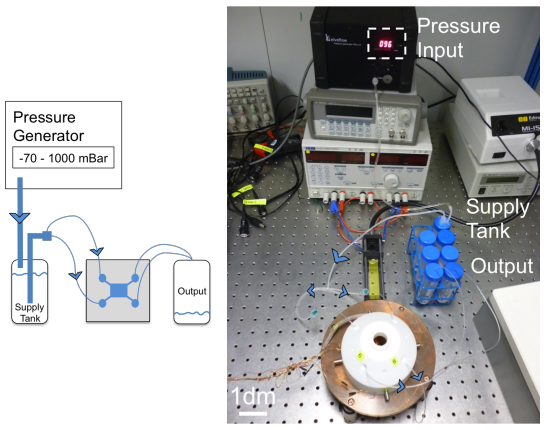

Figure 42: (left) Schematic of the fluidic circuit principle (right) Picture of the circuit.

Methods of control of fluidic flow The first importance of controlling the flow is to evacuate dust or bubbles and recycle completely the liquid in the chamber. The second one is to generate a constant flow to study the robustness of the system to hydrodynamic perturbation. To control it, we can either control in pressure or volume. Controlling using volume - typically with a syringe- constitutes a direct control of the flow but require a special setup to control the

progression of the plunger. A typical manual control would make a quite agressive peak of flux - which often damages permanently the bonding, and does not guarantee a constant flow. A technical solution is to use the device shown in figure.

A more elegant way is to create a pressure gradient by using a pressure generator. The one we use is from Elvesys©and can generate up-to 1 bar pressure (760 mm Hg) without gas supply, if the resistivity of the circuit is low enough. It is highly sufficient to study for example the equivalence of the blood pressure, which maximum value for a school-aged child is 120 mm Hg. We chose a simpler device as we are not trying to control in time the signal. Pressure is adjustable using a potientometer and a pressure display gives us the pressure with a mBar precision.

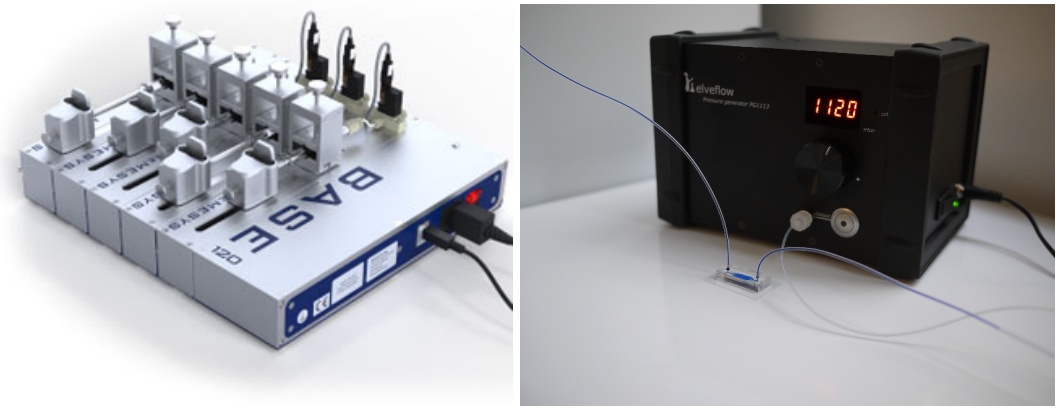

Figure 43: (left) Device used for syringe automated controlled flow (left) Single input pressure generator. We split the tube in two to distribute the same pressure over the two inputs of the chip.

As a reminder [88], it is important to recall the linear dependency for a rectangular cross-sections channel between pressure and flux Q when controlling the circuit in pressure. Solving Stokes equation at low Reynolds number is equivalent to resolve a 2D Poisson equation

$$\Delta u = -\frac{\Delta P}{\mu} \tag{20}$$

and leads to a Fourier series expansion

$$Q = \frac{8Gb}{\mu w} \sum i = 1^{n} \frac{1}{\beta_n^4} (1 - \frac{2}{\beta_n b} th\beta_n \frac{b}{2}) \tag{21}$$

which becomes, by defining the friction factor C (dependent of channel aspect ration $\chi = w/b$), the linear relation

$$Q = C\frac{Gb^3 w}{\mu} \tag{22}$$

As an example, the speed would reach a 7.9 mm/s maximum for a water or IPA solution if the channel is a square ($\chi = 1$) at 1 bar.

3 Dynamics control: Magnetic Force Generation

We aim to control the robot through magnetic waves in any direction of the space. By linear combination, the condition to generate a magnetic flux in any direction of the plan

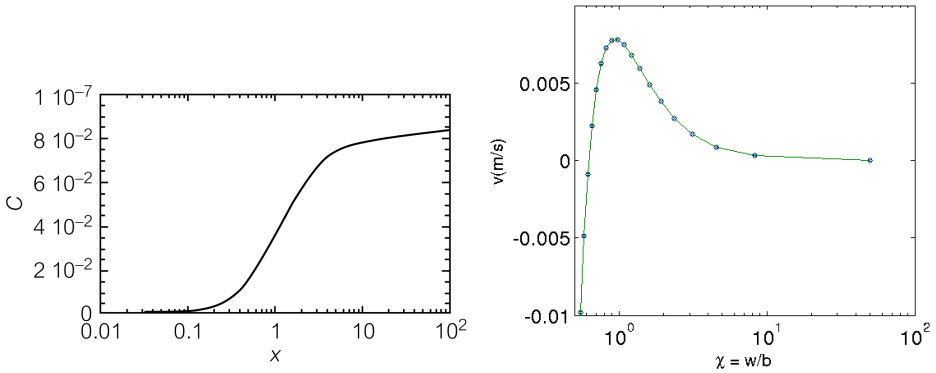

Figure 44: (left) Evolution of friction factor C (defined in the text), for a rectangular channel with $\chi = b/w$ its aspect ratio (right)Evolution of flow average speed for a 1 bar pressure with $\chi = b/w$.

requires at least 2 axis of electromagnets. To generate gradients in any direction, it requires one more for each axis, i.e. 4 axis. The force and torque generated on the ferromagnetic layer are described as

$$\begin{cases} \mathbf{F} = (\mathbf{M}.\nabla\mathbf{B}) \\ \tau = \mathbf{M} \wedge \mathbf{B} \end{cases} \tag{23}$$

As magnetization is a function of ferromagnetic volume,

$$\mathbf{M} = \iiint_{V_{ferromag}} \mathbf{m}\, dV \tag{24}$$

the magnetic forces are body forces. Because of surface effect predominance at microscale and low aspect ratio of the robot, it requires a high B magnetic flux amplitude to overcome natural surface forces.

Our aim is to fabricate two distinct electromagnetic source: one that provides both components (torque and force) and another which only generates torque component, i.e. uniform fields. It is important to maximize the magnetic flux generated in the area of the microfluidic chamber.

We then have designed two different kind of magnetic actuator with complementary functions. We will start describing the design issues for a single electromagnet first then will detail the Helmholtz coils cases as they are a particular case of two electromagnets associated.

3.1 Magnetic flux optimization of a solenoid for in-plane gradient linear superposition

How to design a gradient solenoid to optimize the emitted magnetic flux in the area of the chip while minimizing field non-desired (generally orthoaxial) components? Maximize the current in the circuit, the inductance, minimize the distance with the source? Depending on the constraint, one path is more adapted than another All the designed parts we made were printed on a 3D printer using ABS material. The theoretical spatial resolution is $\approx 0.5mm$ but this precision varies depending on the direction and geometry. Printed structures allow an easy way to satisfy all alignments between coils and orthogonality as well.

Solenoid Fundamentals Electric current generates a magnetic field according to Maxwell Ampere equation,

$$\mathbf{rot}(\mathbf{B}) = \mu_0(j + \frac{\partial E}{\partial t}) \tag{25}$$

and designing a coil with several turns increases the amplitude of the field - see Fig. 45. The notion of polarity is here underlined by the red arrow direction pointing in the direction of the induced magnetic dipole.

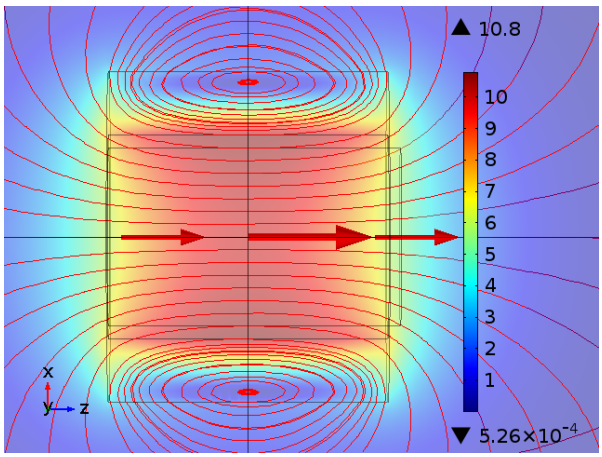

Figure 45: Comsol simulation of a magnetic flux generated by a current in a solenoid, magnetic flux in mT. The electromagnet constitutes a magnetic dipole where its flux amplitude is directly controlled by current intensity. The cylindrical symmetry gives specific properties to the field. If magnetic flux has a straight direction, notice that both field gradient points inside the magnet.

One of the advantages of an electromagnet over a permanent magnet is that the magnetic field can be rapidly switched - depending on the inertia of the circuit- over a wide range of values by controlling the electric current I. However, a continuous supply of electrical energy is required to maintain the field and .

The coil being a solenoid - i.e. having the cylindrical symmetry, the magnetic flux distribution is only dependent of radial and axial position,

$$\mathbf{B}(M) = \mathbf{B}(r,z) \tag{26}$$

and is parallel toward **z** on the axis.

$$\mathbf{B}(z) = B(z)\mathbf{z} \tag{27}$$

Though it remains simple to obtain an analytical expression of the magnetic flux using Ampere Theorem on the axis,

$$\mathbf{B} = \mu_0 \frac{NI}{2a}\left(\frac{z}{\sqrt{z^2+R^2}} - \frac{z+2a}{\sqrt{(z+2a)^2+R^2}}\right) \tag{28}$$

it requires Bessel functions to then obtain a complex analytical expression out of the axis. This is our first motivation to use finite element method to determine the flux distribution and achieve comparative studies. In terms of magnetic flux amplitude optimization, previous

equation is sufficient. But we also need to consider the flux in the axis neigbourhood to minimize the orthoaxial components and decouple each electromagnetic force. The ferromagnetic core increases the magnetic field to thousands of times the strength of the field of the coil alone in the core, due to the high magnetic permeability μ of the ferromagnetic material. This is called a ferromagnetic-core or iron-core solenoid. Finally, we can sum up as followed on Fig. 46 the optimization problem.

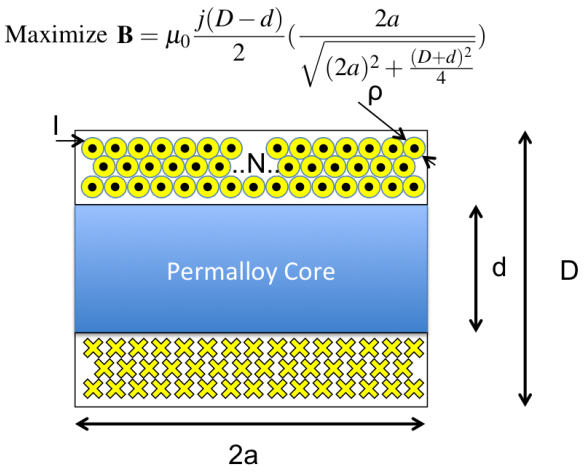

Figure 46: The electromagnet constitutes a magnetic dipole where its flux amplitude is directly controlled by current intensity. The cylindrical symmetry gives specific properties to the field.

3.2 Optimization for energy transfer efficiency

Now that we have drawn the general challenge of designing an electromagnetic device, we need to define clearly parameters dependencies and conclude an optimized configuration for magnetic energy transfer. Several problem can be solved separately. First is the question of wiring, which will define the multi-turn solenoid density of current but will also limit the power of the coil.

Then we have to decide which diameters has our electromagnet, and what are the dimensions of the conducting section. We will see that it is highly depending on the size of the sample and the way we manipulate it.

We will also treat in this section the specific case of Helmholtz coils, which deliver a uniform field in a small area.

Wiring optimization To optimize intensity, we need first to model the geometry of the wiring. We suppose it is uniformly wired on the core with a triangular configuration (see fig.47). The maximum density is then $\frac{\pi}{2\sqrt{3}}$ demonstrated by Thue in 1910) and defines the maximum compacity we can obtain from a wired solenoid.

We then can write

$$N = \lfloor \frac{(D-d)a}{\pi\rho^2} \frac{\pi}{2\sqrt{3}} \rfloor \tag{29}$$

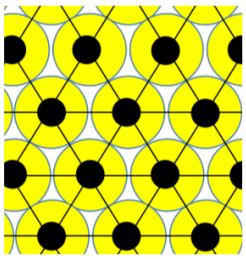

$$c = \frac{\pi r^2}{2\sqrt{3}r^2} = \frac{\pi}{2\sqrt{3}}$$

Figure 47: Compacity of the wiring can be fairly assimilated to a face-centred cubic in 2D

which confirms that having the smallest wire diameter increases the magnetic power. It also increases the resistivity ρ/S thus the Joule effect. It limits the maximum current. As a compromise, we take 0.72 mm (AWG 21) to have a 1.2 A limitation, in case we have important DC current. We can assimilate the multi-loop circuit to a volumic current by the relation

$$NI = jS \tag{30}$$

Solenoid geometry adapted to the sample The outer **diameter**, for a matter of volume, is limited by the minimum distance to the center of the sample - see fig.51. We limit the sample size to 14mm, a good compromise for studying the hydrodynamics of the robot.

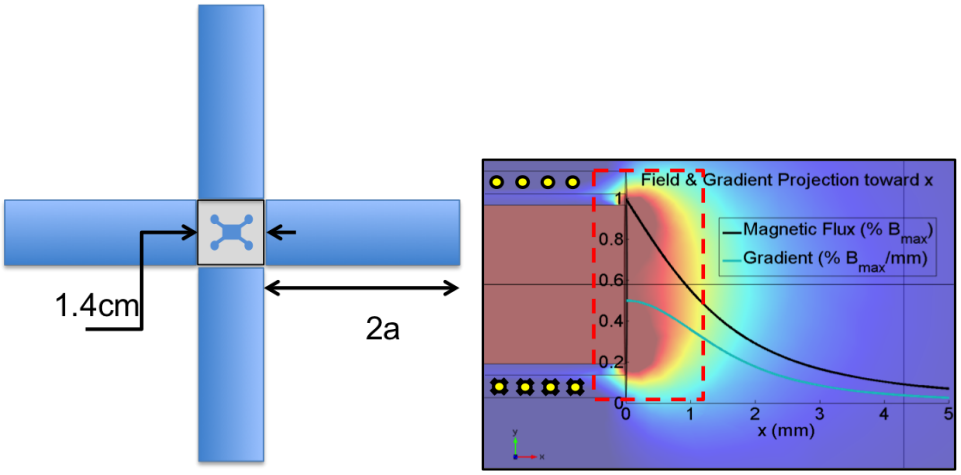

Figure 48: (left) Schematic showing how getting the closest from the chip limits the outside diameter (right) FEM simulation confirms the value of orthoaxial component is inversely proportional to the inner diameter size and remains below 1% in the chamber volume.

Fixing the inner diameter d is then a trade between the magnetic power we induce (the higher is $(D-d)$) and the minimization of the orthoaxial components around the axis neighbourhood. By using FEM simulation, we reach the first value for which

$$\frac{B_{\perp z}}{B} < 1\% \tag{31}$$

in the smallest area including the chamber. We finds 5 mm.

As seen on the previous equation, the **length** of the coil $2a$ only influences the term $\frac{z+2a}{\sqrt{(z+2a)^2+R^2}}$. To minimize below 1% the other term, we need to minimize $\frac{2a}{\sqrt{4a^2+R^2}}$. The value to be below this ratio is $a > 1.76mm$.

The following table sums up the coil geometry and specifications of the Dome electromagnets.

Table 14: Specifications of 4 electromagnets

N	D(mm)	d(mm)	2 a(mm)	Wire diameter ρ (mm)	AWG gauge	I_{max} (A)
160 ± 1	13	7	24	2.2	23	0.361

and the resulting design we adopted was to integrate the electromagnets in a dome structure, guaranteeing axis alignments with a sufficient precision and a possible translation to adapt the axial position and eventually sheltering larger samples.

Figure 49: This dome-shape setup allows to generate gradient in any direction of the horizontal plane.

High-permeability material as electromagnet core Each electromagnet has a core to maintain its mechanical stability and choosing a high magnetic permeability ferromagnetic material has an impact on its electronic behaviour as well as magnetic.

The relative permeability varies from 100 for steel or ferrite to 60000 for a mumetal ($Ni_{79}/Mo_4/Cu_5/Fe$ alloy). High magnetic permeability alloy are typically used in closed magnetic circuit, such as AC/DC transformers, to optimize the field confinement and the gain is almost proportional to the permeability. In our case where it is not closed and only a limited cylinder has high permeability, it is far from proportional but still increases the magnetic amplitude with a non-neglectable value.

Beyond the important permeability, those cores can withstand high levels of magnetic fields without saturating and does not remain magnetized, unlike standard stainless steel. It is important for our applications as the magnetic field is repeatedly switched.

To compare the different model, we have first used litterature references [149]. Comsol©4.4 release have given us access to direct values that can be plotted and compared to illustrate our choices. We will take them as a reference for the rest of the simulation.

Stainless steel annealed offers a much higher saturation level but will also constitute a perturbative permanent magne. We will then sprefer Mumetal because of its lower saturation level and low coercitivity.

It is important to verify how much neglectable is orthoradial component.

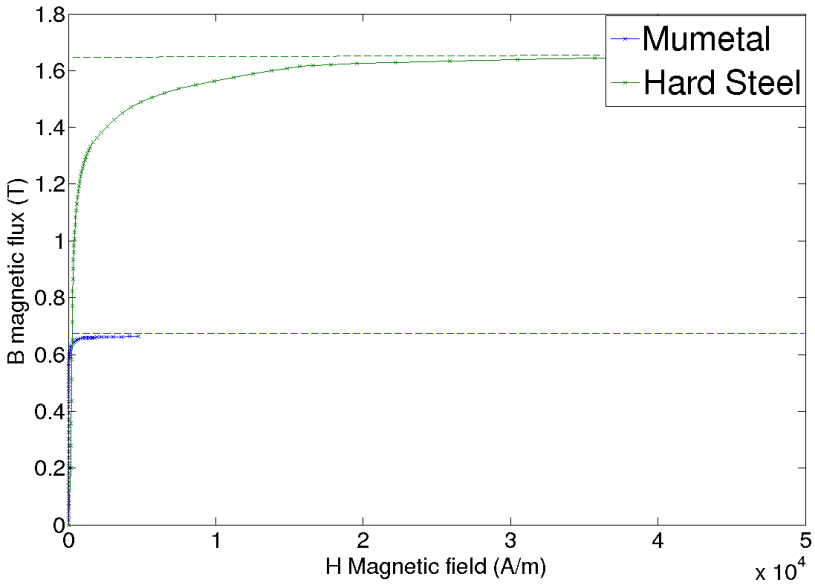

Figure 50: Mumetal and Stainless Steel HB curve. Saturation remains lower for mumetal than a stainless steel.

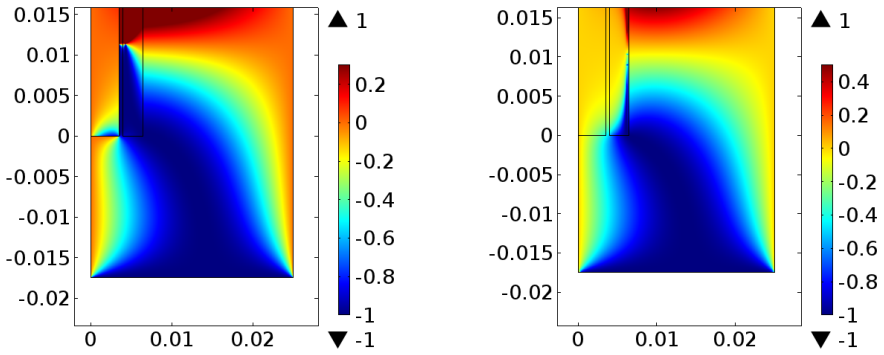

Figure 51: FEM simulation confirms the value of orthoaxial component remains below 1% in the chamber volume. Colors are unitless and plot $\frac{B_\perp}{B}$(left) simulation displays the area of the electromagnets with air instead of a core (right) simulation achieved with a mumetal core, we notice discontinuity at the edge of the electromagnet.

Helmholtz coils case and flux optimization A **Helmholtz pair** is a specific association of two electromagnets without core. It is a device for producing a region of nearly uniform magnetic field, named after the German physicist Hermann von Helmholtz. It consists of two identical circular magnetic solenoid that are placed symmetrically one on each side of the experimental area along a common axis, and separated by a distance 2a equal to the radius R of the coils. Besides creating magnetic fields, Helmholtz coils are also used in experimental setup to cancel external magnetic fields, such as the Earth's magnetic field.

The design we want can be compared to Matryoshka russian dolls. We include each pair in a bigger. As a consequence, there is already a dependency between the outer diameter of a coil and the inner diameter of the bigger one (if it exists).

The small Helmholtz pair first needs to be big enough to remove a sample by hand or with a microcontrolled stage. We fix the inner diameter equals to $d_1 = 50mm$.

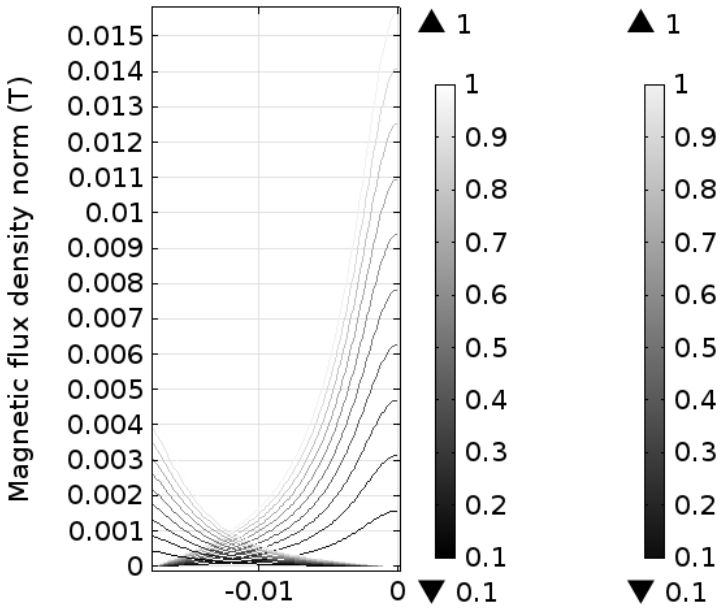

Figure 52: Plot extracted from FEM simulation to compare both magnetic flux distribution and the evolution of gain depending on the position on the radial axis and compare their amplitude with (right) and without (left) core.

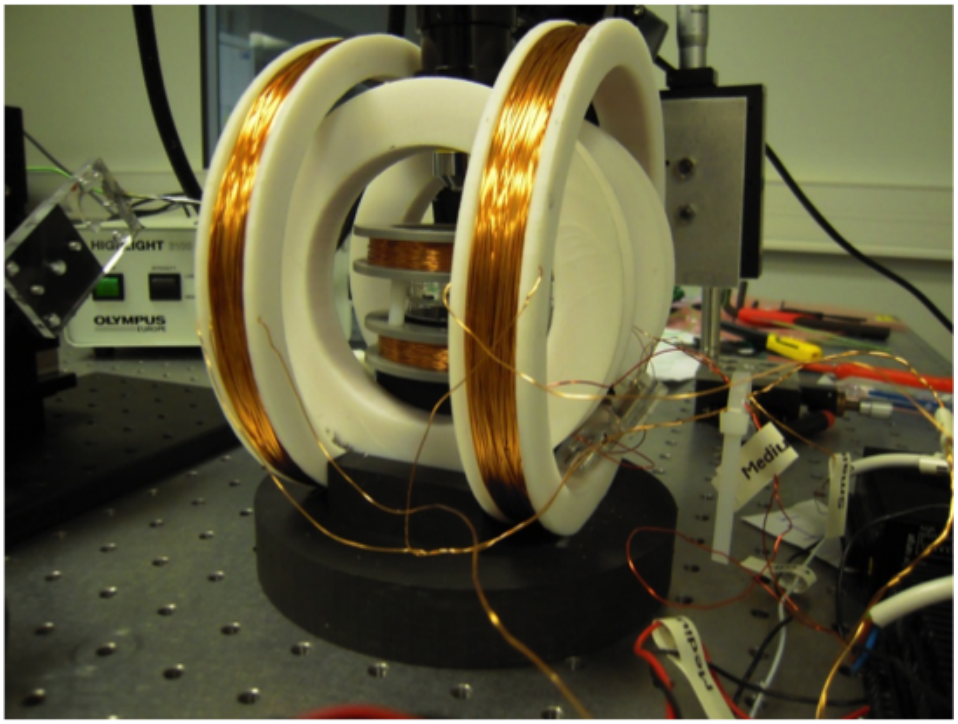

Figure 53: Helmholtz platform generates 3mT maximum uniform field in any direction in standard use conditions, including neglectable heating and no saturation from amplifying circuit.

There is first a general condition for the coils. Each of the them carries an equal electrical current flowing in the same direction. Setting $2a = R$, which is the geometrical condition defining a Helmholtz pair, minimizes the non uniformity of the field at the center of the coils, in the sense of setting $\partial^2 B/\partial x^2 = 0$ (meaning that the first non-zero derivative is $\partial^4 B/\partial x^4$

as explained below), but leaves about 15% variation in field strength between the center and the planes of the coils. A slightly larger value of h reduces the difference in field between the center and the planes of the coils, at the expense of worsening the field's uniformity in the region near the center, as measured by $\partial^2 B/\partial x^2$.

By symmetry consideration and know expression of a finite solenoid magnetic flux on its axis we can compute the field and, taking the center of two coils as the origin O, we obtain

$$B(0) = \frac{4}{5}^{3/2} \mu_0 NI/R \tag{32}$$

The advantage of Helmholtz conditions is that a large neighbourhood of the center displays a uniform field, and $B(0)$ becomes a simple scalar criterion to optimize.

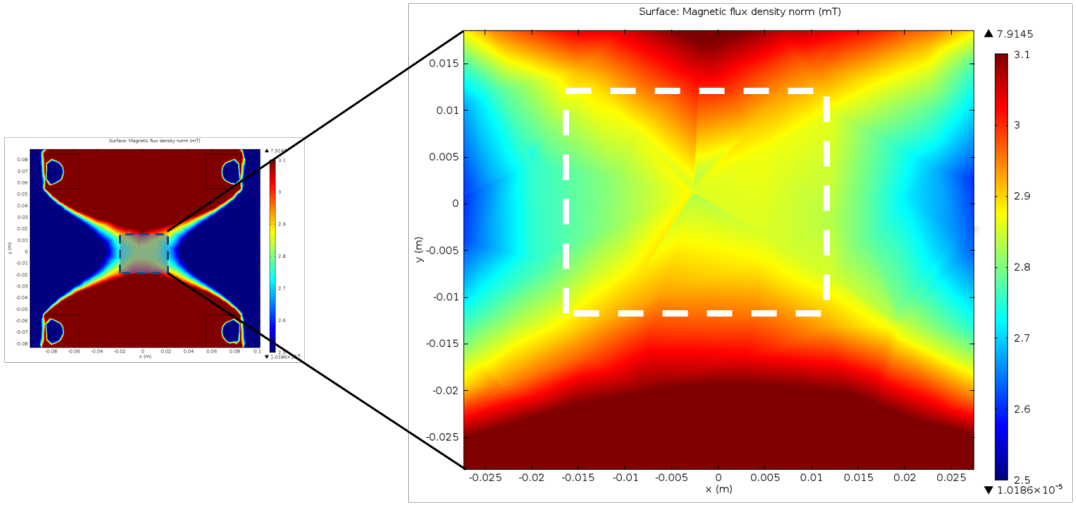

Figure 54: Simulation confirms a 20mm x 40mm section (see white dashed square for a less than 10 % variation of the field amplitude) for each coils axis, widely including the microfluidic circuit.

As we expect less confinement for this setup than for electromagnets, we use bigger wiring, which increase the maximal current but decrease a little the density of the current and increase the magnetic power.

Table 15: Different wiring comparison

Wire diameter r	ρ (Ω/km)	AWG gauge	I_lim (A)
0.64	52.95	22	7
0.56	66.80	23	4.7
0.51	84.20	24	3.5

The following table 16 sums up the coil geometry and specifications from Helmholtz setup. Small coils transfer the highest power but we notice an approximately $3.5mT/A$ linear ratio from the computation we did.

The approximative correspondence between flux B of each axis can be calibrated experimentally as the magnetic flux is linearly dependent of I. As we use a linear amplifier, the circuit itself is linear and $B \propto V_e$. We can estimate from simulation the magnetic flux value and deduce the torque over a nickel ferromagnetic body. It can also gives access to power.

Table 16: Helhomlz specifications

N	D(mm)	d(mm)	2a(mm)	H	ec(mm)	$B_{0,I=1A}$ (mT)
200	73	50	16	13	22	2.92
410	124	88	18	13	40	3.48
325	160	147	20	13	67	1.91

Table 17: Power and magnetic flux of the coils and volumic torque generated at the middle of the Helmholtz device for a voltage input between -10V and 10V

Magnetic flux range (mT,I=1A)	Torque generated ($\mu N/m^2$)
10	10
30	20
20	5

3.3 Power conversion and electrical circuit

Our magnetic flow is the direct consequence of electrons motion in the electrical circuit. The electrokinetic behaviour define the limitation in power and time of the circuit and is a critical boundary to our electric control.

Coils as electrical components Electromagnets have a complex impedance. We can first measure their resistive (real part) value. We measured them using a digital Agilent ohm meter. Same can be done measuring a time-response to a 1v step. The measured time-response corresponds to $\tau = \frac{L}{R}$.

Table 18: Helmholtz device electrical specifications

Helmholtz	big	medium	small
Resistance	22.057	19.25	5.51
Inductance measured	0.001	0.001	0.001
Inductance simulated	0.001	0.001	0.001
τ	0.0057	0.0055	0.0018

Helmholtz device have a τ around $1\mu s$, which makes them responsive enough for 5kHz sampling rate.

We notice, compared to Helmholtz coils, the time-response are close from our signal sampling frequency, and is a limitation for the user who would like to work at higher frequency.

Coils pairs: Helmholtz case In the case of Helmholtz coils, both coils are serial and inductances can be added if we neglect their mutual inductance.

As mutual inductance expression is

$$\mathbf{M} = \iint \mathbf{B}\, dS \tag{33}$$

Table 19: Dome electrical specification

Dome	North	West	East	South
Resistance	1.508	1.543	1.506	1.483
Inductance measured	0.1	0.1	0.1	0.1
Inductance simulated	0.1	0.1	0.1	0.1
τ	91.0	93.4	90.9	89.4

Amplification mode To drive the electromagnetic setup, we need a logic circuit and an amplification of its signal. As we aim to control it through a multi-task PC program, the computer achieves the logic circuit and its digital signal is converted with a s626 DAC card to generate 5kHz sampled analog signal, with a [-10V +10V] range. The required operating mode is easily selected using a dual in-line package (DIP) switch.

Because of the power limitation from the computer, an external bloc is required for amplification. Between a linear amplifier regulated in current or a pulsed width modulated power (PWM) supply, we choose a 4 axis linear amplification bloc with optimized heat dissipation.

Table 20: Comparative table of amplification mode

Amplification type (mT)	Linear power supply	Switching power supply (PWM)
Distorsion	No high frequency noise, but little to the input	switching high frequency noise
Power efficiency	low, with heat dissipation	high
Size & Weight	require heatsinks	important shield for high RF
Output Voltage	varies with load if not regulated, voltage limited by input voltage	small variation with load

Though it provides a little less power, it will reduce considerably the HF noise. As we want to command the magnetic power, which is directly proportional to the input current, we will rather configure the amplifiers for current than voltage regulation.

Electrical gain and frequential behaviour with current regulation mode As we want to achieve physical measurement as well as closed-loop control at up-to 5kHz sampling rate, we need to define the limitations of our electrical system.

Generating a frequential analysis on both setups, we analyze with a 4 channels TDS2024C oscilloscope the output signal and compare it to the input.

Important remarks from Bode diagrams of Fig. 55 are that both of the components have the expected frequential behaviour on the 0-200Hz bandwith. Dephasing with input is constant on each axis and approximately the same The current compensation works well and remain stable for frequency below 1 kHz.

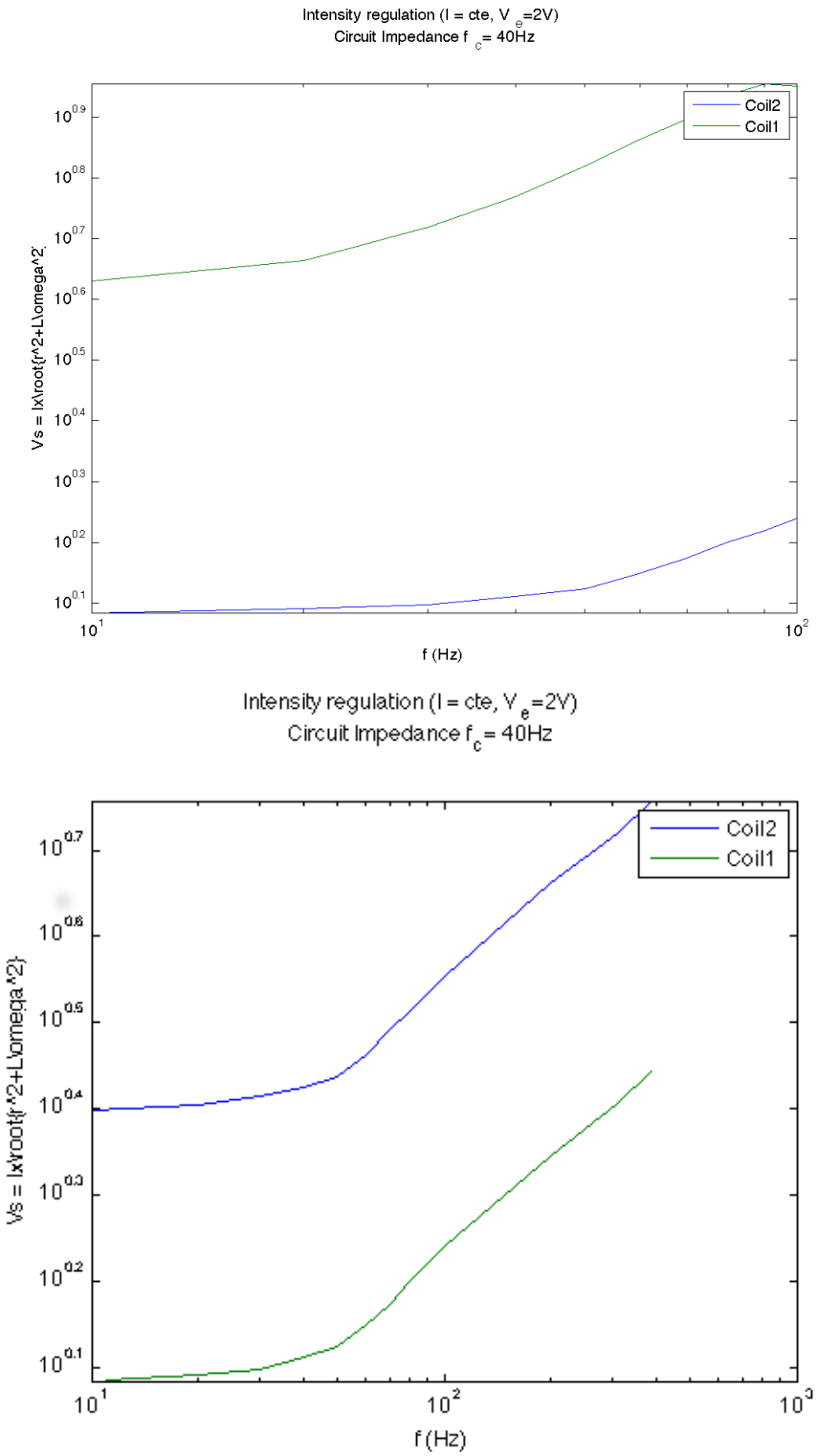

Figure 55: Bode amplitude diagrams: (left) Helmholtz pairs (right) for Dome cores.

3.4 Sampling magnetic signal and treatments

We now need to consider the chain of treatment of our electric signal.

The choice of a linear amplifier rather than a pulsed modulated avoid the perturbation with high harmonics. It particularly have a same constant phase, as observed on Fig. 57, which will

simplify the control in time of the system. We notice the circuit has a small voltage distorsion around 0, which is smoothed by the integrative capacity of inductors.

Both electromagnet can be described as a dipole with a resistive part and an inductive. They have an impedance of $Z = R + jL\omega$, and their expected transfer function is

$$U/I(\omega)_{db} = 2Olog(R) + 10log(1 + (L\omega)^2) \tag{34}$$

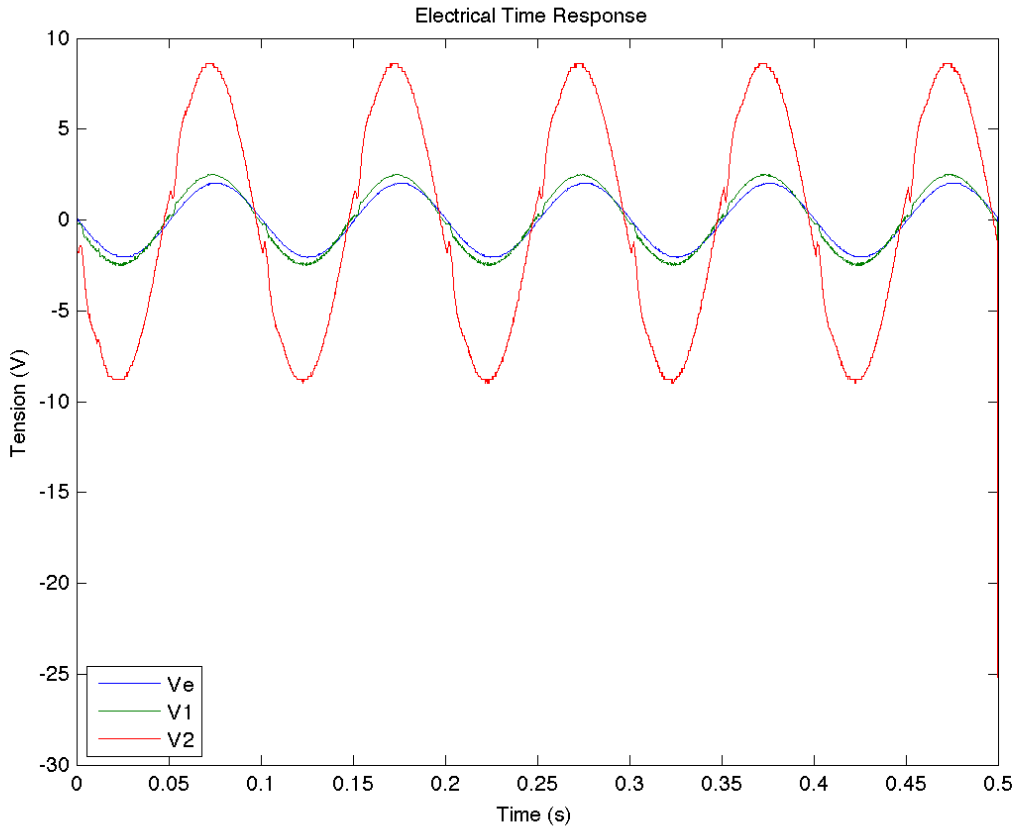

Figure 56: Measured input and comparison in frequency between two electromagnets,Ve being the input voltage from the DAC, V1 and V2 the amplified voltage.

As the electromagnet acts as an integrator on the current intensity, we observe even for frequency higher than 500 Hz a low distorsion signal and a constant phase between DAC signal and amplified output. Above 1kHz, the power efficiency and the signal starts decreasing and would require more effort to obtain a clean measurement. We then have a bandwidth containing from 0 to 1 kHz to do proper measurement.

Though it creates non-linearity beyond 1 kHz, generating other harmonics, we still can work with 5kHz sampled signal to achieve closed loop control.

4 Optical microscopy vision: a fitted solution for magnetic microrobot

For gathering position data on a micrometric body in real-time, localizing and eventually controlling it in closed-loop with the proper actuator, several solutions are available at our intermediary scale as discussed in chapter one. We use magnetic actuation which limits all the solution involving magnetic field or electron imaging and working in-vitro makes visual feedback the most cost-effective candidate.

As detailed in previous sections, we aim to gather data on a microrobot moving at high speed, with a characteristic size varying between $50 - 500\mu m$. It will require a high-throughput camera with a sufficiently high internal clock frequency to be able to reach a good compromise between frame-rate and spatial resolution. One important consequence of fast imaging is a short exposure time. As it gathers fewer light, we will need to optimize our scenes exposure.

4.1 Photonic microscope for a microrobotic platform

Observing a microsystem, here using photonic microscopy (also called optical microscopy), generates several issues that need to be integrated in the design of a microrobotic platform. Using microfluidic as an experimental platform has convenient consequences. It avoids loosing track of the robot, as it is confined in a small chamber fitting the field of vision, and confines the robot in a horizontal plane, avoiding short depth of field issue. It also remove meniscus shape of liquid which generates a lens effect. Even though working in a microfluidic chip helps experimenting our system and defining more precise experimental conditions, a photonic microscope deserves a deep understanding of its principle and its specificities to adapt the right tool to a very specific need.

4.2 Photonic microscope and its optical Principle

A conventional optical microscope is composed of an ocular and at least one objective. Both are assimilated to convex lenses that get from the object a bigger image. Fig. 40 displays a simplified version as several filters are used to correct them.

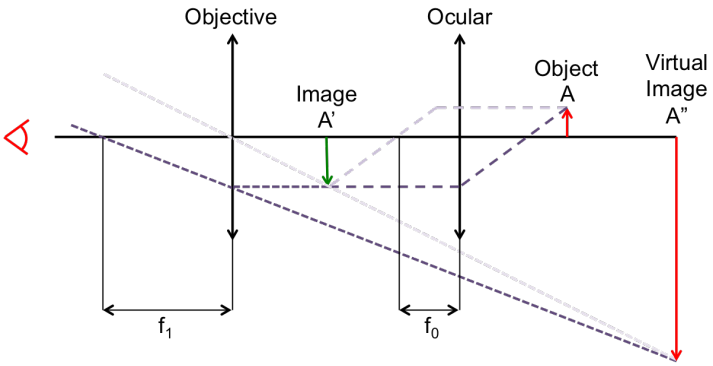

Figure 57: Schematic of a conventional photonic microscope.

Maximum performances of a photonic microscope can reach 2000x and most of the fabricant provide tools. Every changes in the focal or geometry of the lenses as well as their number will modify the specificities of the device.

4.3 Photonic Optic Specificity

The expected performance on this system is both high magnification and spatial resolution. Those performances have several limits: small working distance, depth of field and field of vision, important volume of the objective, high dependency to lighting.

Before optimizing the scene exposure, we must collect as much light as possible, i.e. consider an objective with the highest numerical aperture. In optics, the numerical aperture (NA) of an optical system is a dimensionless number that characterizes the range of angles over which the system can accept light . Different from f-number which is a relative value, it depends on the half angle θ of the maximum accepted cone of light $NA \propto sin(\theta)$ which is itself dependent of the focal of our microscope.

Depth of field (DoF) is typically few microns at our scale and can even be used to measure some material thicknesses such as thick photoresist. Without making too much hypothesis on our system, we know the relation:

$$DoF \propto \frac{1}{\Gamma \times NA} \tag{35}$$

where Γ is the magnification of our optical device.

4.4 Zoom lens: designed for multi-scale applications

We will finally confirm from first observations the performances of the system and its potential for transduction applications.

As we are using a CMOS camera which means the image A" (Fig. 40) is formed in the sensor plane and the ocular is removed. On the other hand, we use more than one objective, and one of them has a variable focal (zoom lens). Using a zoom has the advantage of an important adjustment in the resolution

We use a modular zoom lens system from Navitar (Zoom 6000) that can be configured for wide range of application. Dynamic magnification range can vary between 0.09-393X, images and vivid colors, 0.01-125.68 mm field coverage. Working distance can be varied from 34 to 390 mm.

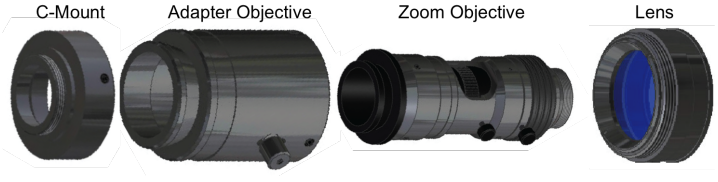

Figure 58: Presentation of the system in order to identify each optical component.

The top adapter (in our case two possibilities: 0.5x and 2x) - see Fig. 58, defines a reference value from which the magnification is varied using the zoom lens. We list it on the Table 4.4.

Table 21: Table of the two different optical configuration

Top adapter	Working Distance	Magnification
0.5x	92	0.35 - 2.25x
2x	92	1.40x - 9x

Lighting device such as a LED ring screwed on the last lens or a semi reflecting mirror injector are not visible on the figure but can be added.

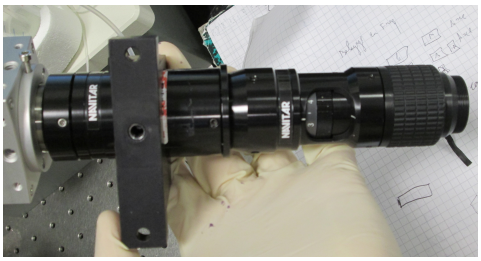

Figure 59: Navitar optical device, here with a 0.5x adapter, specifications and aperture variation impacts on light sensibility.

We see on Fig. 59 the zoom lens used, with attached camera on left and a fixation ring on top. This ring allows the mechanically stable fixation on a holder. The choice of a sufficiently articulated one is important to adapt the position of our vision feedback.

Planar adjustments of the microscope We equip our setup with a sturdy boom stand SMS 200 from Diagnostic Instruments Inc., providing smooth horizontal arm adjustments for the camera. Its base is heavy weighted and is sufficient to not mount it. It includes 3 DOF for tilting and as many for swiveling. Maximum arm load rating being 100 lbs, it is sufficient even with the higher arm length.

5 High throughput imaging for real time control of high dynamics motion

One of the reason to suspect important accelerations, as mentioned in part I, is related to scale effect. The mass term is much smaller and volume $\propto r^3$ decreases faster than surfaces $\propto r^2$, particularly for our high aspect ratio robot The consequence on a simple Newton's second law is

$$\frac{\mathbf{F}}{m} = \mathbf{a} \tag{36}$$

is the divergence when $m \to 0$. Even though fluidic viscosity has a tendency to damp the system, we expect the dynamics to be very sensitive to small variations in forces equilibrium.

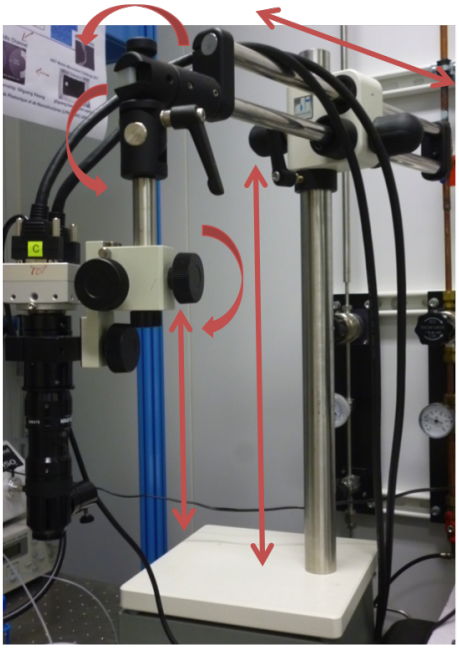

Figure 60: This holder guarantees 6 DOF described by Red arrows. Each axis has sufficient range for user comfort and quick adjustments in position and angle.

Our motivations to use a high throughput imaging is then to correct trajectories in real-time and to analyze motion with a sufficient temporal resolution. Those required performances are pushing the limits of how much information we can store in a computer and, most of all how fast we can process it. Though the technical solution we adopt has a sensor adapted for low exposure scenes, we will also compensate the short exposure time - i.e. short time gathering light, by optimizing the conditions of exposure.

5.1 High speed imaging: hardware limitations

High speed imaging tradeoff: fast camera principle Different vision systems are known to provide faster frame rate than standard $< 100 frame/s$. The best sensor in any case is often CMOS with sufficiently high sensibility to measure at $\ll 10ms$ exposure time.

What will define the frame rate limit of this sensor is

$$1/FR_{max} \lesssim t_exp + t_{ReadOut} + t_{proc} + t_{RAM} \tag{37}$$

where times on the right side of the equation are respectively exposure, readout, processing and RAM (Random Access Memory) of the sensor. As we can neglect processing and RAM refreshing time, depending of the embarked performances -supposedly sufficient, it depends on exposure ($\geq 1\mu s$) and readout time - directly related to the frame size.

The main relation to understand those system is then the throughput rate. How many bits can we process per second? This relation

$$Throughput = Size_x.Size_y.FR.depth \tag{38}$$

sums up what the sensor can deliver. We then have the simple relation $FR_{max}.Size_x.Size_y \approx cst$ that defines the necessary tradeoff when recording at highest performances in terms of

throughput. The key point remain how do we interface the sensor and how fast can we grab the frames. As a computer motherboard will necessary require a PCI express interface to communicate with the frame grabber, whatever are this one performances the bandwith will be limited to 15 GB/s in best case.

Finally, acquisition can be stocked on a direct memory allocation as a stack of pictures in RAM (and can then be transferred to memory on a hard disk. Notice that directly writing on a hard or solid state disk remains too long (600MB/s for SATA interface to $\approx 1GB/S$ for PCIe with last SSD). With sufficiently recent DDR SDRAM 3, we reach a sufficiently high bandwidth $> 10GB/s$ and we can as mentioned previously neglect RAM refreshing time.

Embarked camera VS Camera Link Protocole To analyse dynamics using vision with a sufficient resolution in time, we need a high throughput camera. Models such as Phantom©v-series can reach the $1MHz$ FR as they have their own designed interface and optimized storage transfer but such a signal cannot be processed in real time. We are aiming to achieve automated motion, which means we have to abandon any camera with embarked memory. Moreover, those cameras are more expensive and we don't expect to reach such high frequencies motions.

An intermediary technological solutions that actually reaches its limitation and still fully fits computers PCI express interfaces are CMOS camera using high performances protocol such as Camera Link.

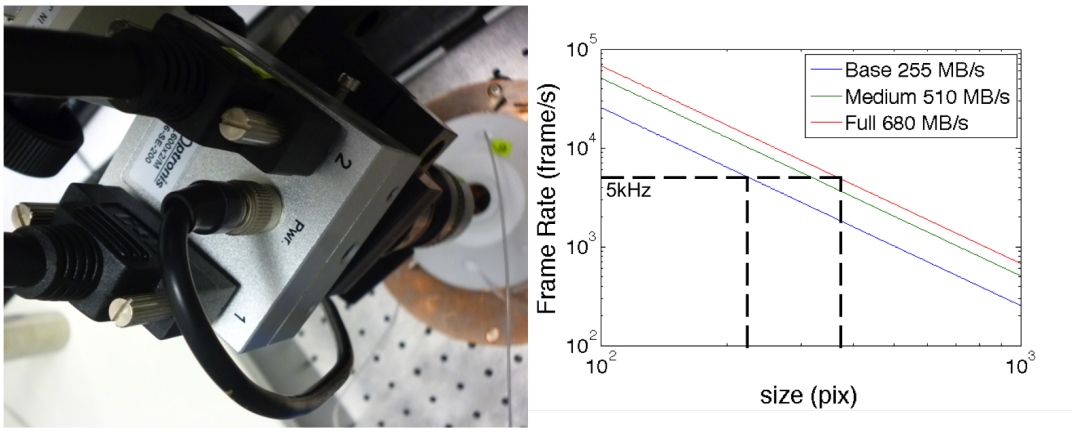

Figure 61: Three different modes of Cameralink comparison and PCI express limitation.

By working in full mode, we can reach high enough throughput for live treatment without saturating memory. The interfacing with the camera being quite user friendly, we can quickly capture frames and treat them using tracking algorithm.

5.2 Overview on the performances of a high speed Camera Link camera

We used CL600x2 fast frame-rate from Optronis camera directly connected via Camera Link protocol (allowing a maximum rate of 255 GBytes/s in FULL configuration). CL protocol is one of the fastest way to obtain directly to the computer such a high framerate and CMOS Camera usually work with it. As we can see on Fig.X graph, camera performances (in green) in term of frame rate are necessary lower than Camera Link limitations.

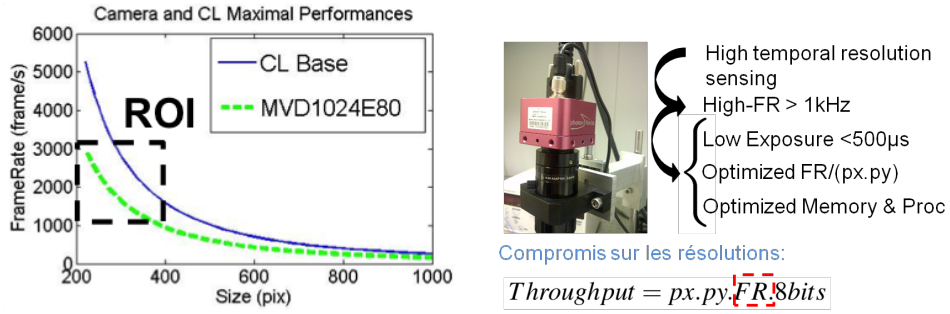

Figure 62: Performances of camera: trade between spatial and temporal resolutions.

5.3 Lighting and contrast issue toward live tracking

Optical solutions to decide whether directly exposing our sample or use its reflectivity have both been made possible on our device, Fig. 63.

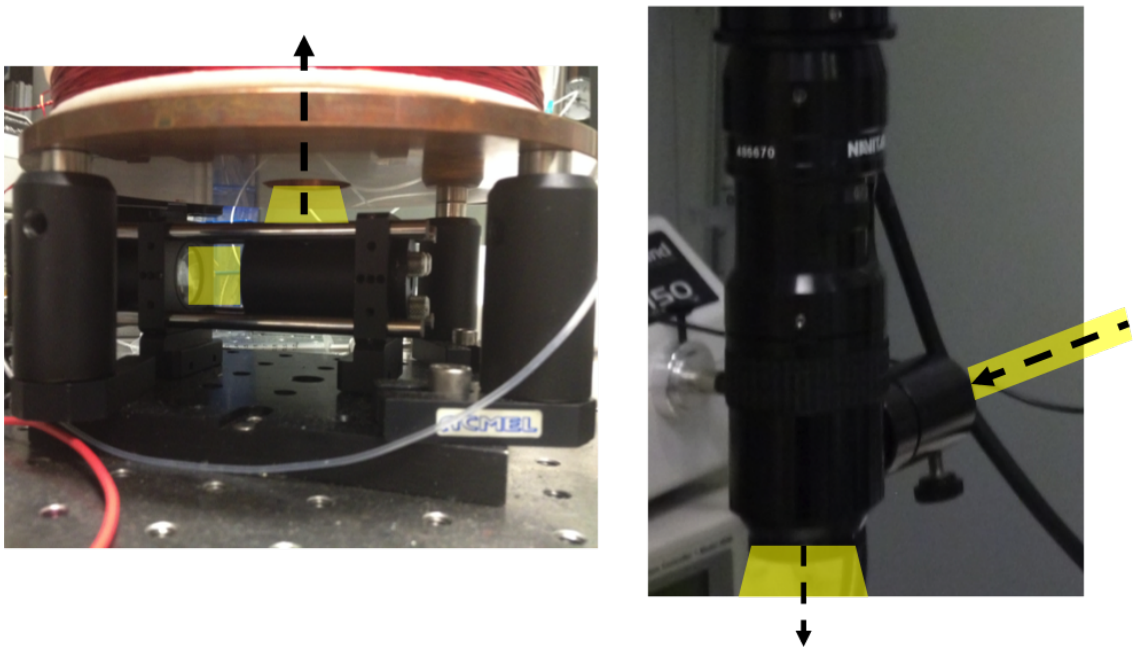

Figure 63: (left) Direct lighting is possible using a side light injection with a semi reflecting mirror integrated to the zoom lens (right) bottom lighting is made possible with a construction on bottom of our device.

Let notice that bottom lighting has the possibility to adjust beam thanks to a double convex lens association and a diaphragm to eventually reduce exposure manually. To reach a sufficient contrast, backward lighting is recommended, though it inverses the contrast (we search for black spot on white) and it does not reflect robot textures.

Transparency or Reflectivity As we use transparent chip, the exposure of our scene has two possibilities: direct lighting or reflection. We insist on the importance to choose a transparent material in the visible spectrum with low absorbance as Pyrex and PDMS. It becomes very challenging to observe a contrast on an opaque substrate such as Si.

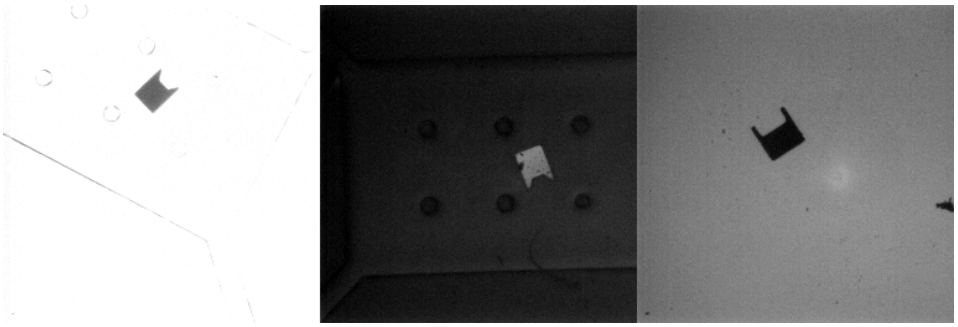

Figure 64: Light source position and substrate absorbance (left) transparent chip (pyrex/PDMS) with a bottom lighting (middle) transparent chip with a top lighting (right) Si opaque chip with a bottom lighting.

It confirms the choice of fabricating our microfluidic chip with transparent materials in visible spectrum.

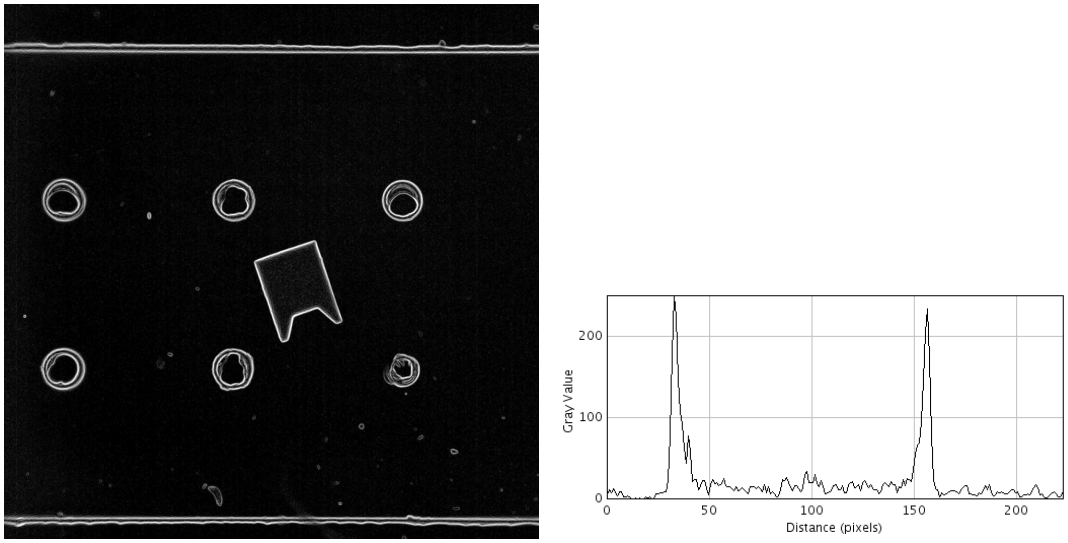

Figure 65: Signal / Noise ratio can be optimized by a small analysis using gradient to see the edges contrast (left). As we can see on the graph (right), there is a sharp window on the corresponding exposure time[3ms 10ms].

The question of bottom lighting and has been summed up in table 22 and we see that it is interesting to have reflexive lighting for observing texture only. Texture can have their importance for shape detection as we will see in next chapter, but in our case where shape is simple to detect, we will prefere transmission lighting.

6 Conlusion: High speed system and challenges

We achieve the summary of our effort to build a performant chain of magnetic actuation and sensing. All the elements of the system form now a chain, from the sample, its direct experimental environment (the fluidic chip) and its magnetic actuator to the sensor. We have designed a system that allows us to integrate an important volume of coils and still integrate a zoom lens sufficiently close from source.

Table 22: Direct vision (backward) versus reflexion vision

Dome	Direct	Reflexion
Contrast	Almost binary	Medium
Stability	High	Low
Details	Low	high

Before determining precisely the dynamics of the robot in liquid and its capacities as a transducer, we initiate a rudimentary experience generating the simplest excitation and observing a first movement. As a conclusive experience before full characterization, we finally observe the time-response of the system to a simple 10V input using separately the two type of magnetic setup: Dome and Helmholtz. This important step justifies on one side the effort toward magnetic energy transfer and on the other side justify the importance of a high performance camera.

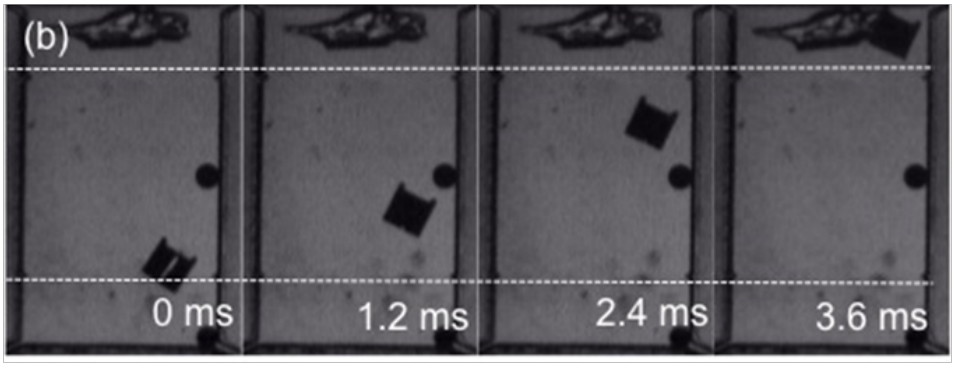

Figure 66: Capture of the robot response to a 10V stimuli using gradient from Dome approaching 1ms.

The spectacular speed of the microrobot from Fig.66 confirms we have overcome the surface phenomenon enough to observe high speed motions and that controlling movements at such a power will require high sampling rate, i.e. high framerate as we use a visual feedback. This example would require $\approx 1kHz$ to have all the motion. We notice from first to second picture that gradient magnetic field generates a torque to align the robot toward the gradient.

Figure 67: Capture of a full rotation achieved by generating a 140 Hz frequency rotating field from Helmholtz setup in less than 10ms.

Fast rotation was achieved doing linear combination of horizontal coils. It shows quite important rotation frequency compared to known mechanical system where substrate adhesion can be smaller [89].

Both figures illustrate the complementarity of the magnetic actuators we designed and

the high dynamics of both. The spectacular speed of the robot confirms we have overcome the surface phenomena and that controlling movements require a high sampling rate. With a more than 1000 bodylength/s maximum speed, the robot movement decomposition requires more than 1000 frame per second to be properly decomposed. Every element of the chain but the microrobot have known performances and limits. Next parts purpose will be to push and characterize the microrobot performances.

Part III

Sensing capacities in microfluid of MMM by dynamics analysis

Summary

Sensing using microagents could improve drastically the patient's diagnosis, reducing also time and costs thus improving its life during treatment. Remote sensing technology has currently entered an era of quantitative analysis, and measuring local physical parameters has a great potential to improve diagnosis as well as autonomy (closed-loop behaviour) of therapy [43] .We here collect more information on the micro-system through high temporal resolution ($< 200\mu s$) microrobotic system. Integrated into a optically transparent microfluidic chip, the microrobot is fully controlled through magnetic field. The mobile magnetic microrobot, integrated in microfluidic and correctly propelled, offers a high precision tool at micrometric scale with fast response and a wide range of motion possible. Integrated microrobots could be used to transmit, from a specific location, information that would otherwise be difficult or impossible to obtain. It could offer more specifically an interesting solution to transmit the time history of a physical signal of interest (e.g. oxygen concentration) or transmit a simple qualitative signal upon detecting the presence of an analyte of interest (e.g. cancer, blood).

This information can be transduced using a variety of methods (e.g. RF, visible light, ultrasound). In our case, we can access enough data through visualized dynamics to obtain data about the robot and its environment. We will detail two complementary approaches using elementary motions (translation, rotation).

An adapted microfluidic device for measurement has been provided for its robustness to higher range of pressure, longer lifespan and glass surfaces. Our technologies and knowledge has allowed us to propose and test a new design that conclude the sensing research around the microrobot.

1 Sensing from dynamics

When the robot moves, it gives us an access to information about itself and its environment. Exploring it helps us to better understand the microrobot with fixed physical parameters, or reciprocally, to extract information from its environment. We will see that low Reynolds liquid provides a particularly adapted environment for measurement.

1.1 Sensing from motion information: scale effect simplifications

Observing the system response to a stimuli is a standard sensing process. Though there exists research teams working on transmitting information using electromagnetic high frequencies and more specifically RF devices [44], observation from the microrobot itself using vision system can provide a wide range of information. The example of a sufficiently compliant structure exists in literature and constitutes a mobile version of a cantilever. It has proven to be useful for measuring mechanical responses from oocyte [150] and aquatic micro organism [22], see Fig. 68.

Global motion of a body is also an important and non-trivial source of information about the physical environment and the robot itself.

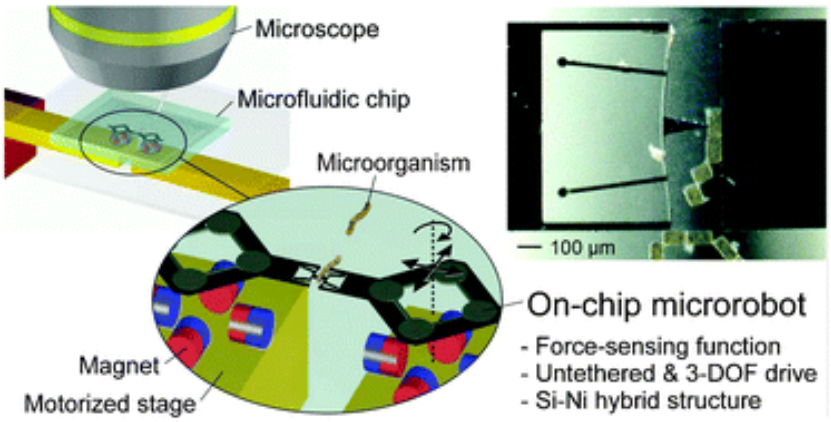

Figure 68: On-chip microorganism manipulation and sensing system with microrobots, by Kawahara [22]. This system consists of a robot control system and a closed microfluidic chip to simulate an actual river environment as an "on-chip biotope". Microorganisms were investigated by using on-chip microrobots with force-sensing structures (force sensors based on mechanic magnifier). The microrobots, with three DOF, could stimulate any point of cells with any amount of pushing force, in situ. Then, the chemical reaction was observed in the stable conditions of the microchip.

Signals have resolution and noise varying drastically with scale. As seen in the chapter I, with scale effect, microsystem in liquid can be described as heavily damped leading to dynamics where inertial effects are negligible. The consequence is that any force f and torque τ applied on the vertical axis $\mathbf{z}$ of a particle in Stokes fluid, because of heavy damping, is directly related to the particle speed v (we neglect the inertial term) and angular speed Ω, respectively.

$$\mathbf{f} \propto \mathbf{v} \tag{39}$$

$$\tau \propto \Omega \tag{40}$$

As we are able to induce a magnetic force and / or a torque over the microrobot - see Fig. 69, we then can observe a proportional response from the kinetics. By measuring with a sufficient sampling rate, we can obtain a spatio-temporally resolved signal from its motion.

From previous chapter, we have observed translational and rotational performances in best case with highest power from our device to be around $v = 1m/s$ and $\Omega = 150rps$, respectively. It justifies an important frame rate, first to decompose properly a rotation it requires at least 10 frame to avoid temporal aliasing (also called stroboscopic effect) and detect precisely the changes in rotation. There is less risk of temporal aliasing for translational motion as the robot trajectory is straightforward, but non-linearities due to substrate adhesion and irregularities can only be analyzed with a sufficient resolution. In our case, as the length of the microfluidic chamber can be crossed in 2 ms, 5000 frame/s allows to decompose the motion with a limited sampling rate of 10 frame / trajectory. These numbers give an idea of the challenges of sensing at a sufficient resolution with the microrobot, and of course framerate can outreach 5kfr/s and the speed given are the physical limits we have currently reached with MagPol.

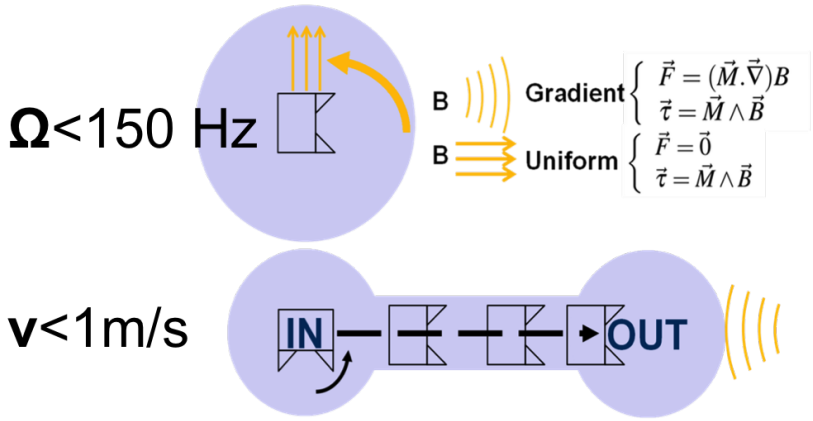

Figure 69: Two methods of actuation and sensing depending on the field distribution: uniform field corresponding to Helmholtz coils (top), gradient field corresponding to Dome setup (bottom).

1.2 Sensing protocols

The sensing chain can be described in three phase, for translational as well as rotational motion.

Emission In Fig.70 (left) we input, amplify and generate a defined range of frequency including the cut-off frequency at a sub-millisecond ($200\mu s$) sampling rate. It can be achieved using the GUI module frmSimpleWavesControler (see Appendix A for more details about the program architecture), generating mathematical signals. Magnetic Coils were voltage-controlled through a data acquisition card (Sensoray©S626, 5kHz sampling frequency) and amplified through Servomotor controller (Maxon Motor©LSC 30/2,50W power $\mid V < 10 \mid$ and $I < 2$). The two types of magnetic setup can be used, depending on what is measured. Helmholtz inductors induce exclusively uniform field on each axis X and Y, inducing exclusively a magnetic torque. Electromagnets from the dome can generate both and will be used for characterizing translations of the microrobot.

Actuation The micro-system described previously - see Fig.70 (middle) - responds to it almost instantaneously (if we neglect inertia from electrical circuit, here coils). A phase shift exists though and breakdown phenomenon is then observed when using a rotating field as the phase is too important. We have already insisted on the care taken in the robot environment question in section 2: perturbation on the robot must be minimized, physics of the chip are well controlled (static flow, dust free liquid), and confinement makes easier to reach high magnetic power. These conditions are also applied for translational motions, though no breakdown phenomenon are observed but rather local perturbations.

Measurement & detection In Fig.70 (right), the acquisition of a sufficient number of frame (thanks to the high speed camera) is then treated by visual tracking which detect visual features of the robot (texture, edge or its whole shape). We can detect the position and orientation with a sufficient spatial resolution to precisely detect when breakdown or perturbations occur.

Artifact due to camera vibration and tracking can be minimized experimentally or filtered during post-treatment. The physical principle of the tracking algorithms and breakdown phenomena are explained further.

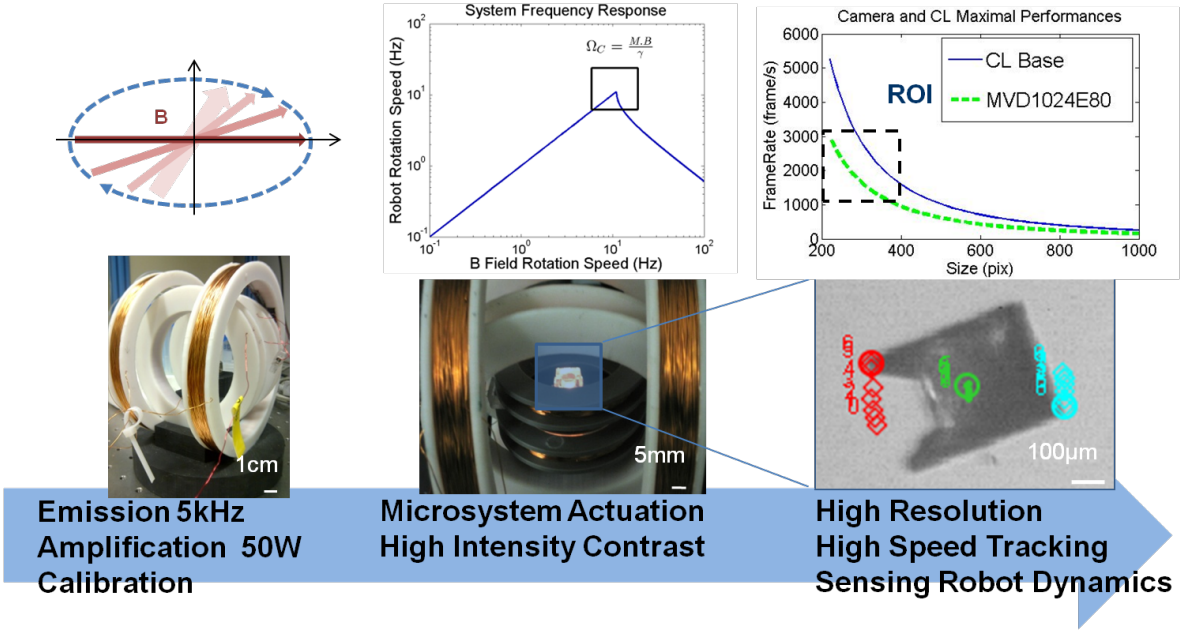

Figure 70: System oriented for magneto-fluidic sensing (left): Emission of calibrated circular magnetic field by electromagnetic circuit and program (middle): All-transparent lab-on-chip integrating backlighting for high contrast and luminosity and Robot transfer function, highlighting how the system respond asymptotically to the transition (right): Fast Camera temporal resolution function of CameraLink Base Configuration and a square frame size (top). Exposure time is fixed to its minimum ($10\mu s$). Tracking dynamics through two distinct points of the robot (bottom).

It is important for user to have a quick control on the Region Of Interest (ROI) and imaging parameters before running a test or an experiment. We defined a GUI module, see Fig. 71 that gives graphical solution to adjust size & position, exposure and framerate.

Writing directly on hard disk, even with SSD, has a tendency to disturb the system. Then recording video is achieved on a predefined circular memory buffer size limited to 4GB, equivalent to ≈ 2 minutes for a $1kframe/s$, $256 \times 256 pixel^2$ sequence. Circular buffer means if maximum is reached, it goes on erasing the first images. This recording strategy is oriented for recording until success of the manipulation or measurement.

1.3 Visual tracking analysis

Elaboration of object tracking algorithms in image sequences is an important issue for research in vision, applications related to visual servoing and more broadly for robot vision [151], but also for visual data treatment. The algorithms mentioned here are used to exploit image sequences from a high-throughput camera.

There exists a wide range of them (see OpenCV software documentation as a good example of possibilities), we will see depending on the scenes we shoot what can be the

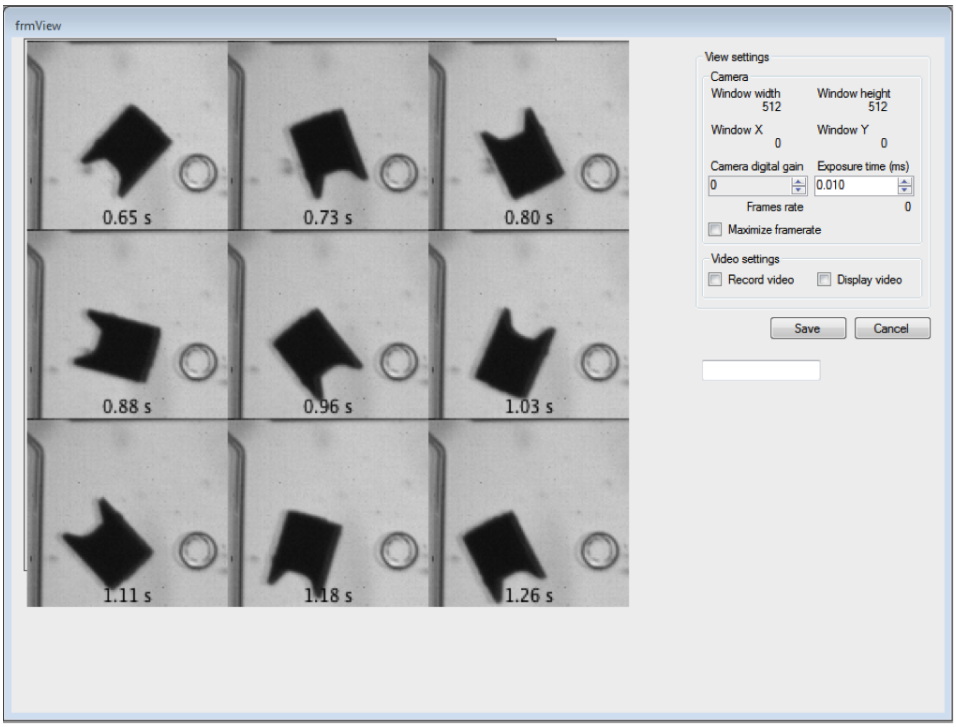

Figure 71: Graphical user interface module developed for visualization and recording of scenes while manipulating the microrobot. It is designed for real time modification. Left part is dedicated to display, maximum size being 1240×1080, right size can adjust numerical parameters of the camera and frame-grabber and define recording sequences; the image here is a montage of a rotational sequence, with time displayed on each frame.

most adapted among three standard one. They are used in this chapter exclusively for post-treatment, which makes temporal performances a lower priority.

High-throughput Camera setup We used the Optronis CL600©, see Fig.72 fast frame-rate camera directly connected via Camera Link protocol (allowing a maximum rate of 680 GB/s in Full configuration). CL protocol is one of the fastest way to gather in real time a high framerate video on a computer, compatible with CMOS sensor output.

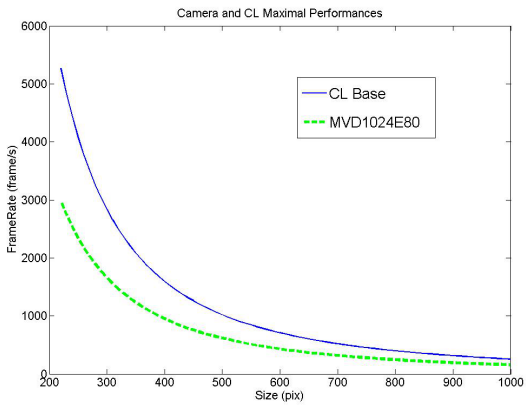

Figure 72: High performance Camera for high temporal resolution visual feedback.

Obtaining higher framerate could be possible only using embarked cameras with their own RAM and cooling system. It is not necessary for the dynamics we observe in our context. It would also make a completely different challenge in term of instrumentation and would not allow servoing and live treatment of data. As we can see on Fig.70 (right) graph, camera performances (in green) in term of frame rate are necessary lower than Camera Link limitations. The frame rate t_{frame}, mainly depending of the exposure time and readout time, is the inverse of the frame time. The minimum frame time is calculated in sequential mode at constant framerate by:

$$t_{frame} = t_{exp} + t_{ReadOut} + t_{proc} + t_{RAM} \tag{41}$$

where times on the right side of (8) are respectively exposure, readout, processing and RAM (memory access). As we can neglect processing and RAM refreshing time, depending of the computer performances - hypothetically sufficient, it depends on exposure ($> 10\mu s$) and readout time - directly related to the frame size. Acquisition are stocked on a direct memory allocation then converted in video and post treated using Tracker©open-source code. Two-points tracking allows extracting the angular phase from the visual data and identifying the breakdown phenomenon with a precision of the size of a pixel ($\approx 1-10 microns$)

Shape Detection algorithm For tracking 2D features, we can count three different algorithms, depending on the kind of scene we want to analyze: Kanade-Lucas-Tomasi (KLT) [152, 153], moving edges tracking and Freeman Chains [151]. They all have been implemented on ViSP (VIsual Servoing Platform) software platform developed by INRIA and our vision technology is based on their work. We encourage the reader for further reading to explore the image processing documentation from ViSP web site and Marchand et al. publications [151].

We already eliminated KLT algorithm of our list, more adapted to textured object with edges that are not simply visible [153]. As our microrobot surface is uniform, there is not enough texture in any case of lighting.

Freeman Chain It tracks the set of pixels with specific range of values. To belong to a blob or dot, a pixel value has to be between a minimum and a maximum value: $\lambda_{min} < I(i,j) < \lambda_{max}$ with I the current image where you track the dot and i, j the pixel coordinates.

We define a connectivity point a point in the connectivity scheme - see Fig. 73 - with intensity also between the ranges. It is part of a border if one or more point in its connectivity scheme is out of range.

Starting from a point A, it tries to reach the "right border". Once the border has been reached, it just consists in following it. This creates a Freeman chain.

This algorithm of course is dependent on the size of the tracked object.

Moving Edges Each point, sampling the curve, is tracked from one image to another along the normal to the curve at this point. This search is performed using convolution in order to have a real-time tracking. The convolution mask depends on the angle in the image of the normal to the curve for the given sample. These masks are preliminarily computed during the initialisation of the algorithm. See figure 74 for more details.

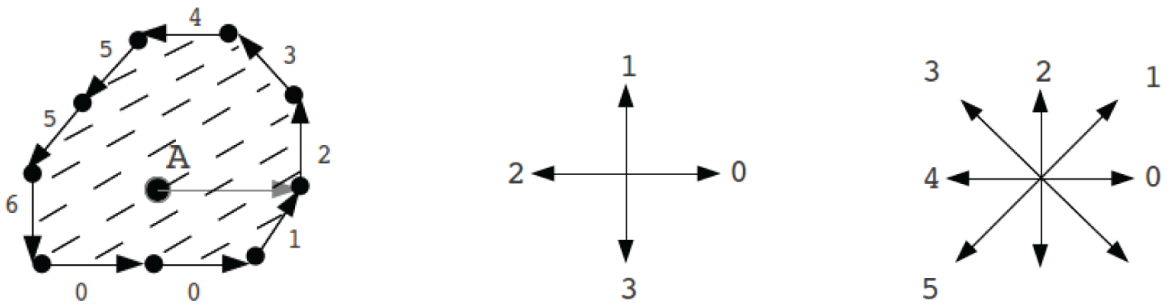

Figure 73: Different elements for minimalistic shape detection.

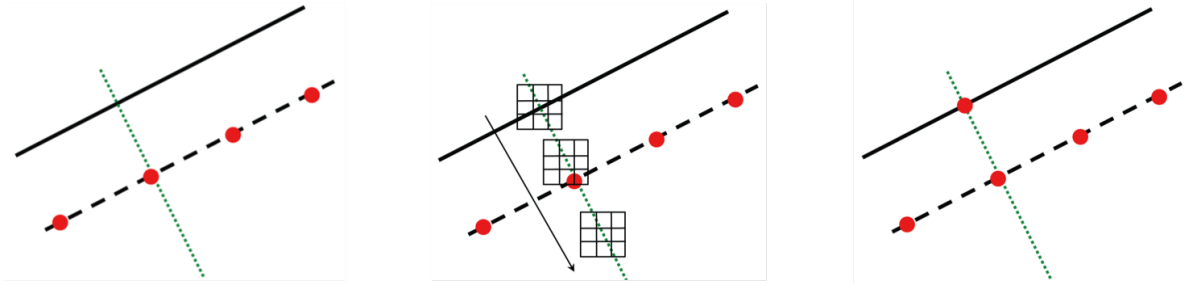

Figure 74: Different elements for minimalistic shape detection.

The important sampling rate thus temporal resolution minimizes variations between two consecutive frames.

Conclusion on algorithm We have reviewed three complementary 2D algorithms that can detect 0D (dots) to 2D structures (areas). We summed up on table 23 their performances to justify our next choices.

Table 23: Comparative table of tracking algorithm and performances in our detection case

Method	Moving Edge	Freeman Chain	KLT
Robustness	fair	excellent	speed dependent
Speed	fast	size dependent	fast
Precision	fair	high	low if few texture
Geometry	line	convex Body	blob

We notice the KLT will not be much considered as robot does not have enough texture. We then focus on detecting either edges mostly for orientation detection or shape for position. Then referring to the table 23 allow to evaluate what will be the conditions on the frame. An important number of pixel on a targeted edge will increase the precision of a Moving Edge, while a small number will make a Freeman Chain faster.

1.4 Position and angular determination

Visual tracking allow detecting a specific point, edge or whole body. From this information, geometrical considerations allow to extract targeted information from the robot.

2D position: barycentre determination Determining the position of robot is possible using many tracking method if we preliminary know the shape of our robot and achieve the right transformation (usually a simple translation). It always comes down to measure a barycentre. Contour detection, in our case using freeman algorithm, is simply the discrete integer on the area defined by the contour (equivalent to the integer on the whole surface)

$$(x,y) = \iint_{Contour} \mathbf{u}\, dS = \sum_{i=1}^{height} \sum_{j=1} segments l_{i,j} \tag{42}$$

It has the advantage of being stable and quick to compute. It is in particular stable to pitch rotation (which is non trivial in the case of edge and single pixel detection algorithm).

Orientation of the microrobot For angular detection, as the robot is symmetric, we could consider its direction of least inertia, as it is described in Shapiro's book [154] and has been applied most recently on helical swimmers in Xu PhD thesis [89]. The problem is the ratio between width and length of the robot is around $4/5$, which is much more than the aforementioned helices and can generate unstability and $\pi/2$ random leap if the orientation change is too brutal between two frames.

Our design shape fits rather well moving edge algorithm described previously, as there are several straight lines we can detect. We will use this one as the angle is then defined by the normal of the line. It would still be possible with more complex edge using non-uniform rational basis spline (NURBS), and would only require a preliminar stronger configuration effort of the parameters adapted for the robot edges detections.

2 Angular position tracking & breakdown phenomenon

The first sensing possibility we notice from robot's motion was its response to rotational magnetic field. With an increasing rotation speed, the robot seems to have a range of frequency during which it fails being synchronized with the field before remaining immobilized. We detail here the physics behind this breakdwon phenomenon to then establish several experiences, varying physical parameters such as the magnetic field power or the liquid medium viscosity.

2.1 Principle of breakdown phenomenon sensing

Preliminary work from Adler [155] predicted that we can already have a quite complex behaviour phenomenon from simple dynamic equations. Several works have been achieved at sub-micrometric scale on suspended sphere. We show here that because of low reynolds number, these results can be extended to a magnetics microrobotic system.

Heavily damped systems As we are working in low reynolds numbers fluid -i.e. stokes flow, we can neglect inertia [88] and supposing viscous drag is the only surface effect acting on the microrobot, we then obtain the simplified equations

$$\mathbf{F_{mag}} + \mathbf{F_{drag}} = \mathbf{M}.\nabla\mathbf{B} + \beta\mathbf{v} = \mathbf{0} \tag{43}$$

$$\tau_{\mathbf{mag}} + \tau_{\mathbf{drag}} = \mathbf{M} \times \mathbf{B} + \gamma_z \dot{\mathbf{theta}} = \mathbf{0} \tag{44}$$

between the forces and torque due to magnetic field and viscous drag, with β and γ_z being the translation and planar rotation drag coefficient. This model supposes no perturbation from the substrate, and we will see in our further experiences the limits of this model.

Under a rotating magnetic field of pulsation ω toward vertical axis, the equation 44 becomes

$$\gamma_z \dot{\theta} + MBsin(2(\theta - \omega t)) = 0 \tag{45}$$

If we name $\chi = \theta - \omega t$ the rotating phase, it turns to simpler equation:

$$d_t \chi = V(\chi) = \omega - \omega_C sin(2\chi) \tag{46}$$

with a cut-off frequency $\omega_C = MB/\gamma_z$, where M is the magnetization of the ferromagnetic layer of the robot, B the flux density of the field, ω its pulsation and θ the particle angular position in horizontal plane. γ_z is the resistive coefficient due to fluid viscosity and substrate roughness and ϕ is the phase difference of the robot angular position with the field phase.

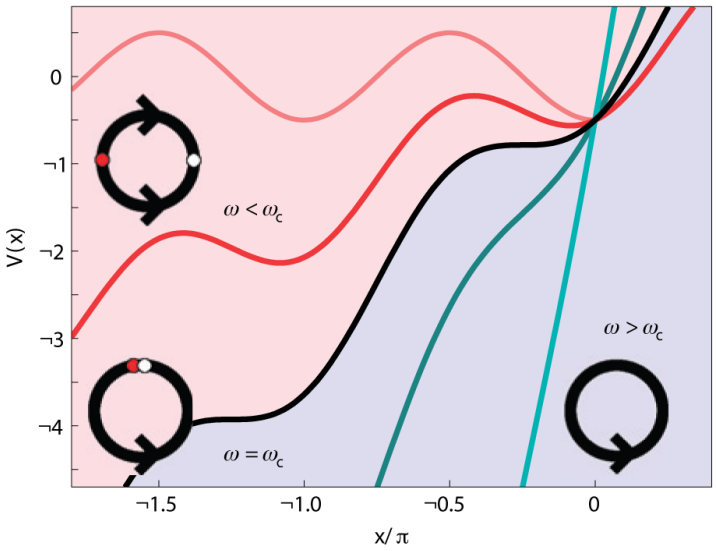

Figure 75: The potential experienced by the microrobot is the same than described by Adler then Pedaci [23] and corresponding phase plots. For different values of ω, we plot the potential V(x) experienced by the ferromagnetic particle ($\omega < \omega_c$, red lines; $\omega = \omega_c$, black line; $\omega > \omega_c$, blue lines) as a function of the angular coordinate in the rotating reference frame x. For these three regimes, we plot representative circular phase plots and indicate the system's fixed points by coloured dots (where a white dot represents the stable fixed point and a red dot represents the unstable fixed point). In a noise-free system, the split at ω_c, evidenced by both the lack of a potential minimum and by the merging of the two fixed points in the phase plot, separates the excitable region at $\omega < \omega_c$ from the periodically modulated one at $\omega > \omega_c$. Here $MB/\gamma_z = 1$ and $\omega = [0;0:5;1;2;6]\omega_c$ from light-red to light-blue.

This parametric ordinary differential equation 46 has led to detailed [155], summarized in Fig. 75 as a quite complex behaviour with a breakdown phenomenon at ω_C generating two different kinetic regimes 47 and 48:

$$< \theta >= \omega, \omega < \omega_C \tag{47}$$

$$< \theta >= \omega - \sqrt{\omega^2 - \omega_C^2}, \omega \geq \omega_C \tag{48}$$

In synchronous regime, for $\omega < \omega_C$, the robot tends quickly to a constant rotating phase $\phi = 1/2asin(\omega/\omega_C)$, see Fig.75. The problem of measuring it is it only gives a relative result: first steps of command (CPU & electronics) delay the actuation of the robot, inducing a variable dephasing i.e. an error on $\omega_{C,measured}$. That is why we rather detect the cut-off frequency using visual observation, obtaining a more precise results. As we see on Fig. 76, asymptotic frequency responses to rotating magnetic fields can be described by 47 & 48; each regime typical temporal response is illustrated by the sin-modulated angular orientation of robot - in black – and B field in red.

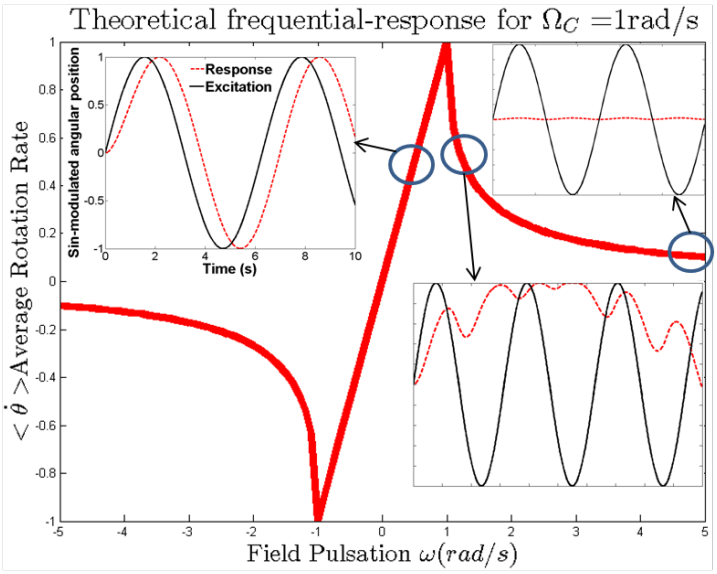

Figure 76: Average rotation rate simulated from equation 46- displaying breakdown phenomenon - and temporal responses simulated using ODE solver (top-left) Synchronous regime (top-right) Immobilization of the robot (bottom-right) asynchronous regime.

2.2 Setup Calibration and experimental protocol

Preliminary calibration Calibration and analysis is one of the preliminary challenge of a Helmholtz setup. For a same voltage input, fabrication and assembly imperfections imply a different magnetic output toward two different axes. The consequence, as shown in the Fig.70 (a), is an ellipticity of the rotational field. To conserve a uniform movement, a calibration is required. Uniformity of the magnetic field (to avoid elliptic aberrations) requires a high fabrication and assembly precision. It is simpler to preliminary correct errors. A first approximation method has been using the robot as a compass while floating or immersed, with even less precision - see [141]. We prepare an untethered microrobot and pick and drop it on the surface of water in small volume. The capillary force removes the robot from our tool and it remains to the surface thanks to surface tension. The floating conditions reduce drastically viscous drag, making the robot like a compass, more sensitive to anykind of perturbations (variation of the amplitudes or direction).

The other more reliable method involves using a Hall effect sensor with a small enough surface to be included in the uniformity zone (assimilated to a 10 mm cube; see Chapter 2 for

more details). It has several advantages:

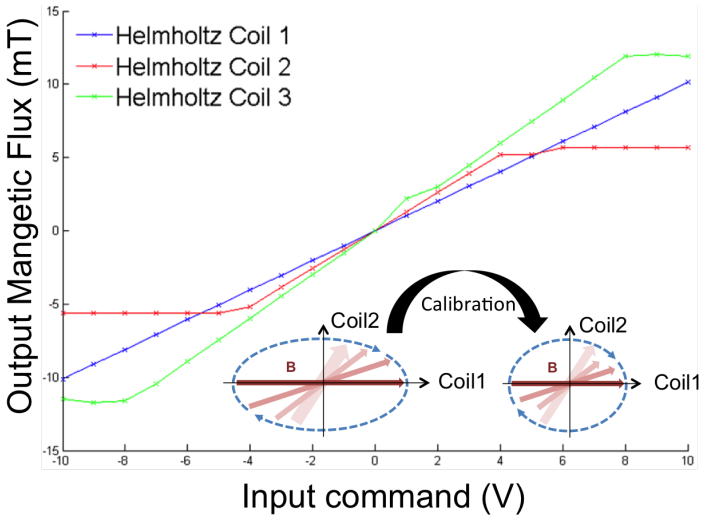

Figure 77: Calibration curves of three pairs of Helmholtz coils to form uniform and constant norm rotating field.

— we can measure several points, controlling the uniformity zone (moving the sensor with a micro positioner)
— we obtain a quantitative relation between magnetic flux and input voltage for each channels
— we can estimate magnetic power actuating on the robot body.

Both methods allow us to determine the relation between magnetic flux in the uniformity zone and the input voltage on the Helmholtz coils (Fig. 77). This calibration is essential to obtain a circular (no ellipticity) field for having a uniform rotation and detect precisely the perturbation of the viscous drag.

Experimental protocol The microrobot, as described in previous sections, is integrated in a glass-PDMS chip, as shown in Fig. 78. It is controlled in pressure to regularly inject isopropanol, avoid bubble contaminations and maintaining a steady static flow during measurement.

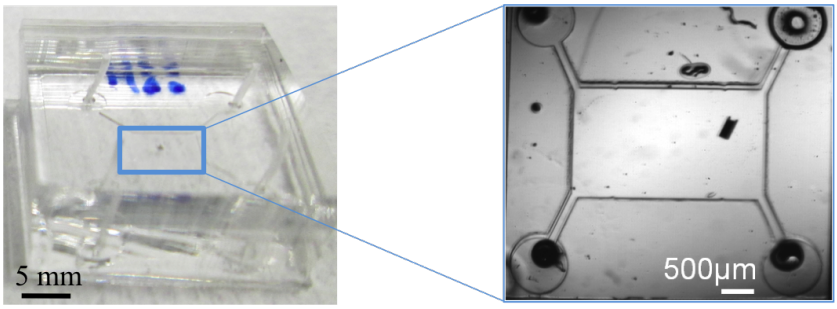

Figure 78: (left) Top view of a microfluidic chip with integrated microrobot (right) Integrated-on-chip micro robot view in the main chamber from optical microscope.

To determine the cut-off frequency we measure $< \omega >$ of the robot on 10 magnetic cycles to detect the breakdown phenomenon. The frequency response scan defines the temporal

resolution. We define the cut-off as the highest frequency with $< \omega >_{AverageRotationRate} = \omega_{FieldPulsation,c}$. For demonstration purpose, we achieve a first scan with 10 Hz step to detect the gross cut-off frequency, and then obtain a more precise value with a second 1Hz step zoom centered on this previous value. Other strategy for quicker convergence can be use such as dichotomy [156]. The comparison in Fig. 76 is done with a simulated frequency response using Runge-Kutta method [157]. The frequency-responses on Fig.80 fit the theory, with the expected proportional dependency between magnetic power and cut-off frequency. It seems that in higher frequency, the experimental responses drop faster. As we are at micro-metric scale, in chaotic regime, the contribution of electrostatic & capillary forces absorb too much energy for Eq. 5 to be verified and a perturbation term should be included to equation 44.

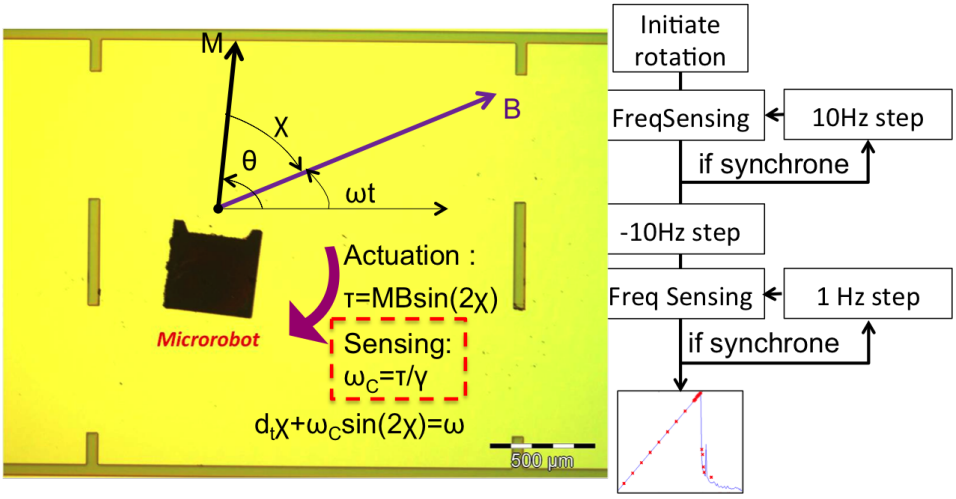

Figure 79: Particular case of rotating uniform field and sensing through a breakdown phenomenon.

At higher frequency $\lesssim 1kHz$, the robot does not respond with our device maximal power and we consider the system as mute – Fig.2.

With an offline tracking, the particle rotation can be simply determined in time by computing the angle formed by two distinct points of the robot (Fig.70 c) after measure. We can determine a value of ω_C, see Fig. 79 by an experimental fitting to the asymptotic behaviour giving us an equation relating fluidic and robots geometry parameters (from striction coefficient) to magnetic inputs.

2.3 Sensing magnetic field intensity

Protocol We used the PDMS chip/robot couple for all this study and realized it in isopropanol at same concentration. We generated the planar circular rotating field with a frequency varying from 1 to 150Hz with a 10Hz step, then zoomed in the breakdown area with a 1 Hz step, knowing from equation 46 that $\omega_c = \frac{MB}{\gamma_z}$. We can analyse dynamics with up-to 40 images per revolution at maximal frequency (frame-rate $> 5kHz$). We then integrate the signal to obtain an average rotation. We repeated the study for different power input (calibrated i.e. no ellipticity). The post-treatment of recorded sequences is done tracking robot shape and measuring angular variation between each frame.

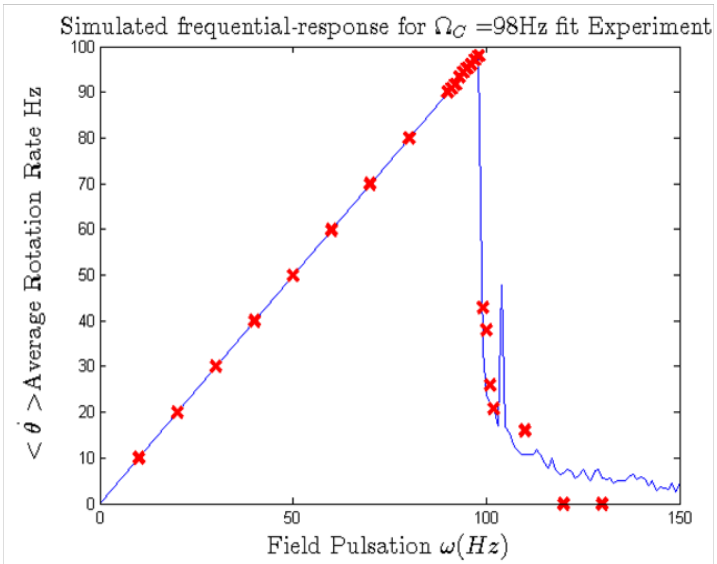

Figure 80: Comparison of simulated solutions (Runge-Kutta method) in continuous line and experimental (with tracking) frequency- response marked point – with a 1 Hz precision. First scan is 10 Hz step. Second, centered around the cut-off frequency is each 1 Hz step.

Observation If we define sensibility of the system as the variation of ω_C depending on the power, we obtain an experimental value of $24.22 rad/(s.mT)$. Nickel being a soft ferromagnetic material of known initial susceptibility $\chi_i = 109$ (unitless) and saturation $M_{sat} = 0.51 \times 10^6 A/m$ [142], we expect the two asymptotic cases:

$$\begin{cases} M \approx \frac{\chi_i B}{\mu_0}, B \ll B_C \\ M \approx M_{sat}, B \gg B_C \end{cases} \tag{49}$$

with M_{sat} the saturated magnetization from the ferromagnetic material, B_C the coercitive field and μ_0 the vacuum permeability. We observe in Fig. 81 two regimes, one fitting a linear response giving us the ratio between magnetization and viscosity ratio and confirming the material at this point is magnetized. If we know approximately from which power to start, fewer points are necessary to determine the coefficient of the line. First qualitative result is the confirmation from graph that the robot is magnetized over 3mT flux, the cut-off frequency being directly proportional to the magnetic flux $\omega_C = (M_{sat}B)/\gamma_z$. A non-magnetized robot would have had a quadratic variation with the magnetic flux $\omega_C = (\chi_i B^2)/(\mu_0 \gamma_z)$. We also obtain quantitative information that allows, as the Ni saturation value is typically $0.51 \times 106 A/m$ at ambient temperature, to approximate the value of the damping coefficient.

2.4 Sensing liquid viscosity

The viscous drag is a stable predominant force at this scale. Dynamics mostly depend on it. The coefficients mentioned in Chapter II.1.1, depending on geometry of the robot, directly defines the hydrodynamics performances of the robot and it is worth noting, varying the robot's medium viscosity, to determine a value of β. More importantly, is the viscous drag the only force at stake in our phenomenon?

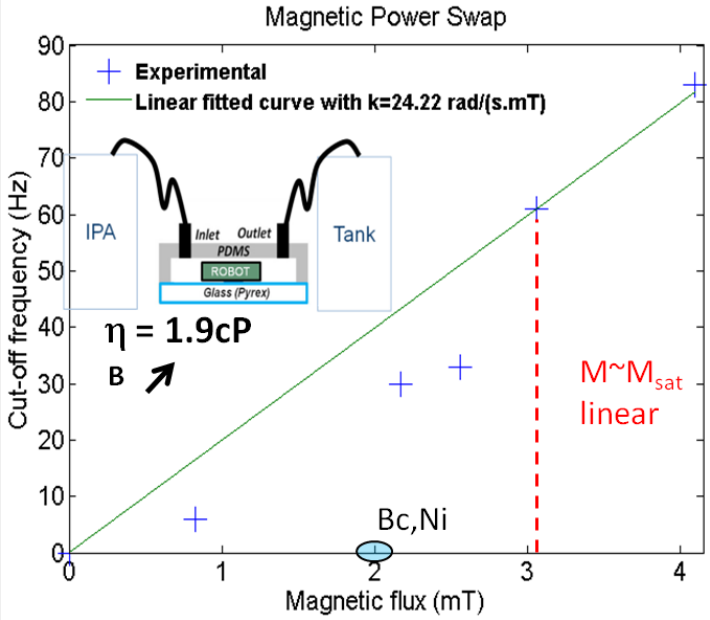

Figure 81: Cut-off frequency in function of a rotating magnetic field amplitude, with linear fitting using least-square method.

Protocol We used the same chip/robot couple for all this study and realized it successively within three different liquid of known viscosity, emptying the tank between each measurement. We used the previous protocol to obtain each cut-off frequency, knowing from equation 46 that $\omega_c = \frac{MB}{\gamma_z}$. We suppose a linear dependency of γ_z, as described in Chapter 2 [158], with fluid viscosity as well as robot geometry. The magnetic power was fixed to 4.09 mT to guarantee a constant power in saturated regime. We can analyse dynamics with up-to 40 images per revolution at maximal frequency (frame-rate $> 5kHz$). We then integrate the signal to obtain an average rotation. We repeated the study for three different power input (calibrated i.e. no ellipticity). The post-treatment of recorded sequences is done using a tracking detecting robot shape and measuring angular variation between each frame.

Observation We have demonstrated our ability to deduce from the breakdown phenomenon the local viscosity of the robot. This could be, once automated, used to quickly determine the viscous drag. Defining the sensibility of the system as the variation of ω_C depending on the power, we obtain an experimental slope of $118.1 s.cP/rad$. As the response is approximately linear ($b = 0.04cP << \nu_{liquid}$) from Fig. 82, the contribution from substrate and interface phenomenon in dynamic regime seems negligible compared to viscosity drag in dynamic regime.

These results apparently comfort us in the hypothesis where the robot always levitate and has no perturbative interaction with its substrate. However, any use can field difficulties in manoeuvring the robot and as we have seen in asynchronous regime or during transition from static to dynamic regime, there exists non-linear phenomenon which are not integrated.

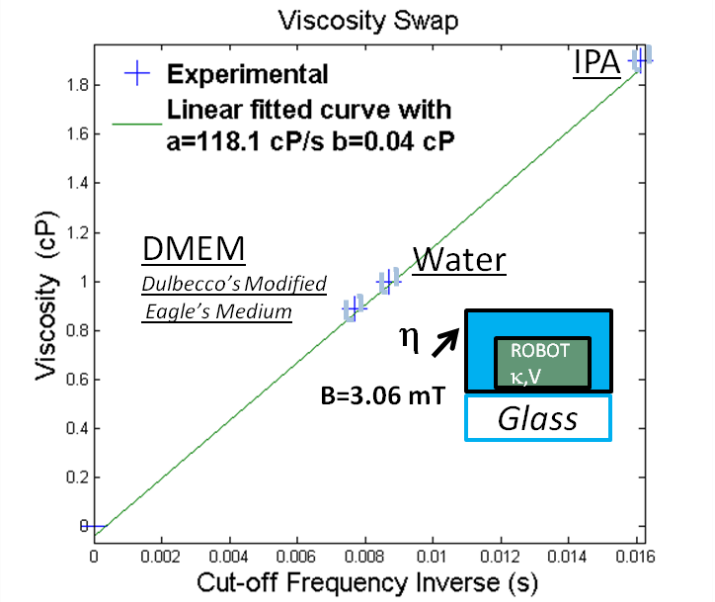

Figure 82: Viscosity in function of Cut-off frequency Inverse, with linear fitting using least-square method.

3 Position tracking for kinetic sensing

We first explain from analogous principle with previous section what we extract from translational kinetic, compared to rotational motions. From this model, exploiting our dome setup detailed in Chapter 2, we are able to use (online or offline) position tracking to extract data from our microrobot in motion. We will see what impact it has on our understanding of the robot and its environment as well.

3.1 Principle and experimental protocol

Sensing from translational motions at micro scale is challenging because systems are more easily subject to unexpected forces from substrate. Because mass is decreased drastically (particularly in our system), huge forces i.e. accelerations are at stake in the motion of our micro-robot. The consequences are difficulties to keep the robot inside field of view and to analyse its dynamics quantitatively. Keeping the robot in a confined chamber avoids loosing robot's track, but the surface resistive forces still disturb its dynamics. We suppose further a constant gradient magnetic field generated by an electromagnet toward a horizontal axis and without any interface perturbation from substrate. In this hypothesis, equation 43 is verified. As the field generated by a solenoid is well known on its axis, we expect a known tendency of the magnetic flux thus the speed of the robot at the neighbourhood of the axis. Simple pulling experience in non-perturbed case provides a way to map the gradient field generated by an electromagnet and obtain a global value of drag coefficient β using numerical fit on the tracked positions. In case the experience is perturbed,

$$-\beta\mathbf{v}+\mathbf{F}+\varepsilon=0 \tag{50}$$

we can estimate the perturbation ε and better understand in-vitro dynamics thanks to quantitative analysis and simpler hypothesis due to glass material.

Position tracking and extracted data The couple chip/robot is the same than in previous rotational experiments, in an isopropyl alcohol solution. We induced a gradient distribution using the dome containing 4 electromagnets on orthogonal axes and sharing a common center - see Chapter II. Being able to generate a force in any direction of the plane by linear superposition of the axes gradients, we can achieve a movement with up-to $30mT$ amplitude of field and $3mT/cm$ gradient and analyse it at high framerate - $6kframe/s$, see Fig. 83. In section II approximation (heavily damped system), microrobot speed is directly related to the viscosity - Eq. (5) - and we can directly obtain the distribution by analysing the movement. Because of small distance from electromagnets and its high proportion of ferromagnetic part, robot can reach high-speed – $556mm/s$, reaching the limits of low Reynolds conditions. We here limit the system power to "small speed" to remain in low Reynolds hypothesis - $< 20mm/s$ that is to say $Re < 10-2$. From sequences and position tracking, we can deduce speed, which according to (5) is directly related to exerted magnetic force. The robot being magnetized, we can evaluate magnetic gradient in one direction. We compare backward and forward motion of the robot by testing each magnetic field polarity [141]. Then we map the magnetic gradient by varying the initial position of the microrobot.

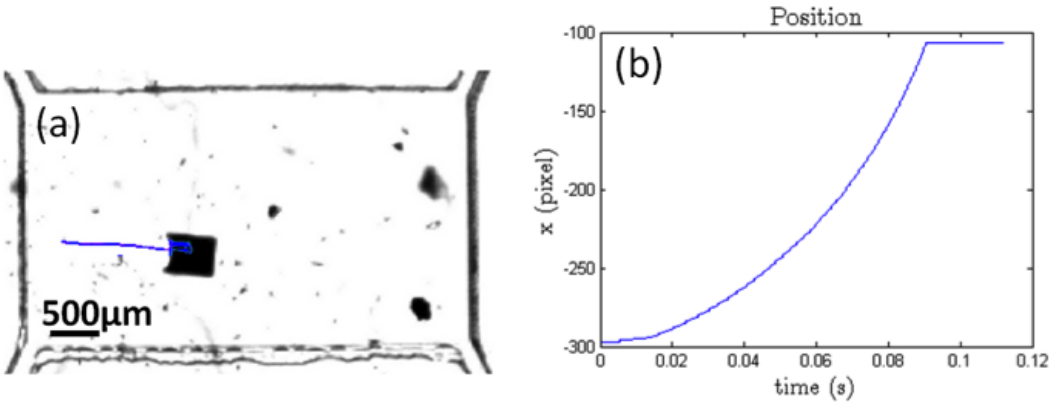

Figure 83: (left) Example of tracked scene using a shape detectio algorithm (right) Resulting x position depending on time.

From motion, we differentiate the data and access speed and acceleration, see Fig.84. As we can notice noise increases with degree of differentiation, we also see appears a comparable curve to the magnetic gradient distribution. We can compute from it the range the delta between magnetic and adhesions forces, and we also can detect eventual non visible obstacles.

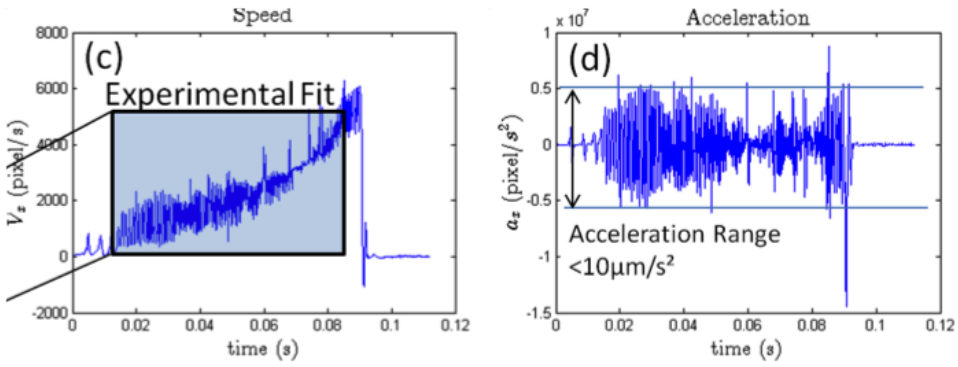

Figure 84: (left) Speed depending on time, (right) Acceleration range.

3.2 Backward VS forward motions

One first result interesting from translational experiences is to compare backward and forward motion. As MagPol offers us the possibility to be driven in both direction, we can compare the difference of performance in terms of hydrodynamics but also the perturbation ε as mentioned in equation 50.

Observations Setup vibrations (from camera) are included as a 1.25 kHz non-trivial component that we clearly see appear on the Fig. 85 and 86. First important result is a repeatable high difference between backward and forward motion in terms of dynamics. Forward motion displays a precisely break at 40% of trajectory (32 ms), creating two different regimes – Fig.6. In pre-break regime, the speed increases. Afterward, the speed reduces drastically and remains approximately constant, which means the microrobot arms contact with substrate changes. The consequence is the appearance of a speed limit independent from the magnetic power, which could be used to estimate the perturbation from substrate. Backward motion does not display this phenomenon and seems to correspond to magnetic flux theoretical distribution, to determine for example the striction coefficient from fluid.

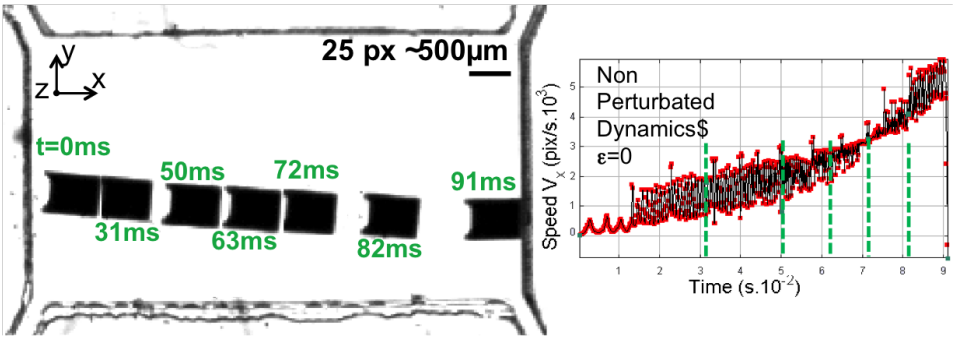

Figure 85: Non- smoothed data extracted from position tracking. Backward motion displays expected dynamics from model.

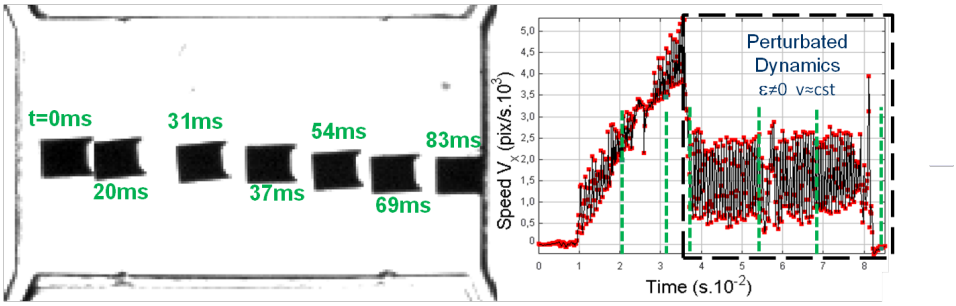

Figure 86: Forward motion includes a perturbation and splits into two different regimes.

3.3 Discussion: Importance of robot pitch angle

Forward motion offers a faster motion (power used is the same), but with perturbed dynamics and a drastic repeatable change halfway of its trajectory, where the magnetic flux gets stronger. We must not forget the vertical distribution of the magnetic field. Our hypothesis

is that robot is not entirely symmetric and its magnetization has a non-zero component toward **z**. On one direction (backward), the robot is always touching with its arm the substrate, which means there is actually a non-visible perturbation which adds up to viscous drag. In the other case (forward), the robot levitates until the equilibrium of force changes due to magnetic field vertical components or viscous drag contribution. The arms start touching the substrate, generating a sudden and stronger perturbation as it is forward.

One important confirmation we deduced from these observation is the impact of pitch angle on the robot. We can vary the relative position of the substrate with the coils axis. Even though the substrate is ideally horizontal, the horizontal distance with the coils axis generates a non zero component toward **z**, inducing a pitch. The observed consequence being an increase of adhesion forces and obstacles probability, we can deduce the contact with the substrate as a key role. The pressure of the flow during the motion can also combine to pitch and maintain the contact.

It is difficult to evaluate from top-view the pitch angle from the robot and 3D-vision investigation could be considered, though requiring an important experimental effort and being quite by the depth of focus of its optics. Another solution would be to superpose a uniform vertical magnetic field to control the influence of pitch angle over the robot trajectory and observe its impact, and eventually if a perfectly horizontal (compared to the substrate surface) could be generated.

4 Glass-Metal-Glass Chip for Highly Reproducible Measurements

We have seen in the previous sections our mobile magnetic microrobot in confined liquid can be applied as untethered transducers with great precision of control and fast time-response (below millisecond). To become a measuring tool, it is interesting to replace its soft microfluidic chip with something more robust to aging, wider thermodynamics or chemical conditions. Moreover surface phenomena become predominant over body forces and make control and propulsion challenging, and surface effects increasingly unpredictable. To conclude this part, we introduce our design of mobile microrobot in a hard glass-metal-glass microfluidic device.

4.1 Soft VS Hard Microfludic

This hard microfluidic device has the advantage of being compact in vertical dimension, see Fig.87 optically transparent for both transmission and reflexion microscopy, chemically inert and more importantly displays less adhesive surfaces.

It has a longer lifespan compared to soft microfluidic - where polymer evolves quickly with time and chemicals absorption. Most importantly, glass hydrophilic surfaces evolve more slowly compared to polymer. In this environment, we can properly study with high repeatability the dynamics of robot and its manipulation capacities.

From Tab. 24, we see GMG chip does not really cost much more in terms of consumable, it is in term of process that it is less interesting than PDMS chip, as the time per chip is 2 times longer, and get worst as number of chip fabricated increases. It is then for the experimental

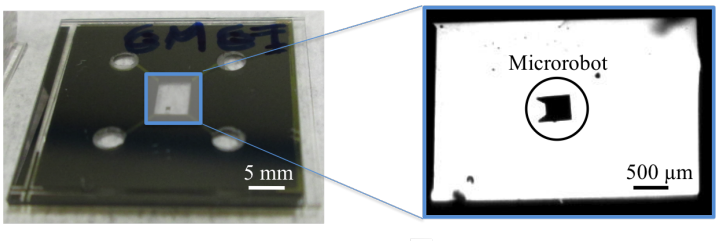

Figure 87: (left) Top view of a microfluidic GMG chip with integrated microrobot (right) Integrated-in-chip micro robot highly contrasted view in the main chamber from optical microscope.

Table 24: Comparative table of hard and soft microfluidic chip technology

Material	Lifespan	Pressure	Porosity	Cost	Process
Soft microfluidic	∝ weeks	fair	high	very low	short
Hard microfluidic	∝ months	high & no deformation	very low	low	long

conditions it provides that it is interesting to develop microrobot in GMG chip.

4.2 Glass-Metal-Glass microfluidic chip process

Integrated microbot in GMG microfludic chip is the convergence of previously known MEMS process to develop the microrobot with hard microfluidic process. We sum up below the current process we use and made a graphic description on Fig.88.

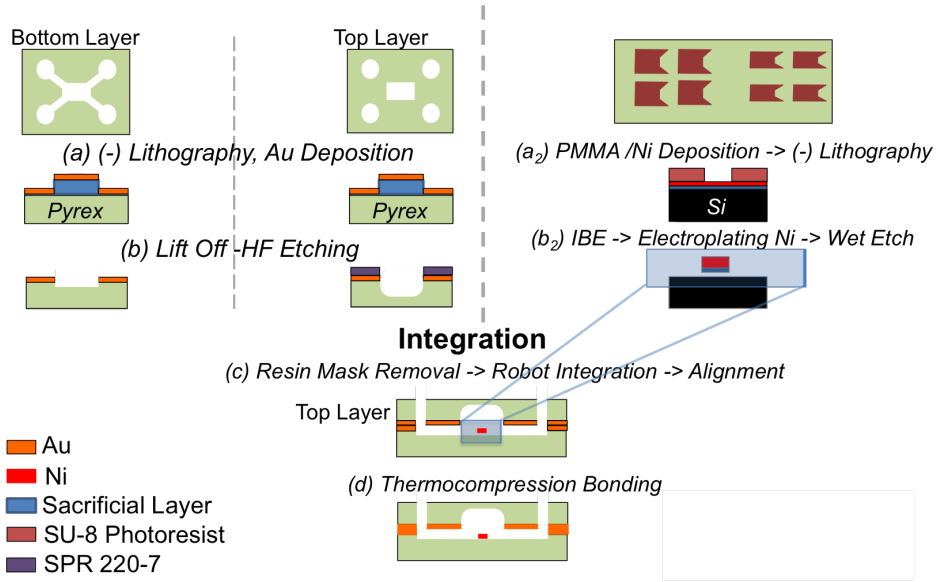

Figure 88: Glass-metal-glass chip (GMG) deep etching, integration of the microrobot, followed by thermocompressed bonding and fluidic interfacing.

Compared to molding techniques mentioned in Chapter II, glass material requires negative approach, i.e. (HF) etching. The other important step which will guarantee the chip hermetic

conditions is a thermocompressed bonding. Both steps require a *Au* mask which has thus a key role in this process and its surface quality must be conserved through different steps.

Glass deep etching Deep etching is a critical phase to obtain a sufficiently deep chamber, so robot can move freely and channels can easily guide the flow (see Fig. 44 from Chapter II). As the most efficient etch is with HF [159] and is isotropic, our design need to consider the lateral etch and the channel have a pipe shape, see Fig.89. The best strategy from literature comes from Illiescu et al. and suggest to use Au thick (300nm) layer [160] protected with a supplementary photoresist.

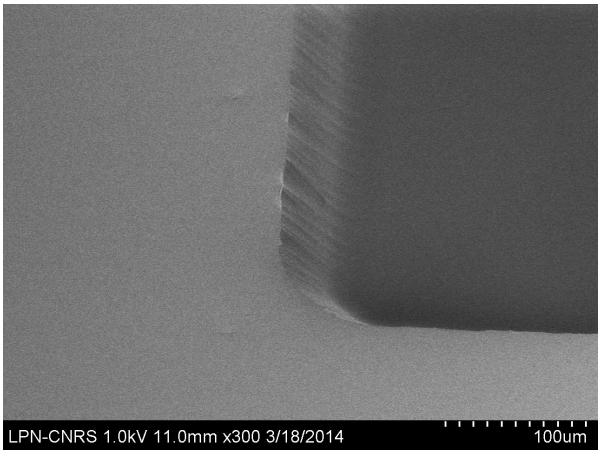

Figure 89: Glass deep etching using HF with adapted *Au*/resin mask.

We fabricate our chip on two Pyrex substrates, deposing 300 nm Au layer with a 30 nm Cr layer for adhesion on Pyrex. The metallic layer provides a etching mask as well as a bonding layer for next steps. We structure the channels pattern on it by a standard lift-off process. We then etch the channels using HF/HCl. To achieve deep etching ($> 80\mu m$) minimizing roughness and defects on the gold masking layer, we combine an electrolytic Au growth ($1\mu m$), baking and coating it afterward with a hard baked thick SPR220-7 on top. Under-etching of channels is impossible to avoid and will sometimes make gold layer collapse or pull off depending on the etching depth. But pinholes, happening because of gold porosity, can be simply overcome as shows the right picture of Fig.90. Avoiding them is necessary to insure a sufficiently strong bond between the two gold layers.

We also achieved via etching on the top part for anticipated punctures using a sandblaster with an adapted taped thick metallic mask. Gross alignment is sufficient as holes diameters are millimetric.

Metal-metal thermocompressed bonding We used thermocompression to fully bond at 300°C the chip. It is a relatively low temperature for a metal (354°C), and when robot is preliminary integrated, we can consider its internal stress unchanged. Gold-gold thermocompressed bonding is robust, repeatable and was optimized for high bond strength and high bond yield by Taklo et al. [161]. It also remains in the continuity of the preliminary etching, as the best etch mask are made of gold.

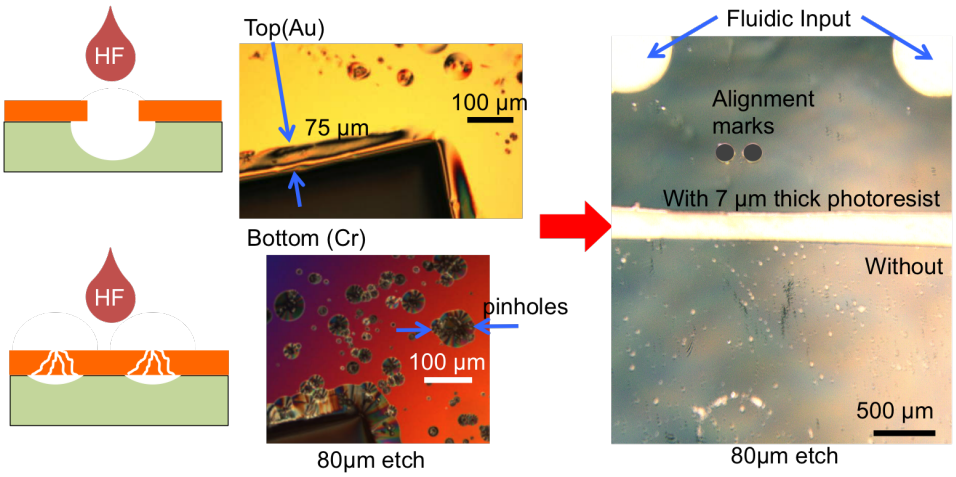

Figure 90: HF etching drawbacks: underetching and pinholes: (left) schematic of principle (middle) illustration of these drawbacks (right) comparaison with an added protective photoresist.

Robot integration Integrated microrobot is identical to the ones used in PDMS chip, for compared performances. It is resistive to high temperature as it is pure ferromagnetic material. Thus it can be integrated by pick and drop as well. One other interesting property from glass edges is they is no risk of adsorption as opposed to a PDMS layer, which can bond with the Nickel layer with very few chances of success to remove.

The consequence is the possibility to reach smaller thickness of chamber and channels, decreasing the low reynolds number limits in speed.

Fluidic interfacing Robots can then be injected or deposed before bonding them. We interface the system by bonding a PDMS layer on top with a oxygen plasma, as for standard PDMS chip.

4.3 On-chip velocity mapping by robot on GMG chip

We can repeat previous translational experiences in this environment with simpler conditions. PDMS layer of the previous chip had a tendency to adsorb object and in particular the robot. To limit this issue, we made our chamber much higher than necessary compare to the vertical size of the robot. Here, mapping velocity, which requires several horizontal trajectory, can be achieved with comparable results, as the surface condition should be the same everywhere and no interruption due to polymer adsorption can happen.

By doing post treatment and analysis of dynamics with static flow and at an ambient temperature, we can characterize the robot mobility in microfluidics. We use it here to map the microrobot velocity for each axis – Fig 91.

We achieve 6 parallel trajectories for one single axis, with a temporally resolved resolution (below ms), and we linearly interpolate the 6 curves to obtain from the scattered data a map. By doing a statistical study – Fig. 92- of the speed toward the radial (top) and axial directions (bottom) of one coil, we can detect the impact of the border effects from the glass chip. The top figure displays radial statistics and allows to precisely locate the coil centre. The high

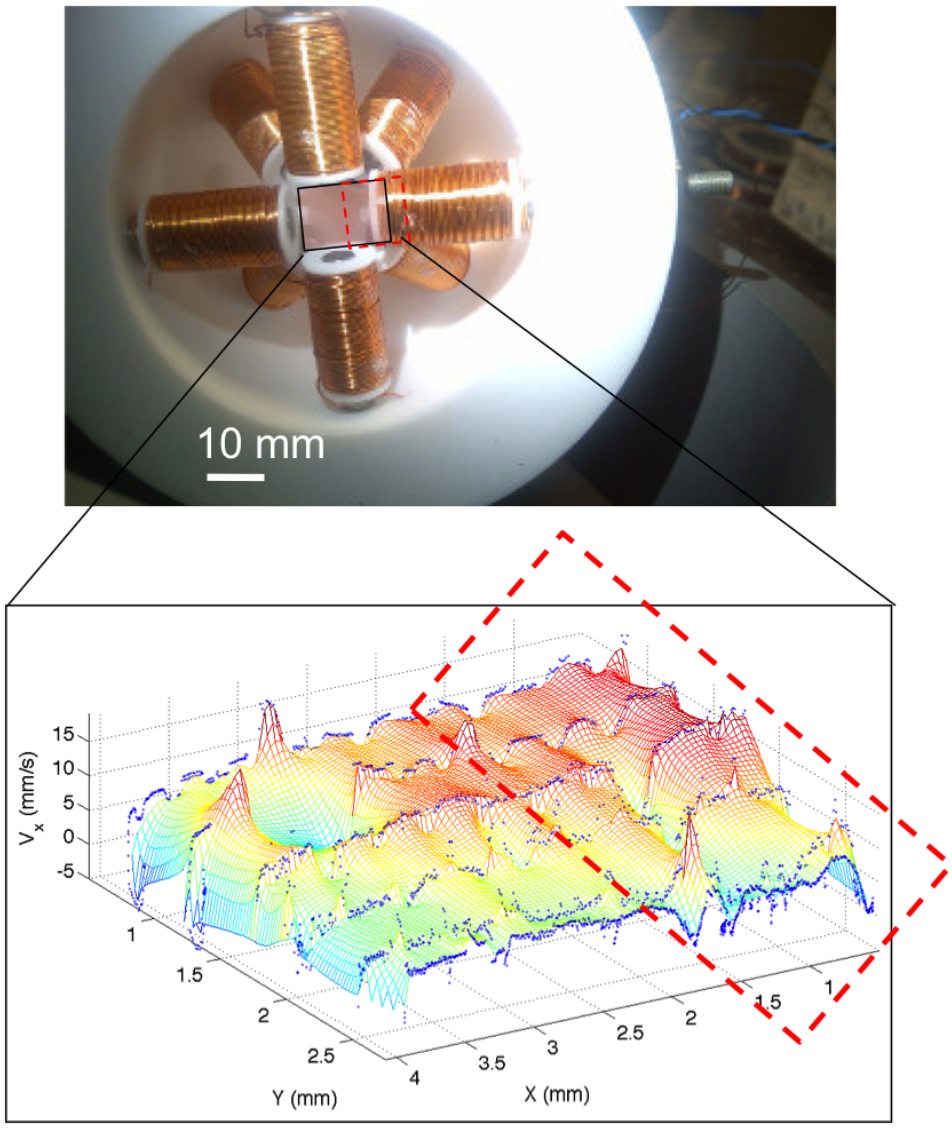

Figure 91: (top) Dome region of interest, bottom view (bottom) Mapping robot speed projection on x by interpolating robot speed distribution. Here, 6 linearly interpolated trajectories while swimming backward.

standard deviation toward the axial direction is due to the quick variation of the magnetic gradient toward the coil axis. This correlates the simulated distribution of the magnetic field and lead to several axes of development.

Finally, GMG chip has allowed several improvement. The measurement offers more relevant results as the dynamics of the robot is completely dependent by the chamber edges. The glass does not evolve much in time and conserve a relatively weak interaction, making the result repeatable and simpler to interpret. Still though, we observe on statistical distribution and mapping some important fluctuation of the speed, which means adhesion forces exist and requires some more interpretation.

GMG chip has also unlocked several possibilities:
— a much wider range of thermodynamics conditions (up-to 15bar, T 60°C)
— alternative design strategy, allowing to scale down channels (with polymer natural adhesion, we have to make channels two to five times deeper.

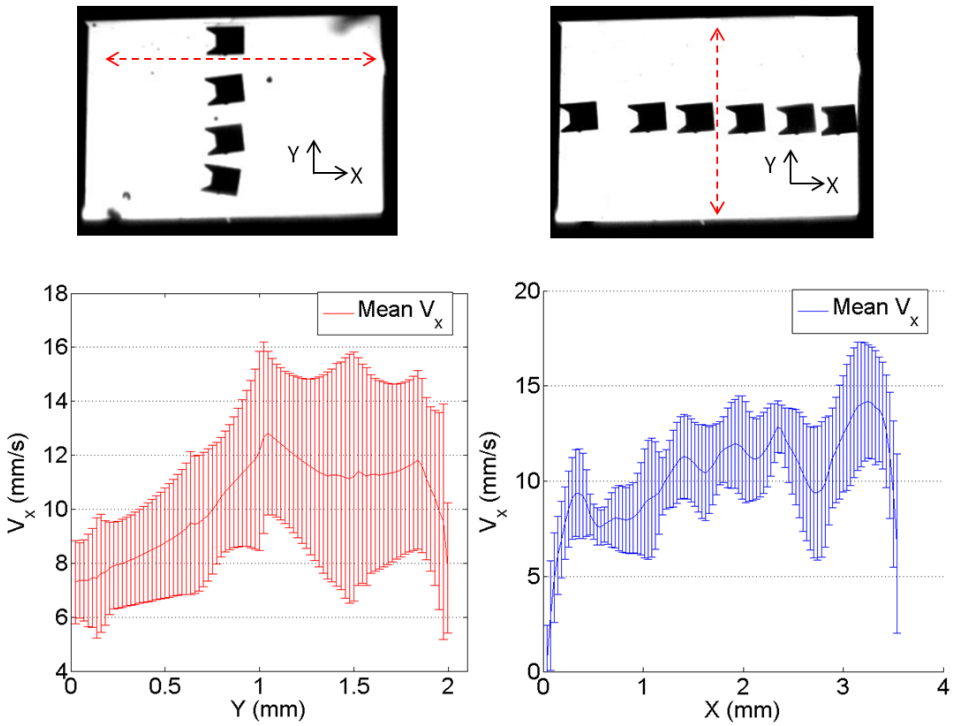

Figure 92: Statistical Analysis of the interpolated distribution. (top) Average axial speed and standard deviation depending on the radial position with the coil axis. (bottom) Average axial speed depending on the axial position with the axis.

4.4 Perspectives of in-glass measurement

It could help us to better understand the dynamics of the robot by doing a comparative study with polymer soft chips as well as a variation of power from the coil. The Glass-Metal-Glass chips can be a promising tool for reproducible transducing applications requiring non-standard physical conditions (high pressure or temperature variations, more inert to aggressive chemicals) and less adhesive surfaces to biological bodies.

This proof of concept will lead to automated batch tests for on-line mapping. Scaling down the robot would show if the perturbations due to adhesion forces increases with size, which might help to identify the kind of phenomenon between the robot and the chip edges.

One final experience that is technologically available on our setup and could lead to additional proof of viscous drag predominance would be generating a pressure gradient and observing the flow impact on our measurement, making it eventually possible to achieve a pressure measurement.

5 Conclusion

We demonstrated that remotely powered microrobotic swimmers integrated to microfluidic devices can serve as wireless physical sensors. The wireless microrobotic swimmers are robust to a large range of physical and chemical environments and provide a high controllability. In future implementations, the capabilities to the magnetic field sensing and viscosity sensing can be applied to detect wide range of external physical conditions (thermally,

chemically, or biologically) by increasing the sensing range and resolution through automated sensing and design optimizations. The translational sensing by polarizable motion capability can estimate the local perturbations or viscous drags. The both rotational and translational sensing, combined with automated motions, may be used in dynamically building physical maps inside microfluidic environments where there is challenges to integrate additional sensors. Our system has demonstrated ability to determine the magnetization of the robot. It can as well act as a calibration tool for rotating magnetic field or a sensor of local viscosity of the fluid. Transducing capacities (sensor as well as actuator) of MagPol in microfluidic chip have been compared to theory and confirmed.

The automation of these test will be precious for real time information about the environment of the user and live diagnosis. For now, obtaining quantitative values requires an important post treatment effort.

Part IV

MMM control in fluidic environment and micromanipulation strategies

Summary

After a technological effort to integrate microrobotic tools in microfluidic environment, we introduce in this chapter the exploration of motions and degrees of freedom allowed by our system. From uniform field as well as gradient field linear combination, we will demonstrate that our device proposes a wide range of motion control that can be controlled by a user interface (UI). This interface can be exploited to provide an open loop control for direct manipulation. As a consequence several new micromanipulation strategies will be studied and a potential evolution of the device will be discussed in the last section.

1 MMM control and manipulation in fluidic environment

This section enumerates the different forces at stake in the system, as they will directly impact our control on the system. We first quantify the induced magnetic force depending on the geometry of the microrobot. Then, we will specify a little further surface forces at stake for further interpretation of micromanipulation.

1.1 Actuation: using magnetic volumic forces

Computing magnetization reveals to be complex for ferromagnetic materials as the dependency between magnetic flux B and magnetization M are non linear [24]. Hopefully, nickel offers a simpler behaviour as it is a soft ferromagnet, i.e. with a thin and narrow hysteresis curve, as represented on Fig. 93. Consequently, a soft ferromagnetic material must have a high initial permeability and a low coercivity. A material possessing these properties may reach its saturation magnetization with a relatively low applied field (i.e., is easily magnetized and demagnetized) and still has low hysteresis energy losses.

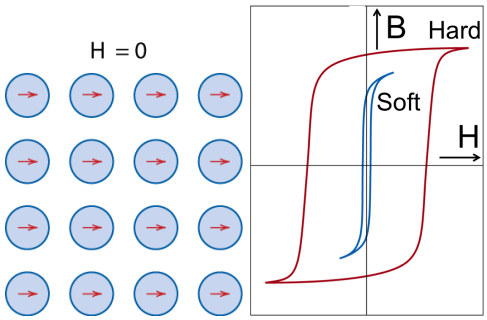

Figure 93: (left) Schematic illustration of the mutual alignment of atomic (blue circles) dipoles (red arrows) for a ferromagnetic material, which will exist even in the absence of an external magnetic field and characterize the remanent magnetization [24] (right)Magnetic hysteresis loop for soft and hard ferromagnetic materials [25].

The saturation field or magnetization is determined only by the material composition. It is simply the product of the number of Bohr magnetons per atom (0.60 for Nickel) [24], the magnitude of the Bohr magneton and the number N of atoms per m^3, or

$$M_s = 0.60 \mu_B N \tag{51}$$

Now, the number of atoms per cubic meter is related to the density ρ, the atomic weight A_{Ni} and Avogadro's number as follows:

$$N = \frac{\rho N_A}{A_{Ni}} \Leftrightarrow M_s = 0.60\mu_B \frac{\rho N_A}{A_{Ni}} \tag{52}$$

For $\rho = 8.9g/cm^3$ density, $M_s = 0.64T$. From equation 52, we can evaluate the range of force from the range of field induced for both setups, using equations from chapter II. Table 25 sums up the relation, with magnitude order of our setups - i.e. gradients from the dome, uniform field from the helmholtz setup.

Table 25: Magnetic flux, gradient and corresponding forces and torque from Helmholtz and Dome setup's electromagnets on a standard $500 \times 400 \times 20\mu m$ microrobot

Property	I(A)	Body force (mN/m^3)	Body Torque (mN/m^2)	B(T)	∇B (T/m)	Force (μN)	Torque (Nm)
Helm. setup 1	$1-5$	-	$0.64-3.2$	$1-5$	0	0	$(2.6-12.8)10^{-15}$
Helm. setup 2	$1-5$	-	$0.64-3.84$	$1-6$	0	0	$(2.6-15.4)10^{-15}$
Helm. setup 3	$1-5$	-	$0.96-4.48$	$1.5-7$	0	0	$(3.8-17.9)10^{-15}$
Dome EM	$1-5$	$0.64-3.2$	$2.7-14$	$4.25-20$	1-5	2.56	$(10.8-56)10^{-15}$

The table gradients are computed from the middle of the chip, on the axis. The variation is non-trivial, and the values are here to have an order of magnitude.

1.2 Low-Reynolds Number Environment: Heavily Damped System

Low Reynolds number flow (even at high speed, where $R_e \approx 10^{-3}$, $Re \ll 1$) can be considered as Stokes flow, i.e. an environment with here strong inertia effects, confirming chapter II section about microrobot design and dynamics. It implies a predictable effect of fluid Standard use of MagPols remains below low Reynolds ($\approx 10^{-2}$ for speed ≈ 1 mm/s) and satisfies easily our hypothesis. In maximal speed case (cf. chapter III high translational speed), which requires using our electromagnets at full power, the change of flow speed induced by the robot is assumed to be neglectable in the volume of the channels.

Dynamics of system can be simply approximated, with hydrodynamics damping effects. We can expect the following dynamics on equation 53 and 54,

$$Id_t^2\theta \approx 0 = MBsin(2\phi) - \beta d_t\theta \tag{53}$$

$$md_t^2 x \approx 0 = (\vec{M}\cdot\vec{\nabla})\vec{B} - \gamma d_t x \tag{54}$$

where I is MagPol moment of Inertia toward $\vec{z}$, β the rotational drag coefficient toward $\vec{z}$, γ the drag coefficient toward $\vec{x}$, θ is the angular position of the magnetic moment M in

the horizontal plane and ϕ the angle between the moment and the generated magnetic field of amplitude B. Because the system is heavily damped, we can also neglect the inertial terms. We can refer to Fig. 94 to see the dependency between robot characteristic size in two different liquid. We see isopropanol (in green) almost double this frontier, being more viscous.

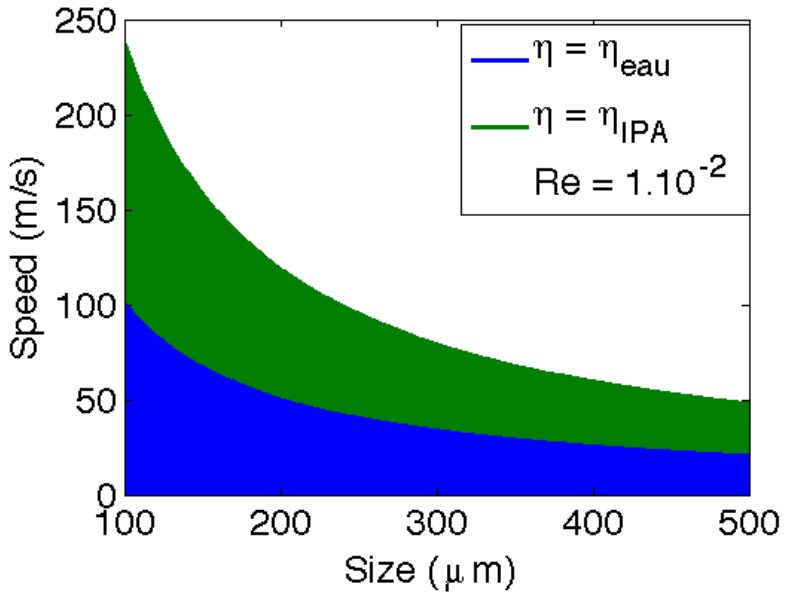

Figure 94: Low Reynolds Number domain for Mobile μRobot depending on its speed.

1.3 Adhesive phenomena influences

The origin of adhesive forces is multiple at microscale. We have underlined in Section I and II the importance of surface phenomenon at our scale and the results of chapter III have shown that in dynamic regime, adhesion forces induce maxima in terms of speed, for time-response as well as maximum velocity from the robot.

A fundamental experience: overcoming static adhesion by yaw rotation One simple experience can help to grasp all the impacts adhesive forces have on our robot mobility. Using a horizontally oscillating single axis field, we observed the time-response of robot depending on the voltage sweep, tracking one of the edge of the robot to get access to a precise angle dependency on time, see Fig. 95.

To obtain the angle, though the shape changes drastically, some tracking including a 3D CAD model exists [73]. It is simpler to plot a one-dimensional curve perpendicular to the bottom edge of the robot, apply a gradient filter - also named Sobel filter, and measure the evolution of the distance between the two maxima. This distance being the projection in-plane of the robot, we can deduce the angle with a reasonable resolution.

Voltages below 2V display a repeatable phenomenon appearing as on graph from Fig. 95 (left) and which let think that first movements changes progressively the substrate-robot contact. This transition signifies contact nature changes during first oscillations. Another unexpected regime happens under $0.5V$, when after several oscillations of full amplitude, the

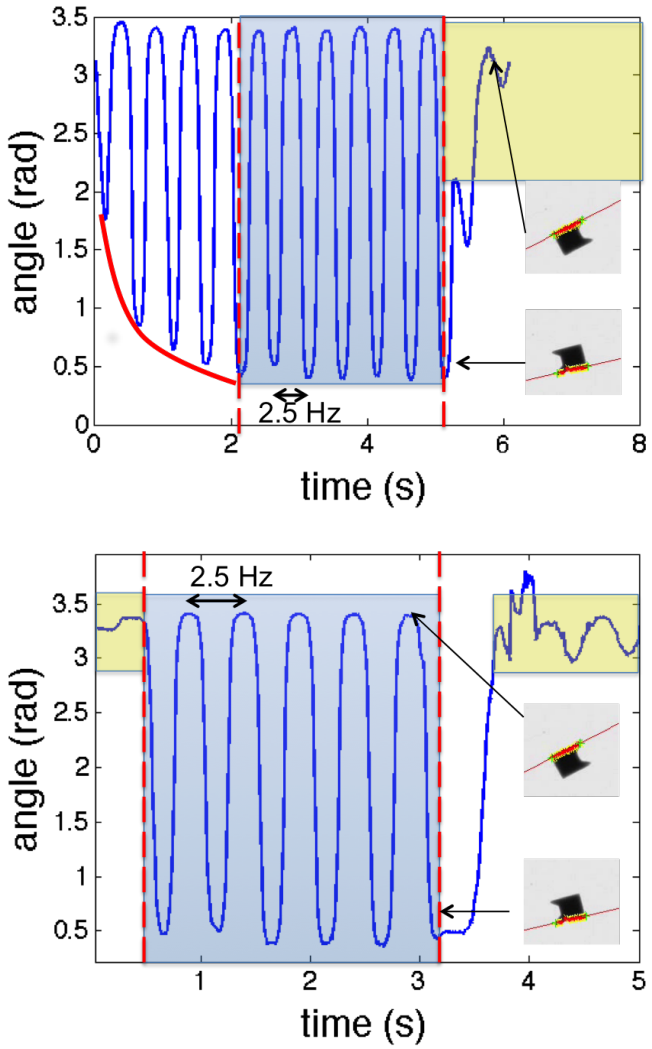

Figure 95: Measured robot angle while exciting it with a 0.4V input (top) and a 0.5V (bottom).

oscillations suddenly shrink drastically, as if the adhesion forces had suddenly evolved again. For voltage input higher than 2V, the robot oscillation is not blocked and no observable transition is observed, which means the magnetic force is sufficient to change in one oscillation the nature of contact.

We also noticed that no oscillation is observed above 9V, which is a first observation of reversing magnetization (it gives us an approximation of nickel coercitive field at ambient temperature).

Different scenarii possible It is very challenging to determine precisely what happens between the robot and the substrate as there is no technique of investigation to our knowledge that can provide us information resolved in time and space about this experience. Physics of interfaces can lead to complex behaviour [162] and models, including nanofluidics [4]. The observation of the fundamental motions of rotation and translation in chapter III has led to summarize three major scenarii which have different impacts on the surface adhesive phenomena as shown in Figure 96.

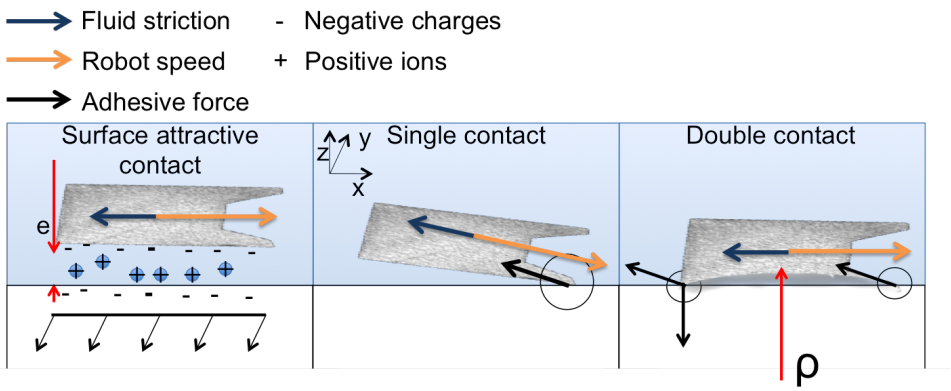

Figure 96: Schematic of three scenarii of contact between the robot and the substrate.

In left scenario of Fig. 96, adhesive force is distributed uniformly on the whole edge of the robot. It induces a supplementary resistance to liquid viscosity. As opposed to solid friction which only generates a resistance toward the directions in the plane, adhesion forces due to electrostatic interaction generates an important pull-in force. This force varies with liquid thickness e between the substrate and the robot. Middle scenario indicates a single contact and in that case one direction will resist more than the other. Though it is not mechanically stable when the robot is static, it could happen when there is an equilibrium between the magnetic pulling force and the adhesion force, due to roughness for example. Finally, the figure on the right supposes a stress generating a curvature on robot, i.e. resistance on both sides. Both sides should show similar resistance, and a pull-off force might be necessary to raise the robot. To better grasp forces at stake, we provide details on the force possibly involved in the model.

Roughness Because we work with smooth Pyrex and *Si* substrate and roughness, does not exceed on this side $< 1nm$. On robot's side, because of nickel growth, roughness is way higher and a simple SEM picture (see chapter II) reveals grains can reach 500nm size. This granularity is almost visible with an optical microscope. Solid friction being the result of both edges rugosity, it might not be the major concert of our context. Moreover, rugosity does not generate pull-in forces.

Fluidic contribution Detailed in chapter II section 1 - hydrodynamicity paragraph, we modelize it with a linear behaviour [79]. The dependency remains to be quite simple with proportionality toward all axes and can be describe as

$$\mathbf{F_{fluid}} = -\beta \mathbf{v} \tau_{\mathbf{fluid}} = -\kappa \omega \tag{55}$$

where β and $\kappa$are constant parameters depending linearly on robot's geometry and viscosity exclusively. Perfect geometrical symmetry cannot always be guaranteed from fabrication imperfection particularily during electrolithic metal layer growth and also during mechanical transfer process to integrate it to the chip.

Overcoming adhesion by pitch rotation In the microscale, the substrate attraction due to electrostatic charges largely dominates the gravity forces in dry environment. In wet environment, even though viscosity dominates, substrate electrostatic forces maintain the microrobot

horizontally on the substrate by adhesion. Using the Helmholtz setup, we can demonstrate by a simple experiment the adhesion force is non neglectable but can be overcome. We induce a step excitation at different power for a on-chip microrobot. We observed a threshold at 0.5V (1.5mT) from which the robot raise and get in vertical position, see Fig. 97.

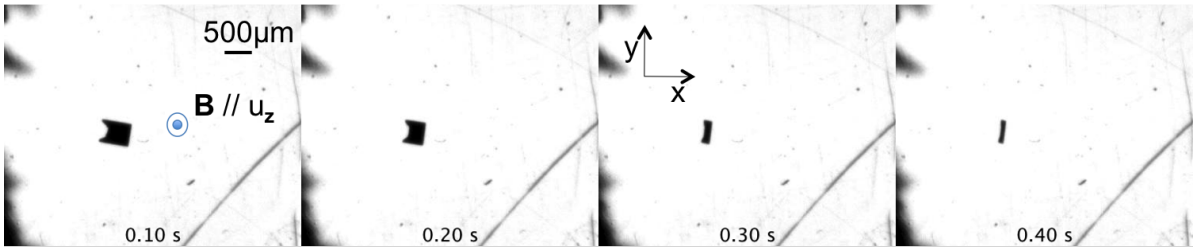

Figure 97: Response to a 1.5mT vertical field is sufficient to get the robot stands almost at $\pi/2$ rad and overcome the surface adhesion.

This threshold phenomenon is actually present on each movement we initiate, and limits the resolution of control. It makes it more difficult to control the robot's motion as the variation of speed is sudden. Increasing the power also increases the pitch angle range, with $\pi/2 rad$ as an expectable limit.

Conclusion for our model What we call adhesion forces is probably the superposition of several phenomenon and it is difficult to estimate which ones (one) predominate(s). Effects also varies depending on the context (initiation of movement x dynamic regime) and we will see that this description will serve as a help for diagnosis when correcting control.

To be in a "comfort zone" for manipulating our robot, it is interesting to be in the range of power where no magnetization reversal happens and static phenomenon are easily overcome. In the example we took, which strictly depends on experimental setup and conditions of the environment, this range is approximately between 2-9V and could be more precisely determined. This section gives a protocol to investigate and conclude by identifying the different threshold and deduce the adapted power range.

2 Teleoperated swim by user interface

In chapter III, we detailed the visual feedback from our system, having the possibility to have up-to 5000 frame per second, with a graphical user interface (GUI) to adjust the parameters of the camera and frame grabber, in particular the ROI. As the users have a real-time visual feedback from microscopic image (with a 30 frames per second display rate), they are able to correct their positions.

It lies down first to decide which magnetic actuator should be chosen between the Helmholtz and the dome setup. We describe then two main ways to control the robot, in force and torque, and deduces the control methods from them. The interfacing can be exclusively done by the GUI but also can include the more user friendly and ergonomic controller as suggested in the chapter II. Finally, we discuss about eventual adjustments of signal control.

2.1 Magnetic control using gradients

The most remarkable speed of our system comes from translation - also named direct pulling. The linear combination of gradients have proven to be an important track to develop control of robot, using permanent magnet driven by motors [22] or electromagnets [131]. From our study of electromagnets distribution, we know there is a radial and orthoradial magnetic force component around their axes. They also varies in amplitude with geometry.

Fast response and control challenges Analogously to rotation, complex movement can be achived such as 8-trajectory loop in Fig.98. We have already shown the speed ability of our system. The problem is the transition from static to dynamics which requires a minimum force. When this threshold force is outreached, the robot motion becomes too fast for the user. It makes this trajectory very difficult to repeat by user's manual control by teleoperation considering the fact that the motion dynamics is much faster than user's visual feedback and sensory motor command. Therefore high speed position visual servoing will be necessary and more described in following Chapter 5.

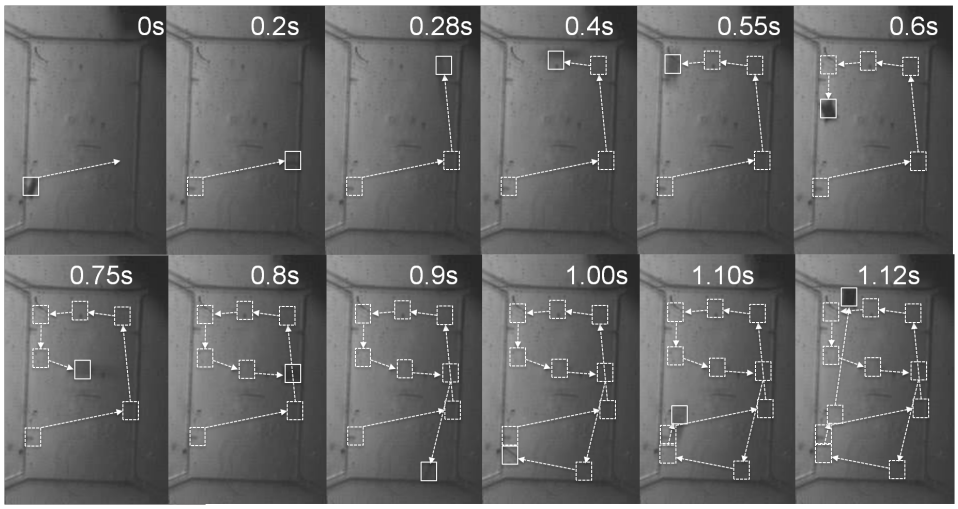

Figure 98: 8 trajectory is achieved in a very fast timing by user's manual teleoperation control using keyboards.

We see on Fig. 98 our time-performance is close from the human vision limits, but still can be improved in terms of control and precision of trajectory.

Adaptation of chip height From experiences from robot manipulation, we notice it can get stuck to the bottom or top surface from the mis-alignement of vertical position of robot to the center axis of electromagnetic coils. Another problem from user generating too fast movements is that it gets stuck on the substrate and or top of the chip. It corresponds to middle scenario of Fig. 96. This vertical motion responsible of a change in physical contact is due either to to the microrobot's symmetrical defects (due to fabrication imperfection), either to its center of gravity position compared to the electromagnets plane. Using different vertical positions of the substrate of the chip compared to the coils axis, we observe an optimized behaviour when it is a bit higher (1-2 mm) than the electromagnets level. As it is difficult to control this thickness with our setup, we use small transparent interface between the chip and the chipholder to change the height of the chip.

If adaptation is done correctly, the equilibrium of pulling forces in horizontal plane function sufficiently well for a controller after few training to get use to the environment physics.

2.2 Magnetic control using uniform field

Uniform field has been mostly used in microrobotics to convert rotating motion in translation using cork-screw propulsion of helical structures. It has recently been reviewed in Xu thesis [89] providing an maneuvering the propulsion speed and direction at several scales with low Reynolds conditions are confirmed. Can we, in our opposed case of an ultra-flat design, use the vertical field for tumbling motion?

Time-response from a static robot The first challenge is to overcome the existing adhesion forces (and of course the gravity, though at this scale and volume of robot, it can be neglected). To do so, we achieve a voltage sweep generating a 1200 ms periodic step. Two responses are observable on Fig. 99 for a low voltage and a high one.

Another important result from the vertical response is the edge in contact with the substrate is fixed. It means adhesion force are sufficient to maintain its position and it confirms scenario II from Fig. 96. This is a key phenomena to convert vertical rotation in translation.

The rise slope, interesting because its dynamics involves magnetic field torque, has two visible regimes when power is not too strong, i.e. 99(top). The first one could be described as

$$\gamma\dot{\theta} + MBsin(\theta) = F_{adh,robot} \tag{56}$$

where θ is the angle with vertical $\mathbf{z}$ axis ($\theta = \pi/2$rad when the robot is horizontal, 0 rad when vertical) M the robot magnetization, B the magnetic flux, and $Fadh, robot$ the unknown adhesion force, because it shows a resistance (due to substrate). It also demonstrates the force decreases quickly with θ. In the other case, the rise is simply a function of magnetic power and viscous effects (we suppose gravity and inertial effects are still negligible compared to forces at stake).

$$\gamma\dot{\theta} + MBsin(\theta) = 0 \tag{57}$$

Fall slope values from Fig. 99 figures are interesting because we observe the free fall to initial position only influenced by adhesion and liquid friction. However it seems to have important variation. It seems that this attraction varies, if we consider the ratio 2 between both time-response.

Principle As there is a substrate resistance from one side of the microrobot robtation, the alignement of the microrobot magnetization toward the vertical component of the magnetic flux also generates a movement toward $\mathbf{x}$. Making a vertical rotating field we can observe the continuous alignement of the robot with the magnetic flux and at least as important a Δx slightly smaller than its length, as seen on Fig. 100

The speed of the motion is the product between $L_{robot}\omega\mu_{sliding}$ where L_{robot} is the robot length toward which is the magnetization, ω is the frequency of the rotating magnetic field and $\mu_{sliding} < 1$ the static friction coefficient.

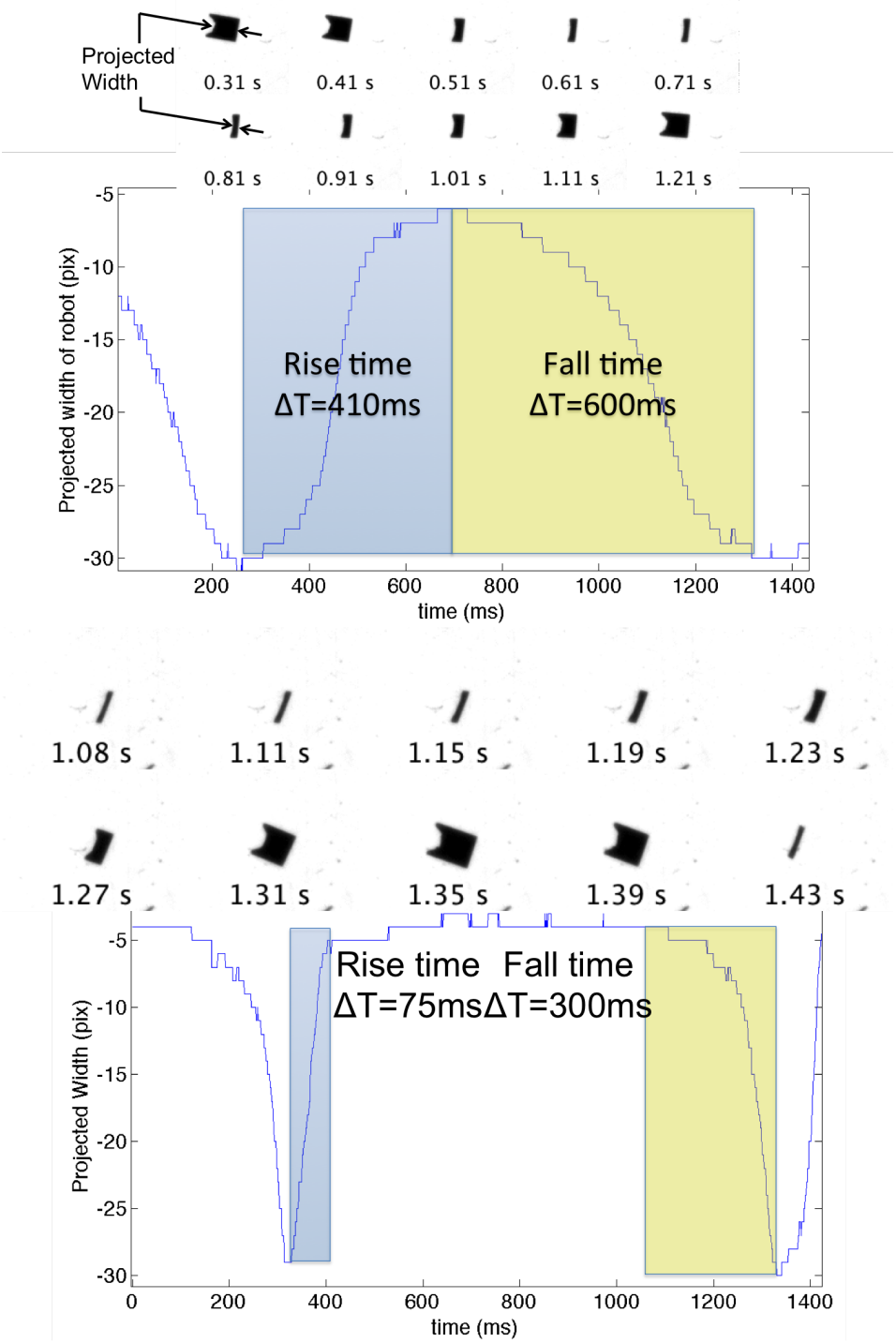

Figure 99: Vertical time-response to voltage step (top) V=2V (bottom)V=9V: the projected width w correspond to $w = W \cdot cos(\theta)$ the projection of the width on the horizontal plane, θ being the pitch angle.

Let notices that two things directly define the speed limitation: adhesion forces and sliding friction. There is a competition between these two phenomenona and both of them limit the performances: adhesion forces, which can be overcome by a sufficient power magnetic power - see section 1.3, phase the robot out of the field and at a certain level, cannot synchronize; sliding frictions become more important as speed increases. Tumbling though, offers several advantages:

— high stability, particularly for user's slower speed
— vertical motion makes the microrobot able to reach narrow width area, as long as the channel depth is high enough

Sliding friction has a tendency to curb higher speed, as μ_s rises and limits the maximum speed.

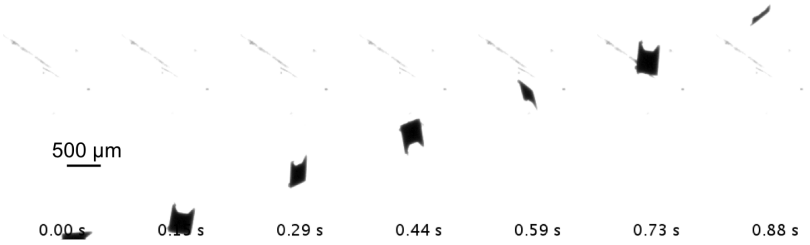

Figure 100: Tumbling demonstration using rotating magnetic field in a vertical plan.

Calibration and steering control From what we have observed in section 1.3 experiences, time-response to overcome adhesion is much shorter in-plane, which could be anticipated. If it is impossible to calibrate vertical field and horizontal field forces over the robot, as adhesion forces are stronger.

It is sill important to calibrate horizontal axes because the direction of the linear combination actually defines the steering angle of the robot. If the horizontal field are not calibrated together, there is a risk to have an ellipse rather than a circle, which gives unnecessary main direction.

2.3 Interfacing: Ergonomy Importance for Manual control

The User Interface is a homemade programmed experimental platform with a GUI on C♯. It allows us to combine the functions of controlling motions, measuring and analyzing them, as synthetized on Fig.101 (left). The low-level mode, used for calibrating devices and analyzing basic motions (rotation and translation in one or combined axis), directly defines the voltage on each coil. The high-level mode, controlled through mouse & keyboard (cartesian coordinate oriented) or joystick (seen on right picture, polar coordinate oriented), is designed for manipulation of micro-objects.

Horizontal motions section is used for rough control using constant input power gradients. Keyboard and joystick control can also be used for finer control, increasing the response to user reflexes.

We compare the three different methods (mouse, keyboard & joystick in speed and precision to control the robot on a simple operation such as a defined trajectory.

Table 26: Ergonomy comparison: of three interfaces using different methods.

Interface	Mouse	Keyboard	Joystick
Coordinate system	Both	Cartesian	Polar
Resolution of control	-	2-5 bits	14 bits
Speed	Poor	Good	Fair

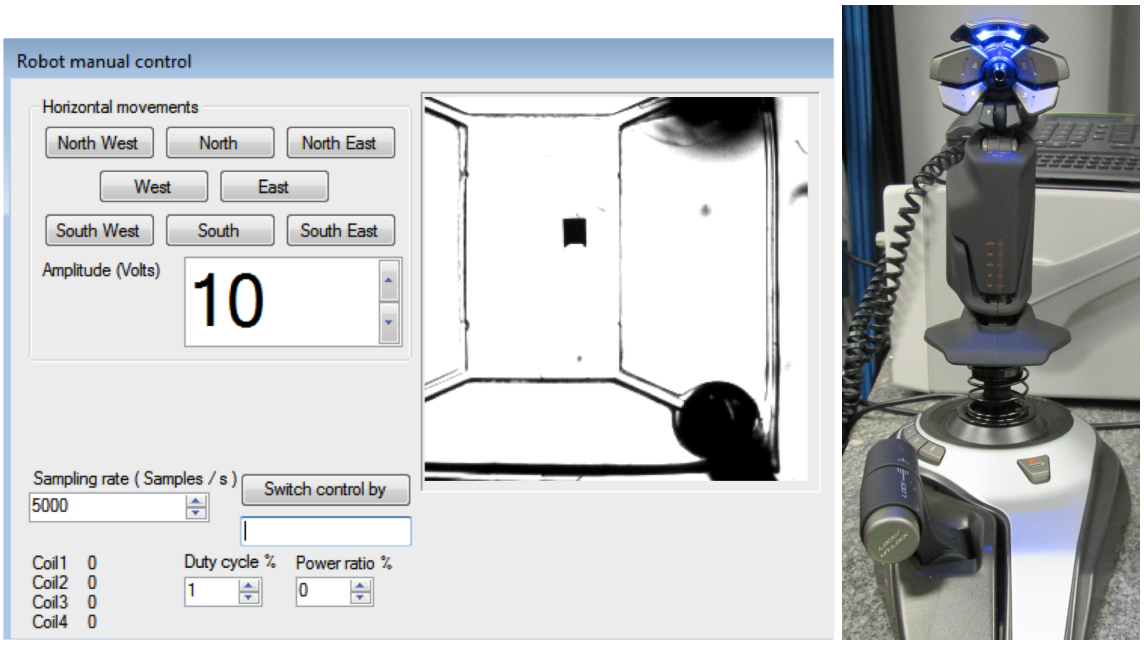

Figure 101: Graphical user interface module developed for different methods of real time control based on cardinal direction for gradient combination. It is one module component of manual teleoperation control to the user interface as shown in the Chapter III.

2.4 Conclusion on methods and toward command corrections

A mobile magnetic microrobot can move with two different modes, they both have advantages drawbacks that are summed up in table 27.

Table 27: Method of propulsion comparison.

Mode	Field type	Field max	Maximum speed	Resolution of control	Stability
Tumbling	Uniform	10 mT	$\approx 20mm/s$	Good	High
Gradient	Gradient	60 mT	$\approx 1m/s$	Low	Low

3 Demonstration of micromanipulation

Being able to manipulate the robot with magnetic forces, it comes naturally to control items with it, using its perfomances to manipulate various scale and structures. We first mention what could be appropriate new micromanipulation strategy. We then propose a new one based on the magnetization of the robot. Finally we demonstrate it experimentally.

3.1 Micromanipulation strategy

As mentioned in the Chapter 1, micromanipulation using mobile microrobot seems to be challenging, particularly when the only action possible is pushing objects as it is the case with

most of mobile microrobot. One of the most challenging micromanpulation tasks is the densly packing assembly of objects in a confined environment.

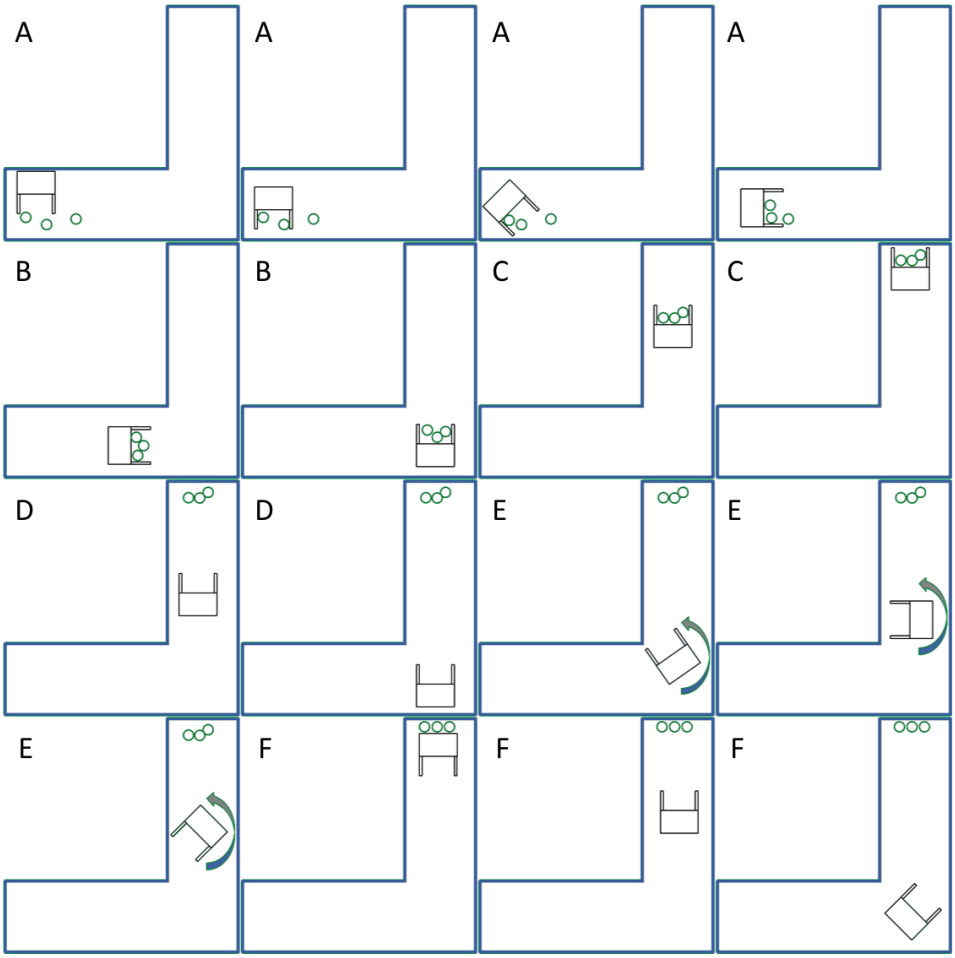

Figure 102: Schematic of MagPol cargo transport manipulation strategy in microfluidic devices: A: collecting particles, B: moving, C: delivery to the target position, D: backward motion reversed polarity, E: change of direction, and F: densly packing assembly by backward motion.

Three different microobjects can serve as target with different properties

— microbeads challenge is to push as much as possible for massive cargo transport
— microbubbles are softer and due to capillarity, have a stronger adhesion. They are more complex to manipulate, can have unpredictable move due to flow or unstable position, and they are closer from biological objects
— right triangles can be densely assembled and requires a high level of precision to densely assemble them in a microchannel

We propose in Fig. 102 a method which has the advantage of combining arms to stabilize objects and accomplish a precision work at the end using the backward edge of the robot. This method is mainly based on the robot ability to be able to control robot's motion.

3.2 Reverse magnetization

What we have previously observed from the experiences in subsection IV.1.3 a competition between the magnetic torque and the pole inversion of magnetic moment. With one of the

Helmholtz pairs, we have previously found the threshold to be around 9V which corresponds to $5mT$. This value is difficult to reproduce on other setup because it is functions of material quality [163]. As it varies widely with electroplating, the range of value varies importantly . Knowing properties from ferromagnetic material in IV.1, we can extra we can depict with Fig. 103 the different configuration of magnetization.

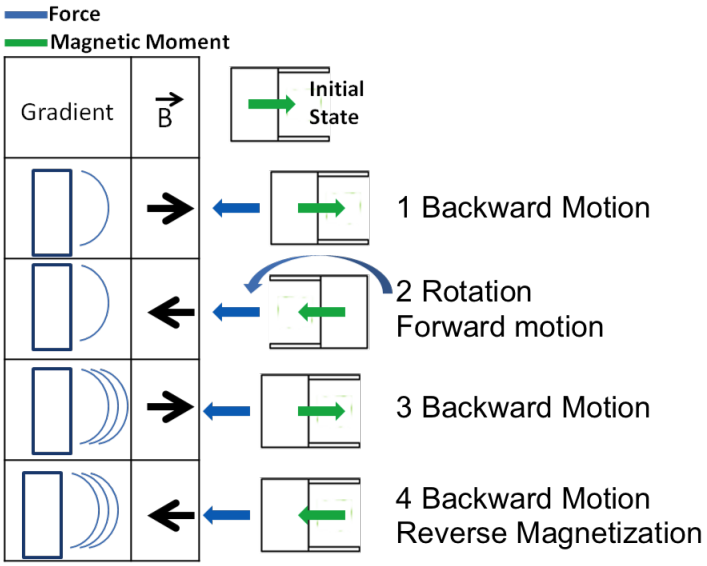

Figure 103: Magnetic microrobot truth table of its magnetization; threshold between strong field and weak field corresponds to the coercitive field.

If the field is sufficiently high and opposed to the magnetization (case 4 of Fig.103), it can outreach a coercive field ($B \geq H_c$) and reverse the magnetization of the ferromagnetic material in the opposite direction, without any angular variation of the orientation. Else, because of an unstable equilibrium, it aligns to the new field, doing a π rad rotation.The different possible combinations in Fig.103 truth table, we suppose our robot initially magnetized (by the low power field) in the direction of robots arms. We generate a gradient in the direction of the robot and observe several possible movements summed up in our graphic. Case 2 corresponds to the π rad angle rotation, case 4 to backward motion by reversing the magnetic moment of the microrobot. We noticed there is only a limited number of polarity directions depending on the shape of the robot which allow exclusively backward and forward motion (no swaying). Further study on a bulk shape could be done to confirm that. It allows the controlled backward motion, one of our key points for manipulation.

3.3 Manipulation using backward motion

This new strategy allows to achieve manipulation and assembly of microbeads in a channel as displayed on Fig. 104, illustrating the last phase F. This is a particularly important result as we could fear from the small size of these beads (here $50\mu m$) that they would climb over the microrobot, its thickness i.e. contact zone with the beads being very thin. It seems like adhesion forces have a tendency to stabilize the beads on the substrate too.

Control precision allows to achieve every phase with enough force for microbeads. Reverse polarization allows to achieve backward motion (Fig.104, 1^{st} and 4^{th} combination) in a

confined channel or to pull the robot back after placing an object without necessarily make a complete turn. It also allows to work with the opposite face of our robot forward, in our case more adapted to push densely the grossly assembled beads. We observe immediate backward motion, with same energy than formard movement, to move 5 beads at the same time, being limited by the size of the edge. Speed being quite high ($0.5mm/s$) with this load, kinetic energy is sufficient to move more dense object.

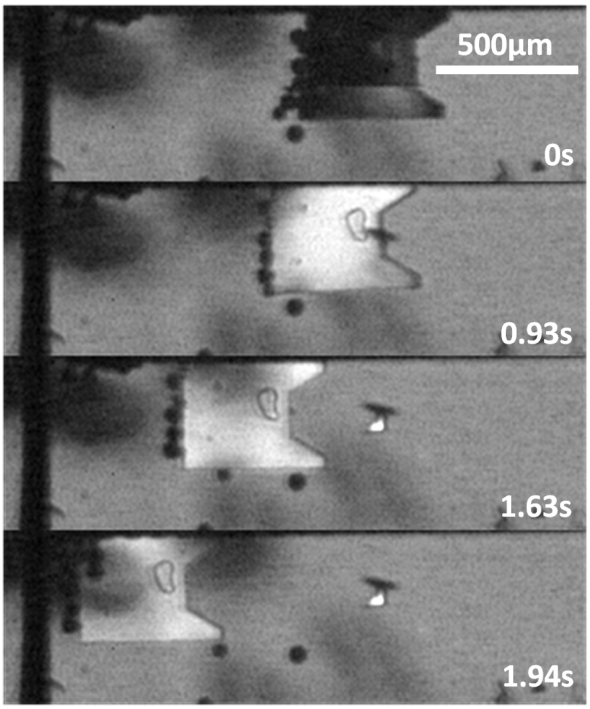

Figure 104: Backward manipulation and assembly of $50\mu m$ microbeads in $\approx 2s$ on a 1mm distance of microchannel.

Many geometries can be tested with beads and it is also important to try backward and forward pushing on softer object. Bubbles is a fitting candidate which brings us closer from biological objects and which are strongly in capillary interaction with walls of the chamber We see on Fig. 105 both direction are able to steadily displace the bubble.

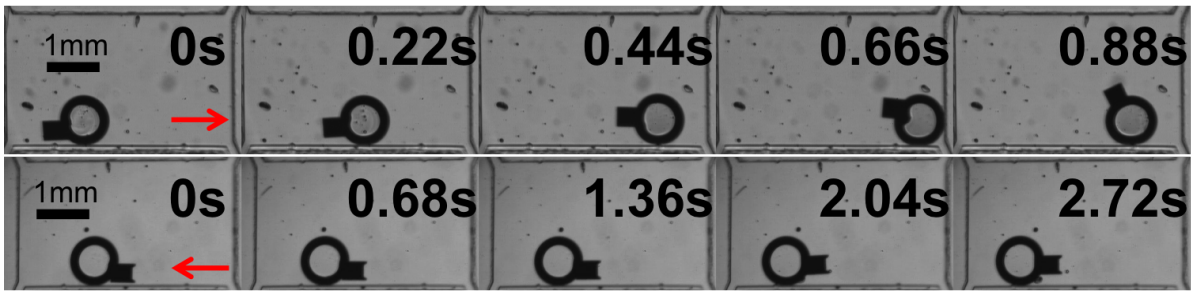

Figure 105: Bubble manipulation backward and forward comparison.

4 Conclusion

Though using gradients is the most instinctive way of moving the robot, during operation by users, it can meet two kind of problems. The first one has been mentioned and is the very high speed of robot's motion. The minimum force required to intiate the motion of the robot drives it already too fast (low inertia implying very high accelerations). The second is a consequence and is that under a too strong force, vertical component might be too strong and block the robot on the substrate, making even small movements impossible.

Next step could be manipulation using rotating vertical field combined with direct pulling to complement each other's movement, particularly in condition where the objects can easily get stuck on a wall. As an ultra-flat microrobot, MagPol could interpose between targeted object and wall surface. The challenge would first to create a magnetic setup combining gradients and uniform magnetic fields. One possibility could be to decouple the control of each pair of Helmoltz coils.

Part V

Visual servoing of MMM

Summary

Previous chapters have built a microrobotic platform and demonstrated that one single robot was operable. From this, a wide range of localized actions - including ultra-fast propulsion efficiency (Ch.2), local environment sensing (Ch.3) and cargo transport micromanipulation (Ch. 4), could be considered. To impact experimental biology and get closer to applications:

- *a critical amount of the forementioned transducing operations can be necessary*
- *a sufficient speed / precision ratio must be reached, as the window of opportunity of certain phenomena and the dynamics of the robot can be too fast for user(human visual system speed of processing being around 500ms [164])*

One possible angle to develop high-throughput systems with mobile micro agents is to use multiple control and develop a swarm strategy. But the speed/precision ratio gets worst as controlling several agents necessarily increases the algorithm complexity compared to a single one. And this supposes we are able to control each agent separately (which is not the case with magnetic fields only)

Automating motion of a single robot in a liquid environment can drastically increase the throughput of microscale operations (manipulation of micro objects, and sensing in liquid). Being able to precisely control one of them, high dynamics control could lead to equivalent action of a swarm as well as overcoming instability from adhesion issues.

We first detail our planned trajectory control law. We propose a fast imaging algorithm allowing from a single camera the 2D visual servoing of the robot. The architecture of our program needs consequently a small summary. To confirm this approach experimentally, we have defined cycles of a typical 8-trajectory inspired from ICRA mobile microrobotics challenge and observed precision and repeatability, using our knowledge from robot's dynamics to obtain the best experimental conditions. We conclude by a discussion considering further improvement.

1 Visual Servoing

Having performed post treatment analysis through previous sections experiences, it is natural to close the 2D control-loop using tracking algorithms. We first introduce the control law we use and its simplifications. As we are aiming for a high sampling($\approx 200\mu s$) rate in our loop, it requires a fast tracking algorithm for real-time treatment, which will be detailed in this section as well.

1.1 Control Law

This system law is based on dynamic Look and Move control [26], synthetized on Fig. 106.

The term dynamic means we run in parallel the vision part and the actuation. It requires a specific care on the difference of rate between two, but provide faster time-response. It consists in positioning to a desired situation $\mathbf{r}*(t_n)$ a microrobot in the position $\mathbf{r}(t_n)$, evaluating at each iteration t_n a same visual feature. In our case, this is the gravity centre. It is the simplest feature we can find (a point) but has the disadvantage to not offer a control on the orientation.

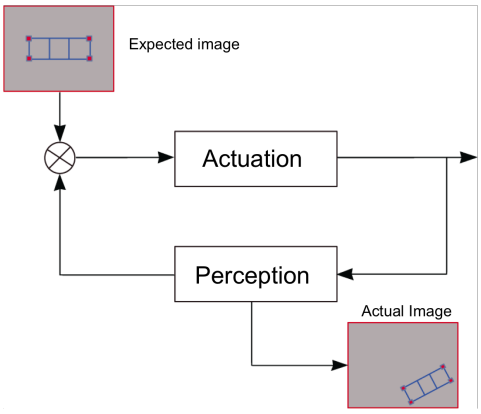

Figure 106: Look and move servoing, deeply described in Espiau et al. article [26].

Another important difference compared to standard microrobot control as described in Tamadazte thesis [73] is that we work with a mobile actuator but an immobile camera, which simplifies the computing and the formalism to describe it. To better understand what is at stake in the control of the robot, it is important to go deeper in the description of the block diagrams, as we mix discrete-time transfer functions for the vision treatment with continuous-time ones in the analog electromagnetic circuit, see Fig 107 where all the parameters are bidimensionnal, F being the magnetic force, I the current in the electromagnetic (EM) device, V the voltage command from the DAC to the amplification system, r^{ast} and r respectively the expected and actual position, $e = r^{ast} - r$, and m the pixel matrix constituting the feedback image.

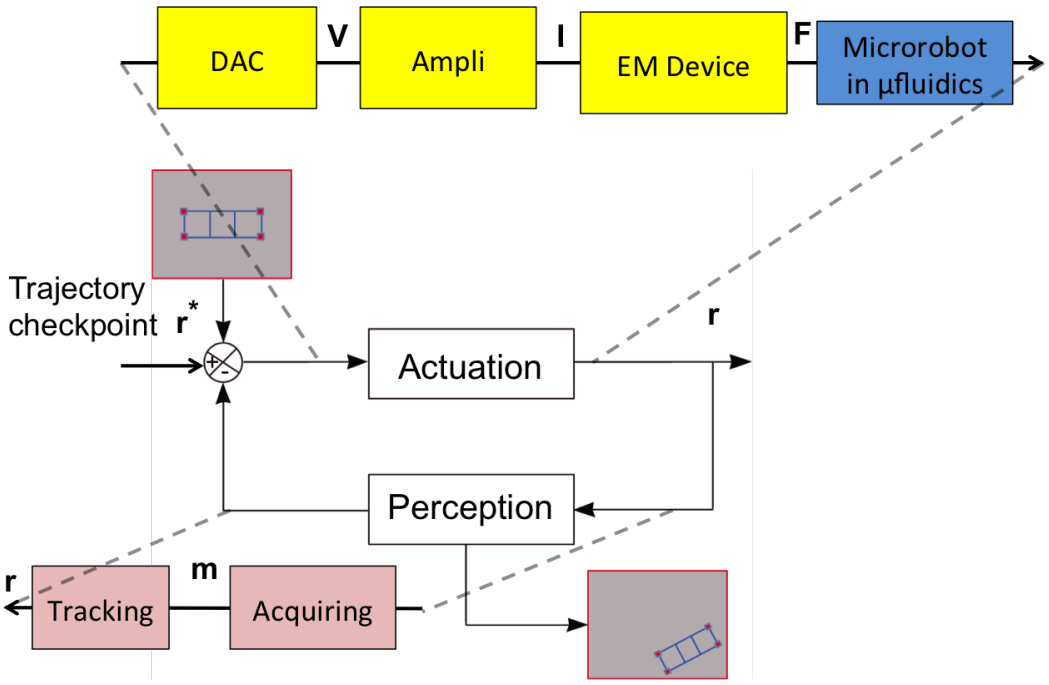

Figure 107: Block-diagram of the visual servo control of the MMM.

Several approximations, based on previous sections, are made in our model and need to be underlined for later interpretation. We also remind the reader that we work in-plane and all our vectors have 2 components. Considering what have been studied in this scale:

— DAC + Amplification circuit set can be approximated, with a sufficiently high sampling rate - refer to Chapter II section 3.4 for further details on the intensity regulation mode, to

$$\frac{I}{e(p)} = \frac{K_{elec}}{pL+r} \tag{58}$$

L and r being the inductance and resistance of the coils and K_{elec} the amplifier gain depending on its configuration. Supposing the amplifiers remain in linear regime, this block can be summed up as a low pass filter limited mostly by the inertia of the coils.

— Electromagnetic forces over the robot requires several strong hypothesis: we suppose a constant gradient only toward their axis direction $\mathbf{F_{mag}} = F_{mag,u}\mathbf{u} = \nabla\mathbf{B}.\mathbf{u}M_{s,robot}\mathbf{u}$, $\nabla\mathbf{B}$ and $M_{s,robot}$ being respectively the magnetic flux gradient and the saturation magnetization of the robot, u being the direction of the electromagnet

— MMM ferromagnetic material is always in saturated regime $\mathbf{M} = \mathbf{M_s}$ and with ideal symmetry so it does not generate movement in other directions than the axis of the coil $\mathbf{F_{mag}} = K_{mag}\mathbf{I}$, K_{mag} being the global electromagnetic gain (constant, supposing the gradient uniform) and $\mathbf{I}$ being the current going through the electromagnetic setup

— microfluidic chip only generates a strong viscous drag, and inertia of the robot can be neglected so that $\mathbf{F_{mag}} = \mathbf{F_{visc}} = \beta\mathbf{v_{robot}}$ which from what is said previsouly implies $\mathbf{F_{mag}}(p) = K_{fluid}\mathbf{r_{robot}}(p) = F$, beta being the translational viscosity drag coefficient. Though we have clearly seen from previous section adhesion forces are non-neglectable in static regime, we suppose it to be neglectable in dynamic regime, i.e. during a trajectory control.

We then sum up the theoretical model of our analog open-loop chain as the following transfer function

$$\frac{r}{e(p)} = \frac{K_{elec}}{R+pL}\frac{K_{fluid}}{p} \tag{59}$$

We now need to detail what consists in the feedback loop of our visual command and demonstrate it is fast enough to extract the robot position.

1.2 Comparison between expected position and measurement

As a reminder from chapter II, one important property of the Dome setup is to generate magnetophoretic forces in any direction of the plan, thanks to linear combination of the gradients. As a consequence, the force generated by the electromagnets are necessariy attractive. A change of sign in the commanding voltage and consequently, in current and magnetic field polarity, only changes the torque then the orientation of the robot.

In terms of control law, the comparator is not exactly a simple substractor:

Algorithm 1.1: COMPARATOR$(r*, r)$

comment: One-dimension, here x, test

if $x* - x > 0$

then $\begin{cases} V_{x^-} = 0 \\ V_{x^+}(p) = C_-(p)(x* - x)(p) \end{cases}$

else $\begin{cases} V_{x^+} = 0 \\ V_{x^-}(p) = C_+(p)(x - x*)(p) \end{cases}$

We notice the voltage input is always positive. The adopted terminology try to be coherent from precedent model, V_{x^-} and V_{x^+} defining the voltage input on x^- and x^+ electromagnets and C(p) is the eventual correction we use. In all the study done here, it is a proportional gain with a boundary $\leq 10V$.

1.3 Realtime position tracking by fast position tracking

One important condition is required for using a visual information in visual servoing: the existence of a vision algorithm detecting the information, with a fast enough time response to remain below the command sampling rate (defined by the maximum between camera sampling rate and the electrical circuit). We then develop tests on a simulator and demonstrate its performances.

Vision algorithm Our precedent instrumentation efforts have significantly simplified the observed scene as:

— The camera always have the same position
— The contrast are optimized for a high signal to noise ratios
— The vibration are minimized by an anti-vibration table

The tracking algorithm can be summarized in the following pseudo code 1.2. It analyses every new frame and provide in case of success the current center of gravity or a error message in case of failure. Object frame contains a function returning pixel intensity Frame(i,j) and Frame.x Frame.y properties are the dimensions of the acquired frame. Enl defines the enlargement of the region of interest (ROI) in which the next position of the robot is searched. λ_1 and λ_2 are the contrast threshold by which we can eliminate texture different from the robot's. S and C are parameters defining the reference value of area and perimeter of the robot, ε_C and ε_S the tolerance interval length to narrow shape detection and selection.

Algorithm 1.2: MINIMAL TRACKING($Image, Frame, Enl, \lambda_1, \lambda_2, S, C, \varepsilon_C, \varepsilon_S$)

comment: Is the position of the robot known?

if YES

then comment: The Region of Interest is a rectangular neighbourhood centered on the robot

$$\begin{cases} ROI.x = Enl.x \\ ROI.y = Enl.y \end{cases}$$

else comment: The Region of Interest is the whole frame

$$\begin{cases} ROI.x = Frame.x \\ ROI.y = Frame.y \\ CoG.x = Enl.X/2 \\ CoG.y = Enl.Y/2 \end{cases}$$

comment: Segment collection and sorting

$$\textbf{for } j \leftarrow Frame.y/2 - CoG.y \textbf{ to } Frame.y/2 + CoG.y$$
$$\textbf{do} \begin{cases} \textbf{for } i \leftarrow Frame.x/2 - CoG.x \textbf{ to } Frame.x/2 + CoG.x \\ \quad \textbf{do} \begin{cases} \textbf{if } \lambda_1 < Frame(i,j) < \lambda_2 \begin{cases} \textbf{if } curseg = 0 \\ \quad \textbf{then} \begin{cases} curseg = 1 \\ segment(curseg) = (i,j) \end{cases} \\ \quad \textbf{else} \begin{cases} curseg++ \\ segment(curseg) = (i,j) \end{cases} \end{cases} \\ \quad \textbf{else} \begin{cases} \textbf{if } curseg > 0 \\ \quad \textbf{then} \begin{cases} curseg = 0 \\ segmentcollection += segment \end{cases} \end{cases} \end{cases} \end{cases}$$

comment: Shape selection

$$\textbf{if } shapecollection.size > 0$$
$$\textbf{then} \begin{cases} minshape = frame \\ \textbf{for } k \leftarrow 1 \textbf{ to } shapecollection.size \\ \quad \textbf{do} \begin{cases} shape = shapecollection(k) \\ \textbf{if } \mid shape.surf - S \mid < \varepsilon_S \,\&\, \mid shape.contour - C \mid < \varepsilon_C \\ \quad \textbf{then} \begin{cases} \textbf{if } minshape.surf - shape.surf > 0 \\ \quad \textbf{then } \{minshape = shape \end{cases} \end{cases} \end{cases}$$
$$\textbf{else } \{ERROR$$

comment: Selection

This algorithm speed is typically quadratic($\mathcal{O}(n^2)$) as it consists in a two-dimensional array analysis. It depends only on the frame size, and the only degree of freedom is minimizing the frame sizes and the operation per pixel. The initialization requires drastically more time. The result of the algorithm returns at least the center of gravity features (CoG_x and CoG_y), and eventually more like the whole surface detected and contour.

Notice that we have also access to moments for a neglegible cost, which in case of sufficient symmetry gives us access to orientation without edge detection [165], as mentioned in chapter III.

This algorithm was the result of a sufficient experimental effort and is very severe in terms of preliminar hypothesis: we know the shape of the robot, no other items of equivalent size must enter the chamber. The border of the microfluidic chamber as well can generate wrong results of the tracking. It can be graphically summed as follow in Fig.108.

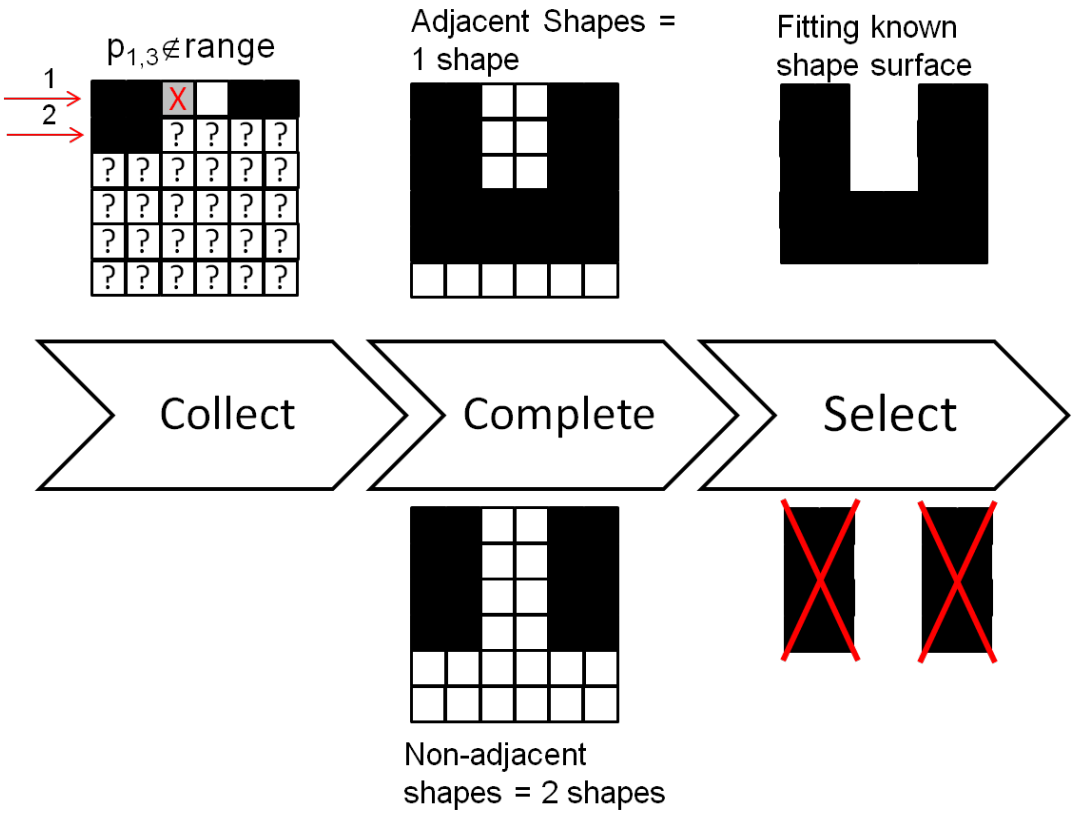

Figure 108: Tracking Principle, three phase are necessary to detect the right shape: (left) segment collection (middle) shapes detection (right) best shape selection.

Graphical User Interface As we have several parameters to adjust and adapt it to changes of contrast and size, it is important to use an adapted graphic interface Fig. 109 for the user.

We make the correspondence with the input of the algorithm1.2 The high and low threshold respectively correspond to λ_2 and λ_1. Contour (optional) and surface criteria are defined by their dimensions and tolerance, and the shape detected can vary (to cover wider possibility of design). Finally, tracking enlargement define the rectangular perimeter sizes in which we research next visual feature, centered on previous position.

Notice that it is possible and useful to display the contour, surface and mire to see the different feature and have a visual confirmation of the tracking accuracy and stability. For real experiments calibration, it is important to verify as a second confirmation our parameters allow a sufficiently wide variation of lighting. As the light fiber is a gaussian distribution, there are spatial variation of contrast even though our lens increase the variance (width) of this distribution.

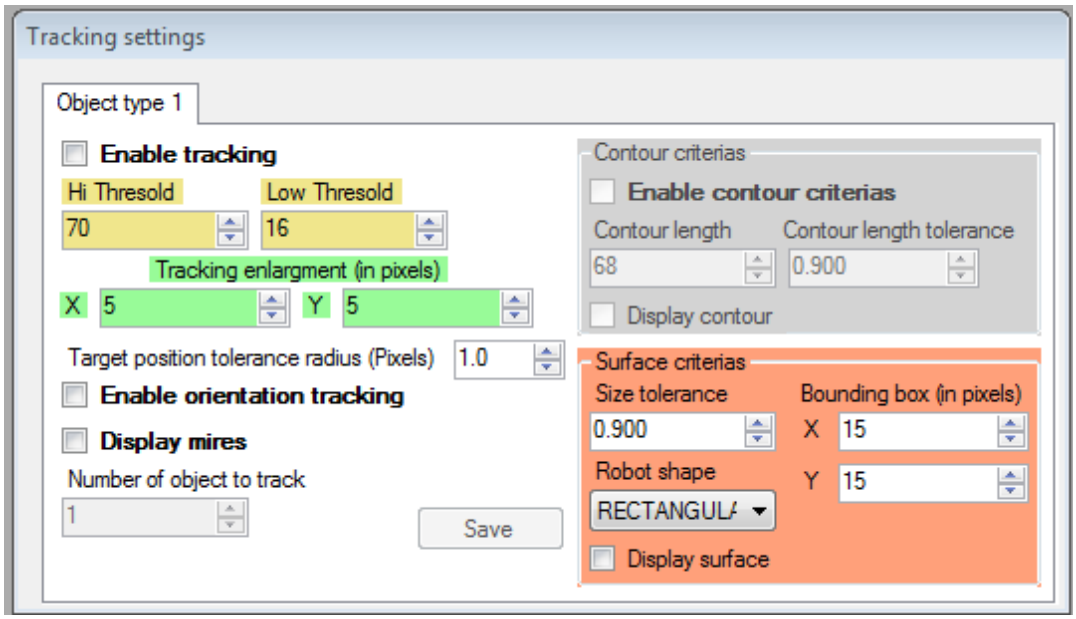

Figure 109: GUI frame used for parametrizing the tracking.

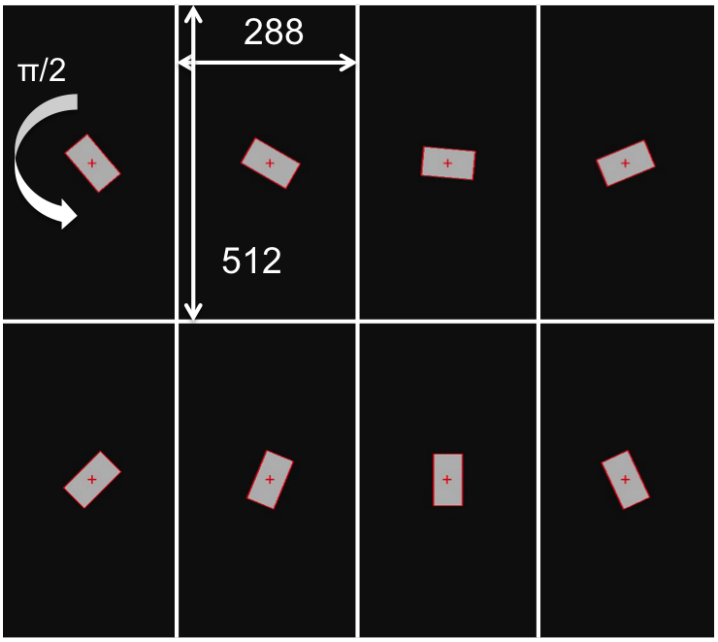

Figure 110: Tracking tested on a simulator.

Simulator It is important to first demonstrate the tracking performances over a simulation on a generated image, in our case - see Fig.110- a rotating rectangle. This rotating rectangle is generated virtually by C# libraries and measurement is achieved between the three phasis described in Fig.108.

We can display the contour as a red perimeter, the covered surface in transparent blue, the center of gravity red cursor, all of them fitting precisely the template shape of the simulator on a sufficiently wide range of contrast.

Simulation allows to repeat a high number of time the same algorithm on an identical ideal

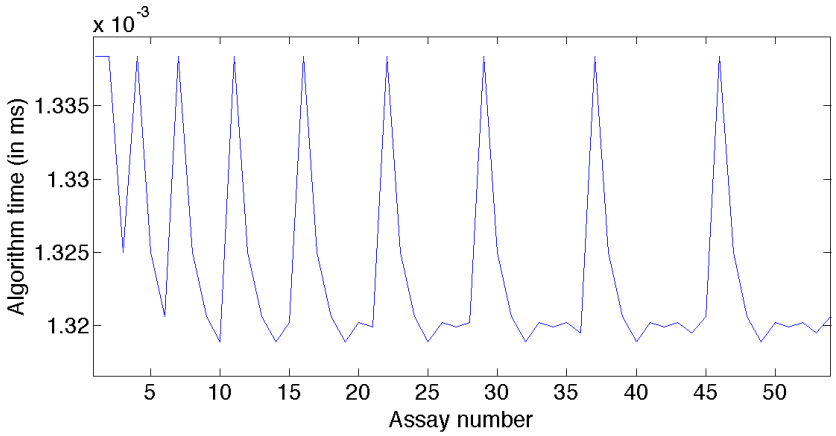

Figure 111: Plot of tracking temporal performances and precision.

image and deduce the statistical performances, as it varies with the computer's process status. The performances displayed on Fig.111 were tested in a worst case scenario where the robot's previous position is not known, simulated robot's dimensions $70 \times 70 pix$ are quite important as well as the frame dimensions -$512 \times 512 frame$. It shows how another thread managed by the computer periodically disturb it. We can also conclude that with this size the global time of the algorithm is around 1ms, which means it is sufficient to reach $200 \mu s$ bound for dynamic tracking with a region of research reasonable enlargement. We will also reduce the size of the frame for safer conditions.

The Fig. 112 displays a not optimized non-uniform contrast. The robot remain tracked, even when close from borders which are critica situations for the tracking algorithm, as segments are connected.

2 Path planning control

Different ways to control the input of our command loop can be achieved, from real-time servoing using a controller to preliminary defined trajectory. We show here how a continuous preliminary trajectory can be simply defined by users then converted in terms of command. Then we detail how we procede to achieve a parallel treatment using multi-thread programming.

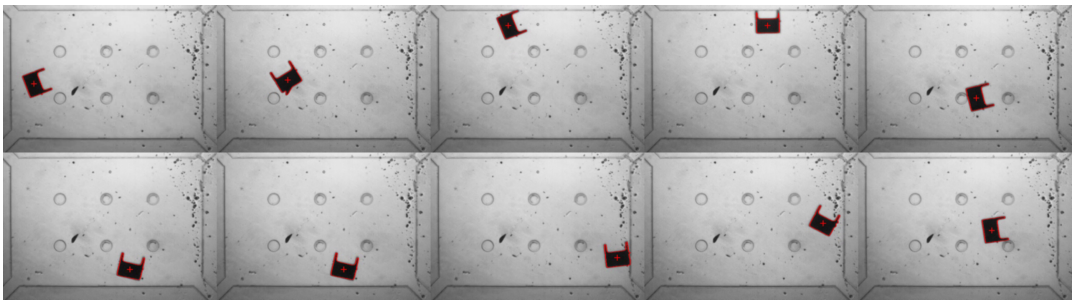

Figure 112: Tracking proof on an non-optimized contrast.

2.1 Path definition and approximation

The path can be defined by interpolation or approximation. We extract here a picture of current position of the robot to clearly define over it the required trajectory. We use control points defined by a user using a dedicated GUI and obtain a piecewise-defined path - see Fig. 113. Once aquired the path can be saved and reloaded for saving time or simply repeat

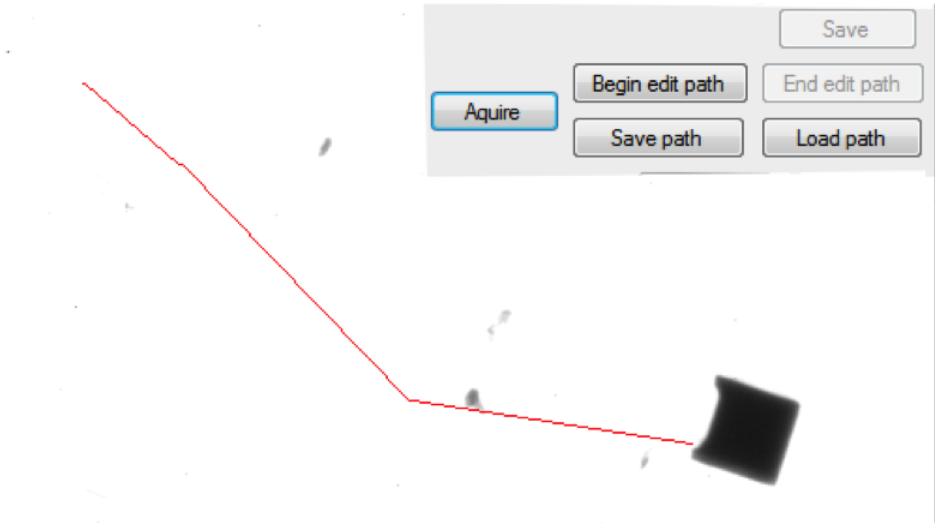

Figure 113: Path definition: image of the robot can be refreshed pushing acquire. It serves as a reference for position, defined path is in red.

and compare performances.The program does not automatically refresh image to minimize ressources from the CPU, it is then up-to the user to refresh it before defining a new trajectory. During the run, nothing is displayed as the performances observation with a 30 frame/s display. Instead, a non-encoded video and a table are saved on the disk, when target is reached.

2.2 From path to command

Several conditions can be defined to respond to a commanded trajectory [166]. If in our case, we aim to achieve a speed demonstration, it could, with a different context, be constrained in terms of precision in space and time. It is important to still provide boundaries in speed (i.e. voltage) to avoid too brutal forces on the robot and overheating on linear amplifiers, which heats up easily.

One other key issue is how we define the different passages. We use a pseudocode description 2.1 again to describe it.

Algorithm 2.1: PATHTOCOMMAND$(Path, i, CoG, \varepsilon)$

comment: Compare the distance with current control point and ε

if $\| Path_i - CoG \|_2 < \varepsilon \& i = Path.size$
then $\{ Endoftrajectoryori = 1$
else if $\| Path_i - CoG \|_2 < \varepsilon \& i < Path.size$
then $\{ i++$

The path is a list of points and i is the positing on this list. CoG defines the robot's center of gravity lastly evaluated. ε is the radius of the circle in which we consider the destination to be reached.

2.3 Multi-thread programming

As suggested at the beginning of this chapter, the robot look and move control run in dynamic mode. The multi-core architecture allows to attribute one thread per core i.e. allows them to work in parallel.

We sums up in the following graphic 114 how is the time management

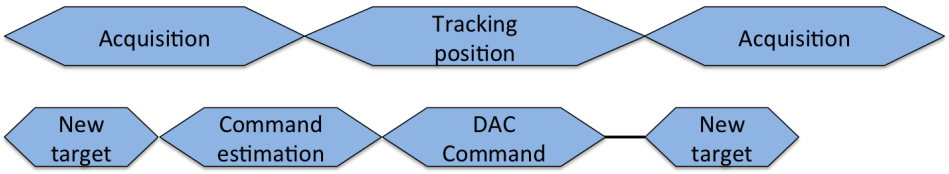

Figure 114: Graphic architecture of the multi-thread program

The most time-expensive part of the vision chain is the tracking, itself most expensive part being shape detection.

Hardware A hardware minimum configuration is important for the process of each image but not only for tracking purpose. CPU speed will allow to directly reduce the tracking time and other operations, but increasing the number of core is also improvings to have more threads. We must not forget to have a sufficient RAM (random access memory) space to record the entire sequence and a sufficent data rate. We use a standard Pentium (R) D architecture with a 2.80 GHz CPU equipped of 2 Go de RAM DDRAM 3. As it is a quite minimal configuration, performances of our feedback control could be easily improved.

3 Automated plannified trajectory: Observed dynamics and corrections

Now that we have defined command law and visual servoing, we experience the performances of the system. We first need to facilitate the interface for user to run and adapt parameters quickly.

3.1 GUI Parametrization

The functionalities of the GUI displayed on Fig. 115 allow to minimize the other thread during performances. We can refresh the image manually by pushing capture button on the left, while displaying from frmView is ticked off. Notice that the frame rate written in frmView does not correspond necessarily to the one used, as it is a minimum between the sampling rate and the maximal frame rate according to the camera parameters. As mentioned

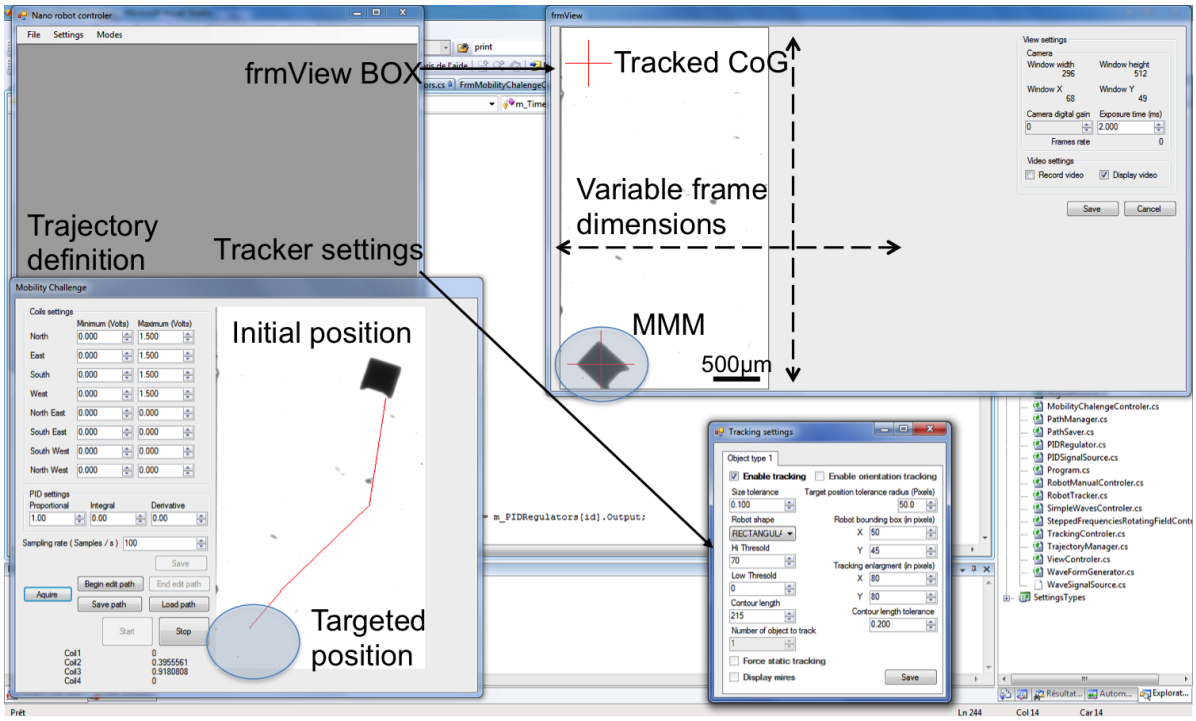

Figure 115: GUI ensemble to proceed to an automated trajectory.

in previous section 1.2 of this chapter, we define boundaries on our voltage outputs to coils, equivalent to limit the maximum speed. Though a proportional corrector exists, we have not implemented at this time other component I and D of PID as the system already has an important order and does not require more integration.

3.2 Observation

Several preliminary issues can be apprehended and avoided thanks to chapter III and IV observations on dynamics, and correction of section V.1.1 model

— brutal interruption of motion due to a change of contact between robot and substrate.
— saturation mode in linear amplifiers. A 5V boundary avoids any saturation on every axis and conserve a relatively important power

We observed a repeatable 8-trajectory in a relatively long completion time $< 1s$. We make repetition possible by looping the control, i.e. doing an infinite cycle from the path list.

We here clearly see the problem coming from the horizontal axis, and a specific proportional gain might reduce this instability.

3.3 Correction generating interruptions

Though several issues disturb the system ability to repeat the same trajectory with precision and speed, there exists solutions to overcome each of them. The first one comes from the substrate. It might be interesting to complete our understanding of adhesion perturbative forces with the following description on Fig. 117.

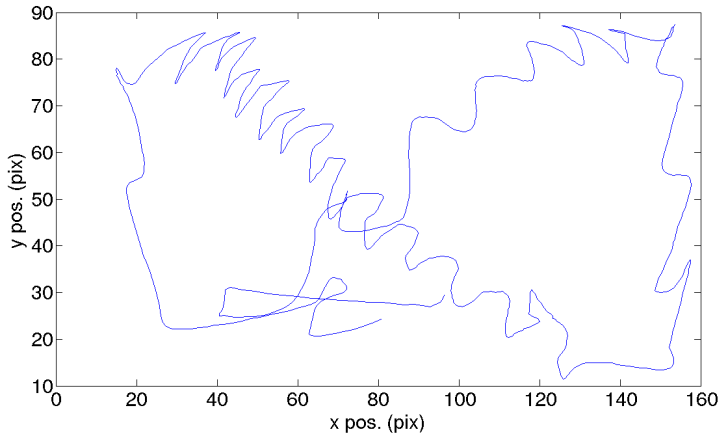

Figure 116: Sequence of a 8 loop trajectory with unstability of the robot.

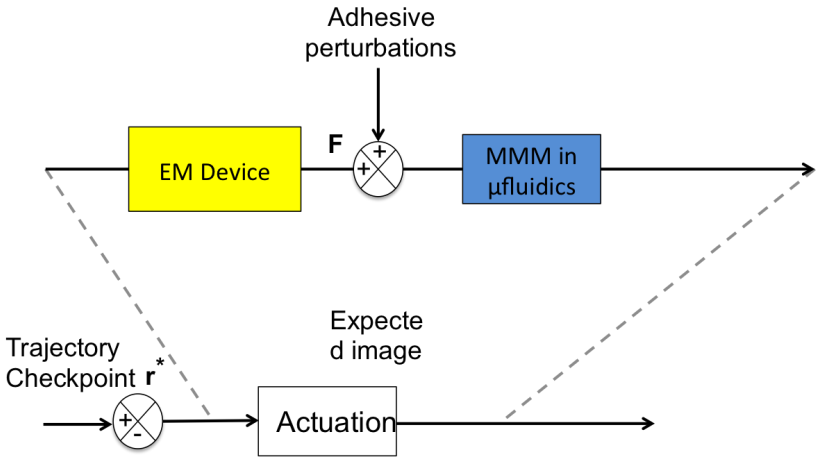

Figure 117: Adhesion forces are perturbation located between the electromagnetic device and the microrobot.

Observation from chapter III and IV shows that these are particularly important when
— robot is immobile
— orientation of the robot is tilted

In any case, the force is singular, its amplitude vary with experimental conditions and place on the substrate. It is then very challenging to deduce an analytical model or try a blind (with no idea) correction (typically proportional-integral-derivative controller). As mentioned in chapter IV, there is a transition time between the perturbed regime and the free regime. Most of the time, the blockage happens during the trajectory due to a tilt from the robot. Increasing the power is a wrong reaction as it will put more pressure on the contact now engaged with the substrate. Instead, by generating a same order of time interruption, the robot contact get loose enough to restart motion. This problem can be solved by generating interruptions in the signal or adaptating the position of the substrate surface compared to the coils plans. The problem of this solution is we abandon the characteristic time of our microrobot to get back to standard contact between itself and the substrate. It leaves us to important problem of development and engineering to improve the performances of the system.

Another issue is oscillation instability. They are mostly due to a to strong response from the coils to robot's position shift, which makes the position impossible to adjust. We use a

proportionnal correction on the two electromagnets and deduce the following curve Fig. 118. This proportionnal correction can be compared to a scaling factor. It can be optimized by

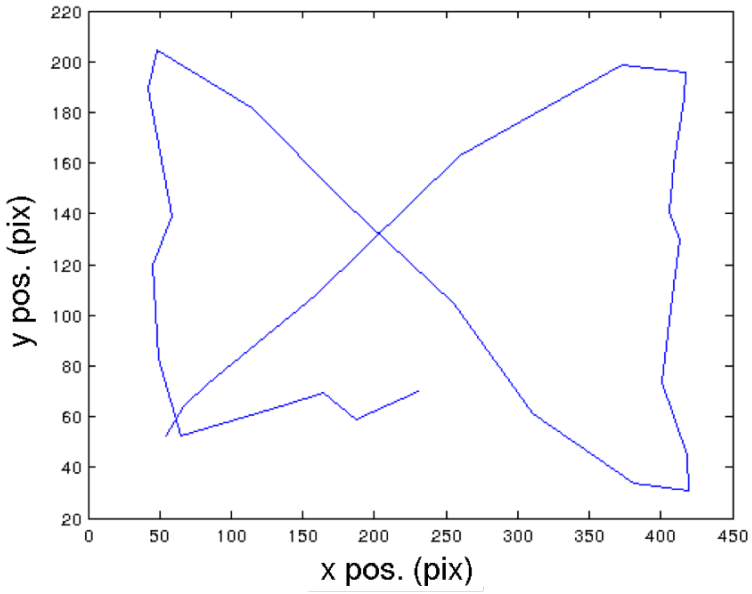

Figure 118: Sequence of a 8 loop trajectory achieved including regular.

checking the displayed completion time until reaching an extremum.

4 Summary: Toward Semi-automatic mode: haptic

What we have achieved in this visual servoing chapter is milestone result with simplistic methods. It is in an important goal as we reach complex trajectory under 1s time. It opens-up to several questions and development tracks, among them the quantitative study of a correction making the system robust to a wider range of experimental conditions.

We have talked about the parametric future optimization, but let's not forget that users seek for different method of control. In particular, as we aim to develop the microrobot for minimally invasive surgery, it is important to talk about the possibility of real time control. Though it requires more responsivity from user, manual control using visual feedback can be more stable and precise. Next-step would be to detect other items so we can estimate the distances and provide a force feedback with a haptic device.

This would compensate the reactivity issue from the user allowing a real time trajectory control and correction. It would be also very profitable for micromanipulation, with or without force feedback.

*Conclusion and perspective When I arrived at LPN, mobile microrobotics activities were starting and few experiences existed inside microfluidic chips. The MagPier design, resulting from a collaboration with FEMTO institute and ISIR since 2009, had just started to be integrated into chip. It displayed fast dynamics in dry environment but was not particularly controllable in liquids: too high $\frac{friction}{actuation}$ force ratio, less optimized shape and fabrication process. The control was based on a microcontroller or rudimentary programs without thread management and user interface, no integrated sensing functions and no visual servoing algorithm. This context gave me a wide range of possibility to explore and important degrees of freedom. I decided studying visual servoing and transducing of ultra-fast mobile microrobots in microfluidics with -complementary magnetic actuators, dome and helmholtz setup.

This research has been achieved thanks to a strong technological development, made possible thanks to the exceptional framework, i.e. manpower and machine, that LPN constitutes. Parallel efforts have been done in bibliographical work and in a biomedical training at Institut du Cancer Gustave Roussy in order to grasp the advantages and drawbacks of microrobotics offered to biomedical applications, and how we could position our system. The principal technological steps that have successively constituted my path were:

— a mobile microrobot integrated in PDMS-chip technology able to achieve high dynamics operations
— an experimental platform optimized for mobile magnetic microrobot control through magnetic waves with a sufficiently wide range of power and precision for characterisation
— a multi-thread programmed platform with high sampling rate imaging, facilitated interfacing with user, allowed RT tracking algorithm

This is on this technological foundation that my three principle axes of research have been based on. As a conclusion of this thesis work, we draw up the progression and perspective of these three thematics. We try to provide on each a synthetic list of our achievements as well as guidelines for further progression, in a subjective order of priority.

Mobile microrobots for in-vitro sensing We have first demonstrated the dynamics capacities of our devic - i.e. a Magnetically actuated Mobile Microrobot's capacities of propulsion at low Reynolds number microfluidic environments, introducing first an original design of ultra-thin polarizable mobile micro agent. The performances of this mobile agent are also the result of a global electromagnetic system driven by a computer. A great care has been taken to the development of magnetic actuator, optimized electrically and closely located to the sample. The microfluidic chip has allowed to work in a controlled liquid environment with a control over key physical parameters.

What have then been at stake is to analyse dynamics of robot to be able to quantify and compare its kinetic performances and upgrade the design - the first half of our virtuous circle of development. The surface walls of microfluidic chambers responsible for the adhesion effects needed to be understood to be integrated to our physical model then overcome. The experimental tool developed and the precision of algorithm have confirmed some expected phenomenon related to low Reynolds number. Examining rotation and translation, two complementary fundamental motions, we have understood and improved our comprehension of Mobile Magnetic Microrobot(MMM) motions. Moreover, all the data we have on the robot can be related by linear relations to physical parameters of environments. If the robot has known parameters (geometry, material and magnetic flux), we are able to obtain information from its environment. Numerous experiences can be achieved to study the quantitative impact

of parameters variation such as chip/electromagnets relative position, surface roughness, viscosity, adhesion forces. The possibility to inspect the very challenging contact between the microrobot and the substrate will help to get a clearer understanding of the physics. We have achieved the following results on the environmental sensing:

— viscous and magnetic power sweep using breakdown phenomenon while rotating
— mapping of the robot speed during translation
— transition from static to dynamic regime

and they provided us important information to further improve the behaviour of our robot. It seems that movement changes drastically the nature of surfaces contact, simplifying the dynamics as well. The height difference between the substrate of the chip and the electromagnets has a strong impact on the vertical orientation of the microrobot due to **z**-component of the magnetic field.

Often in literature,deformations of the structures is analysed to obtain physical data and better understand our system and its environment. It is less true for dynamics and the created methods we have developed needs fem efforts to be pushed to become a general systematic tool.Through investigation on this sensing aspect of microrobots, I contributed to add the knowledge on the vision algorithm to the microrobotics activities in LPN. According to our observations, next important steps of development:

— a fast angular detection algorithm, allowing real time treatment to achieve fast measurement and batch processing
— an increased control on the vertical position and orientation of the microfluidic stage
— new methods to deeper understand certain regime: breakdown phenomenon excitability zone or static position forces
— explore Glass-Metal-Glass environment with eventual surface treatment and conditioning and deeper chamber depth
— imbedded alternative sensing capacity
— a scaling-down campaign, in particular to see the scale dependency of adhesion forces

Micromanipulation strategies extension and pulling action Micromanipulation issues have been at the root of our reflexion and have an important impact over our choice of MagPol's planar shape and scale. In parallel to the analysis of robot dynamics, the manipulation of micro-object close to biological bodies requires sufficiently large range of manipulation force and high enough positioning precision of MagPol with user's real-time teleoperation. Our objective quickly aimed at cargo transport of single or massive particles and densely packing assembly in microchannel by users, inspired from IEEE/NIST microassembly competition simulating as well as current needs in single and multiple cells handling in biology. This requires dedicated design of robots and teleoperated control system with high user operability.

An important effort to understand the design and control of electromagnets allowed high enough performances in particular on the increased magnetic force and versatile control and analysis tool. It was important to have this range of possibilities to enhance our exploration of manipulation function. The micromanipulation using mobile microrobot can be described as a chain with the components of user, computer, actuator and microrobots. Each of the following improvements on:

— an user's teleoperation interface with different options of ergonomy depending on the application
— a anywhere access in 2D plan using rotating uniform magnetic field / superposed gradient field

— a backward motion using magnetization phenomenon exploitation for new micromanipulation strategy
— a smoother motion thanks to correction of user command and a new bilayer (nickel / silicon nitride) design

have led to very high mobility performances, achieving complex trajectories (8-trajectory at the limit of user reactivity). They have also allowed us to achieve demonstration of progress on massive artificial objects manipulation (spherical shape such as bubble or beads). The first rank of our team at Karlsruhe 2013 edition of IEEE/NIST microassembly challenge confirmed the high performances of our system. Using a joystick or a keyboard, we successfully demonstrated the densly packing assembly of micro triangles in the microchannel.

Though the microrobot displays strong performances to turn our research toward application fields related to biology, there is further technological improvement to consider. We can mention the following steps of development for our system:

— demonstration on biological objects: yeast, bacterium *e. coli* or oocytes
— develop original micromanipulation strategy using tumbling motion
— extend to prehensive manipulation for pulling strategy, embedding new capacities in the robot structure
— couple gradient and uniform field to achieve tumbling or pulling motions in parallel

Closed-loop control of a mobile microrobot In addition to the propulsion and micromanipulation performances with sensing functionalities, closed-loop control of mobile microrobot has a key role toward practical applications. First it allows to reduce user dependency and makes the mobile microrobot accessible to the largest number of user. Second, it makes the system robust enough from the flow perturbations in case of propulsion through microchannels in biological applications.

We have understood from the dynamic analysis of microrobot's transfer function could not be simply described with analytical expressions, as it is dependent on the substrate and the microrobot operation. Dynamic regime, robot shape and adhesion forces have yet to be controlled and explored. This research direction strongly relies on our technological developments, and any improvement of this technology could have an impact. This field requires strong experimental efforts, particularly for statistical analysis and batch measurement. We have contributed to it by achieving:

— real-time position tracking and visual servoing at high frame rate
— 8-loop and circular pre-defined trajectories completion
— proportionnal correction by interruption and alignement of robot with its actuators

These progresses are narrow compared to ambition of microrobotic toward in-vivo applications but have already perform sufficient performance to be ranked # 1 at NIST Mobility challenge, edition 2014 at Hong Kong. On the one hand, some performances as for example imaging capacity to drive the robot with sufficient precision in time and space through skin and tissues completely outreach this thesis work and will of course constitute important technological steps. Using a microscopic vision system with visible light narrows the application to transparent environmen such as microfluidics, but the obtained results obtained can be extrapolated to more sophisticated imaging.

Many technological aspects can progress quickly keeping the microrobot's global principle. The software control loop becomes the most critical part. It can evolve by unlocking algorithm for tracking as trajectory correction like:

— a semi-automated control, if possible including force feedback
— a PID or Kalman filtering for robustness to adhesive forces non-linearities
— an automated micromanipulation, if possible by detection the object to move
— an orientation servoing using higher dimension visual features and adapted new electromagnetic setup

and some of this list items our also depending on our future understanding of adhesive perturbations.

On the hardware side, i.e. the microrobots, microfluidics and magnetic actuators can further be improved. It would complement the effort made on automationwith the following approaches:

— a smoother and steadier responding microrobot, like the bilayer microrobot called MagBil initiated
— a microfluidic chip with controlled and minimized adhesive part
— a faster time-response from electromagnetic coils, reducing their inertia

Conclusion Due to their micro sizes and high controllability, microrobots constitute a high potential for minimally invasive medicine and a high-throughput tool for biomedical diagnosis. The exploration of artificial mobile micro agents has been made possible only recently and is the the convergence of parallel development of micro computer increasing performances of treatment on one side and and the micro/nanofabrication process on the other side. Magnetic control - thanks to its high degrees of freedom, the possibility of control in 2D and its non-hazardous effects - remain one of the most promising path to propel them in liquids. A wide range of taxa have emerged and are now gathering toward concrete applications, thanks to their micrometric dimensions, high dynamics, high controllability and compatible integration to microfluidics.

This thesis could not of course provide exhaustive answer to each of these three axis of research forementioned. We rather propose an original angle, focusing on robot advantages from dynamics at low reynolds in confined microfluidics chambers. I sincerely hope the techniques and process developed as well as the physical model explored will bear the fruits for next generation design and microphysics exploration, getting ready for a very soon extension to biological bodies. I particularly wish a good and fruitful thesis to Antoine Barbot, new PhD student from our team, who has now (2014) been engaged on mobile microrobot dynamics for a year.

References

[1] Anthony P. F. Turner. Biosensors: sense and sensibility. *Chemical Society Reviews*, 42(8):3184–3196, April 2013.

[2] S. Franc, S. Borot, P. Y. Benhamou, B. Guerci, H. Hanaire, A. Faret, Y. Reznik, C. Simon, Al. Penfornis, and G. Charpentier. La pompe patch jewel® (debiotech) est plus précise, sensible et confortable que les pompes conventionnelles. *Diabetes & Metabolism*, 39, Supplement 1:A108, March 2013.

[3] M. Kumemura, D. Collard, R. Tourvielle, N. Lafitte, K. Montagne, S. Yoshizawa, D. Fourmy, C. Yamahata, L. Jalabert, Y. Sakai, S. Takeuchi, T. Fujii, and H. Fujita. Integrated MEMS platform with silicon nanotweezers and open microfluidic device for molecular and cellular biomechanical assays. In *2011 IEEE 24th International Conference on Micro Electro Mechanical Systems (MEMS)*, pages 67–70, January 2011.

[4] Adrien Plecis. *Etude et contrôle de la charge de surface dans les dispositifs micro/nanofluidiques : nouveaux outils pour les sciences séparatives*. PhD thesis, Paris 11, January 2008.

[5] Anne claire Louer. *Préconcentration sélective immunologique en nanofluidique : vers l'identification rapide d'agents du risque biologique*. PhD thesis, Université Paris Sud - Paris XI, September 2013.

[6] Ministère de l'éducation nationale, de l'enseignement supérieur et de la recherche française. A la découverte du nanomonde, 2005.

[7] R.S. Fearing. Survey of sticking effects for micro parts handling. In *1995 IEEE/RSJ International Conference on Intelligent Robots and Systems 95. 'Human Robot Interaction and Cooperative Robots', Proceedings*, volume 2, pages 212–217 vol.2, August 1995.

[8] Kevin Y. Ma, Pakpong Chirarattananon, Sawyer B. Fuller, and Robert J. Wood. Controlled flight of a biologically inspired, insect-scale robot. *Science*, 340(6132):603–607, March 2013.

[9] G. Hwang and H. Hashimoto. Note: Helical nanobelt force sensors. *Review of Scientific Instruments*, 83(12):126102, December 2012.

[10] Berg, H.C. Bacterial motility and behavior.

[11] Xiao Yan and Dong Sun. Cell patterning with robotically controlled optical tweezers. In *2013 IEEE/RSJ International Conference on Intelligent Robots and Systems (IROS)*, pages 490–495, November 2013.

[12] Gilgueng Hwang, Rémy Braive, Laurent Couraud, Antonella Cavanna, Ouerghi Abdelkarim, Isabelle Robert-Philip, Alexios Beveratos, Isabelle Sagnes, Sinan Haliyo, and Stéphane Régnier. Electro-osmotic propulsion of helical nanobelt swimmers. *The International Journal of Robotics Research*, 30(7):806–819, January 2011.

[13] Sangwon Kim, Famin Qiu, Samhwan Kim, Ali Ghanbari, Cheil Moon, Li Zhang, Bradley J. Nelson, and Hongsoo Choi. Fabrication and characterization of magnetic microrobots for three-dimensional cell culture and targeted transportation. *Advanced Materials*, 25(41):5863–5868, November 2013.

[14] Masaya Hagiwara, Tomohiro Kawahara, Yoko Yamanishi, Taisuke Masuda, Lin Feng, and Fumihito Arai. On-chip magnetically actuated robot with ultrasonic vibration for single cell manipulations. *Lab on a Chip*, 11(12):2049–2054, June 2011.

[15] Dominic R. Frutiger, Karl Vollmers, Bradley E. Kratochvil, and Bradley J. Nelson. Small, fast, and under control: Wireless resonant magnetic micro-agents. *The International Journal of Robotics Research*, November 2009.

[16] Ioan Alexandru Ivan, Gilgueng Hwang, Joel Agnus, Nicolas Chaillet, and Stephane Regnier. NIST and IEEE challenge for MagPieR: The fastest mobile microrobots in the world. *IEEE Robotics & Automation Magazine*, 20(2):63–70, June 2013.

[17] N. Shinjo and G.W. Swain. Use of a shape memory alloy for the design of an oscillatory propulsion system. *IEEE Journal of Oceanic Engineering*, 29(3):750–755, July 2004.

[18] Stefano Fusco, George Chatzipirpiridis, Kartik M. Sivaraman, Olgaç Ergeneman, Bradley J. Nelson, and Salvador Pané. Chitosan electrodeposition for microrobotic drug delivery. *Advanced Healthcare Materials*, 2(7):1037–1044, July 2013.

[19] Franziska Ullrich, Christos Bergeles, Juho Pokki, Olgac Ergeneman, Sandro Erni, George Chatzipirpiridis, Salvador Pané, Carsten Framme, and Bradley J. Nelson. Mobility experiments with microrobots for minimally invasive intraocular surgery. *Investigative Ophthalmology & Visual Science*, 54(4):2853–2863, April 2013.

[20] L. Ferlazzo, E. Cambril, F. Leroy, L. Largeau, and O. Mauguin. Electrodeposited masks for high aspect ratio etching applications. *JNTE 10 French Symposium on Emerging Technologies for micro-nanofabrication*, 10:76–77, 2010.

[21] J. Zhang, K. L. Tan, G. D. Hong, L. J. Yang, and H. Q. Gong. Polymerization optimization of SU-8 photoresist and its applications in microfluidic systems and MEMS. *Journal of Micromechanics and Microengineering*, 11(1):20, January 2001.

[22] Tomohiro Kawahara, Masakuni Sugita, Masaya Hagiwara, Fumihito Arai, Hiroyuki Kawano, Ikuko Shihira-Ishikawa, and Atsushi Miyawaki. On-chip microrobot for investigating the response of aquatic microorganisms to mechanical stimulation. *Lab on a Chip*, 13(6):1070–1078, February 2013.

[23] Francesco Pedaci, Zhuangxiong Huang, Maarten van Oene, Stephane Barland, and Nynke H. Dekker. Excitable particles in an optical torque wrench. *Nature Physics*, 7(3):259–264, March 2011.

[24] William D. Callister and David G. Rethwisch. *Fundamentals of Materials Science and Engineering: An Integrated Approach*. John Wiley & Sons, May 2012.

[25] Kenneth M. Ralls, Thomas H. Courtney, and John Wulff. *Introduction to Materials Science and Engineering*. Wiley, September 1976.

[26] Bernard Espiau, François Chaumette, and Patrick Rives. Une nouvelle approche de la relation vision-commande en robotique. 1990.

[27] Microbotics, June 2014. Page Version ID: 609712422.

[28] Biomedical sciences, July 2014. Page Version ID: 619120834.

[29] OECD. Dépenses totales de santé par tête. Santé : Tableaux-clés de l'OCDE, Organisation for Economic Co-operation and Development, Paris, 2014.

[30] IRDES. Healthcare expenses 2012, france, 2012.

[31] La france, championne des nouvelles technologies médicales, February 2014.

[32] Technologies médicales : cinq start-up françaises à la pointe, February 2014.

[33] Health, demographic change and wellbeing, 2014.

[34] Quatrième révolution industrielle : 3 projets d'usine du futur - techniques de l'ingénieur, May 2014.

[35] Les perspectives du marché du diagnostic in vitro en france : Les echos etudes, March 2012.

[36] Cangel Pui Yee Chan, Wing Cheung Mak, Kwan Yee Cheung, King Keung Sin, Cheuk Man Yu, Timothy H. Rainer, and Reinhard Renneberg. Evidence-based point-of-care diagnostics: Current status and emerging technologies. *Annual Review of Analytical Chemistry*, 6(1):191–211, 2013.

[37] Samuel K. Sia and Larry J. Kricka. Microfluidics and point-of-care testing. *Lab on a Chip*, 8(12):1982, 2008.

[38] Anne-Claire Louër, Adrien Plecis, Antoine Pallandre, Jean-Christophe Galas, André Estevez-Torres, and Anne-Marie Haghiri-Gosnet. Pressure-assisted selective preconcentration in a straight nanochannel. *Analytical Chemistry*, 85(16):7948–7956, August 2013.

[39] Alan E. Guttmacher, Francis S. Collins, Muin J. Khoury, Linda L. McCabe, and Edward R.B. McCabe. Population screening in the age of genomic medicine. *New England Journal of Medicine*, 348(1):50–58, January 2003.

[40] Aris Persidis. High-throughput screening. *Bio/technology*, 16(5):488–489, May 1998.

[41] Leland C. Clark and Champ Lyons. Electrode systems for continuous monitoring in cardiovascular surgery. *Annals of the New York Academy of Sciences*, 102(1):29–45, October 1962.

[42] M. Shichiri, R. Kawamori, Y. Yamasaki, N. Hakui, and H. Abe. Wearable artificial endocrine pancrease with needle-type glucose sensor. *Lancet*, 2(8308):1129–1131, November 1982.

[43] E. Meng and R. Sheybani. Insight: implantable medical devices. *Lab on a Chip*, 14(17):3233–3240, July 2014.

[44] D. Panescu. Emerging technologies [wireless communication systems for implantable medical devices]. *IEEE Engineering in Medicine and Biology Magazine*, 27(2):96–101, March 2008.

[45] Diana M. Rodriguez Tobon. *RFID application for biological telemetry*. 2005.

[46] Robin Hui Liu and Piotr Grodzinski. Development of integrated microfluidic system for genetic analysis. *Journal of Micro/Nanolithography, MEMS, and MOEMS*, 2(4):340–355, 2003.

[47] M. V. Yezhelyev, A. Al-Hajj, C. Morris, A. I. Marcus, T. Liu, M. Lewis, C. Cohen, P. Zrazhevskiy, J. W. Simons, A. Rogatko, S. Nie, X. Gao, and R. M. O'Regan. In situ molecular profiling of breast cancer biomarkers with multicolor quantum dots. *Advanced Materials*, 19(20):3146–3151, October 2007.

[48] Elsa Mazari. *Microsytèmes magnétiques et électriques pour la modification spatio-temporelle de voies de signalisation biologiques*. Paris 11, July 2013.

[49] Lequan Zhang, Xiaochen Xu, Changhong Hu, Lei Sun, Jesse T. Yen, Jonathan M. Cannata, and K. Kirk Shung. A high-frequency, high frame rate duplex ultrasound linear array imaging system for small animal imaging. *IEEE transactions on ultrasonics, ferroelectrics, and frequency control*, 57(7):1548–1557, July 2010.

[50] Medtronic. Activa® PC+s press release, deep brain stimulation system enables research toward personalized treatment of neurological and psychological diseases, 2013.

[51] Laparoscopic surgery - what is it?, 2012.

[52] Leo Y. T. Chou, Kevin Ming, and Warren C. W. Chan. Strategies for the intracellular delivery of nanoparticles. *Chemical Society Reviews*, 40(1):233–245, December 2010.

[53] Tobias Neuberger, Bernhard Schöpf, Heinrich Hofmann, Margarete Hofmann, and Brigitte von Rechenberg. Superparamagnetic nanoparticles for biomedical applications: Possibilities and limitations of a new drug delivery system. *Journal of Magnetism and Magnetic Materials*, 293(1):483–496, May 2005.

[54] B Hildebrandt. The cellular and molecular basis of hyperthermia. *Critical Reviews in Oncology/Hematology*, 43(1):33–56, July 2002.

[55] Yuanyuan Su, Xinpan Wei, Fei Peng, Yiling Zhong, Yimei Lu, Shao Su, Tingting Xu, Shuit-Tong Lee, and Yao He. Gold nanoparticles-decorated silicon nanowires as highly efficient near-infrared hyperthermia agents for cancer cells destruction. *Nano Letters*, 12(4):1845–1850, April 2012.

[56] J E Wickham. The new surgery. *British Medical Journal (Clinical research ed.)*, 295(6613):1581–1582, December 1987.

[57] B. Kübler U. Seibold. Sensorized and actuated instruments for minimally invasive robotic surgery. pages 482–485, 2004.

[58] Nicolas Chaillet and Stéphane Régnier. *Microrobotics for Micromanipulation*. Wiley-ISTE, London, UK : Hoboken, NJ, 1 edition edition, July 2010.

[59] Tim Chapman. Lab automation and robotics: Automation on the move. *Nature*, 421(6923):661–666, February 2003.

[60] Yuji Haraguchi, Tatsuya Shimizu, Tadashi Sasagawa, Hidekazu Sekine, Katsuhisa Sakaguchi, Tetsutaro Kikuchi, Waki Sekine, Sachiko Sekiya, Masayuki Yamato, Mitsuo Umezu, and Teruo Okano. Fabrication of functional three-dimensional tissues by stacking cell sheets in vitro. *Nature Protocols*, 7(5):850–858, May 2012.

[61] Fiona J. Gilbert, Susan M. Astley, Maureen G.C. Gillan, Olorunsola F. Agbaje, Matthew G. Wallis, Jonathan James, Caroline R.M. Boggis, and Stephen W. Duffy. Single reading with computer-aided detection for screening mammography. *New England Journal of Medicine*, 359(16):1675–1684, 2008.

[62] Michael Goldfarb, Brian E. Lawson, and Amanda H. Shultz. Realizing the promise of robotic leg prostheses. *Science Translational Medicine*, 5(210):210ps15–210ps15, June 2013.

[63] Gabriel I. Barbash and Sherry A. Glied. New technology and health care costs - the case of robot-assisted surgery. *New England Journal of Medicine*, 363(8):701–704, 2010.

[64] George M. Whitesides. The origins and the future of microfluidics. *Nature*, 442(7101):368–373, July 2006.

[65] George Whitesides. The lab finally comes to the chip! *Lab on a Chip*, 14(17):3125–3126, July 2014.

[66] S. Sakuma, B. Turan, and F. Arai. High throughput mechanical characterization of oocyte using robot integrated microfluidic chip. In *2013 IEEE/RSJ International Conference on Intelligent Robots and Systems (IROS)*, pages 2047–2052, November 2013.

[67] Taisuke Masuda, Miyako Niimi, Hayao Nakanishi, Yoko Yamanishi, and Fumihito Arai. Cancer cell separator using size-dependent filtration in microfluidic chip. *Sensors and Actuators B: Chemical*, 185:245–251, August 2013.

[68] Elsa Mazari, Xuan Zhao, Isabelle Migeotte, Jérôme Collignon, Charlie Gosse, and Aitana Perea-Gomez. A microdevice to locally electroporate embryos with high efficiency and reduced cell damage. *Development (Cambridge, England)*, 141(11):2349–2359, June 2014.

[69] Yajing Song, Péter Gyarmati, Ana Catarina Araújo, Joakim Lundeberg, Harry Brumer, and Patrik L. Ståhl. Visual detection of DNA on paper chips. *Analytical Chemistry*, 86(3):1575–1582, February 2014.

[70] Mahdi Azizian, Mahta Khoshnam, Nima Najmaei, and Rajni V. Patel. Visual servoing in medical robotics: a survey. part i: endoscopic and direct vision imaging - techniques and applications. *The International Journal of Medical Robotics and Computer Assisted Surgery*, pages n/a–n/a, September 2013.

[71] Reza Seifabadi, Sang-Eun Song, Axel Krieger, Nathan Bongjoon Cho, Junichi Tokuda, Gabor Fichtinger, and Iulian Iordachita. Robotic system for MRI-guided prostate biopsy: feasibility of teleoperated needle insertion and ex vivo phantom study. *International Journal of Computer Assisted Radiology and Surgery*, 7(2):181–190, March 2012.

[72] Kishan Dholakia, Peter Reece, and Min Gu. Optical micromanipulation. *Chemical Society Reviews*, 37(1):42–55, December 2007.

[73] Brahim Tamadazte. *Vision 3D et Commande par asservissements visuels pour la micromanipulation et le micro-assemblage de MEMS. Application à l'automatisation d'une station de micro-assemblage.* PhD thesis, Université de Franche-Comté, November 2009.

[74] T. Nammoto, K. Hashimoto, S. Kagami, and K. Kosuge. High speed/accuracy visual servoing based on virtual visual servoing with stereo cameras. In *2013 IEEE/RSJ International Conference on Intelligent Robots and Systems (IROS)*, pages 44–49, November 2013.

[75] O. Kermorgant. Partial visibility constraint in 3d visual servoing. In *2013 IEEE/RSJ International Conference on Intelligent Robots and Systems (IROS)*, pages 572–577, November 2013.

[76] H. Hawkeye Irving King. *Human-Machine Collaborative Telerobotics: Computer Assistance for Manually Controlled Telesurgery and Teleoperation*. Thesis, April 2014. Thesis (Ph.D.)–University of Washington, 2014.

[77] O. A. J. van der Meijden and M. P. Schijven. The value of haptic feedback in conventional and robot-assisted minimal invasive surgery and virtual reality training: a current review. *Surgical Endoscopy*, 23(6):1180–1190, June 2009.

[78] Marc J. Madou. *Fundamentals of Microfabrication: The Science of Miniaturization, Second Edition*. CRC Press, March 2002.

[79] Etienne Guyon, Jean-Pierre Hulin, and Luc Petit. *Hydrodynamique physique*. CNRS Editions, Les Ulis, 3e édition edition, September 2012.

[80] Céline Hoffmann, Elsa Mazari, Sylvie Lallet, Roland Le Borgne, Valérie Marchi, Charlie Gosse, and Zoher Gueroui. Spatiotemporal control of microtubule nucleation and assembly using magnetic nanoparticles. *Nature Nanotechnology*, 8(3):199–205, March 2013.

[81] A. Sanati Nezhad. Microfluidic platforms for plant cells studies. *Lab on a Chip*, 14(17):3262–3274, July 2014.

[82] David R. Walt. Protein measurements in microwells. *Lab on a Chip*, 14(17):3195–3200, July 2014.

[83] A. K. Capulli, K. Tian, N. Mehandru, A. Bukhta, S. F. Choudhury, M. Suchyta, and K. K. Parker. Approaching the in vitro clinical trial: engineering organs on chips. *Lab on a Chip*, 14(17):3181–3186, July 2014.

[84] Zoltán Göröcs and Aydogan Ozcan. Biomedical imaging and sensing using flatbed scanners. *Lab on a Chip*, 14(17):3248–3257, July 2014.

[85] Jacob N. Israelachvili. *Intermolecular and Surface Forces, Third Edition: Revised Third Edition*. Academic Press, Burlington, MA, 3 edition edition, June 2011.

[86] Michaël Gauthier. *Micromanipulation robotique en milieu liquide.* PhD thesis, Université de Franche-Comté, May 2011.

[87] Sébastien Alvo. *Etude, modélisation et mesure des forces d'adhésion à l'échelle microscopique.* PhD thesis, Université Pierre et Marie Curie - Paris VI, October 2012.

[88] Patrick Tabeling. *Introduction to Microfluidics*. Oxford University Press, November 2005.

[89] Tiantian Xu. *Propulsion Characteristics and Visual Servo Control of Scaled-up Helical Microswimmers*. PhD thesis, Université Pierre et Marie Curie - Paris VI, March 2014.

[90] Chytra Pawashe, Steven Floyd, and Metin Sitti. Modeling and experimental characterization of an untethered magnetic micro-robot. *The International Journal of Robotics Research*, 28(8):1077–1094, January 2009.

[91] Gilgueng Hwang, H. Salmon, L.A. Ivan, J. Agnus, N. Chaillet, S. Regnier, and A. Haghiri-Gosnet. Large range versatile wireless microrobotic manipulators in microfluidic devices. In *2013 IEEE 26th International Conference on Micro Electro Mechanical Systems (MEMS)*, pages 1179–1182, January 2013.

[92] Andrew T. Baisch, Onur Ozcan, Benjamin Goldberg, Daniel Ithier, and Robert J. Wood. High speed locomotion for a quadrupedal microrobot. *The International Journal of Robotics Research*, page 0278364914521473, May 2014.

[93] Gabe Nelson, Aaron Saunders, Neil Neville, Ben Swilling, Joe Bondaryk, Devin Billings, Chris Lee, Robert Playter, and Marc Raibert. PETMAN: A humanoid robot for testing chemical protective clothing. *Journal of the Robotics Society of Japan*, 30(4):372–377, 2012.

[94] Robert Wood, Radhika Nagpal, and Gu-Yeon Wei. Flight of the robobees. *Scientific American*, 308(3):60–65, 2013.

[95] Timothy S. Arthur, Daniel J. Bates, Nicolas Cirigliano, Derek C. Johnson, Peter Malati, James M. Mosby, Emilie Perre, Matthew T. Rawls, Amy L. Prieto, and Bruce Dunn. Three-dimensional electrodes and battery architectures. *MRS Bulletin*, 36(07):523–531, 2011.

[96] Purcell, EM. Life at low reynolds number. *American Journal of Physics*, 1973.

[97] Howard C. Berg and Douglas A. Brown. Chemotaxis in escherichia coli analysed by three-dimensional tracking. *Nature*, 239(5374):500–504, October 1972.

[98] Dongwook Kim, Albert Liu, Eric Diller, and Metin Sitti. Chemotactic steering of bacteria propelled microbeads. *Biomedical Microdevices*, 14(6):1009–1017, December 2012.

[99] S. Martel, W. Andre, Mahmood Mohammadi, Zhao Lu, and Ouajdi Felfoul. Towards swarms of communication-enabled and intelligent sensotaxis-based bacterial microrobots capable of collective tasks in an aqueous medium. In *IEEE International Conference on Robotics and Automation, 2009. ICRA '09*, pages 2617–2622, May 2009.

[100] Andrey Sokolov, Mario M. Apodaca, Bartosz A. Grzybowski, and Igor S. Aranson. Swimming bacteria power microscopic gears. *Proceedings of the National Academy of Sciences*, 107(3):969–974, January 2010.

[101] Wei Gao, Xiaomiao Feng, Allen Pei, Christopher R. Kane, Ryan Tam, Camille Hennessy, and Joseph Wang. Bioinspired helical microswimmers based on vascular plants. *Nano Letters*, 14(1):305–310, January 2014.

[102] A. Ashkin, J. M. Dziedzic, J. E. Bjorkholm, and Steven Chu. Observation of a single-beam gradient force optical trap for dielectric particles. *Optics Letters*, 11(5):288–290, May 1986.

[103] S. Fukada, H. Maruyama, T. Masuda, and F. Arai. 3d fabrication and manipulation of hybrid nanorobots by laser for single cell analysis. In *2012 International Symposium on Micro-NanoMechatronics and Human Science (MHS)*, pages 479–481, November 2012.

[104] Hisataka Maruyama, Fumihito Arai, and Toshio Fukuda. On-chip pH measurement using functionalized gel-microbeads positioned by optical tweezers. *Lab on a Chip*, 8(2):346–351, February 2008.

[105] H. Marino, C. Bergeles, and B.J. Nelson. Robust electromagnetic control of microrobots under force and localization uncertainties. *IEEE Transactions on Automation Science and Engineering*, 11(1):310–316, January 2014.

[106] Zhenlong Wang, Yangwei Wang, Jian Li, and Guanrong Hang. A micro biomimetic manta ray robot fish actuated by SMA. In *2009 IEEE International Conference on Robotics and Biomimetics (ROBIO)*, pages 1809–1813, December 2009.

[107] E. Smela. Conjugated polymer actuators for biomedical applications. *Advanced Materials*, 15(6):481–494, March 2003.

[108] Joshua Gafford, Ye Ding, Andrew Harris, Terrence McKenna, Panagiotis Polygerinos, Donal Holland, Arthur Moser, and Conor Walsh. Shape deposition manufacturing of a soft, atraumatic, deployable surgical grasper1. *Journal of Medical Devices*, 8(3):030927–030927, July 2014.

[109] Dominic R. Frutiger. *MagMites: Design, Fabrication, and Control of Wireless Resonant Magnetic Micromachines for Dry and Wet Environments*. PhD thesis, ETHZ, 2010.

[110] E. Diller, Naicheng Zhang, and M. Sitti. Bonding methods for modular micro-robotic assemblies. In *2013 IEEE International Conference on Robotics and Automation (ICRA)*, pages 2588–2593, May 2013.

[111] H. Salmon, L. Couraud, and Gilgueng Hwang. Swimming property characterizations of magnetic polarizable microrobots. In *2013 IEEE International Conference on Robotics and Automation (ICRA)*, pages 5520–5526, May 2013.

[112] Zhenlong Wang, Guanrong Hang, Jian Li, Yangwei Wang, and Kai Xiao. A micro-robot fish with embedded SMA wire actuated flexible biomimetic fin. *Sensors and Actuators A: Physical*, 144(2):354–360, June 2008.

[113] Pierre Pouponneau, Gaël Bringout, and Sylvain Martel. Therapeutic magnetic microcarriers guided by magnetic resonance navigation for enhanced liver chemoembilization: a design review. *Annals of Biomedical Engineering*, 42(5):929–939, May 2014.

[114] S. C. Esteves, R. K. Sharma, A. J. Thomas, and A. Agarwal. Improvement in motion characteristics and acrosome status in cryopreserved human spermatozoa by swim-up processing before freezing. *Human Reproduction*, 15(10):2173–2179, January 2000.

[115] Isabelle Fitton, Roel J. H. M. Steenbakkers, Lambert Zijp, Joop C. Duppen, Emile F. I. Comans, Saar H. Muller, Peter J. C. M. Nowak, Coen R. N. Rasch, and Marcel van Herk. Retrospective attenuation correction of PET data for radiotherapy planning using a free breathing CT. *Radiotherapy and Oncology: Journal of the European Society for Therapeutic Radiology and Oncology*, 83(1):42–48, April 2007.

[116] J. Duryea, M. Magalnick, S. Alli, L. Yao, M. Wilson, and R. Goldbach-Mansky. Semiautomated three-dimensional segmentation software to quantify carpal bone volume changes on wrist CT scans for arthritis assessment. *Medical Physics*, 35(6):2321–2330, June 2008.

[117] Venkatasubramaniam S. Kalambur, Bumsoo Han, Bruce E. Hammer, Thomas W. Shield, and John C. Bischof. In vitro characterization of movement, heating and visualization of magnetic nanoparticles for biomedical applications. *Nanotechnology*, 16(8):1221, August 2005.

[118] Sheila C Rankin. CT and MRI. *Surgery (Oxford)*, 23(5):162–165, May 2005.

[119] Hooman Azmi and Michael Schulder. Stereotactic accuracy of a 3-tesla magnetic resonance unit. *Stereotactic and Functional Neurosurgery*, 80(1-4):140–145, 2003.

[120] Kiyoyuki Chinzei, Ron Kikinis, and Ferenc A. Jolesz. MR compatibility of mechatronic devices: Design criteria. In Chris Taylor and Alain Colchester, editors, *Medical Image Computing and Computer-Assisted Intervention - MICCAI'99*, number 1679 in Lecture Notes in Computer Science, pages 1020–1030. Springer Berlin Heidelberg, January 1999.

[121] Eric Aboussouan Ouajdi Felfoul. Real-time positioning and tracking technique for endovascular untethered microrobots propelled by MRI gradients. pages 2693–2698, 2009.

[122] (first) Lutz, Philippe. Détail des projets financés ASTRID | ANR - agence nationale de la recherche, 2013.

[123] T. Sievers and S. Fatikow. Visual servoing of a mobile microrobot inside a scanning electron microscope. In *2005 IEEE/RSJ International Conference on Intelligent Robots and Systems, 2005. (IROS 2005)*, pages 1350–1354, August 2005.

[124] Sylvain Martel, Charles C. Tremblay, Serge Ngakeng, and Guillaume Langlois. Controlled manipulation and actuation of micro-objects with magnetotactic bacteria. *Applied Physics Letters*, 89(23):233904, December 2006.

[125] David B. Camarillo, Thomas M. Krummel, and J. Kenneth Salisbury Jr. Robotic technology in surgery: Past, present, and future. *The American Journal of Surgery*, 188(4, Supplement 1):2–15, October 2004.

[126] Makoto Hashizume, Kouzou Konishi, Norifumi Tsutsumi, Shohei Yamaguchi, and Rinshyun Shimabukuro. A new era of robotic surgery assisted by a computer-enhanced surgical system. *Surgery*, 131(1 Suppl):S330–333, January 2002.

[127] Jean V. Joseph, Manit Arya, and Hitendra R. H. Patel. Robotic surgery: the coming of a new era in surgical innovation. *Expert Review of Anticancer Therapy*, 5(1):7–9, February 2005.

[128] Bradley J. Nelson, Ioannis K. Kaliakatsos, and Jake J. Abbott. Microrobots for minimally invasive medicine. *Annual Review of Biomedical Engineering*, 12:55–85, August 2010.

[129] Eric K. Sackmann, Anna L. Fulton, and David J. Beebe. The present and future role of microfluidics in biomedical research. *Nature*, 507(7491):181–189, March 2014.

[130] Anirudha D. Jagtap and Cameron N. Riviere. Applied force during vitreoretinal microsurgery with handheld instruments. In *Proc. 26 th Intl. Conf. IEEE Eng. Med. Biol. Soc*, pages 2771–2773, 2004.

[131] K. Berk Yesin, Karl Vollmers, and Bradley J. Nelson. Modeling and control of untethered biomicrorobots in a fluidic environment using electromagnetic fields. *The International Journal of Robotics Research*, 25(5-6):527–536, January 2006.

[132] Alan W Flake. Surgery in the human fetus: the future. *The Journal of Physiology*, 547(Pt 1):45–51, February 2003.

[133] M. Berris and M. Shoham. Febotics - a marriage of fetal surgery and robotics. *Computer Aided Surgery: Official Journal of the International Society for Computer Aided Surgery*, 11(4):175–180, July 2006.

[134] Shuvo Roy, Lisa A. Ferrara, Aaron J. Fleischman, and Edward C. Benzel. Mems and neurosurgery. In Mauro Ferrari, Tejal Desai, and Sangeeta Bhatia, editors, *BioMEMS and Biomedical Nanotechnology*, pages 95–123. Springer US, January 2007.

[135] Blaine Kristo, Joseph C. Liao, Hercules P. Neves, Bernard M. Churchill, Carlo D. Montemagno, and Peter G. Schulam. Microelectromechanical systems in urology. *Urology*, 61(5):883–887, May 2003.

[136] Daniel A. Fletcher and Julie A. Theriot. An introduction to cell motility for the physical scientist. *Physical Biology*, 1(1):T1, March 2004.

[137] Zhanhui Wang, Min-Cheol Kim, Manuel Marquez, and Todd Thorsen. High-density microfluidic arrays for cell cytotoxicity analysis. *Lab on a Chip*, 7(6):740–745, June 2007.

[138] Famin Qiu, Li Zhang, Kathrin E. Peyer, Marco Casarosa, Alfredo Franco-Obregon, Hongsoo Choi, and Bradley J. Nelson. Noncytotoxic artificial bacterial flagella fabricated from biocompatible ORMOCOMP and iron coating. *Journal of Materials Chemistry B*, 2(4):357–362, December 2013.

[139] Allison P. Berke, Linda Turner, Howard C. Berg, and Eric Lauga. Hydrodynamic attraction of swimming microorganisms by surfaces. *Physical Review Letters*, 101(3):038102, July 2008.

[140] Li Zhang, Tristan Petit, Yang Lu, Bradley E. Kratochvil, Kathrin E. Peyer, Ryan Pei, Jun Lou, and Bradley J. Nelson. Controlled propulsion and cargo transport of rotating nickel nanowires near a patterned solid surface. *ACS Nano*, 4(10):6228–6234, October 2010.

[141] H. Salmon, L. Couraud, and G. Hwang. Using breakdown phenomenon as mobile magnetic field sensor in microfluidics. In *2013 IEEE/RSJ International Conference on Intelligent Robots and Systems (IROS)*, pages 2041–2046, November 2013.

[142] David C. Jiles. *Introduction to Magnetism and Magnetic Materials, Second Edition*. CRC Press, June 1998.

[143] Y. C. Fung. *Biomechanics*. Springer New York, New York, NY, 1990.

[144] Alexander E. Smith, Zhibing Zhang, Colin R. Thomas, Kennith E. Moxham, and Anton P. J. Middelberg. The mechanical properties of saccharomyces cerevisiae. *Proceedings of the National Academy of Sciences*, 97(18):9871–9874, August 2000.

[145] Ida Dulińska, Marta Targosz, Wojciech Strojny, Małgorzata Lekka, Paweł Czuba, Walentyna Balwierz, and Marek Szymoński. Stiffness of normal and pathological erythrocytes studied by means of atomic force microscopy. *Journal of Biochemical and Biophysical Methods*, 66(1–3):1–11, March 2006.

[146] J. K. Luo, M. Pritschow, A. J. Flewitt, S. M. Spearing, N. A. Fleck, and W. I. Milne. Effects of process conditions on properties of electroplated ni thin films for microsystem applications. *Journal of The Electrochemical Society*, 153(10):D155–D161, January 2006.

[147] P. Svarnas, A. Plecis, C. Nanteuil, D. Duong, C. David, M. Muller, and Y. Chen. Glass-based nanofluidic device for biomolecule preconcentration study. *The European Physical Journal - Applied Physics*, 44(03):245–253, 2008.

[148] Kristina Grifantini. Lab-on-a-chip made of paper, May 2008.

[149] E. P. Wohlfarth. *Ferromagnetic Materials: A Handbook on the Properties of Magnetically Ordered Substances*. North-Holland Publishing Company, 2013.

[150] Shinya Sakuma, Keisuke Kuroda, Chia-Hung Dylan Tsai, Wataru Fukui, Fumihito Arai, and Makoto Kaneko. Red blood cell fatigue evaluation based on the close-encountering point between extensibility and recoverability. *Lab on a Chip*, 14(6):1135–1141, February 2014.

[151] E. Marchand and François Chaumette. Feature tracking for visual servoing purposes. *Robotics and Autonomous Systems*, 52(1):53–70, 2005.

[152] Bruce D. Lucas and Takeo Kanade. An iterative image registration technique with an application to stereo vision. In *IJCAI*, volume 81, pages 674–679, 1981.

[153] Carlo Tomasi and Takeo Kanade. Detection and tracking of point features. Technical report, International Journal of Computer Vision, 1991.

[154] Linda Shapiro. *Computer Vision and Image Processing*. Academic Press, April 1992.

[155] Robert Adler. A study of locking phenomena in oscillators. *Proceedings of the IEEE*, 61(10):1380–1385, October 1973.

[156] Dichotomy, September 2014. Page Version ID: 626048561.

[157] Runge–kutta methods, September 2014. Page Version ID: 621465037.

[158] Luc Petit, Jean-Pierre Hulin, and Étienne Guyon. *Hydrodynamique physique*. EDP Sciences, December 2012.

[159] K.R. Williams, K. Gupta, and M. Wasilik. Etch rates for micromachining processing-part II. *Journal of Microelectromechanical Systems*, 12(6):761–778, December 2003.

[160] Ciprian Iliescu, Francis E. H. Tay, and Jianmin Miao. Strategies in deep wet etching of pyrex glass. *Sensors and Actuators A: Physical*, 133(2):395–400, February 2007.

[161] M. M. V. Taklo, P. Storås, K. Schjølberg-Henriksen, H. K. Hasting, and H. Jakobsen. Strong, high-yield and low-temperature thermocompression silicon wafer-level bonding with gold. *Journal of Micromechanics and Microengineering*, 14(7):884, July 2004.

[162] Lydéric Bocquet and Jean-Louis Barrat. Hydrodynamic properties of confined fluids. *Journal of Physics: Condensed Matter*, 8(47):9297, November 1996.

[163] M. S. Miller, F. E. Stageberg, Y. M. Chow, K. Rook, and L. A. Heuer. Influence of rf magnetron sputtering conditions on the magnetic, crystalline, and electrical properties of thin nickel films. *Journal of Applied Physics*, 75(10):5779–5781, May 1994.

[164] S. Thorpe, D. Fize, and C. Marlot. Speed of processing in the human visual system. *Nature*, 381(6582):520–522, June 1996.

[165] Berthold Horn. *Robot Vision*. MIT Press, January 1986.

[166] Xavier Broquère. *Planification de trajectoire pour la manipulation d'objets et l'interaction Homme-robot*. PhD thesis, Université Paul Sabatier - Toulouse III, July 2011.

Publications

International Journals

H. Salmon, L. Couraud, G. Hwang, Intl J. of Robotics Research (in preparation), 2014

H. Salmon, L. Couraud, C. Roblin, G. Hwang, Microelectronics Engineering (in preparation), 2014

H. Salmon, L. Couraud, G. Hwang, "Mobile Microrobotic Sensor in Microfluidics using High-Temporal Resolution Dynamics Analysis" Scientific Report (under review) , 2014 .

G. Hwang, H. Salmon, S. Alvo, I. A. Ivan, J. Agnus, N. Chaillet, S. Régnier, A.-M. Haghiri-Gosnet "Mobile microrobotic manipulator in microfluidics" Sensors and Actuators A: Physical, 2013.

International Conferences Proceedings

H. Salmon, L. Couraud, C. Roblin and G. Hwang "Glass-Metal-Glass Microfluidic Chip for Mobile Microrobotic and Applications" 40th Intl Conf. on Micro and Nano Engineering (MNE), 2014.

H. Salmon, L. Couraud, G. Hwang "Using breakdown phenomenon as mobile magnetic field sensor in microfluidics". IEEE/RSJ Intl Conf. on Intelligent Robots and Systems (IROS), 2041-2046, 2013.

H. Salmon, L. Couraud and G. Hwang "Swimming Property Characterizations of Magnetic Polarizable microrobots" IEEE Intl Conf. on Robotics and Automation, 5520 - 5526, 2013.

G. Hwang, H. Salmon, I. A. Ivan, J. A., N. Chaillet, S. Régnier, A.-M. Haghiri-Gosnet "Large range versatile wireless Micro-robotic Manipulators in Microfluidic Devices" IEEE 26th Intl Conf. on Micro Electro Mechanical Systems (MEMS), 2013.

G. Hwang, H. Salmon, L. Couraud, N. Allemandou, E. Cambril, L. Ferlazzo, D. Decanini "Fabrication and Characterization of Ultra-fast Thin-film Microrobots" 38th Intl Conf. on Micro and Nano Engineering (MNE), 2011.

G. Hwang, I. A. Ivan, J. Agnus, M. Rakotondrabe, E. L. Perez, S. Meriema, H. Salmon, S. Haliyo, N. Chaillet, S. Régnier, A.-M. Haghiri-Gosnet "Remotely powered floating microswimmers as colloidal microparticle manipulators" 37th Intl Conf. on Micro and Nano Engineering (MNE), 2011.

Awards

A. Barbot, H. Salmon, L. Couraud and G. Hwang, "# 1 Award for NIST and IEEE Micro Mobility Challenge",2014

H. Salmon, L. Couraud and G. Hwang, "# 1 Award for NIST and IEEE Micro Assembly

Challenge", 2013.

H. Salmon, L. Couraud and G. Hwang "Qualif. and participation for NIST and IEEE Mobile Microrobotics Challenges", 2012-2014.